

Proceedings of the 19th International Symposium on Advanced
Technology (ISAT-19)

Engineering Innovation for Food and Nutrition Security

14 January 2021

Los Baños, Laguna, Philippines

A Virtual Conference organized by the
University of the Philippines Los Baños



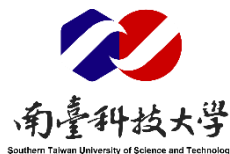
Co- organized by
Danang University of Science & Technology, Vietnam



Kogakuin University of Technology & Engineering, Japan



Southern Taiwan University of Science & Technology



Edited by the
19th International Symposium on Advanced Technology

Published by the
Kogakuin University of Technology & Engineering, Japan

ISSN 2434-4273

Table of Contents

| | |
|---|----|
| About ISAT-19 | 6 |
| Message from the UPLB Chancellor | 7 |
| Message from the Rector, DUT | 8 |
| Message from the President, KUTE | 9 |
| Message from the President, STUST | 10 |
| General Programme | 11 |
| Keynote Speeches | 12 |
| Engineering innovation for food and nutrition security: Design parameters and strategies for improvement of the food system to achieve food and nutrition security in the Philippines and elsewhere | 12 |
| Bright and dark sides of wheat flour foods | 12 |
| Plenary Presentations | 13 |
| The therapeutic effects of pomegranate on urinary bladder urothelial carcinoma | 13 |
| An intelligent control for robot by using internet | 14 |
| Technical Presentations | 15 |
| Architecture & Civil Engineering | 15 |
| Effect of temperature on structural deformation of Tran Thi Ly cable-stayed bridge | 16 |
| Development of concrete compressive strength predictive models based on non-destructive evaluation | 17 |
| Bio-mediated soil improvement is a potential method for mitigating soil erosion | 19 |
| Corrosion of steel with nanosilica coating using electrochemical impedance spectroscopy | 21 |
| Research on housing thermal environment and improvement of insulation performance in Australia | 23 |
| Study on strong motion characteristics near active faults | 25 |
| Development of the diagnosis and repair technologies for deteriorated wood materials | 27 |
| The study on the vacant lot reclaim design using green infrastructure technique | 29 |
| The study on the minimum and low cost vacant lot management approach | 31 |
| Traffic analysis and validation of customized local traffic simulator using PTV VISSIM | 33 |
| Artificial Intelligence & Smart Systems | 35 |
| Automatic cell segmentation and defect detection in electroluminescence images of solar photovoltaic modules | 36 |
| Development of individual cell components analysis method for tissue sample with TOF-SIMS | 38 |
| Development of a low-cost UAV pesticide sprayer for rice production system | 40 |
| An intelligent control for robot by using Internet | 42 |
| The development of Phalaenopsis cultivation environmental monitoring and control system based on IoT devices | 44 |
| Pulse signal-based emotion classification study by support vector machine | 46 |
| Neural-network-based classifier for breast cancer using FTIR signals obtained from tissues | 48 |
| Extracting keywords from videos to build a content-based search and recommendation system | 50 |

| | |
|--|-----|
| 3-dimensional analysis of cochlear structure using CT data..... | 52 |
| Effects of variations in the parameters of EBMA in motion estimation accuracy | 56 |
| Energy & Transportation | 58 |
| A pilot study on using rice straw as fuel for paddy drying | 59 |
| Isolation, characterization, and screening of purple non-sulfur bacteria for biohydrogen production | 60 |
| Comparison of temperature and relative humidity as exogenous variables for weekday load forecasting | 62 |
| Evaluation of the capacity value of a solar power plant in the Visayas grid, Philippines | 64 |
| A proposed self-powered data acquisition system for an agricultural pump testing rig | 66 |
| Food & Health | 68 |
| Synthesis of modified chitosan containing multi-hydroxyl group for adsorption boron | 69 |
| Ethanol extraction of bioactive compounds from waste onion leaves by conventional and microwave-assisted methods | 70 |
| Utilization of waste onion leaves for food applications..... | 72 |
| Evaluation of simulation model for constant temperature deep-bed drying of hybrid rice seeds..... | 74 |
| Prediction of moisture content of peanut kernel using near-infrared hyperspectral imaging technique | 76 |
| Visible and near-infrared spectroscopy for rapid prediction of sugarcane quality | 78 |
| Disease indexing for mango (<i>Mangifera indica</i> L. cv. 'Carabao') fruits using machine vision | 80 |
| Recirculating system with gravel and fluidized sand filter for catfish production..... | 82 |
| Efficacy of pomegranate peel extracts against urothelial carcinoma <i>in vitro</i> and <i>in vivo</i> | 84 |
| Modeling the effect of vitamin D intake on mortality in Vietnamese men | 86 |
| Synthesis of modified chitosan containing multi-hydroxyl group for adsorption boron | 88 |
| Classification skin defect of jujube by using spectral images | 90 |
| Effects of thin-layer drying temperature and tempering on hybrid rice seed | 92 |
| Human Engineering..... | 94 |
| Ergonomic keyboard for English and Tagalog languages..... | 95 |
| Construction of a Kalman filter for real time motion measurement | 97 |
| A study of the folding umbrella stick with solar-powered LED lighting..... | 99 |
| Development of infants suits for motion measurement | 101 |
| Motion analysis of infants using musculoskeletal model..... | 103 |
| A study on motion measurement for early screening for neurological disease | 105 |
| Experiment on selecting evaluation words for sensory evaluation of beautiful gait | 107 |
| Reducing bias and improving contrast of parametric images in positron emission tomography | 109 |
| A study on the view factor in sensory evaluation of human movement..... | 111 |
| Information & Communications Technology | 113 |
| A research on new type of local information dissemination system (D-ZEV System) | 114 |
| Enhancement of network infrastructure for security and communication at Danang General Hospital | 116 |

| | |
|--|-----|
| Radiation patterns of MgO and AlN evaluated by angle-resolved cathodoluminescence measurements | 118 |
| Performance of adaptive control CRE in multi-band heterogeneous mobile networks | 120 |
| Heterogeneous mobile networks using millimeter wave with three-dimensional beamforming | 122 |
| Field and virtual assessment for recurring hurricane reconnaissance in U.S. Gulf Coast | 124 |
| A study on dynamic path establishment method using superposition coding in EON | 126 |
| GPS positioning accuracy improvement by using drone in relay type GPS | 128 |
| Electrical characterization of Zr-based ReRAM with a sandwiched resistive switching layer | 130 |
| Transmission performance against subcarrier spacing of OFDM in multipath fading channels | 132 |
| User throughput improvement by three-dimensional beamforming in mobile systems | 134 |
| Realization of monolithic blue μ -LED pixels and their color conversion by phosphors | 136 |
| Parametric study of fabrication processes of micro-LED array and characterization of emission properties | 138 |
| Improving belief propagation decoding performances of polar codes using permuted factor graphs | 140 |
| Fundamental research for full duplex communications | 142 |
| Telemedicine using TVWS technology for rural consultations in the Philippines | 144 |
| Printed 8-port MIMO antennas for 5G C-band access point applications | 146 |
| Four-port MIMO antennas on USB device for 5G C-band applications | 148 |
| MIMO antennas of coupled-fed PIFAs for laptop computers | 150 |
| Tx power optimization of pico-eNB for multiband heterogeneous mobile networks | 152 |
| Materials, Mechanical & Manufacturing Engineering | 154 |
| Synthesis of polyhydroxybutyrate / cellulose / calcium carbonate bioplastic composites using heat-assisted solution casting method | 155 |
| Design thinking driven requirements elicitation method based on role-based prototyping | 157 |
| Improvement of production resource planning process at DAIWA Vietnam Co., Ltd. | 159 |
| Development of cassava (<i>Manihot esculenta</i> Crantz) mechanical planter | 161 |
| Structure of jet deflected by secondary flow | 163 |
| Selection of polyhydroxyalkanoates (PHA) extraction and recovery protocol using AHP-GRA | 165 |
| Fluorine concentration dependence on electrical and optical properties of In_2O_3 transparent film ... | 167 |
| Performance evaluation of a locally designed water pump | 169 |
| Motion of gas bubbles induced by cavitation bubbles | 171 |
| Development of a portable carrot harvester | 173 |
| Flow control using interaction between synthetic and continuous jet | 175 |
| Compositional analysis of black carbon aerosols by means of TOF-SIMS and SNMS | 177 |
| Structure of jet with velocity oscillation at slot | 179 |
| Electrochemical evaluation of physical / chemical coated positive electrode for lithium-ion batteries | 181 |
| Fabrication of core-shell structures using TiO_2 and PANI for methyl orange removal | 183 |
| Ferroelectric characteristics of $\text{SrBi}_2\text{Ta}_2\text{O}_9$ thin film and application | 185 |

| | |
|---|-----|
| To enhance mechanical property of PBI thin-film by E-beam irradiation..... | 187 |
| Aerodynamic characteristics of soccer balls focusing on drag crisis | 188 |
| Water Resources Engineering | 190 |
| Suitability analysis for SSIP through GIS-based water resources assessment | 191 |
| Simulating the impacts of deficit irrigation on corn yield and water productivity using coupled DSSAT CERES-Maize and Aquacrop models | 193 |
| Assessing the impacts of climate change on irrigation diversion water requirement in the Philippines | 195 |
| GIS-based suitability analysis of small water impounding projects (SWIPs) in CALABARZON region | 197 |
| Poster Presentations | 199 |
| Pictures of the ISAT-19 Conference | 203 |
| YouTube Links to Video Presentations and Recorded Presentations | 205 |
| Best Paper Awardees | 206 |
| Best Poster Awardees | 208 |
| Steering Committee..... | 210 |
| Program & Registration Committee | 210 |
| Technical Committee | 210 |
| Awards Committee | 211 |
| Technical & Administrative Support | 211 |



About ISAT-19

The International Symposium on Advanced Technology (ISAT) is an annual event organized and spearheaded by the Engineering Departments of Kogakuin University (KU) of Japan in 2002 for future cooperation between universities. ISAT focuses on joint research in the applied sciences devoted to resolving pressing national and social issues. Other consortium universities include The University of Danang- University of Science and Technology (DUT) in Vietnam, Southern Taiwan University of Science and Technology (STUST) in Taiwan, and the University of the Philippines Los Baños (UPLB). The UPLB was officially recognized as a member of the consortium through the College of Engineering and Agro-industrial Technology in 2017.



As previously announced, we had planned the 19th International Symposium on Advanced Technology (ISAT-19) in Clark City, Pampanga, Philippines in October 2020 and had to postpone it due to COVID-19. After consultation with the members of the consortium universities, it was decided to hold ISAT-19 as an online symposium instead on January 14, 2021.

The ISAT-19, organized by the UPLB, was held as a virtual conference for the first time, with the theme “Engineering Innovation for Food and Nutrition Security”. Presentations in this symposium included two keynote presentations, two plenary lectures, 56 oral presentations, and 45 poster presentations. Oral and poster presentations were organized into eight parallel sessions which included Food and Health, Artificial Intelligence and Smart Systems, Information and Communications Technology, Materials, Mechanical and Manufacturing Engineering, Energy and Transportation, Architecture and Civil Engineering, Human Engineering, and Water Resources Engineering. Awards for Best Paper and Best Poster presentation were given to presenters. ISAT-20 will be hosted in Japan by Kogakuin University.

Message from the UPLB Chancellor

Warm greetings!

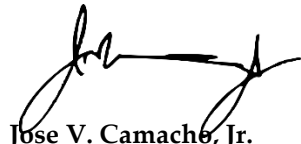
UPLB is proud to host the online iteration of the International Symposium on Advanced Technology. For this year, our theme, “Engineering Innovation for Food and Nutrition Security,” is highly relevant as we face current global issues. A continuously increasing global population, climate change disasters, and a raging pandemic have actively spotlighted the importance of having a secure and nutritious food supply during times of crisis.

With the advent of the Fourth Industrial Revolution, applying the latest technologies and scientific breakthroughs in other fields toward food and nutrition security by way of food engineering is critical. UPLB’s own College of Engineering and Agro-Industrial Technology has contributed and continues to contribute to this pool of ground-breaking technologies. This helps in the creation not only of a future-proof UPLB, but also of future-proof societies, by keeping up with the global standards and developing technologies meant to better the nation’s agricultural sector and food industry.

Whether it is in production, processing, packaging, or storage, the aspects of the food value chain to which engineering innovations can be applied are many and varied. This symposium was a good venue in which these aspects were discussed. I congratulate the participants who listened to our speakers and asked critical questions during the open forum.

We consider ISAT 19 symposium as a platform for collaboration among our respective institutions particularly on research. ISAT-19 has been an enlightening, educational, and inspirational experience for all of us. We are honored for the opportunity to host it this year, and we look forward to its next iteration.

Mabuhay!



Jose V. Camacho, Jr.

Chancellor, University of the Philippines Los Baños



Message from the Rector, DUT

The University of Danang – University of Science and Technology (UD-DUT) has since its establishment in 1975 predicated its leading position in the system of higher education in Vietnam and in Southeastern Asia. Not only is UD-DUT a center for training highly-qualified human resources in various industrial fields, but also a hub for scientific research, innovation and technology transfer for Central Vietnam and for the whole country. In that spirit, UD-DUT is very proud to be one of four sponsors for the International Symposium on Advanced Technology (ISAT). This yearly-organized symposium is a valuable forum aiming to promote scientific and technologic exchange between leading scientists, researchers for the purpose of resolving pressing national and social issues.



The 19th ISAT is hosted by the University of the Philippines Los Baños, and specifically this event remarks the first virtual symposium since its establishment in 2002 by Kogakuin University in Japan. The main theme of ISAT-19 is “Engineering Innovation for Food and Nutrition Security” in which many specific topics will be covered, including “Food and Health”, “Artificial Intelligence and Smart Systems”, “Information and Communications Technology”, “Materials, Mechanical and Manufacturing Engineering”, “Energy and Transportation” and “Architecture and Civil Engineering”. I truly believe that the technical program, with a broad range of specific discussion topics and with participants’ positive contributions, will make ISAT-19 more productive and fruitful. I also truly believe that successful outcomes from ISAT-19 will certainly contribute response to emerging questions that the world is facing in the coming decades, particularly world food structure.

I would like to express my sincere thanks to the organizing committee members and wish you a pleasurable and rewarding ISAT-19.

Sincerely yours,

A handwritten signature in black ink, which appears to read 'Doan Quang Vinh', written over a horizontal line.

Prof. Doan Quang Vinh

Rector, The University of Danang – University of Science & Technology

Message from the President, KUTE

It is my great honor for celebrating the ISAT-19, the 19th International Symposium on Advanced Technology.

This academic meeting began in 2002 and is being held annually in turn between partner universities. When ISAT-18 was held at Southern Taiwan University of Science and Technology in the fall of 2019, all the partner universities agreed to hold the next meeting at the University of the Philippines in 2020, yes. Since then, all the committee members of the Organizing Committee have made great efforts to hold this important event in Manila.

However, the ISAT-19 could not be held during in FY2020, as well as the Olympic & Paralympic Games in Tokyo, due to the COVID-19. The terrible infection of the virus is spread in the world and interferes with the person-to-person direct contact still now. On the other hand, this important symposium ISAT aims to develop the sustainable society by promoting "close relationship construction." Such construction is the opposite target to the destruction by COVID-19.

The committee members in each institution shared important awareness and decided to hold the ISAT-19. It is a terrific determination. For overcoming the serious interferes by the COVID-19, online-style ISAT was contrived and we can communicate with each other safely to achieve an important part of ISAT. I hope the mutual and direct exchange will be recovered as soon as possible, to attain the remaining part of ISAT giving us the cultural exchange.

Under any circumstances, ISAT is convinced of a great opportunity to gather wisdom regarding "science and technology" and continuously contribute to the development of sustainable society.

I appreciate to all the committee members. I thank to all the committee members and the staff who supported this event, we can enjoy safe and active online communication. I am looking forward to singing and listening favorable songs together with all of you again in the near future!



Mitsunobu Sato

President, Kogakuin University of Technology & Engineering (KUTE – Tokyo)



Message from the President, STUST

Distinguished guests, honorable scholars and professors,
Ladies and Gentlemen, good morning.

First, it is our greatest pleasure to attend “The 19th International Symposium on Advanced Technology (ISAT-19)”. On behalf of Southern Taiwan University of Science and Technology (STUST), I am most grateful to all the participants who contributed to the success of this conference by sharing your professional expertise and valuable experiences. This year, the conference theme centers on “Engineering Innovation for Food and Nutrition Security”, to address one of the most urgent concerns shared by all of us in Asia. It is my belief that the diligent discussions in ISAT-19 on this theme and other topics like AI & Intelligent systems, Energy and Transportations, Information Technology and Structures and Civil Engineering shall lead to a better and safer world for us to live.



The year 2021 is the nineteenth consecutive year of holding ISAT. With our continuous efforts, ISAT conference is becoming well known to the academic circles. This is evidenced by the fact that, despite the Covid-19 pandemic, the ISAT-19 in the online format still attracts many article submissions and there are encouragingly more than 93 paper presentations this year. On this day, through the brainstorming, interactions and discussions among the scholars and experts as well as graduate students and professors, we believe this conference will be most successful and full of inspiring new ideas.

Finally, I would like to thank you for your continuous support and contribution to this conference. I would also wish to express my sincerest hope for the great success of the conference, and for your findings of new opportunities in the ever-growing realm of advanced technology.

A handwritten signature in black ink, reading "Deng-Maw, Lu".

Deng-Maw, Lu

President, Southern Taiwan University of Science & Technology

General Programme

| | |
|---|---|
| 08:50AM – 09:00AM | LOG-IN AND ROLL CALL |
| 09:00AM – 09:05AM | PHILIPPINE NATIONAL ANTHEM |
| 09:05AM – 09:45AM | <p>OPENING CEREMONY</p> <p>Dr. Jose V. Camacho Jr. Chancellor, UPLB</p> <p>Prof. Mitsunobo Sato President, KUTE</p> <p>Prof. Deng-Maw Lu President, STUST</p> <p>Dr. LE Thi Kim Oanh Vice Rector, DUT</p> |
| 09:45AM – 10:15AM | <p>FIRST KEYNOTE SPEAKER</p> <p>Academician Eufemio T. Rasco Jr. Chair of the Agricultural Sciences Division, National Academy of Science and Technology, Department of Science and Technology</p> |
| 10:15AM – 10:45AM | <p>SECOND KEYNOTE SPEAKER</p> <p>Prof. Masaharu Yamada Professor, Kogakuin University of Technology and Engineering</p> |
| 10:45AM – 11:15AM | <p>FIRST PLENARY SPEAKER</p> <p>Prof. Ting-Feng Wu Chair, Department of Biotechnology and Food Technology, Southern Taiwan University of Science and Technology</p> |
| 11:15AM – 11:45AM | <p>SECOND PLENARY SPEAKER</p> <p>Dr. Nguyen Hoang Mai Electrical Engineering Department, Danang University of Science and Technology</p> |
| 11:45AM – 12:15PM | OPEN FORUM |
| 12:15PM – 01:30PM | LUNCHBREAK AND POSTER PAPER VIEWING |
| 01:30PM – 04:35PM | PARALLEL SESSIONS |
| 04:35PM – 04:50PM | ANNOUNCEMENT OF WINNING PAPERS AND POSTERS |
| 04:50PM – 05:00PM | <p>CLOSING ADDRESS</p> <p>Prof. Takashi Watanabe Vice President, KUTE</p> |
| Master of Ceremonies: Dr. Butch G. Bataller (Chem Eng Dept., CEAT, UP Los Baños) | |

Keynote Speeches

Engineering innovation for food and nutrition security: Design parameters and strategies for improvement of the food system to achieve food and nutrition security in the Philippines and elsewhere

Dr. Eufemio T. Rasco Jr.

Academician and Chair, Agricultural Sciences Division, National Academy of Science & Technology,
Department of Science & Technology

In this short talk, I emphasized the need for understanding the problem of food security and nutrition as a systems problem that requires a holistic view and solutions that are based on the recognition of interconnectedness of steps and processes.

Our present food system is dysfunctional. To correct it requires no less than transformation or

re-design rather than piecemeal improvements as we have seen in the past.

As the first steps for transformation, I talked about 6 design parameters and corresponding strategies, 4 key challenges to engineers and scientists, 1 key challenge to policy makers, and 3 trade-offs that policy makers need to manage. The list is not exhaustive and only meant to stimulate discussion.

Bright and dark sides of wheat flour foods

Prof. Masaharu Yamada

Kogakuin University of Science & Technology, Japan

INTRODUCTION: Wheat flour has contributed to humankind as one of the most important food materials since ancient times. There are two reasons for the contribution. One is that it can be cultivated in a wide range of areas, including elevated regions in the tropics and sub-tropics. And the other is the existence of gluten protein fraction that can be processed into various foods such as bread and noodles. The speaker has been studying wheat and wheat flour for many years, and is in a position to promote wheat flour foods, but on the other hand, it is also true that wheat flour has negative aspects such as allergies and intolerance.

BAKER'S ASTHMA: Respiratory allergy (bakers' asthma) has been known since Roman times and is currently one of the most important forms of occupational allergy. Since this respiratory allergy is caused by inhaling wheat flour and invading the flour protein directly into the blood vessels from the alveoli, it is essential for the operator to wear a mask.

FOOD ALLERGY: Wheat is listed among the 'big six' food allergens which together account for about 90% of all allergic responses. Several wheat proteins have been reported to be responsible for allergic responses to the ingestion of wheat products but only one syndrome has been studied in detail. Wheat-dependent exercise-induced anaphylaxis (WDEIA) is a well-defined syndrome in which the ingestion of a product containing wheat followed by physical exercise can result in an anaphylactic response.

INTOLERANCE: Dietary intolerance to wheat is almost certainly more widespread than allergy, notably coeliac disease (CD) which is estimated to affect 1% of the population of Western Europe. Celiac disease is a long-term immune disorder that primarily affects the small intestine.

The only known effective treatment is a strict lifelong gluten-free diet, which leads to recovery of the intestinal mucosa, improves symptoms, and

reduces the risk of developing complications in most people.

CONCLUSION: Diseases caused by wheat flour foods, of course, have genetic factors, but on the

other hand, they also have an aspect due to eating habits such as overeating and eating without chewing well. We would like to enjoy wheat flour foods such as bread and noodles after understanding the above negative aspects.

Plenary Presentations

The therapeutic effects of pomegranate on urinary bladder urothelial carcinoma*

Prof. Ting-Feng Wu

Chair, Department of Biotechnology & Food Technology, Southern Taiwan University of Science & Technology, Taiwan

Pomegranate (*Punica granatum* L.) fruit has been reported to have inhibitory activities to many types of tumors. This study investigated the molecular mechanism underlying the inhibitory impacts of Taiwanese local pomegranate fruit on urinary bladder urothelial carcinoma. We implemented two bladder cancer cell lines and xenografted mice to examine the effects of pomegranate. MTT, Western immunoblotting, and immunohistochemical staining were used for research in this study. The findings of the 3-(4,5-dimethylthiazol-2-yl)-2,5-diphenyltetrazolium bromide assay showed that the ethanol extract of pomegranate peel demonstrated better inhibitory activities to human urinary bladder urothelial carcinoma T24 and J82 cells than those of pulp. The ethyl acetate part of peel ethanol extract possesses the best suppressive efficacy against urinary bladder urothelial carcinoma cells. The PEPE2 fraction of eight fractions (PEP1 to PEP8)

obtained from the ethyl acetate part with Diaion HP-20 column chromatography had the best inhibitory effects. The flow cytometry and apoptotic examinations' data implied that the repressive impacts of PEPE2 fraction resulted from the bladder cancer cell apoptosis. Besides, xenografted human bladder tumors were created in nude mice to translate the cell line results. The results of animal studies demonstrated that the ethyl acetate part (2, 5, 10, and 100 mg/kg) could dwindle the volume and weight of T24 tumors. The findings of tumor specimens with terminal deoxynucleotidyl transferase-mediated deoxy-uridine triphosphate nick end-labeling assay showed that xenografted tumors underwent apoptosis. This study implicated the possibility that the non-edible pomegranate peel waste may be re-used to produce an affordable and hopeful chemopreventive nutraceutical to prevent the incidence or recurrence.

* An extended abstract of this presentation can be found in the Food & Health session

An intelligent control for robot by using internet*

Dr. Nguyen Hoang Mai

Electrical Engineering Department, Danang University of Science & Technology, Vietnam

Motion robot control is a widely researched problem today, especially applied to vehicles or perform human replacement tasks in dangerous places, quarantine areas, and difficult activities, search and rescue or reduce the intensity of people. In recently, the Covid-19 epidemic requires that there are field hospitals waiting to serve when needed. This article introduces the

fabrication of a remote motion robot using IoT technology, which combines image processing and PID controller to bring food and utensils for patients isolated in the hospital with payload. up to 80kg. Studies on dynamics, motion dynamics and human safety are also included in the content for design problems. Experiments on real robots support the theory of the research process

* An extended abstract of this presentation can be found in the Artificial Intelligence & Smart Systems session

Technical Presentations

Architecture & Civil Engineering

| | | |
|-----------------------------|---|--|
| Moderator | : | Dr. Richelle G. Zafra |
| Panelists | : | Dr. Marloe B. Sundo, Dr. Eric Augustus J. Tingatinga, Dr. Oscar Victor M. Antonio Jr. |
| Technical Assistants | : | aProf Jedidiah Joel C. Aguirre, aProf Andre C. Cruz |
| 01:30PM – 01:35PM | Welcome Remarks and Introduction of Panel Members | |
| 01:35PM – 01:50PM | The Study on the Minimum and Low Cost Vacant Lot Management Approach | <u>Isamu Kimoto*</u> , Saki Nakano, Arata Endo (KUTE) |
| 01:50PM – 02:05PM | Bio-mediated Soil Improvement Is A Potential Method for Mitigating Soil Erosion | <u>Tung P. Hoang*</u> , Huyen T. Do, Xuan T. M. Nguyen, Thien Q. Tran, and Lang H. Vo (DUT) |
| 02:05PM – 02:20PM | Corrosion of Steel with Nanosilica Coating using Electrochemical Impedance Spectroscopy | <u>Marish S. Madlangbayan*</u> , Martin Joseph R. Sundo, Alvin Karlo G. Tapia, Ronaniel A. Almeda, Milagros M. Peralta, Engelbert K. Peralta (UPLB) |
| 02:20PM – 02:35PM | The Study on the Vacant Lot Reclaim Design Using Green Infrastructure Technique | <u>Saki Nakano*</u> , Isamu Kimoto, Arata Endo (KUTE) |
| 02:35PM – 02:50PM | Development of concrete compressive strength predictive models based on non- destructive evaluation | <u>Bien Dave Papasin*</u> , Richelle G. Zafra, Jedidiah Joel C. Aguirre, and Mark Joel B. Uaje (UPLB) |
| 02:50PM – 03:05PM | Development of the diagnosis and repair technologies for deteriorated wood materials | <u>Yusuke Harada*</u> , Masaki Tamura (KUTE) |
| 03:05PM – 03:20PM | Traffic Analysis and Validation of Customized Local Traffic Simulator using PTV VisSim | David Louie C. Manansala, <u>Ma. Bernadeth B. Lim*</u> , Andre C. Cruz , Harvey S. Maunahan (UPLB) |
| 03:20PM – 03:35PM | Study on strong motion characteristics near active faults | <u>Takumi Kiryu*</u> , Yoshiaki Hisada, Shinya Tanaka (KUTE) |

Effect of temperature on structural deformation of Tran Thi Ly cable-stayed bridge*

Do Anh Vu ^{1,a*}, Vo Duy Hung ^{1,b}, Le Van Hien ^{2,c}

¹ University of Science and Technology – The University of Danang, Danang, Vietnam

² University of Transport and Communications

^a davu@dut.udn.vn, ^b vdhung@dut.udn.vn, ^c hienlv@utc.edu.vn

Abstract

The cable-stayed bridge can across very long span but it is sensitive to external excitation. Among of that, temperature is one of the main factors cause damage to the cable-stayed bridge. The impact of temperature makes a lot of challenges in management and maintain of bridge. Therefore, understanding the temperature effect is a key issue in bridge design and management. This study concentrates on investigating the behaviors of Tran Thi Ly cable-stayed bridge due to thermal effects. Firstly, 3D-model will be simulated by FEM

software, then the verification will be carried out by comparing with field measurement data. Next, the thermal-induced structural deformation and internal forces will be elucidated clearly. Then, the dynamic characteristics of bridge will be figured out through vibration mode shape. Finally, some critical comments will be provided.

Keywords

Tran-Thi-Ly cable-stayed bridge; FEM; temperature effects; internal forces, vibration mode shaped

* Oral paper presentation

Development of concrete compressive strength predictive models based on non-destructive evaluation*

Bien Dave B. Papasin ^{1,a,*}, Richelle G. Zafra ^{1,b}, Jedidiah Joel C. Aguirre ^{1,c} Mark Joel B. Uaje ^{1,d}

¹Department of Civil Engineering, College of Engineering & Agro-Industrial Technology, University of the Philippines Los Baños, Philippines

^abbpapasin@up.edu.ph, ^brgzafra@up.edu.ph, ^cjcaguirre@up.edu.ph, ^dmbuaje@up.edu.ph

Abstract

When assessing the condition of existing reinforced concrete structures for seismic performance analysis or building restoration, it is crucial to identify the concrete compressive strength. Concrete compressive strength is established through destructive testing and non-destructive testing (NDT). Destructive testing, through the standard concrete compressive test, is the most common method of evaluating concrete compressive strength. This is done by testing 4" x 8" or 6" x 12" cylindrical concrete samples under compression load applied by a Universal Testing Machine (UTM) until the specimens fail. This method is expensive and may pose risk for older and deteriorated structures since too much extraction of concrete core samples can cause problems on the structure's stability. NDT, on the other hand, uses correlation methods, which is an indirect method of measuring concrete strength. In other cases, NDT is used in conjunction with destructive testing to lessen the extracted cores from the structure. NDT, compared to destructive testing, requires less manpower and is less expensive in the long run, however the reliability of NDT models is still in question, and their applicability is limited.

Nondestructive tests commonly utilized for concrete compressive strength prediction are the rebound hammer test and the ultrasonic pulse velocity test. The rebound hammer test is a common NDT technique which determines the surface hardness of the concrete. The rebound hammer produces an impact when applied to a surface. The equipment measures the ratio between the amplitude of the produced compression wave with the reflected wave which is the parameter rebound number (RN) [1]. A high

RN means the concrete surface is stiff and has high strength.

For the UPV tests, the UPV equipment measures the velocity of the wave that passes through concrete. If discontinuities within the concrete exists, the speed of the wave decreases. The parameter UPV is then correlated with the concrete strength since more discontinuities within the concrete makes the concrete weaker.

Currently, NDT models are not reliable in terms of accuracy and usage. This study therefore aims to establish models with confidence intervals that correlate the compressive strength (f'_c) with parameters from nondestructive tests, RN (Rebound Number) from rebound hammer tests and UPV (Ultrasonic Pulse Velocity) from UPV tests, wherein data modelling will consider concrete samples that follow the ACI 211.1 (1991) mix design for normal weight concrete [2].

METHODOLOGY: In this study, NDT model forms that were commonly used in previous NDT studies were considered. Three model sets were developed: RN model sets, UPV model sets and model sets that uses both RN and UPV parameters. The most accurate model for each set was then identified.

Four sets of 6" x 12" cylindrical samples were prepared with each set having expected strengths of 2000, 3000, 4000 and 5000 psi respectively, with 10 samples for each design strengths, having a total of 40 samples. The samples were then subjected to nondestructive tests and standard compressive strength tests to obtain the parameters needed for developing the NDT models: RN, UPV, and the actual compressive strength of the concrete samples.

* Oral paper presentation

The model forms analyzed in this study were the widely used forms when calibrating on-site data with linear, quadratic, and power forms using only RN, only UPV, and both RN and UPV. Microsoft Excel was used to perform the different regression analysis for this study. To assess whether the models fit the modelling data, their adjusted R^2 and standard error S were considered. The confidence and prediction intervals of the models were also analyzed.

For the predictive ability of the generated models, the root-mean-square error (RMSE) was computed by testing the models on independent data sets obtained from previous studies [3], [4], [5].

RESULTS AND DISCUSSION: A total of nine models were developed: linear RN, linear UPV, quadratic RN, quadratic UPV, power RN, power UPV, bilinear, double quadratic and double power. It was then found that the three most accurate models for each set are the power RN model, the power UPV model, and the bilinear model. The models are summarized in Table 1 and their accuracy test in Table 2.

Table 1. Developed Model Equations.

| Name | Equation |
|-----------|---|
| Power RN | $f'_c = 0.159884 (RN^{1.432041})$ |
| Power UPV | $f'_c = 3.77083E-14 (UPV^{4.056903})$ |
| Bilinear | $f'_c = 13.2114 + 1.1748 RN - 0.006279 UPV$ |

Table 2. Accuracy test summary of the most accurate models for each set of models.

| Model | Ave. RMSE | S | Adj. R^2 |
|-----------|-----------|--------|------------|
| Power RN | 5.74 | 3.2312 | 0.5236 |
| Power UPV | 11.01 | 4.2424 | 0.1742 |
| Bilinear | 5.98 | 3.241 | 0.5193 |

CONCLUSION: The power UPV, while is the best model for the UPV model set, is not recommended for field use for it has low correlation and high RMSE. The power RN and bilinear models have higher correlation and low RMSE values, making them more suitable for field use. In conclusion, among the nine models, the power RN and the bilinear model have the potential to predict the measured data.

Keywords

Concrete, NDT, ultrasonic pulse velocity, rebound hammer, modelling

References

- [1] AKASHI, T., & AMASAKI S. 1984. Study of the stress waves in the plunger of a rebound hammer at the time of impact. United States: American Concrete Institute Special Publication.
- [2] ACI 211.1-91. 1991. Standard practice for selecting proportions for normal, heavyweight, and mass concrete. USA: American Concrete Institute.
- [3] Diola, N., Batin, K. G., Orozco, C., & Perez, R. 2010. Correlating non-destructive test results to the compressive strength of concrete. Paper presented at 5th Engineering Research and Development for Technology (ERDT) Conference. Manila: ERDT Consortium.
- [4] Jain, A., Kathuria, A., Kumar, A., Verma, Y., & Murari, K. 2013. Combined use of non-destructive tests for assessment of strength of concrete in structure. Procedia Engineering, 54, 241–251. doi: /10.1016/j.proeng.2013.03.022
- [5] Masi, A., Chiauzzi, L., & Manfredi, V. 2016. Criteria for identifying concrete homogeneous areas for the estimation of in-situ strength in RC building. Construction and Building Materials, 121, 576-587. doi: /10.1016/j.conbuildmat.2016.06.017

Bio-mediated soil improvement is a potential method for mitigating soil erosion*

Tung P. Hoang ^{1,a*}, Huyen T. Do ^{2,b}, Xuan T. M. Nguyen ^{3,c}, Thien Q. Tran ^{1,d}, Lang H. Vo ^{1,e}

¹ Faculty of Road & Bridge Engineering, University of Danang - University of Sci & Tech, Vietnam

² Faculty of Project Management, University of Danang - University of Sci & Tech, Vietnam

³ Faculty of Chemical Engineering, University of Danang - University of Sci & Tech, Vietnam

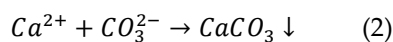
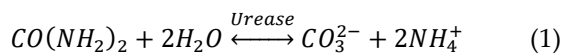
^a hptung@dut.udn.vn, ^b huyendt@dut.udn.vn, ^c ntmxuan@dut.udn.vn, ^d tqthien@dut.udn.vn,

^e vhlng@dut.udn.vn

Abstract

Coastal areas have been impacted by soil erosion due to climate change and global warming. There are many technical methods which have been used to mitigate the effects of soil erosion. Most of those methods are to either provide a protection or enhance engineering properties of coastal soil. Recently, to achieve a sustainability goal, research works have been focused on a sustainable method following natural processes rather than man-made solutions for the soil erosion issue. A new proposed soil improvement method was bio-mediated soil which employed a microbial induced carbonate precipitation (MICP) technique to enhance a natural cementation process of soil [1].

The MICP method uses a process of microbial ureolysis, in which urease producing bacteria break down urea to generate carbonate ions, following an introduction of calcium source to precipitate calcium carbonate within soil matrix (Eqs. 1&2). The calcium carbonate precipitation filled void spaces in soil structure and bridged soil grains together to reduce permeability and increase strength of natural soil.



The research work employed the MICP method to inject into sandy soil, as well as to spray on the surface of silty sand soil [2], [3]. The effects of MICP were to significantly improve strength and to reduce permeability of soil, in order to mitigate the erosion of soil. Two bench scale experimental

models of soil were stabilized using the MICP method. A pocket penetrometer test was used to determine the changing of soil strength. Fig. 1 shows an increase in compression strength within both types of soil after different number of bio-treatment. The bio-treated sandy soil samples provided much higher strength than bio-treated silty sand soils. The results were in line with previous data from [2]. The highest unconfined compressive strength (UCS) of MICP-treated soil were approximate 900 kPa and 550 kPa for sandy soil and silty sand soil after 6 treatment, respectively.

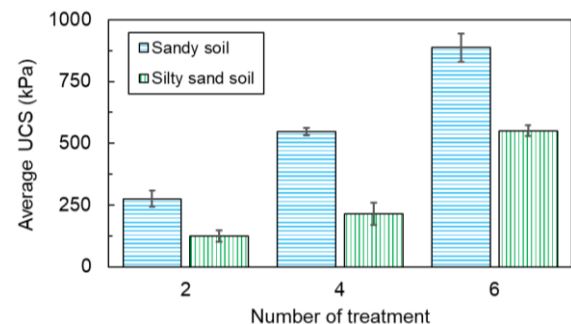


Fig. 1. UCS of bio-treated soil

A measurement of seepage rate with the bio-mediated sandy soil was the range of 37-66 mm/day at 6 treatments (as shown in Fig. 2). A significant reduction of seepage in MICP-treated sand compared to un-treated sand (i.e. 0 treatment) can be used for mitigating an internal erosion of soil levees/dikes at coastal areas. The reduction of bio-treated sand also was observed at a similar ratio from previous research work [4].

* Oral paper presentation

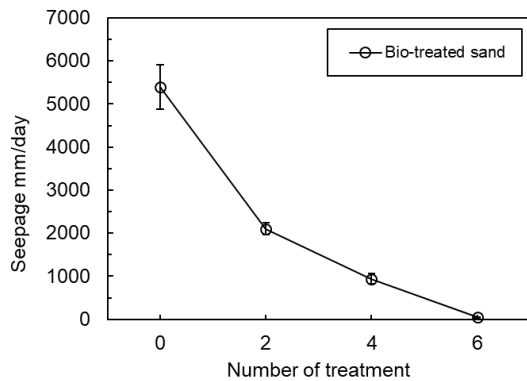


Fig. 2. Effect of bio-treated numbers on seepage of sandy soil

A microstructural analysis using scanning electron microscopy (SEM) and energy-dispersive X-ray (EDX) were performed to investigate the bonding of calcium carbonate precipitation within sandy soil samples. Fig. 3(a) shows sand particles were bond by clusters of calcium carbonate precipitation at the contact points, in order to increase the UCS as obtained in Fig. 1. In addition, the void within sand matrix was filled with CaCO_3 precipitation to reduce the seepage. The clusters of CaCO_3 precipitation and sand was confirmed in the EDX image (Fig. 3(b)) which presented the bright/white and dark/black colors for calcite minerals and sand particles, respectively. The calcium carbonate precipitation deposited at sand grains contact points and void spaces, would increase strength and reduce permeability of samples. In order that the bio-mediated can be a method to mitigate the erosion of soil. The bio-mediated method could produce cementation binder under ambient conditions which should be a sustainable method for construction for replacing ordinal Portland cement.

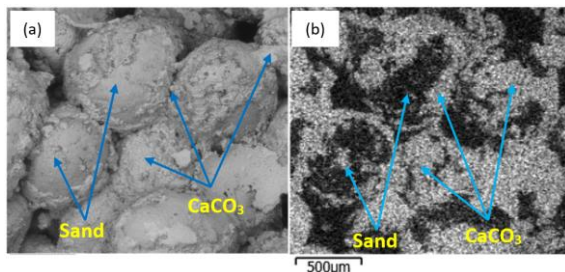


Fig. 3. Microstructural analysis: (a) SEM, (b) EDX

Although, the strength and permeability properties of bio-treated soil were investigated, a resistance of erosion has not been evaluated yet. Therefore, the research works would suggested a flume test for further investigating the resistance of soil erosion for a levee embankment model, which was treated by MICP. The erosion test is going to conduct for confirming that the MICP technique would be a potential method for mitigating erosion of soil.

Keywords

Soil improvement, sustainable method, bio-mediated soil, microbial process, calcium carbonation

References

- [1] T. Hoang, J. Alleman, B. Cetin, and S. G. Choi, "Engineering Properties of Biocementation Coarse- And Fine-Grained Sand Catalyzed by Bacterial Cells and Bacterial Enzyme," *J. Mater. Civ. Eng.*, vol. 32, no. 4, pp. 1–15, 2020, doi: 10.1061/(ASCE)MT.1943-5533.0003083.
- [2] T. Hoang, J. Alleman, B. Cetin, K. Ikuma, and S.-G. Choi, "Sand and silty-sand soil stabilization using bacterial enzyme induced calcite precipitation (BEICP)," *Can. Geotech. J.*, pp. 1–66, 2018, doi: <https://doi.org/10.1139/cgj-2018-0191>.
- [3] X. Jiang, C. Rutherford, B. Cetin, and K. Ikuma, "Reduction of Water Erosion Using Bacterial Enzyme Induced Calcite Precipitation (BEICP) for Sandy Soil," in *Geo-Congress 2020 GSP 320*, 2020, pp. 104–110.
- [4] J. Chu, V. Stabnikov, and V. Ivanov, "Microbially Induced Calcium Carbonate Precipitation on Surface or in the Bulk of Soil," *Geomicrobiol. J.*, vol. 29, no. 6, pp. 544–549, 2012, doi: 10.1080/01490451.2011.592929.

Corrosion of steel with nanosilica coating using electrochemical impedance spectroscopy*

Marish S. Madlangbayan ^{1, a*}, Martin Joseph R. Sundo ^{1, b}, Alvin Karlo G. Tapia ^{2, c}, Ronaniel A. Almeda ^{1, d},
Milagros M. Peralta ^{2, e}, Engelbert K. Peralta ^{1, f}

¹ College of Engineering & Agro-Industrial Technology, Univ. of the Philippines Los Baños, Philippines

² College of Arts & Sciences, Univ. of the Philippines Los Baños, Philippines

^a msmadlangbayan@up.edu.ph, ^b mrsundo@up.edu.ph, ^c agtapia@up.edu.ph, ^d raalmeda@up.edu.ph,

^e mmperalta@up.edu.ph, ^f ekperalta@up.edu.ph

Abstract

This study investigated the performance of steel coated with sodium silicate hydrate containing 2.5% (w/v) nanosilica from rice husk ash (RHA) using Electrochemical Impedance Spectroscopy (EIS). The nanosilica, shown in Figure 1, was synthesized from RHA by the Nanoscience and Technology Facility Instrumentation and Analytical Services Laboratory of the University of the Philippines Los Baños (UPLB). The physical properties of nanosilica are summarized in Table 1 and its crystallography determined through X-ray Powder Diffraction (XRD) is shown in Figure 2.



Fig. 1. Nanosilica synthesized by UPLB

Steel samples with diameter of 16 mm and thickness of 4 mm were coated using the dip coating method. One set of samples was coated with red oxide primer and another set was coated

with sodium silicate hydrate containing nanosilica. A separate set was left with no coating at all. The prepared specimens were submerged in 3.5% (w/v) sodium chloride solution to instigate corrosion. After 7 days, the specimens were subjected to EIS at 20Hz to 20MHz range of frequency.

Table 1. Properties of nanosilica

| Property | Value |
|-----------------------|------------------------------|
| Average particle size | 24.39 ± 0.38 nm |
| Surface area | ~260 – 300 m ² /g |
| Pore radius | ~16 – 19 Angstrom |
| Pore volume | ~0.246 cc/g |

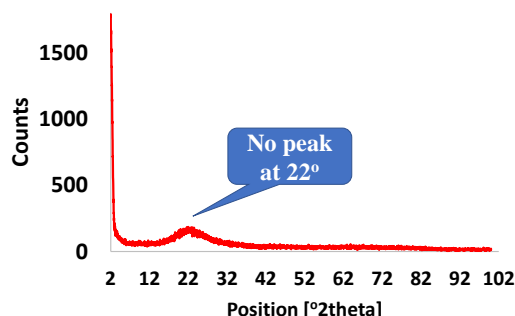


Fig. 2. Crystallography of the nanosilica

Using EIS, Nyquist and Bode plots are generated [1]. The Nyquist and Bode plots are shown in Figures 3 and 4. The Nyquist and Bode plots show that specimens coated with the nanosilica have a similar performance to specimens coated with red oxide primer.

An Equivalent Circuit Model (ECM), shown in Figure 5, was used to quantitatively determine the coating resistance and capacitance values presented in Table 2. The graph of the ECM was

* Oral paper presentation

fitted to the sample's Nyquist plot. Its elements represent the solution's resistance, coating's capacitance (C_c) and resistance (R_p) [2]. Capacitance with lower values have better coating performance as it is defined as the ability to store charges in between mediums. Thus, the more charge the coating stores, the more porous it is. Alternatively, the coating with the higher resistance represents better coating performance.

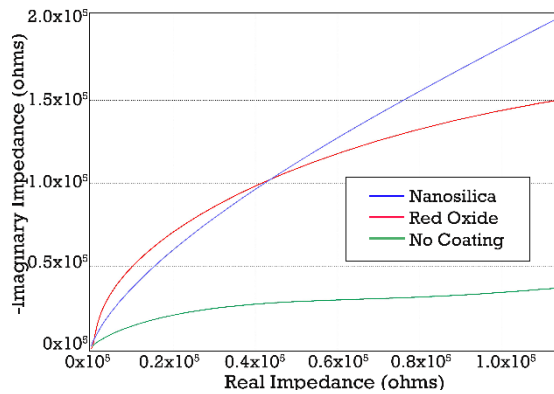


Fig. 3. Nyquist Plot of the coatings

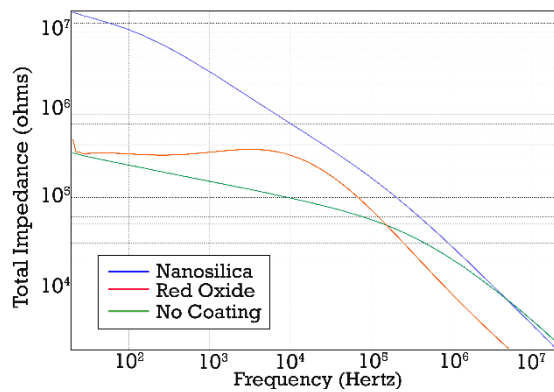


Fig. 4. Bode Plot of the coatings

Randles circuit

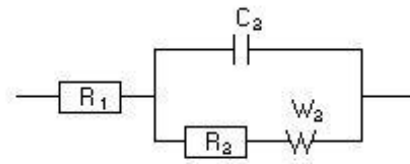


Fig. 5. Equivalent circuit model

Table 2. Capacitance and resistance values for the coatings

| | Capacitance (Farads) | Resistance (Ohms) |
|-----------------|----------------------|-------------------|
| No coating | 4.18 E-12 | 17.3 E3 |
| 2.5% Nanosilica | 1.95 E-12 | 13.5 E4 |
| Red Oxide | 1.54 E-13 | 16.0 E4 |

The resistance of the nanosilica coating is of the same order as that of the red oxide primer while its capacitance is one order lower. On the other hand, red oxide primer still showed superior coating resistance compared to the sodium silicate hydrate containing nanosilica.

KEYWORDS

Corrosion, nanosilica, electrochemical impedance spectroscopy

REFERENCES

- [1] Cesiulis, H., Ramanavicius, A., Ragoisha, G. and Tsyntsaru, N. 2016. Chapter 1: The Study of Thin Films by Electrochemical Impedance Spectroscopy. Nanostructures and Thin Films for Multifunctional Application: DOI 10.1007/978-3319-30198-3_1
- [2] Danaee, I. Kazemi, M. and Zaarei, D. 2014 Deposition and Corrosion Behavior of Silicate Conversion Coatings on Aluminum alloy 2024. wiley-vch.de/home/muwf

Research on housing thermal environment and improvement of insulation performance in Australia*

Ayaka Masuda ^{1,a,*}, Yusuke Nakajima ^{1,b}

¹ School of Architecture, Kogakuin University, Tokyo, Japan

^a dm20051@ns.kogakuin.ac.jp, ^b yusuke@cc.kogakuin.ac.jp

Abstract

In recent years, the energy demand has increased in the hot and humid regions of Asia, owing to its rapid economic development. Similarly, Australia, which also houses a vast hot and humid region, is a large economic power. Furthermore, because of its receptive immigration policies, population growth is expected in the future, along with the consequent increase in housing demands. In this research, we first investigated the characteristics of climate temperature and legal issues. We surveyed mainly in the well-populated areas because Australia has a large land area and diverse climate zones. Figure 1 shows Australia's climate classification.



Fig. 1. The climatic zones of Australia

Among them, the survey focused on Brisbane, where population is increasing rapidly due to immigration policy. We then examined the proposal of the house specifications and equipment for implementing environment-friendly housing appropriate for its climate. In this study, we investigated the indoor-/outdoor-environment and heat load trends of the houses in Australia. In particular, regarding the housing specifications and performances, we conducted surveys on housing specifications, environmental performances, energy-

consumption trends, among others, while paying attention to the differences in regions and the construction methods. The results show that there are some issues with both housing performance and equipment specifications, and that the Australian housing environment does not consider energy savings. Australia has detailed housing regulations, like NCC (National Construction Code) [2] but it is not mandatory and we have found that many existing homes do not comply with them.



Fig. 2. The model building



Fig. 3. The floor plan

Therefore, we conducted a heat load simulation in a local house to identify problems and consider improvements. Figures 2 and 3 show the drawings ordered from Brisbane house maker A. Using simulation software called BEST-H, we changed the type of insulation and windows on the outer walls of existing houses. BEST-H is a residential version program of a comprehensive building and equipment energy consumption calculation tool (BEST) for

* Poster paper presentation

studying smart wellness (health and energy saving) housing. As a result, it was found that these performances affect the indoor environment, we made a proposal for improvement with housing building materials that contribute to the improvement of the indoor environment and energy saving performance. When the effect was confirmed by simulation, a certain improvement was seen.

Annual heating/cooling thermal load was 20.8 GJ, with 13.4 GJ for cooling, and 7.4 GJ for heating. These results suggest that heat-shielding measures and efficient use of cooling are important in dwellings in Brisbane. Next, models were established with the following specifications:

Pattern 1: Modification eliminating heat insulation from the outer and front walls.

Pattern 2: Modification doubling the length of the roof overhangs (from 45 cm to 90 cm).

Pattern 3: Modification changing the windows from single glazed to low-E double-glazing (heat shielding).

Pattern 4: Modification by heat-insulating the front outer wall.

Pattern 5: Adoption of all patterns (2-4).

The results are shown in Table 1. It should also be noted that the energy saving standard in regions 5–7 in Japan ($UA=0.87$) lies below that of the reference model, and Patterns 3 and 4 indicate that the thermal load with the reference model is somewhat greater than with the standard energy saving model in regions 5–7 in Japan.

1) The heating degree day for Brisbane is ca. 253 (degree days), which is close to the value for Naha; however, the daily temperature variation in Brisbane is very high. Therefore, a detailed investigation of the heating load is considered necessary.

2) Some dwellings have a high level of heat insulation, and it can be interpreted that the spread of environmentally high-performing buildings is still a work in progress.

3) In the simulation results, a reference model with specifications of a house building company in the area in question resulted in a somewhat higher thermal load than the energy saving standard in regions 5–7 of Japan; however, the thermal load was ca. 1.5 times greater in the case of outer walls without heat insulation, which are assumed not to be uncommon among existing dwellings in the area in question. It was also confirmed that a decrease of the order of 30% in the thermal load is possible using low-E glazing for windows and improving the shelter from the roof overhang.

Keywords

Thermal environment, insulation performance, heat load, energy conservation

References

- [1] Isochronous data in epw format. <https://www.ladybug.tools/epwmap/>
- [2] NCC. <https://ncc.abcb.gov.au/ncc-online/NCC>
- [3] Australian Ministry of Environment and Energy. <https://www.environment.gov.au>

Table 1. Breakdown of annual processing heat load

| | Total skin heat loss (W/K) | UA value (W/m ² K) | η_{AC} value (%) |
|-----------------------|----------------------------------|----------------------------------|-----------------------------|
| Standard model | 486.51 | 0.93 | 1.9 |
| Pattern 1 | 840.12 | 1.61 | 2.7 |
| Pattern 2 | 486.51 | 0.93 | 1.8 |
| Pattern 3 | 438.85 | 0.84 | 1.9 |
| Pattern 4 | 417.18 | 0.80 | 1.7 |
| Pattern 5 | 369.52 | 0.71 | 1.6 |

Study on strong motion characteristics near active faults*

Takumi Kiryu ^{1,a}, Yoshiaki Hisada ^{1,b}, Shinya Tanaka ^{2,c}

¹ Department of Architecture, Kogakuin University, Japan

² Tokyo Electric Power Services Company, Japan

^a dm19023@ns.kogakuin.ac.jp, ^b hisada@cc.kogakuin.ac.jp, ^c s.tanaka@tepsco.co.jp

Abstract

INTRODUCTION: The authors have been studying how to set an epicenter model for evaluating seismic motion of long-period ground motion including permanent displacement near a surface seismic fault (For example, Tanaka et al. (2018) ¹⁾). The proposed method is to set an epicenter model using a strong motion recipe in the seismogenic layer, extend the slip distribution to shallower than the seismic layer, and standardize it to shallower than the seismic layer. Wide slip based on the Yoffe function ²⁾. It uses a velocity-time function. Here, we show the results of studies on the 2014 Northern Nagano Earthquake (Mw6.2), 1992 Landers Earthquake (Mw7.3), 1999 Kocaeli Earthquake (MW7.5).

EPICENTER FAULT MODEL SETTING: The macroscopic aspect was set with reference to Hikima et al.(2015)⁷⁾ for the 2014 northern Nagano earthquake, Wald and Heaton (1994)⁸⁾ for the 1992 Landers earthquake, and Sekiguchi and Iwata (2002) ³⁾ for the 1999 Kocaeli earthquake. Next, assuming the depth of the upper end of the seismogenic layer, microscopic parameters were set in the seismogenic layer based on the strong motion recipe. Fujii and Matsu'ura (2000) ⁴⁾ was used as the average stress drop, and the asperity area ratio was 22%. The asperity position is based on the center of each segment. The slip velocity-time function shallower than the seismogenic layer uses the normalized Yoffe function by Tinti et al.(2005). The parameters τ_S and τ_R required for setting are calculated by giving the slip amount set shallower than the seismogenic layer to the regression equation by Tanaka et al.(2018). Figure 1 shows the positional relationship between the set epicenter fault model and the target observation points.

SEISMIC MOTION EVALUATION BASED ON THEORETICAL METHODS: Figure 2 shows the set seismic source model and the evaluation results by the wavenumber integration method⁵⁾ for a period of 1 second or longer. Here, the ground models used for seismic motion evaluation are Hikima et al.(2015) for the 2014 northern Nagano earthquake, Wald and Heaton (1994) for the 1992 Landers earthquake, and Sekiguchi and Iwata (2002) for the 1999 Kocaeli earthquake. Was set as a reference. The target cycle is basically a cycle of 1 to 10 seconds, but a cycle of 1 second or more is targeted at points near the surface seismic fault. It can be seen from Fig. 2 that the observation record can be reproduced in general.

SUMMARY: For the 2014 Northern Nagano Earthquake and the 1999 Kocaeli Earthquake, based on Tanaka et al. (2018), we set a source fault model based on a strong motion recipe considering the shallowness of the earthquake layer, and the period 1 by theoretical method. It was shown that the observation record of more than a second can be reproduced. We plan to study other earthquakes in the future.

Keywords

Estimation of strong ground motion, Surface earthquake fault, 1999 Kocaeli Earthquake, 2014 Northern Nagano Earthquake, 1992 Landers earthquake.

References

- [1] Tanaka et al. (2018): Architectural Institute of Japan, No. 752
- [2] Tinti, E. et al.(2005): Bulletin of the Seismological Society of America, Vol. 95, No. 4.
- [3] Sekiguchi and Iwata(2002): Rupture process of the 1999 Kocaeli, Turkey, earthquake estimated

* Oral paper presentation; authors acknowledge the use of GMT to create diagrams for this paper

from strong-motion waveforms. Bull. Seis. Soc. Am 92

[4] Fujii, Y. and M. Matsu'ura, (2000) : Regional Difference in Scaling Laws for Large Earthquakes and its Tectonic Implication, Pure and Applied Geophysics, 157

[5] Hisada (1997): Efficient calculation of normal mode solution and Green's function in stratified soil, Architectural Institute of Japan, No.501

[6] Anderson et al.(2000):Implications for seismic hazard analysis, in Kocaeli, Turkey, Earthquake of August 17, 1999, Reconnaissance Report, Earthquake Spectra 1

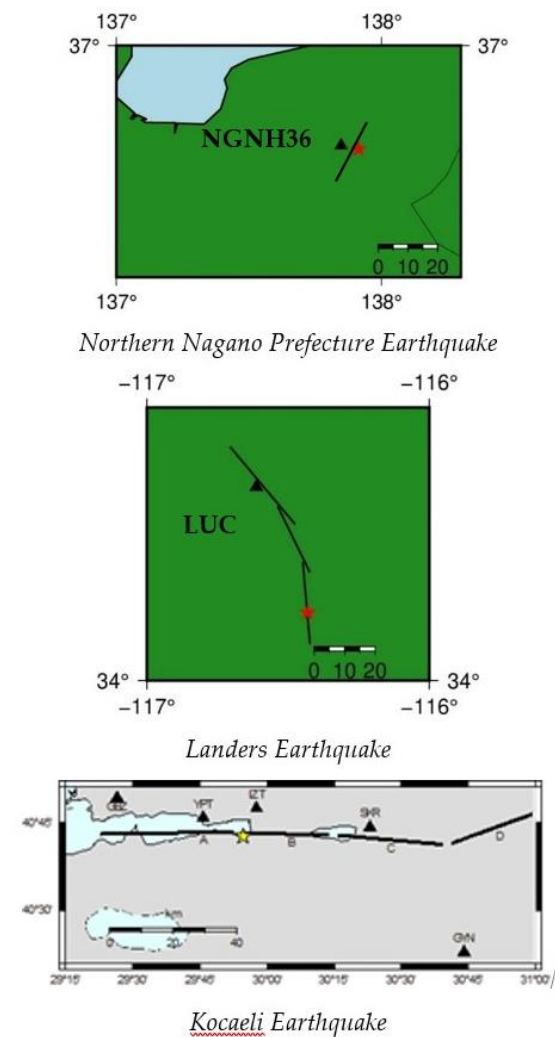


Fig. 1. Setting of seismic source fault model

[7] Kazuto Hikima, Ryoichi Nakamura, Tomiichi Uetake (2015): Source process of the 2014 Northern Nagano Earthquake (Mj6.7) -Analysis considering broadband earthquake waveforms near the source- 2015 Fall Meeting, S15-14

[8] David J. Wald and Thomas H. Heaton(1994): Spatial and Temporal Distribution of Slip for the 1992 Landers, California, Earthquake- Bulletin of the Seismological Society of America, Vol. 84, No. 3, pp. 668-691.

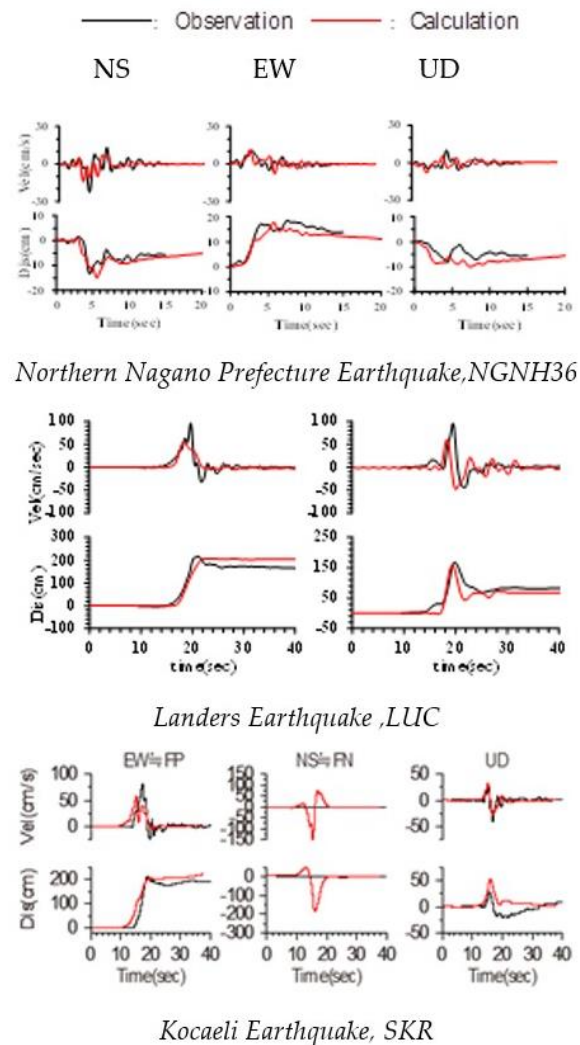


Fig. 2. Evaluation results by Hisada and Bielak (period of 1 second or more)

Development of the diagnosis and repair technologies for deteriorated wood materials*

Yusuke Harada ^{1,a*}, Masaki Tamura ²

¹ Dept.of Architecture, Graduate School of Engineering, Kogakuin Univ, Tokyo, Japan

² Department of Architecture, Kogakuin University, Tokyo, Japan

^a dm20044@ns.kogakuin.ac.jp

Abstract

Many of Japan's important cultural architectures are made of wood materials, and the non-destructive diagnosis and repair methods for them are required to be practiced preserving their initial appearances and performances. This study has two objectives. The first is to create the estimating charts on the eating damages by termites of wood materials introducing standard data regarding the density, ultrasonic propagation velocity, and dynamic modulus of test specimens. By the using of the charts, it could be evaluated the density and dynamic modulus properties in the construction fields by using ultrasonic propagation velocity against the target wood materials damaged by termites. The second is to made clear the traces of eating damages by termites inside the wood materials and to develop the injecting repair methods using acrylic silicone agents for deteriorated wood materials. As a result of research, the high correlation data charts could be presented in the relationship between the density of non-deteriorated woods and the ultrasonic propagation velocity on measuring from the butt end of test specimens. In addition, it was cleared that the internal eating damage hole was not straight route but complicated route, it is considered that when the repair agent is injected into the wood hole, it is necessary to increase injection in several times each Injection holes.

INTRODUCTION: Wooden materials have been used in buildings for a long time in Japan, and many wooden buildings have achieved historical values. In recent years, there has been a movement to evaluate the traditional technologies and techniques, and in 2020, "Traditional technique for inheriting traditional architectural craftsmanship and wooden structures" was

registered as an intangible cultural heritage by UNESCO. However, the number of skilled craftsmen have continued to decline, and it is difficult for craftsmen alone to repair and maintain the buildings and the historical values. In particular, eating damages by termites reduces the strength of wooden buildings, so it is important to take measures to extend the life of the building. This study has two objectives. The first is to create the estimating charts on the eating damages by termites of wood materials introducing standard data regarding the density, ultrasonic propagation velocity, and dynamic modulus of test specimens. By the using of the charts, it could be evaluated the density and dynamic modulus properties in the construction fields by using ultrasonic propagation velocity against the target wood materials damaged by termites. The second is to made clear the traces of eating damages by termites inside the wood materials and to develop the injecting repair methods using acrylic silicone agents for deteriorated wood materials.

EXAMINATION OF WOOD PERFORMANCE JUDGEMENT METHOD BY ULTRASONIC WAVES: In examining the method for determining the performance of wood by ultrasonic waves, we created a past damage data standard mainly using Japanese domestic timber. This outline describes the relationship between the density in a healthy state, the ultrasonic propagation velocity, and the dynamic elastic modulus. In Figure 3, orange is the normal state and blue is the hydrous state. From this result, the measurement result in the direction of butt end showed a proportional relationship between the density and the ultrasonic propagation velocity. In addition, the values of ultrasonic propagation

* Oral paper presentation

velocity and the dynamic elastic modulus tended to decrease as the water content increased.



Fig 1. Ultrasonic propagation velocity measuring instrument (left)

Fig. 2. Dynamic modulus measurement (right)

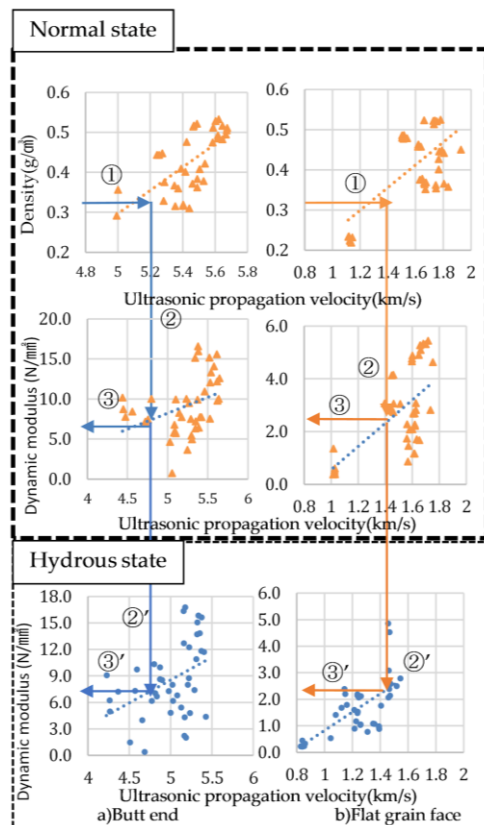


Fig. 3. Relationship diagram

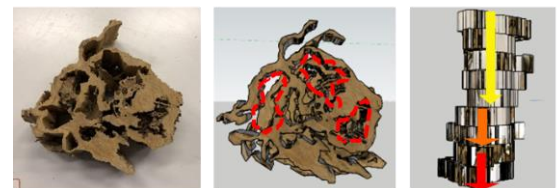
TRACES OF DAMAGED BY TERMITES INSIDE WOOD: For the traces of damaged by termites inside the wood, the test specimens that were excessively damaged were cut every 50 mm and the internal damaged by termites was investigated. This summary describes the results of modeling the specimens cut every 50 mm to the center of the annual rings. Figure 3 shows the modeling connected by 250 mm from the bottom end, and Fig. 4 shows the model connected by 418

mm. As a result, the route changed significantly twice between 418 mm, and the shape of damaged by termites also changed significantly.

CONCLUSION: In this study, a proportional relationship was found between the density and the ultrasonic propagation velocity of the wood end surface. In addition, the ultrasonic propagation velocity and dynamic modulus decreased significantly in the hydrous state. Therefore, it is necessary to consider the water content during the inspection. In addition, from the traces of termite damage inside the test piece have changed many times, it is necessary to consider the shape of the internal damage when injecting resin.



a) Modeling with a length of 250 mm



b) Modeling with a length of 418 mm

Fig. 4. Concatenation of specimen modeling damaged by termites

Keywords

Wood, termite, culture, diagnosis, repair

References

- [1] Kazuo Sumiya, 1965, Relations between defects in wood and velocity of ultrasonic wave, Wood Research: Report of Wood Research Institute, Kyoto University, 34: 22-36
- [2] Cultural Property Building Preservation Technology Association, 1979, Hakogi House (thousand years the house) Preservation and Repair Work Report, Important Cultural Property Hakogi House Repair Committee

The study on the vacant lot reclaim design using green infrastructure technique*

Saki Nakano ^{1, a*}, Isamu Kimoto ^{1, b}, Arata Endo ^{3, c}

¹ Graduate School of Engineering, Kogakuin University, Japan

² School of Architecture, Kogakuin University, Japan

^a dm20039@ns.kogakuin.ac.jp, ^b dm20018@ns.kogakuin.ac.jp, ^c arata@cc.kogakuin.ac.jp

Abstract

INTRODUCTION: In recent years, Japan has entered a society with a declining population, and the number of vacant lots, especially in suburban residential areas, has been increasing due to the declining demand for housing. As the number of vacant lots increases, illegal dumping of garbage and overgrowth of weeds occur, leading to deterioration of the landscape and devastation of the neighborhood environment. Therefore, it is necessary to design effective use of land without building in vacant lots. Furthermore, the use of green infrastructure technology is effective for sustainable land use.

PHYSICAL SETTING: The first is the design method of physical setting as green infrastructure. The site is covered with recycled local bark waste that infiltrates rainwater. In the center of the site, several raised bed gardens are developed which separates nature-oriented area and people rest area from active area. In the nature-oriented area, bioswale is designed along the retaining wall which catches the rainwater runoff from the east and south street of the site. Seven native species of plants are planted in this area which is *Lythrum anceps*, Daylily, Golden lace, Lizard's tail, Snake strawberry, Thoroughwort, *Sanguisorba*. People can enter and touch those natural settings. In addition, three plant composters are set up in the north side of the site and compost is made using the grass discharged from mowing.

COOPERATION WITH LOCAL RESIDENTS: The second is to develop a friendly and easy-to-use green design in cooperation with local residents. After this place was opened to public, the site was incrementally changed according to the local needs and usage trend through daily use. Particularly, several “flowers planting workshop”

and “furniture repair workshop” that involves local residents have been held to customize the site setting.

CONCLUSION: As a result of those green infrastructure design and daily management, the water retention function of the entire site was improved by 1.5 times compared to the previous vacant lot. Furthermore, this green-oriented site design has caused, not only people play and rest, but also vegetable gardening and morning local farmers markets and so on. It can be said that the design of the vacant lot using green infrastructure technique has contributed to the creation of a local community.

Keywords

Vacant lot, green infrastructure, local community



Fig. 1. Map of the site

* Oral paper presentation



Fig. 2. Covered with recycled local bark



Fig. 3. Bioswale



Fig. 4. Compost



Fig. 5. Flowers planting workshop



Fig. 6. Furniture repair workshop



Fig. 7. Winer market in square

Table 1. Water retention rate of the entire site before

| Before | | | | | |
|------------------------|------------------|-----------------------|--|--|---|
| Type | | Area(m ²) | A Precipitation (m ³) (Area × 0.1m/hr) | Water retention coefficient of material(mm/hr) | B Water retention of site material(m ³) |
| Roof,Tent | | 0 | 0 | 0 | 0 |
| Paving | | 0 | 0 | 0 | 0 |
| Soil | | 0 | 0 | 7 | 0 |
| Permeable paving | | 0 | 0 | 100 | 0 |
| Water retention paving | | 0 | 0 | 100 | 0 |
| Green infrastructure | Forest | 0 | 0 | 230 | 0 |
| | Bio swale | 0 | 0 | 140 | 0 |
| | Farm | 0 | 0 | 200 | 0 |
| | planting | 0 | 0 | 100 | 0 |
| | Rooftop greening | 0 | 0 | 60 | 0 |
| | Grass | 0 | 0 | 20 | 0 |
| | Mulching | 0 | 0 | 50 | 0 |
| | Planter | 0 | 0 | 100 | 0 |
| | Grassland | 1000 | 100 | 50 | 50 |
| | | Total A | 100 | Total B | 50 |
| | | | | Runoff reduction rate =B/A | 50 |

Table 2. Water retention rate of the entire site after treatment

| | | After | | | |
|------------------------|------------------|-----------------------|--|--|---|
| Type | | Area(m ²) | A Precipitation (m ³) (Area × 0.1m/hr) | Water retention coefficient of material(mm/hr) | B Water retention of site material(m ³) |
| Roof,Tent | | 2 | 0.2 | 0 | 0 |
| Paving | | 0 | 0 | 0 | 0 |
| Soil | | 0 | 0 | 7 | 0 |
| Permeable paving | | 20 | 2 | 100 | 2 |
| Water retention paving | | 0 | 0 | 100 | 0 |
| Green infrastructure | Forest | 0 | 0 | 230 | 0 |
| | Bio swale | 100 | 10 | 140 | 14 |
| | Farm | 4 | 0.4 | 200 | 0.8 |
| | planting | 250 | 25 | 100 | 25 |
| | Rooftop greening | 0 | 0 | 60 | 0 |
| | Grass | 0 | 0 | 20 | 0 |
| | Mulching | 500 | 50 | 50 | 25 |
| | Planter | 4 | 0.4 | 100 | 0.4 |
| | Grassland | 120 | 12 | 50 | 6 |
| | Total A | 100 | Total B | 73.2 | |
| | | | Runoff reduction rate =B/A | 73.2 | |

The study on the minimum and low cost vacant lot management approach*

Isamu Kimoto ^{1,a,*}, Saki Nakano ^{1,b}, Arata Endo ^{2,c}

¹ Graduate School of Engineering, Kogakuin University, Japan

² School of Architecture, Kogakuin University, Dr. Eng

^a dm20018@ns.kogakuin.ac.jp, ^b dm20039@ns.kogakuin.ac.jp, ^c arata@cc.kogakuin.ac.jp

Abstracts

INTRODUCTION: In recent years, the number of vacant lots has been increasing in a depopulated society. In vacant lots, litter and overgrowth of weeds cause devastation to the neighborhood environment. Moreover, in the suburbs, where housing demand is expected to decrease, it is necessary to find ways to make better use of vacant lot without constructing buildings.

Consequently, the aim of this research is to develop a prototype of open space using a vacant lot, a shrinking urban resource.

RESEARCH METHODOLOGY: The study site is a vacant lot at Asao-ku, Kawasaki City. It was set aside as a public utility site during the land readjustment project. However, because the use plan was abandoned, the property became vacant. In addition, the site was not used because it was in a Category 1 low-rise exclusive residential districts. Therefore, the land remained vacant for 30 years, and the government only maintained and managed it.



Fig.1 Study site before and after

There are three design and management strategy as prototype such as “low-cost”, “minimum management”, and “applicable for the other vacant lots”. Such strategies will minimize work and costs related to the management of vacant land. Eventually, the method will be established

as a generalized method and deployed as a method that can be adapted to other vacant lots

Low cost means that reducing maintenance costs through do-it-yourself (DIY) methods and involving neighbors participations. Two specific initiatives are furniture repair and mowing to preserve the ecosystem.

The furniture maintenance included repairs and repainting. We did not outsource the work, but reduced the cost by using DIY techniques and doing the work ourselves. At the same time, by involving the neighbors in the project, it contributed to community development.

Mowing to preserve the ecosystem keeps the plantation area healthy. Weeds are pulled out while observing plants with neighborhood children. This allows them to participate in the maintenance and management while learning.



Fig. 2 Mowing and observing plants



Fig. 3 Repair and repaint furniture

Minimum management means that simple daily management based on safe patrolling, cleaning, and planting care routine with no fixed caretaker on the site. It reduces administrative and labor costs. Specifically, in order to maintain the landscape, we pick up trash, water the plants, rewrite the bulletin board, and make light mowing. We do it once a week, and in the summertime we do it twice a week to take care of weeds and plants. By communicating with the users during management tasks, it is easier for us

* Oral paper presentation

to be recognized as a community-based open space.



Fig. 4. Take care of plant



Fig. 5. Rewriting the bulletin board

In order to cope with the increasing number of vacant lots, it is necessary to generalize the method of this study so that it can be adapted to other vacant lots. Therefore, in this study, work records and activity surveys are conducted during minimum management.

In the minimal management work record, we record the following items on a sheet: date, time, weather, type of dumped garbage location, number of users and their behavior, and photography. This allows us to collect quantitative data for analysis.

CONCLUSION: As a prototype, we were able to show that the environment could be maintained with weekly management tasks and gained insight into the use of vacant lot. Also, by incorporating DIY work, we were able to keep the cost of hardware maintenance at the same level as asphalt paving. In addition, we were able to build a good relationship with neighbors that might contribute to DIY works and maintain green environment.

In this study, we have succeeded in promoting management efficiency and public participation as one of the vacant lot reuse in suburban neighborhood, but the generalization as applicable design is not yet at a level that can be established as a methodology.

Keywords

Vacant lot, management, open space, low cost, DIY

| Kanadokoro Work Checksheet | | | Date and Time | Weather | Worker | | Writer | SNS | |
|----------------------------|-------|--------------|--|---------------|-----------------|----------------|-------------|---------------------|----------------------------------|
| | | | 2020/04/29 1330-15:00 | Fine | Kimoto.Nakano | | Kimoto | ○ | |
| | | | Garbage (Plot on a map) | | | Work Checklist | | | |
| | | | No. | Categories | Area | Contents | Check | Remark | Categories of users |
| | | | 1 | Other | G,F | cleaning | ○ | | Parent and child |
| | | | 2 | Food packages | F | watering | ○ | Flower Bed | Old people |
| | | | 3 | | | bulletin board | ○ | Updating messages | |
| | | | 4 | | | Rainwater tank | × | | |
| | | | 5 | | | Garbage | ○ | | |
| | | | 6 | | | Other | ○ | Composter agitation | |
| | | | Activity Survey | | | | | | |
| | | | Who | | | Where | What | | |
| | | | No. | Gender | Age | Area | Activity1 | Details | Remark |
| | | | a | Women | Play age(0~6) | E | Playing | Furniture | a-b are groupe(Parent and child) |
| | | | b | Men | Adult(19~60) | B,E | Watch over | | a-b are groupe(Parent and child) |
| | | | c | Men | Play age(0~6) | B,E | Playing | Furniture | c-d are groupe(Parent and child) |
| | | | d | Men | Adult(19~60) | B,E | Watch over | | c-d are groupe(Parent and child) |
| | | | e | Men | Old people(60~) | B | Break | | |
| | | | f | Men | Adult(19~60) | B,C,E | stroll | | f-g are groupe(Couple) |
| | | | g | Women | Adult(19~60) | B,C,E | stroll | | f-g are groupe(Couple) |
| | | | h | Men | Adult(19~60) | B | Take a meal | | h-i are groupe(Parent and child) |
| | | | i | Women | Play age(0~6) | B | Take a meal | | h-i are groupe(Parent and child) |
| j | Women | Adult(19~60) | C,E,G,F | stroll | | | | | |
| | | | View of the open space / Heard from the Neighbors | | | | | | |
| | | | The temperature was getting warmer and more comfortable. There were many people having lunch or taking a break at Kanadokoro. | | | | | | |

Fig. 6. Work report and activity survey sheet

Traffic analysis and validation of customized local traffic simulator using PTV VISSIM*

David Louie C. Manansala ^{1, a}, Ma. Bernadeth B. Lim ^{1, b*}, Andre C. Cruz ^{1, c}, Harvey S. Maunahan ^{1, d}

¹Department of Civil Engineering, College of Engineering & Agro-Industrial Technology, University of Philippines Los Baños, Philippines

^adcmansala1@up.edu.ph, ^bmblim4@up.edu.ph, ^caccruz4@up.edu.ph, ^dhsmahan@up.edu.ph

Abstract

Traffic simulation tools are used to evaluate traffic congestion problems and assess appropriate traffic control strategies. However, the accessibility and availability of traffic simulation software have been a challenge since these simulators are too expensive. Consequently, the University of the Philippines Diliman, Intelligent Transport Systems Laboratory, developed software known as Customized Local Traffic Simulator or LocalSim. This software considers the local traffic features and the Filipino driver's behavior. Since LocalSim is newly developed, it is necessary to validate the accuracy and reliability of its results when applying to a signalized intersection in the Philippines.

The main objective of this study is to assess the reliability and consistency of results simulated by LocalSim compared to the well-known and widely used simulation package which is the PTV VisSim [1]. The Lopez Avenue-National Highway signalized intersection which is located at Batong Malake, Los Baños, Laguna was selected as the study area. This research assessed four peak hour traffic volume composed of different vehicle types namely cars, jeep, motorcycle, tricycle, truck, and bus. The most common vehicle in the intersection is the motorcycle with approximately 43.25% on the average. This initial traffic volume was used for the simulation of LocalSim. On the other hand, the traffic considered for PTV VisSim was converted using passenger car equivalent factor (PCEF) to accommodate the other types of vehicle which are not featured in the software such as the tricycle and jeepney.

The LocalSim and PTV VisSim were used to simulate the traffic condition. Figure 1 shows the microsimulation model set up considering all the existing road parameters and traffic signal timing phase in the intersection.

To replicate the traffic condition on Lopez Avenue-National Highway Intersection, several simulations were done using LocalSim and PTV VisSim. For this research, the observed measures of performance (MOPs) for LocalSim are the average travel time and the

average intersection delay of each vehicle while only the travel time was considered for PTV VisSim.

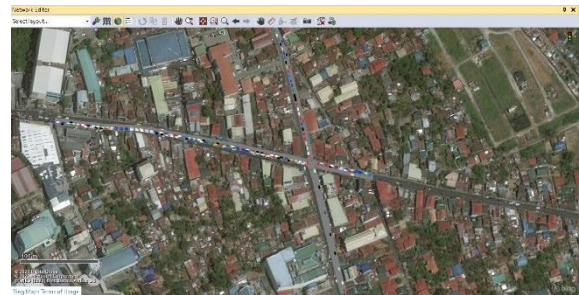


Fig. 1. Microsimulation model of the intersection with traffic volume data set up for the simulation software

The estimation of average delay per vehicle per cycle caused by all the movements in the signalized intersection was computed using the cycle length (C), time allocation of red signal (r), and critical flow value of the cycle (γ). This is mathematically shown in Equation 1, where, d is the delay (s/veh), C is the traffic signal cycle length (s), r is the time allocation of red signal (s) $\gamma = V/SFR$ is the critical flow value of the cycle. This critical flow value is the ratio of volume and saturation flow rate. The saturation flow rate for this research is assumed to be 2000 pcu/hr since there is a limitation on the records.

$$d = \left(\frac{1}{2C} \right) \left(\frac{r^2}{1-\gamma} \right) \quad (1)$$

The MOP used to validate the results of LocalSim is the average travel time which was gathered after the forty (40) 3600-second simulation runs [2]. For the validation, different goodness-of-fit measures were considered such as Normalized Root Mean Square Error (RMSN), Root Mean Square Percentage Error (RMSPE), Correlation Coefficient (r), Geoffrey E. Havers Statistics (GEH), Theil's Inequality Coefficient U, and the three components of U (bias, variance, and covariance proportion). The result for RMSN and RMSPE is acceptable since it is below 15% [3]. Also, the results of GEH and r are considered a good match since it is below 5 [3] and above 0.8 [4], respectively. The U for each peak hour is acceptable since it is less than the upper limit of 0.3 [4]. Considering all the simulations done on the

* Oral paper presentation

research, the average results for RMSN, RMSPE, r, GEH, and U are 0.073586, 0.070422, 0.996496, 1.158621, and 0.03477, respectively. This results indicate that the travel time results of LocalSim [5] are considerable and can replicate the travel time system of PTV VisSim.

The proposed traffic improvement scenario of decreased cycle length increased cycle length, and no tricycle policy was analyzed. The summary of the comparative analysis between the results of the base case and the proposed alternative scenario is shown in Table 1. To simplify, all the average travel time of proposed alternatives decreased and the most drop with almost 35 seconds was in the No tricycle policy. However, the average intersection delay on the no tricycle policy has no significant improvement to the base case result. On the other hand, the decreased cycle length was the most improved alternative scenario since it has a major decrease in both MOPs (average travel time and average intersection delay). Nevertheless, the increased cycle length gives a considerable improvement on average travel time but not on the intersection delay it causes on the intersection.

Based on the results, the most improved alternative is the decreased cycle length since it has a significant improvement on average travel time compared to the base case. Consequently, the decreased cycle length has the lowest intersection delay among all the alternatives. Although this consideration will result in a longer intersection queue length.

Table 1. Comparison between the base case and the average measures of performance for each alternative scenario

| MOPs | Base Case | Reduced cycle length | Increased cycle length | No tricycle policy |
|------------------------------------|-----------|----------------------|------------------------|--------------------|
| Average Travel Time (s) | 294.01 | 271.21 | 286.10 | 260.30 |
| Average Intersection Delay (veh/s) | 98.96 | 85.94 | 116.89 | 98.63 |

Findings in the study show that the use of LocalSim can replicate the current traffic scenario. However, there are suggestions for improvement of the features and analysis coverage which can be more representative of the Filipino traffic scenario.

For software improvement, the developers of LocalSim can enhance the graphical view for the agents to be more user-friendly. Equally, the adjustment of the program to be available for computers with lower specifications computers of future users of the software. The addition of pedestrian features on LocalSim can be added for the next study as another consideration. Since the localism was developed to take into account features according to Filipino context, the addition of dynamic lane features should be present in the micro simulator since it is an ordinary behavior of Filipino drivers. Also, to further lessen longer queues on the simulation, the motorcycle users in the simulation should have an option for lane splitting. The proposed alternatives in this paper can also be used by future researchers for a different study area and micro simulator.

Keywords

traffic analysis, traffic simulation, measures of performance, PTV VisSim, LocalSim

References

- [1] Vinayaka B. 2016. Saturation and delay model microsimulation using VisSim - a case study. Reva Institute of Technology, Bangalore, Karnataka in India. International Journal of Engineering Research & Technology.
- [2] Recongco, M.L. 2020. Performance assessment of traffic signal cycle optimization models and lane configuration options using local traffic simulator LocalSim. Undergraduate Thesis (Bachelor of Science in Civil Engineering) - University of the Philippines Los Baños.
- [3] Balakrishna, R., Antoniou, C., Ben-Akiva, M., Koutsopoulos, H. N., & Wen, Y. (2007). Calibration of microscopic traffic simulation models: Methods and application. Transportation Research Record, 1999(1), 198-207
- [4] Hourdakis J, Michalopoulos PG, Kottommannil J. 2003. Practical procedure for calibrating microscopic traffic simulation models. Transportation Research Record, 1852(1): 130-139.
- [5] Taguiam EM, Palmiano H.S. n.d. Validation and comparative analysis of a customized local traffic simulator (LocalSim). University of the Philippines Diliman.

Technical Presentations

Artificial Intelligence & Smart Systems

| | | |
|----------------------|--|---|
| Moderator | : | Dr. Rossana Marie C. Amongo |
| Panelists | : | Dr. Ralph Kristoffer B. Gallegos, Dr. Diana Marie R. de Silva, aProf Erwin P. Quilloy |
| Technical Assistants | : | aProf. Adrian A. Borja, aProf. Romel A. Arrobang |
| 01:30PM – 01:35PM | Welcome Remarks and Introduction of Panel Members | |
| 01:35PM – 03:20PM | Human Engineering Parallel Sessions | |
| 03:20PM – 03:35PM | Development of a Low-cost UAV Pesticide Sprayer for Rice Production System | <u>Eldon P. De Padua*</u> , Rossana Marie C. Amongo, Erwin P. Quilloy, Delfin C. Suministrado, Jessie C. Elauria (UPLB) |
| 03:35PM – 03:50PM | Automatic Cell Segmentation and Defect Detection in Electroluminescence Images of Solar Photovoltaic Modules | Keh-Moh Lin, <u>Harshad Kumar Dandage</u> , Horng-Horng Lin, You-Teh Lin and Yeou-Jiunn Chen (DUT) |
| 03:50PM – 04:05PM | An Intelligent Control for Robot by Using Internet | <u>Nguyen Hoang Mai*</u> , Nguyen Van Thuan, Phan Thi Mai and Le Van Hung and Nguyen Dac Quy (DUT) |
| 04:05PM – 04:20PM | Effects of variations in the parameters of EBMA in motion estimation accuracy | <u>Melvin C. Ilang-Ilang*</u> (UPLB) |
| 04:20PM – 04:35PM | Neural-network-based classifier for breast cancer using FITR signals obtained from tissues | <u>Rock Christian V. Tomas*</u> , Anthony Jay Sayat, Andrea Nicole Atienza, Jannah Lianne Danganan, Ma. Rollene Ramos, Allan Fellizar, Lara Mae Angeles, Ruth Bangaoil, Abegail Santillan, Pia Marie Albano (UPLB) |

Automatic cell segmentation and defect detection in electroluminescence images of solar photovoltaic modules*

Keh-Moh Lin ¹, Harshad K. Dandage ², Horng-Horng Lin ^{3,a*}, You-Teh Lin ¹, Yeou-Jiunn Chen ²

¹Department of Mechanical Engineering, Southern Taiwan University of Science & Technology, Taiwan

²Department of Electrical Engineering, Southern Taiwan University of Science & Technology, Taiwan

³Department of Computer Science & Information Engineering, Southern Taiwan University of Science & Technology, Taiwan

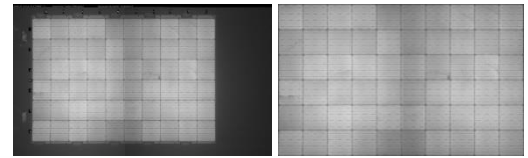
^ahhlin@stust.edu.tw

Abstract

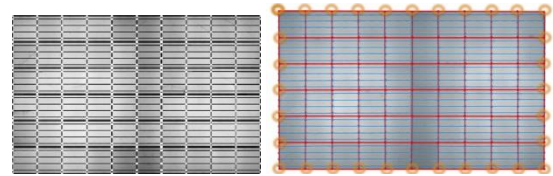
MOTIVATION: Automatic inspection of electroluminescence (EL) images of photovoltaic (PV) modules for defect detection is an important research topic in PV panel manufacturing. As a PV module usually consists of a plural number of single-crystalline silicon (sc-Si) solar cells, dividing an EL module image into solar cell images for *cell-based* defect detection is an efficient treatment to manufacturing quality check. We thus propose an automatic solar cell segmentation method based on the structural joint analysis of Hough lines, and a defect detection approach for solar cell inspection based on deep learning for this practical application.

METHODS: For segmenting solar cells, four processing steps, as illustrated in Fig. 1, are proposed, including: (i) *panel region localization* by contour tracing⁰, (ii) *Hough line estimation*⁰, (iii) *grid and busbar identification*, and (iv) *cell extraction*. Particularly, in step (iii) for structural joint analysis, the intersections of estimated Hough lines are identified and matched to reference cell grid structures to locate cell boundaries accurately. Within cell images, abnormal regions, such as cracks, deface and broken fingers, are manually labeled into defect class, and then used to train deep CNN detectors^{0,0}.

RESULTS: We firstly evaluate the accuracies of solar cell segmentation by using a test set of 1380 cells from 23 panel images, where cell boundaries are manually labeled. The resulting segmentation errors along x- and y-directions are 1.6 and 1.4 pixels, respectively, in average. Some examples of cell segmentation are demonstrated in Fig. 2.



(a) Panel region localization from a source image (left).



(b) Hough line estimation (left), and grid (in red) and busbar (in blue) identification (right)



(c) Cell extraction

Fig. 1. The processing steps of cell segmentation.

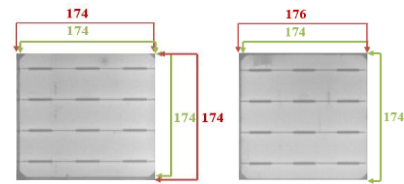


Fig. 2. Examples of solar cell segmentation results, where the green and red labels correspond to the true and the extracted cell boundaries, respectively.

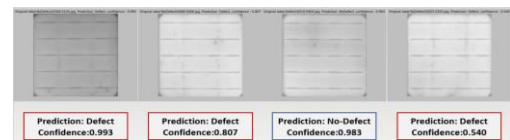


Fig. 3. Examples of defect cell classification⁰.

* Oral paper presentation

Regarding the defect detection assessments, the approach of panel-based defect detection and a prior study of defect cell classification⁰, are compared with the proposed approach of cell-based defect detection. While, in 0, the precision and recall rates of defect cell classification achieve, respectively, 99.3% and 99.7% in testing based on ResNet⁰, specific defect locations cannot be identified, as shown in Fig. 3. Field operators may not be able to know where and why the CNN classifier determines a cell image as defect, and may need to pay extra attention to justify results.

On the other hand, the panel- and the cell-based detection approaches with YOLOs^{0,0} are adopted to further locate defect positions. For the panel-based approach, a whole EL image is fed to YOLOv4⁰ to detect and mark defect regions by bounding boxes. We prepare 96 EL panel images for training and 23 images as a benchmark for testing, in which all the defect regions are manually labeled. As a result, the precision and recall rates for the test set are only 51.0% and 69.0%, respectively, probably due to large variations of defect sizes. Examples of the detection results in EL panel images are given in Fig. 4.

The proposed cell-based defect detection, implemented with YOLOv3⁰ or YOLOv4⁰, is actually more effective than the panel-based approach. Specifically, 1,257 cell images containing defects are selected for training, and 308 cell images generated from the same benchmark set of 23 EL images, as used in the panel-based approach, are introduced for testing. While the precision and recall rates for YOLOv3 are 79.0% and 76.0, respectively, the corresponding rates for YOLOv4 are 100% and 96.0%. The testing results for YOLOv3 and YOLOv4 are sampled and shown in Fig. 5. These results validate the benefit of combining cell segmentation with deep learning for optical defect detection.

Conclusion – In summary, the proposed cell-based approach using YOLOv4 for defect detection outperforms both the cell-based defect classification with ResNet and the panel-based defect detection with YOLOv4 in the experiments. Our approach has novel features of (i) accurate panel region localization and cell segmentation, (ii) effective defect identification based on cell units, and (iii) new computational scheme of integrating cell segmentation and deep learning for defect detection of photovoltaic modules.

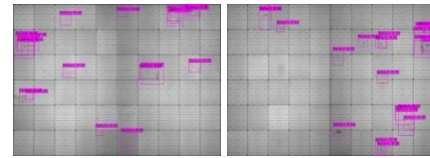
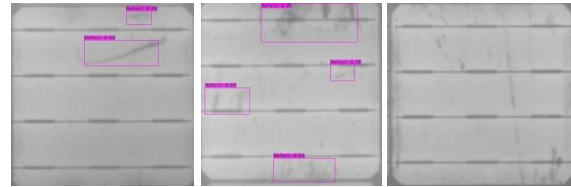
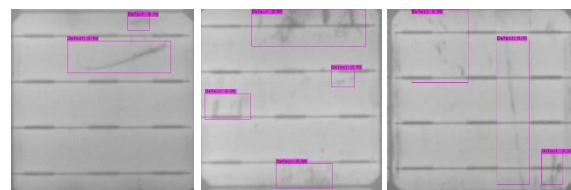


Fig. 4. Examples of defect detection of the panel-based approach.



(a) YOLOv3 detection results of cell images.



(b) YOLOv4 detection results of cell images.

Fig. 5. Comparisons of YOLOv3 and YOLOv4 detection results for the proposed cell-based approach.

Keywords

Electroluminescence image; photovoltaic module; cell segmentation; defect detection.

References

- [1] Chang, F., Chen, C.-J. 2003. A component-labeling algorithm using contour tracing technique. *Int'l Conf. Document Analysis and Recognition (ICDAR)*.
- [2] Galambos, C., Kittler, J., Matas, J. 1999. Progressive probabilistic Hough transform for line detection. *IEEE Conf. Computer Vision and Pattern Recognition (CVPR)*.
- [3] Redmon, J., Farhadi, A. 2018. YOLOv3: An incremental improvement. *arXiv:1804.02767*.
- [4] Bochkovskiy, A., Wang, C.-Y., Liao, H.-Y. M. 2020. YOLOv4: Optimal speed and accuracy of object detection. *arXiv:2004.10934*.
- [5] Lin, Y.-T., Lin K.-M., Dandage, H. K., Lin, H.-H. 2020. Development of a deep learning algorithm for automatic detection of defects in electroluminescence images of single crystalline silicon photovoltaic modules. *Int'l Symposium Novel and Sustainable Technology*.
- [6] He, K., Zhang, X., Ren, S., Sun, J. 2016. Deep residual learning for image recognition," *IEEE Conf. Computer Vision and Pattern Recognition (CVPR)*.

Development of individual cell components analysis method for tissue sample with TOF-SIMS*

Kenta Shirasu ¹, Kazuya Tamura ¹, Masato Morita ², Kumiko Nagase ³, Wakako Hamanaka ³,
Masatoshi Kakihana ³, Tatsuo Ohira ³, Norihiko Ikeda³, Tetsuo Sakamoto ^{1,2,b}

¹ Graduate School of Electric Engineering & Electronics, Kogakuin University, Japan

² Department of Applied Physics, School of Advanced Engineering, Kogakuin University, Japan

³ Division of Thoracic & Thyroid Surgery, Tokyo Medical University, Japan

^a cm20028@ns.kogakuin.ac.jp, ^b ct13087@ns.kogakuin.ac.jp

Abstract

INTRODUCTION: Cancer is one of the leading causes of death in Japan. Although various methods of treating cancer have been proposed, there is no absolute cure. The individual cells composing a cancer are genetically unstable, therefore, as the cancer cells repeat division, the diversity of the constituent cell types increases. Due to this, cancer cells have different characteristics even if they have the same onset site, and the need for treatment methods that take into account the diversity of cancer has been advocated. When tumor tissue is analyzed, the difference between the tumor and non-tumor areas can be analyzed with the tissue scale resolution. Such analysis cannot capture the diversity of individual cells in the tumor. Inorganic elements in cells are closely related to the behavior of cancer cells, and also interact with each other and are active in cells. Inorganic elements in cells has been analyzed using ICP-MS or SIMS, so far. However, owing to different characters of tumor cells, the results of these two methods cannot be related with each other. Therefore, an analysis techniques for a large number of individual cells will be important for a deep understanding of cancer. The FIB-TOF-SIMS developed in our laboratory has a high spatial resolution and can simultaneously image inorganic components in a label-free manner without the need for special sample processing. In this study, individual cells were extracted from rat lung tissue samples, and the

components of each cells were imaged from a tissue.

EXPERIMENTAL: The TOF-SIMS used in this study was developed by Prof. Sakamoto^[1]. It is equipped with a Ga focused ion beam (FIB). Secondary ion mass spectrometry (SIMS) is an analytical method in which the surface of a sample is irradiated with an ion beam, and secondary ions secondarily emitted through sputtering are measured by a mass spectrometer (MS). Since the biological sample contains water-soluble components, the components volatilize in the TOF-SIMS apparatus which is a high vacuum inside. Since inorganic elements are water-soluble components, the samples were freeze-dried in this study to analyze them. Freeze-drying method is a method in which a biological sample is dried by sublimation of water under low pressure in frozen state.

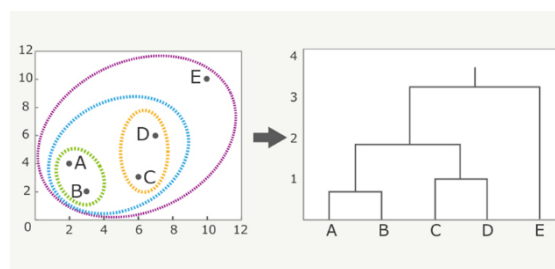


Fig.1. Outline of hierarchical cluster

In addition, cluster analysis was performed on the data obtained by SIMS analysis. Cluster analysis is a method of classifying data into several populations by using the similarity as a clue when two or more data exist. Cluster analysis is used not only for research in various

* Poster paper presentation

fields, but also in commercial fields such as marketing^{[2][3]}.

RESULT AND DISCUSSION: Fig. 2 shows the total ion image of the sample and an image of extracting the components of each block of the sample. Components were extracted from the white areas, and the component data was analyzed by cluster analysis.

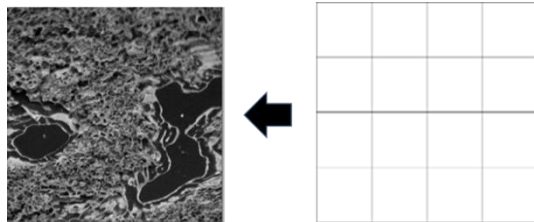


Fig.2. The Image of extraction from SIMS analysis data

Therefore, it was possible to extract and evaluate the components for each of a plurality of cells from a part of the tissue section sample. In the

future, we will compare the data obtained by analyzing samples in various states.

Keywords

Biological, surface analysis, SIMS

References

- [1] T. Sakamoto, M. Koizumi, J. Kawasaki, J. Yamaguchi. 2008. Development of a high lateral resolution TOF-SIMS apparatus for single particle analysis. *Applied Surface Science*. 255. 1617.
- [2] M. Kondo, H. Oi, S. Suga, S. Miyamoto. 1993. The acoustic environmental awareness of residents in high-rise apartment houses by the free response method. 458. 91-100.
- [3] T. Namatame. 2007. Progress of Data Analysis in Marketing. *Transdisciplinary Federation of Science and Technology*. 2-5.

Development of a low-cost UAV pesticide sprayer for rice production system*

Eldon P. De Padua ^{1,2,a*}, Rossana Marie C. Amongo ^{2,b}, Erwin P. Quillooy ^{2,c},
Delfin C. Suministrado ^{2,d}, Jessie C. Elauria ^{3,e}

¹ Department of Agricultural & Biosystems Engineering, Visayas State University, Philippines

² Agribiosystems Machinery & Power Engineering Division, Institute of Agricultural & Biosystems Engineering, University of the Philippines Los Baños, Philippines

³ Agricultural, Food & Bioprocess Engineering Division, Institute of Agricultural & Biosystems Engineering, University of the Philippines Los Baños, Philippines

^aepdepadua@up.edu.ph, ^brcamongo@up.edu.ph, ^cepquillooy@up.edu.ph, ^ddcsuministrado@up.edu.ph, ^ejcelauria@up.edu.ph

Abstract

INTRODUCTION: The use of Unmanned Aerial Vehicle (UAV) for agricultural applications is becoming popular in huge farms recently [1]. It is a promising agricultural technology due to its safe and easy maneuverability. It also keeps the operator safe from pesticide spray exposure and direct inhalation of harmful spray mist [2].

However, UAV Sprayer use in countries with low land-area-to-farmer ratio such as the Philippines [3] may not be as popular as to those with huge land-area-to-farmer-ratio. One of the primary reasons for this can be due to the high cost of commercially available UAV Sprayers in the country. In the Philippines, the typical market price ranges from about eight hundred thousand pesos to about one million five hundred thousand pesos (~Php 800, 000 – ~Php 1,500,000) depending on the advanced capabilities of the UAV Sprayer. Prompted by this problem, a locally made automated UAV pesticide sprayer for rice production system that is much cheaper than the current market price but can perform the basic functions of a UAV pesticide sprayer was developed.

METHODOLOGY: The UAV Pesticide Sprayer has an autopilot flight control system. Pixhawk 2 Cube and Arduino Uno were used as flight and spray controllers, respectively, while Mission Planner 1.3.68 was used as the UAV sprayer's

ground control station. Figure 1 shows the UAV pesticide sprayer assembly.



Fig. 1. The Unmanned Aerial Vehicle (UAV) Pesticide Sprayer Assembly

Subsequently, a flight plan for autonomous operation with 527 m² area, 45 waypoints, and 11 rows was prepared (Fig. 2). Using this flight plan, the UAV Pesticide Sprayer's field performance was evaluated based on its total endurance, traveled distance, operating speed, operating altitude, and climb rate [4].



* Oral and poster paper p

resentation; poster title: "The use of UAV Sprayer for Rice Production System"

Fig. 2. The flight plan of the UAV Pesticide Sprayer using Mission Planner 1.3.68.

Single Factor Analysis of Variance (ANOVA) at 5% level of significance was used to check if there is any significant difference in the UAV pesticide sprayer's performance with and without load, respectively. Also, a simple cost analysis of the developed UAV sprayer was performed. The simple cost analysis was done relative to the UAV's tank capacity and field capacity.

RESULTS AND CONCLUSIONS: The summarized result of the performance test of the UAV Pesticide Sprayer is presented in Table 1. The computed percent difference of the UAV sprayer's Total Endurance was 62.37%. Single-factor ANOVA also suggests that there is a significant difference between the mean values of the Total Endurance of the UAV Pesticide Sprayer with load and no load. This implies that the addition of load had increased the flight time of the UAV Pesticide Sprayer.

On the other hand, no significant differences were found in the total distance travelled, typical operating altitude, operating speed, and climb rate of the UAV Pesticide Sprayer with and without load. It means that the addition of load to the UAV Pesticide Sprayer had not caused significant changes in the abovementioned UAV performance indicators.

Table 1. Field performance test result based on UAV design parameters of Torun 1999.

| Parameters | Tank Capacity | | Percent diff. (%) | p-value |
|-------------------------------|---------------|---------|-------------------|----------------------|
| | With Load | No Load | | |
| Total Endurance, min | 4.11 | 2.53 | 62.37 | 0.0033* |
| Total Distance Travelled, m | 292.61 | 237.43 | 23.24 | 0.0683 ^{NS} |
| Typical Operating Altitude, m | 1.60 | 1.66 | 3.60 | 0.8617 ^{NS} |
| Operating Speed, m/s | 2.18 | 2.37 | 8.13 | 0.2205 ^{NS} |
| Climb Rate, cm/s | 52.88 | 54.37 | 2.74 | 0.8085 ^{NS} |

Note: *significant; NS – not significant

Furthermore, Table 2 shows the computed cost of the locally developed UAV Pesticide Sprayer per liter load (tank capacity) and field capacity (ha/h). Relative to its tank capacity, the UAV sprayer is roughly around Php 63, 000.00 or around 1, 260 USD. On the other hand, in terms of its field capacity, the cost of the UAV Pesticide Sprayer is around Php 140,000.00 (2,800 USD). Typically, the costs in terms of tank capacity and field capacity of commercially available UAV Pesticide Sprayers in the Philippines are about Php 90,000.00 (1,800 USD) and Php 240,000.00 (4,800 USD), respectively.

Table 2. Cost of the locally developed UAV pesticide sprayer in terms of Tank and Field Capacities

| Parameter | Value |
|---------------------------|-------------|
| Tank Capacity, L | 1 |
| Field Capacity, ha/h | 0.45 |
| Cost, Php | 63, 144.00 |
| Cost per Liter, Php/L | 63, 144.00 |
| Cost per ha/h, Php/(ha/h) | 140, 320.00 |

Hence, the locally developed UAV pesticide sprayer is much cheaper than the commercially available imported units in the Philippines.

Keywords

Unmanned Aerial Vehicle, UAV Sprayer, Low-cost UAV Sprayer, Aerial Spraying

References

- [1] Rao Mogili UM, Deepak BBVL. 2018. Review on application of drone systems in precision agriculture. *International Conference on Robotics and Smart Manufacturing (RoSma2018)*. Procedia Computer Science 133 (2018) 502–503.
- [2] Desale R, Chougule A, Choudhari M, Borhade V, Teli S. 2019. Unmanned aerial vehicle for pesticides spraying. *IJSART*.5. 79-82.
- [3] Philippine Statistics Authority (2012). Special report - highlights of the 2012 census of agriculture. Ref. No. 2015-71. 21 December 2015. Retrieved from psa.gov.ph.
- [4] Torun E. 1999. UAV requirements and design consideration. *RTO SCI Symposium on Warfare Automation: Procedures and Techniques for Unmanned Vehicles*. Ankara, Turkey, 26-28 April 1999. RTO MP-44. pp B4-1:B4-2.f

An intelligent control for robot by using Internet*

Nguyen Hoang Mai ^{1,a}, Nguyen Van Thuan ¹, Phan Thi Mai ¹, Le Van Hung ¹, Nguyen Dac Quy

¹ Electrical Engineering Department, Danang University of Science & Technology, Vietnam

^a nhmai@dut.udn.vn

Abstract

INTRODUCTION: Robots were basically required to serve quarantine zones, but in fact robots can serve many different fields such as medical [1], [2], [8], [10], education [5], military [4], [7], [11], community philanthropy, and can even extend to commercial areas such as freight, freight in stock [3], [14], [18]. There are many applications of robots. The problem is how to control the robot to move flexibly in a limited environment, and at the same time the ability to be controlled remotely. Since then, IoT devices are introduced to apply controls. Utilizing 2.4GHz band wifi combined with image processing with wide-angle camera, the robot allows the operator to see front, back, and both sides for movement, and cargo rack frames are automatic control to deliver goods to the user without having to move much. In the design requirements of the project, the robot needs to be moved in a narrow space with a road width of 1.5m. The quarantine areas are designed to meet this requirement. The moving space diagram is shown in Figure 1. In order for the robot to rotate its head, the width of the path must be greater than the diagonal of the robot's largest cross section. The robot motion is designed in the OXYZ coordinate system as shown in Figure 1.

MODELING OF THE SYSTEM: The movements in all directions of the robot still follow the classical mechanical motion equation, the most familiar being the Lagrange I or II equation. In general, we can see it as a robot that moves on a plane, but to be true to reality, we still have to consider a robot moving in 3D space, meaning that when moving sideways, the robot can still move up, down in the OZ direction is considered to be the oscillation direction. Robot motion modeling Robot coordinates are determined by

two components (assuming negligible change in altitude):

$$x = r \cos \theta, y = r \sin \theta \quad (1)$$

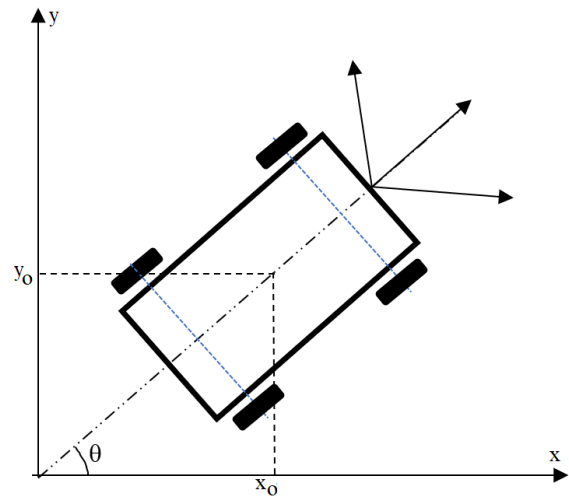


Fig 1. Description of robot motion



Fig 2. The COVID quarantine zones of hospital

Equation (1) used to decide position and angle instantaneously in OX axis. The speed of robot is followed:

$$\begin{cases} \dot{x} = \dot{r} \cos \theta - r \dot{\theta} \sin \theta \\ \dot{y} = \dot{r} \sin \theta + r \dot{\theta} \cos \theta \end{cases} \quad (2)$$

* Oral and poster paper presentation

If robot has oscillation in OZ axis with ϕ angle, which $\phi < \pi/2$, then speed OZ direction will appearance:

$$\begin{cases} z = r \tan \phi \\ \dot{z} = \dot{r} \tan \phi + r \dot{\phi} \frac{1}{\cos^2 \phi} \end{cases} \quad (3)$$

After calculating the differentials for the variables r, ϕ, θ and time, we will have the robot's motion equation:

$$F(r) = \frac{1}{2} m \left[2\ddot{r} + \dot{\phi} \left(1 + \frac{\sin^2 \phi}{\cos^2 \phi} \right) \left(\dot{r} \tan \phi + r \dot{\phi} \frac{1}{\cos^2 \phi} \right) + \tan \phi \left(\dot{r} \tan \phi + r \dot{\phi} \frac{1}{\cos^2 \phi} + \dot{r} \dot{\phi} \frac{1}{\cos^2 \phi} + r \ddot{\phi} \frac{1}{\cos^2 \phi} + r \dot{\phi}^2 \frac{2 \sin \phi}{\cos^3 \phi} \right) \right] + mg \tan \phi \quad (4)$$

$$F(\phi) = \frac{1}{2} m \ddot{r} \frac{1}{\cos^2 \phi} \left(\dot{r} \tan \phi + r \dot{\phi} \frac{1}{\cos^2 \phi} \right) + \frac{1}{2} m r \left(-\dot{\phi} \sin 2\phi \cos^{-3} \phi \right) \left(\dot{r} \tan \phi + r \dot{\phi} \frac{1}{\cos^2 \phi} \right) + \frac{1}{2} m r \frac{1}{\cos^2 \phi} \left(\dot{r} \tan \phi + r \dot{\phi} \frac{1}{\cos^2 \phi} + \dot{r} \dot{\phi} \frac{1}{\cos^2 \phi} + r \ddot{\phi} \frac{1}{\cos^2 \phi} - r \dot{\phi}^2 \sin 2\phi \cos^{-3} \phi \right) - \frac{1}{2} m \left[\left(\dot{r} \frac{1}{\sin^2 \phi} + 2r \dot{\phi} \frac{\sin \phi}{\cos^3 \phi} \right) \left(\dot{r} \tan \phi + r \dot{\phi} \frac{1}{\cos^2 \phi} \right) \right] + mgr \frac{1}{\sin^2 \phi} \quad (5)$$

$$F(\theta) = m r \ddot{\theta} + \frac{1}{2} m r^2 \ddot{\theta} - m(-\dot{r} \sin \theta - r \dot{\theta} \cos \theta)(\dot{r} \cos \theta - r \dot{\theta} \sin \theta) + m(\dot{r} \cos \theta - r \dot{\theta} \sin \theta)(\dot{r} \sin \theta + r \dot{\theta} \cos \theta) \quad (6)$$

MECHANICAL DESIGN OF ROBOT BODY: The robot body consists of two main parts: the sliding mechanism for the trays and the movement mechanism of the vehicle. Analysis of sliding tray structure: each sliding tray has dimensions 500 x 500 x 70 and is expected to carry a load of 10 kg. In all, there are 4 sliding trays with a total height of 600 mm as shown in Figure 2. After calculating the maximum force limit from (4) ... (6), the motors are selected according to the capacity corresponding to the maximum speed is 3m/s, the total weight is 67 kg, the static friction force according to the actual surface of the road should not be specified, but within the range of 0.1 - 0.2 gravity. Here the distance r is a reference constant, so the force $F(r)$ is determined by the dynamic

friction force and the drag force resistance. The independent dc motors are defined with the power $P = M\omega$, where $M = 120 \text{ N.cm}$, $\omega = 4\pi \text{ rad / s}$ because the gearbox has a rotating output of 120 rpm. Based on equations (4)... (6), calculate the maximum motor power of 45 W Analysis of the sliding tray structure: including 4 rear sliding trays and 2 fixed front trays, 4 sliding trays with dimensions 530 x 473 x 70 mm → Trays material: 201 stainless steel sheet -Thickness: 0.8 mm 201 stainless steel combination -Thickness: 0.5 mm, bending through many stages → into the tray. Use a 42 – 38 mm stepper motor to move the tray with the following parameters: 42 * 42 * 38 mm, shaft diameter: 5mm, voltage: 12 V, maximum current: 1.2 A, step 1.8 degrees, maximum torque: 400 Nm. Surface smooth friction coefficient: $\mu = 0,1$.

DESIGN AN IOT CONTROLLER: IoT control is inserted into the robot to ensure that the robot can be remotely controlled to ensure the safety of operators and supervisors as the working conditions of the robot are extreme. The IoT here is actually using the internet environment to command control. However, due to the signal delay in the transmission line, real-time assurance needs to be done by a local coordinate system. The safety of the user is also strictly required in the event of a vehicle failure that cannot be controlled via the IoT channel. The IoT uses embedded microcomputer Rapsberry PI 3+, Arduino pro mini and Atmega 2560, module wifi ECS468.

Keyword:

Robot, IoT, controller, image processing, rescue, defense, quarantine area, damage area

References

- [1]. Amruta A. Mujumdar and Dr. Mrs. Shailaja Kurode, 2013, Second Order Sliding Mode Control for Single Link Flexible Manipulator, Proceedings of the 1st International and 16th National Conference on Machines and Mechanisms (iNaCoMM2013), IIT Roorkee, India, Dec 18-20 2013, pp 700 – 705.
- [2]. Arun Prasad K.M, Bindu M. Krishna and Usha Nair, 2013, Modified Chattering Free Sliding Mode Control of DC Motor, International Journal of Modern Engineering Research (IJMER), Vol.3, Issue.3, May-June. 2013 pp-1419-1423

The development of Phalaenopsis cultivation environmental monitoring and control system based on IoT devices*

Ding-Horng Chen ^{1,a*}, Tasi-Rong Chang ^{1,b}, Chien-Chuan Ko ^{2,c}, Tzu-Ying Wang ^{1,d}

¹ Department of Computer Science & Information Engineering, Southern Taiwan University of Science & Technology, Taiwan

² Department of Computer Science & Information Engineering, National Chiayi University, Taiwan

^a chendh@stust.edu.tw, ^b trchang@stust.edu.tw, ^c kocc@mail.ncyu.edu.tw, ^d zywang0607@stust.edu.tw

Abstract

Phalaenopsis is a popular flower crop and gains high economic value in Taiwan with its beautiful flower shape. Novel flower breeding and cultivation techniques are the competitive advantages of Taiwan's orchid industry. Phalaenopsis is cultivated in a greenhouse. The main factors affecting the growth of phalaenopsis include temperature, humidity, light intensity, moss humidity, electrical conductivity and carbon dioxide concentration. In this paper, several low power consumption phalaenopsis sensors with Wi-Fi and Bluetooth functions are integrated by the Micropython technology to develop the phalaenopsis growth monitoring system. The environmental and physiological parameters of the phalaenopsis are immediately transmitted to the cloud storage, and presented in a responsive and interactive visualized manner.

In this paper, we have developed a system that using Micropyton, ESP32 and IOT technology to monitor the environmental variables of Phalaenopsis greenhouse. This system uses the Internet of Things technology to collect data from different sensors and establishes a front-end responsive webpage that visualizes the physiological sensing parameters of Phalaenopsis (such as temperature, humidity and soil conductivity). Users can monitor the data of the Phalaenopsis growth environment at any time, Figure 1 shows the system architecture diagram developed in this paper.

SYSTEM DESIGN: The system developed in this paper uses the following sensors: ESP32, MH-Z16, DHT22, GY-302, ssd1306, three-in-one power module, RS485 to UART converter, soil three-in-

one sensor (soil temperature Humidity, EC) and PH sensors. The connection of each component and ESP32 is shown in Figure 2. Among them, the three-in-one soil and the PH sensor need to convert RS485 signals to UART signals through a signal converter, the functionally descriptions are shown in Table 1.

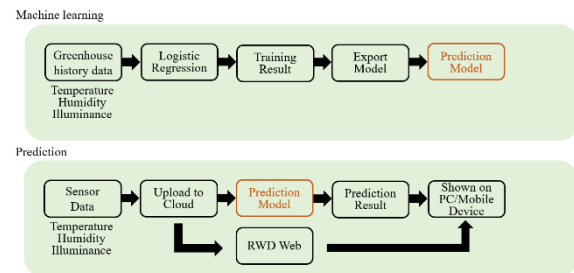


Fig. 1. The system architecture diagram

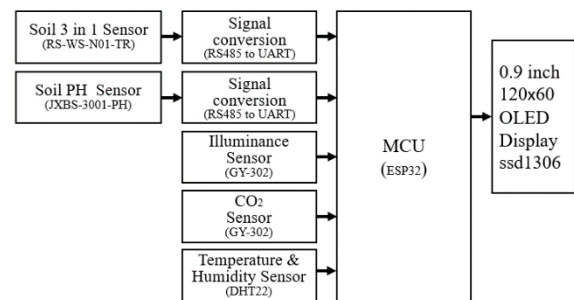


Fig. 2. The component diagram

EXPERIMENTAL RESULTS: The system developed in this paper includes environmental sensors to measuring carbon dioxide, light intensity, and environmental temperature and humidity; and plant growth parameter sensors to measure electrical conductivity, temperature and humidity and the PH value of sphagnum moss soil. The circuit configuration of this system is shown in the figure 3. The soil sensor and pH sensor will be inserted on the plant. All sensor

* Poster paper presentation

data will be transmitted to the cloud database to record date, illuminance, environment and sphagnum temperature and humidity, CO₂, EC Value and PH Value.

Table 1. The components and sensors description

| Model | Description | Power supply |
|-----------------------|---|--------------|
| ESP32 | Chipest | 5V |
| MH-Z16 | Measure CO ₂ | 5V |
| DHT22 | Measure temperature and humidity of the environment | 5V |
| GY-302 | Measure the strength of sunlight | 3.3V |
| ssd1306 | LCD | 5V |
| 3 in 1 power model | Supply 3.3V, 5V and 12V | DC |
| RS485 to UART | Convert the signal | 5V |
| 3 in 1 sensor of soil | Measure temperature and humidity of the moss | 5-12V |
| PH sensor | Measure PH of moss | 12-24V |

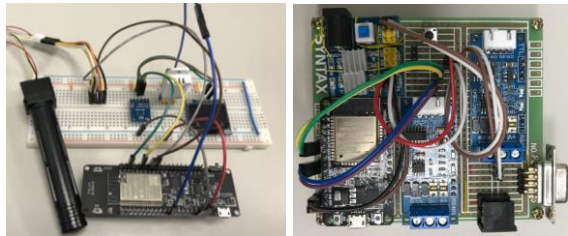


Fig. 3. The environmental (left) and the plant growth parameter sensors (right)

The phalaenopsis growth data including the hub number, gateway number, environmental temperature and humidity, illuminance, temperature and humidity of aquatic medium, and conductivity of sphagnum moss, etc., are presented through a responsive web page as shown in Figure 4.

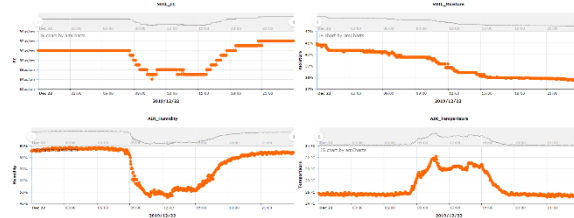
CONCLUSION: The system proposed in this paper can monitor plant physiological parameters in real time, including medium temperature and humidity, environmental temperature and humidity, light, EC value, etc. Compared with commercially available greenhouse sensors, this system has better functions but lower cost.

Keywords

Phalaenopsis cultivation, supervisory control and data acquisition, Internet of Things

| Hub100001e6 #1 | | Hub100001e6 #2 | | Hub10000100 #3 | |
|--------------------------|---------------------|--------------------------|---------------------|--------------------------|---------------------|
| Daily Chart | Monthly Chart | Daily Chart | Monthly Chart | Daily Chart | Monthly Chart |
| Hub_ID | 100001e6 | Hub_ID | 100001e6 | Hub_ID | 10000100 |
| Last Update | 2020-01-20 10:07:06 | Last Update | 2020-01-20 10:06:46 | Last Update | 2020-01-20 10:05:52 |
| Temperature | 27.3 °C | Temperature | 27.3 °C | Temperature | 27.3 °C |
| Humidity | 85 % | Humidity | 79 % | Humidity | 77 % |
| EC | 0.1 ds/m | EC | 0.2 ds/m | EC | 0.28 ds/m |
| Illuminance | 9322 Lux | Illuminance | 9123 Lux | Illuminance | 7223 Lux |
| Temperature of Moss | 22.7 °C | Temperature of Moss | 26.1 °C | Temperature of Moss | 26.3 °C |
| Humidity of Moss | 45 % | Humidity of Moss | 54 % | Humidity of Moss | 36 % |
| CO ₂ | 543 ppm | CO ₂ | 543 ppm | CO ₂ | 543 ppm |
| Illuminance accumulation | 1.7 mol/day | Illuminance accumulation | 1.64 mol/day | Illuminance accumulation | 1.46 mol/day |

(a)



(b)

Fig. 4 The sensor data display: (a) The data display by hub category; (b) The data trend

References

- [1] M.-S. Liao et al., 'On precisely relating the growth of Phalaenopsis leaves to greenhouse environmental factors by using an IoT-based monitoring system', *Computers and Electronics in Agriculture*, vol. 136, pp. 125–139, Apr. 2017, doi: 10.1016/j.compag.2017.03.003.
- [2] S. R. Prathibha, A. Hongal, and M. P. Jyothi, 'IoT Based Monitoring System in Smart Agriculture', in *2017 International Conference on Recent Advances in Electronics and Communication Technology (ICRAECT)*, 2017, pp. 81–84, doi: 10.1109/ICRAECT.2017.52.
- [3] A. Khattab, A. Abdelgawad, and K. Yelmarthi, 'Design and implementation of a cloud-based IoT scheme for precision agriculture', in *2016 28th International Conference on Microelectronics (ICM)*, 2016, pp. 201–204, doi: 10.1109/ICM.2016.7847850.
- [4] P. J. Sarkar and S. Chanagala, 'IoT based Digital Agriculture Monitoring System & Their Impact on Optimal Utilization of Resources', vol. 01, no. 01, p. 6.

Pulse signal-based emotion classification study by support vector machine*

Boyao Zhang ^{1,a*}, Hisaya Tanaka ^{2,b}

¹ Graduate School of Engineering Kogakuin University, Japan

^a em20010@ns.kogakuin.ac.jp, ^b hisaya@cc.kogakuin.ac.jp

Abstract

Issues such as stress and depression have led to a dramatic increase in the number of people choosing to commit suicide due to mood changes. Emotional distress has become a health hazard that must be taken seriously. Emotion recognition has also become an important research direction in the field of human-computer interaction. Current research on emotion recognition is mainly based on facial expressions, text content, physiological signals of body posture, etc. In this study, emotion recognition is based on the pulse signal in the physiological signal.

METHODS: The study includes pulse signal collect, preprocess, feature extraction, and classifier classification.

The pre-processing of pulse wave was done by wavelet threshold method, which filters out the low frequency noise and removes the baseline drift to get a pure pulse wave signal^[1]. As shown in Figure 1 and Figure 2.

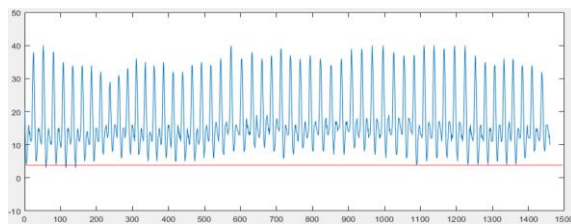


Fig. 1. Original signal

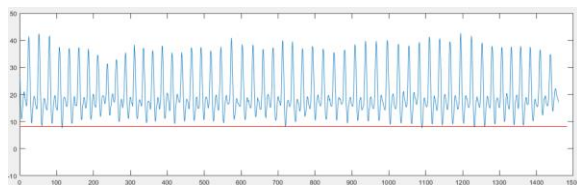


Fig. 2. Pulse wave signal after pre-processing

The pulse wave features were extracted by using peak and trough detection and wavelet transformation^[2]. Figure 3 is a partial signal after

marking. Fig. 4 is a schematic diagram of wavelet decomposition in wavelet transform, which is used to propose high frequency and low frequency signals of each layer after decomposition.

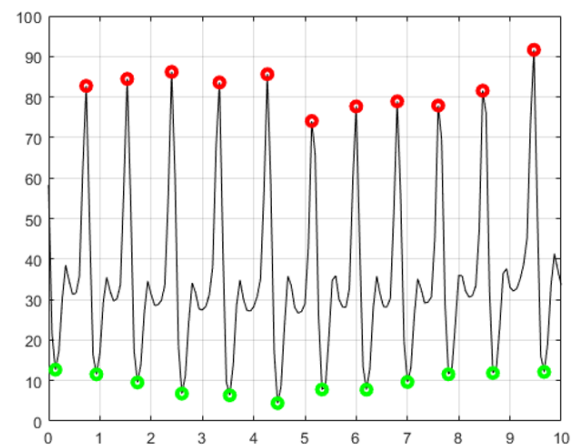


Fig. 3. Pulse wave signal with peaks and valleys marked

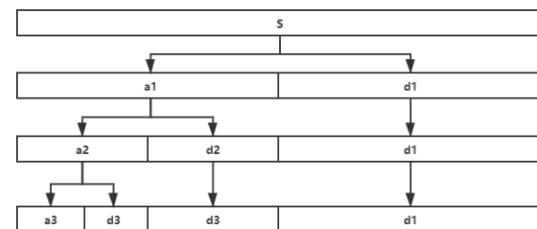


Fig. 4. Schematic diagram of wavelet transform (s: original signal; di: high frequency signal; ai: low frequency signal)

After formula calculation, 87 features were extracted in the time and frequency domains.

$$Max = \max(data) \quad (1)$$

$$Min = \min(data) \quad (2)$$

$$Median = \text{median}(data) \quad (3)$$

$$Mean = \text{mean}(data) \quad (4)$$

$$Std = \text{std}(data) \quad (5)$$

* Poster paper presentation

$$ttp = diff(data) \quad (6)$$

For the classification of the features, the LIBSVM classifier was used in this study^[3].

$$\min_{w,b,\xi} \frac{1}{2} w^T w + C \sum_{i=1}^l \xi_i \quad (7)$$

Use the radial basis function as the base function of LIBSVM.

$$e^{-\gamma|u-v|^2} \quad (8)$$

EXPERIMENT RESULTS: In the design experiment, the public pulse signal data of the MIT emotion computing group was used as the experimental data, and the positive and negative emotion classification based on the pulse wave signal was realized, with an average classification accuracy of 67%. The average classification accuracy was 65.3% in the four basic emotions (calm, joy, sadness, and anger) based on the pulse model.

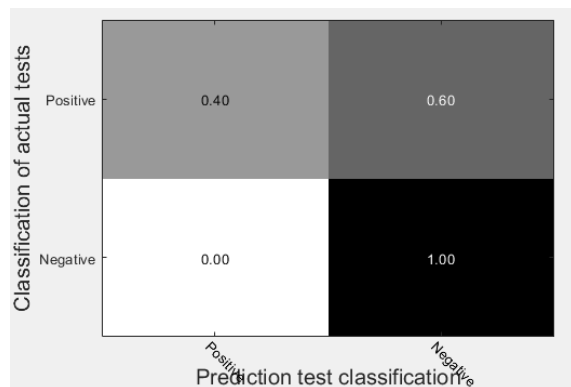


Fig. 5. Examples of classification results of positive and negative emotions

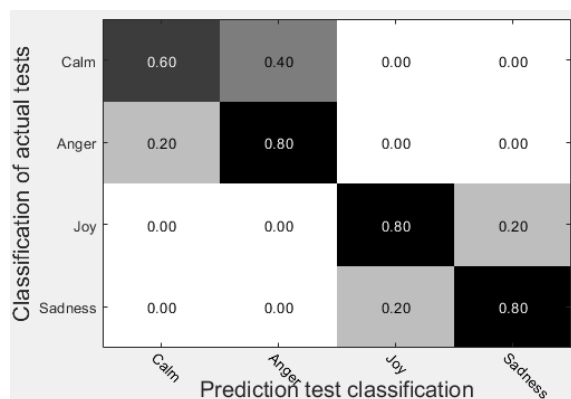


Fig. 6. Examples of classification results of the four emotions

CONCLUSION: After successfully classifying the four basic emotions, it was intended to design emotion elicitation experiments in the following experiments. It is planned to complete a series of experiments ranging from the emotional elicitation of the subject to the successful analysis of the subject's pulse signal and the classification of emotions. Although it is possible to successfully classify emotions based on pulse signals in this study, there is still much room for improvement in the classifier. It is believed that after continuous improvement of the algorithm, better recognition results will be obtained.

Keywords

Pulse signal; emotion recognition; support vector machine; feature extraction; wavelet transform

References

- [1] Sun, Wei, Ning Tang, and Guiping Jiang. "Study of characteristic point identification and preprocessing method for pulse wave signals." *Sheng wu yi xue Gong Cheng xue za zhi= Journal of Biomedical Engineering= Shengwu Yixue Gongchengxue Zazhi* 32.1 (2015): 197-201.
- [2] Long Z, Liu G, Dai X. Extracting emotional features from ECG by using wavelet transform[C]//2010 International Conference on Biomedical Engineering and Computer Science. IEEE, 2010: 1-4.
- [3] Chih-Chung Chang and Chih-Jen Lin, LIBSVM : a library for support vector machines. *ACM Transactions on Intelligent Systems and Technology*, 2:27:1--27:27, 2011

Neural-network-based classifier for breast cancer using FTIR signals obtained from tissues*

Rock Christian Tomas ^{1,a*}, Anthony Jay Sayat ², Andrea Nicole Atienza ², Jannah Lianne Danganan ², Ma. Rollene Ramos ², Allan Fellizar ^{3,4,5}, Lara Mae Angeles ^{6,7}, Ruth Bangaoil ^{3,4}, Abegail Santillan ^{3,4}, Pia Marie Albano ^{2,3,4,b}

¹Department of Electrical Engineering, University of the Philippines Los Baños, Laguna, Philippines

²Department of Biological Sciences, College of Science, University of Santo Tomas, Manila, Philippines

³Research Center for the Natural and Applied Sciences, University of Santo Tomas, Manila, Philippines

⁴The Graduate School, University of Santo Tomas, Manila, Philippines

⁵Mariano Marcos Memorial Hospital and Medical Center, Ilocos Norte, Philippines

⁶Faculty of Medicine and Surgery, University of Santo Tomas, Manila, Philippines

⁷University of Santo Tomas Hospital, Manila, Philippines

^arvtomas1@up.edu.ph, ^bpsalbano@ust.edu.ph

Abstract

Breast cancer is the most prevalent type of cancer among women. Cancer diagnosis is performed through the microscopic examination of hematoxylin and eosin (H&E)-stained tissue by an experienced pathologist. This approach is, however, prone to bias since it greatly relies on visual examination. Hence, there is a need to develop more sensitive and specific method to diagnose cancer [1][2]. Here, the Fourier transform infrared (FTIR) spectrum of 166 labeled breast tumors (78 benign, 88 malignant) were investigated across the IR fingerprint region (1850 cm^{-1} to 860 cm^{-1}). The FTIR spectrum of each tissue sample was labeled based on their respective H&E biopsy performed by two experienced pathologists [3].

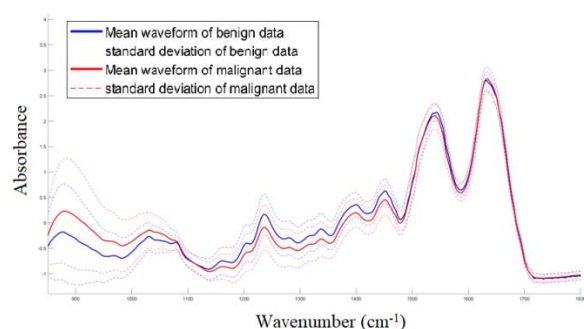


Fig 1. Mean spectrum of malignant and benign samples

All obtained IR spectra were normalized using z-score normalization in order to eliminate bias from range value discrepancies among IR samples

[4]. The obtained IR samples also underwent baseline correction using the rubber band method with 64 baseline points. Figure 1 shows the mean spectrum of the malignant and the benign samples collected. To discriminate the tissue samples, three (3) feed forward neural network (FNN) models of varying layer size ($n = 2$, $n = 4$, $n = 8$) and layer width were designed to discriminate the spectral data [5]. A grid search was performed in order to determine a sub-optimal value for the models' layer width and learning rate. The surface curve of the performed optimization is shown in Figure 2.

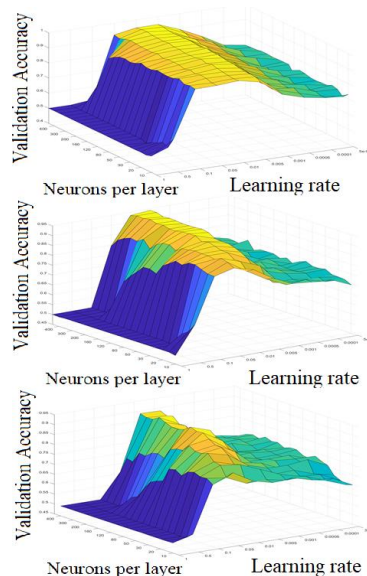


Figure 2. Optimization surface plot for FNN2, FNN4 and FNN8 (top to bottom)

* Oral and poster paper presentation

In order to evaluate each model, a 10-fold cross validation method was performed where 70% was used for training, 15% for validation and 15% for testing. The validation set was used for assessing the performance of each hyperparameter combinations for the optimization. In order to assess the performance of the neural network models, the metrics – area under the curve (AUC), accuracy (ACC), positive predictive value (PPV), specificity rate (SR), negative predictive value (NPV), and recall rate (RR) – were obtained from the test set and averaged for comparison. The cross validation procedure was repeated over twenty (20) times to ensure stability. All neural network models were compared to the performance of six (6) machine learning models – logistic regression (LR), Naïve Bayes (NB), decision trees (DT), random forest (RF), support vector machine (SVM) and linear discriminant analysis (LDA) – for benchmarking. MATLAB 2020b was used to model the neural networks, as well as the 6 machine learning models. The performance results of the models are shown in Table 1.

The FNN models were able to outperform the LR, NB, DT, RF, and LDA for all metrics. However, the FNN models were only able to surpass the SVM in terms accuracy, NPV and SR by ~5.24%, ~3.22%, and ~1.45%, respectively. On average, the FNN model performed with an AUC of $90.29\% \pm 0.22\%$, an accuracy of $95.68\% \pm 0.33\%$, a PPV of $91.25\% \pm 1.25\%$, a NPV of $92.99\% \pm 1.17\%$, a SR of $87.68\% \pm 1.82\%$, and a RR of $92.85\% \pm 1.39\%$. In conclusion, the neural-network-based models were able to excellently discriminate breast cancer based on the FTIR spectra of tissues. The authors

recommend that the variation of breast cancer tumors across the IR functional regions be investigated.

Keywords

Breast cancer, infrared spectroscopy, neural networks, machine learning, diagnosis

References

- [1] Su KY, Lee WL. Fourier transform infrared spectroscopy as a cancer screening and diagnostic tool: a review and prospects. *cancers (basel)*. 2020;12(1):115. Published 2020 Jan 1. doi:10.3390/cancers12010115.
- [2] Cohen Y, Zilberman A, Dekel B, Krouk E. Artificial neural network in predicting cancer based on infrared spectroscopy. *Int. Conf. on Intelligent Decision Tech (IDT)*. 2020, pp 141-153. Doi:10.1007/978-981-15-5925-9.
- [3] Bangaol R, Santillan A, Angeles LM, Abanilla L, Lim A Jr, Ramos MC, et al. (2020) ATR-FTIR spectroscopy as adjunct method to the microscopic examination of hematoxylin and eosin-stained tissues in diagnosing lung cancer. *PLoS ONE* 15(5): e0233626. <https://doi.org/10.1371/journal.pone.0233626>.
- [4] Costa F, Marques A, Arnaud-Fassetta G, et al. Self-Normalizing Neural Networks Günter. In: 31st Conf. Neural Inf. Process. Syst. (NIPS). 2017, pp. 99–112.
- [5] Sala A, Anderson DJ, Brennan PM, et al. Biofluid diagnostics by FTIR spectroscopy: A platform technology for cancer detection. *Cancer Lett* 2020; 477: 122–130.

| | AUC (%) | ACC (%) | PPV (%) | NPV (%) | SR (%) | RR (%) |
|-------------|-------------|-------------|-------------|-------------|-------------|-------------|
| LDA | 71.58±11.84 | 66.17±10.20 | 77.67±13.47 | 55.98±15.34 | 74.35±11.80 | 61.56±9.65 |
| LR | 86.27±9.58 | 65.05±12.63 | 68.83±31.57 | 60.79±41.06 | 53.46±32.44 | 73.00±23.96 |
| NB | 66.90±10.90 | 64.69±10.41 | 54.44±16.24 | 77.40±15.09 | 60.23±9.62 | 74.22±15.28 |
| DT | 69.03±12.83 | 69.38±11.58 | 69.56±15.82 | 69.56±17.37 | 67.79±13.58 | 73.19±12.93 |
| RF | 84.63±9.30 | 76.78±9.49 | 76.94±14.56 | 76.60±14.88 | 76.18±12.23 | 79.91±10.88 |
| SVM | 95.72±4.94 | 90.44±7.78 | 91.03±9.61 | 89.77±10.33 | 90.56±9.68 | 91.40±8.34 |
| FNN2 | 90.05±9.95 | 96.06±7.07 | 89.83±12.57 | 94.19±10.57 | 85.56±18.33 | 94.34±10.54 |
| FNN4 | 90.48±10.30 | 95.54±8.07 | 91.72±12.06 | 92.93±12.81 | 88.38±17.47 | 92.63±13.31 |
| FNN8 | 90.35±10.10 | 95.46±7.55 | 92.18±11.88 | 91.85±12.67 | 89.04±16.75 | 91.58±13.47 |

Table 1. Diagnostic performance of models.

Extracting keywords from videos to build a content-based search and recommendation system*

Shu-Chen Cheng ^{1,a*}, Jin-Fong Tseng ^{1,b}

¹ Department of Computer Science & Information Engineering, Southern Taiwan University of Science & Technology, Tainan, Taiwan

^akittyc@stust.edu.tw, ^bma8g0203@stust.edu.tw

Abstract

INTRODUCTION: In recent years, more and more people use video platforms to search for courses of interest to learn new skills and knowledge. But not all the searched results are suitable. The search results provided by the video platform need to be further filtered to meet the needs of learners.

Unlike static articles where you can quickly browse the content, it takes a lot of time to filter the video content by watching the entire video. Based on video content, this study constructs a keyword search and recommended video system.

The system extracts keywords from the content of the videos to classify and label them, to help learners filter videos quickly and recommend highly relevant videos to learners. At the same time, based on the Apriori algorithm, the system calculates the correlation between each keyword. The system will automatically expand the keyword dictionary, so that the system can intelligently update the video database through the expanded keyword dictionary. The system workflow is shown in Fig. 1.

METHODS: Before the video, this system first collects and analyze web articles about computer science to build a keyword dictionary. When web crawlers collect videos from YouTube through existing keyword dictionary, videos are labeled with the given keywords. After collecting the video, the system extracts the text content of the video in three ways:

- Use speech recognition to convert the voice content of the video into text.
- Use optical character recognition to capture the text in the video screen.

- Get the video description.

Merge three results to calculate the value of Term Frequency-Inverse Document Frequency (TF-IDF), and use the TF-IDF value of the keyword as the basis for video recommendation. The TF-IDF formula shown below.

$$TF\text{-}IDF(T_i, D_j) = TF(T_i, D_j) \cdot IDF(T_i) \quad (1)$$

$TF\text{-}IDF(T_i, D_j)$ is the weight of the calculation T_i (means word) in the file D_j (means the file which the word is located). $TF(T_i, D_j)$ is the frequency at which T_i appears in D_j . $IDF(T_i) = \log(\frac{|D|}{|DF(T_i)|})$, $|D|$ is the number of all files in the training set, $DF(T_i)$ is the number of files containing T_i .

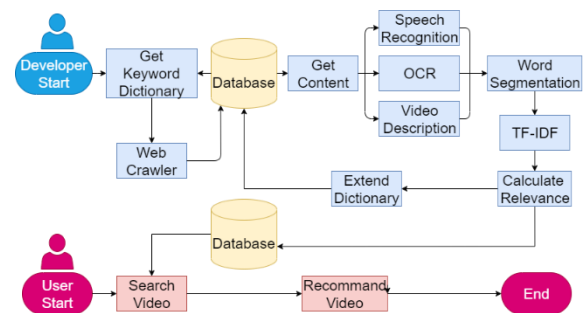


Fig. 1. Workflow of video search and recommendation system.

EXPERIMENT RESULTS: This study collects 400 videos for calculation and analysis. According experiment results, extracting the content-based keywords from the video by the system are highly relevant to the label, showing that the system is feasible in practical application. The results are shown in Fig. 2. Type in search keywords by the user, the system recommends the videos that calculated by the system based on the TF-IDF value.

CONCLUSION: This study constructs a system to analyze video content by extracting keywords.

* Poster paper presentation

The system now only provides English videos. In the future, we hope to expand this system to multiple languages in order to collect more comprehensive teaching videos to promote computer science education.

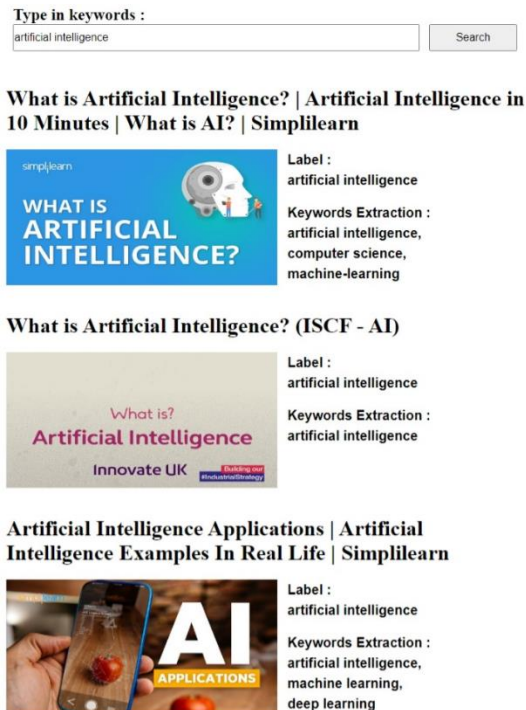


Fig. 2. Type in search keywords and return recommended videos.

References

- [1] Kaur, J., & Gupta, V. (2010). Effective approaches for extraction of keywords. *International Journal of Computer Science Issues (IJCSI)*, 7(6), 144.
- [2] Najafabadi, M. K., Mahrin, M. N. R., Chuprat, S., & Sarkan, H. M. (2017). Improving the accuracy of collaborative filtering recommendations using clustering and association rules mining on implicit data. *Computers in Human Behavior*, 67, 113-128.
- [3] Setiawan, E. I., Wicaksono, A. J., Santoso, J., Kristian, Y., Sumpeno, S., & Purnomo, M. H. (2018, November). N-Gram Keyword Retrieval on Association Rule Mining for Predicting Teenager Deviant Behavior from School Regulation. In *2018 International Conference on Computer Engineering, Network and Intelligent Multimedia (CENIM)* (pp. 325-328). IEEE.
- [4] Wu, H. C., Luk, R. W. P., Wong, K. F., & Kwok, K. L. (2008). Interpreting tf-idf term weights as making relevance decisions. *ACM Transactions on Information Systems (TOIS)*, 26(3), 1-37.

3-dimensional analysis of cochlear structure using CT data*

Hsu Sungchun ^{1,a}, Fukuoka Yutaka ^{1,b}

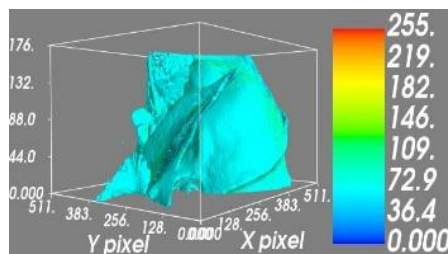
¹ Department of Electrical Engineering & Electronics, Graduate School of Engineering, Kogakuin University, Tokyo, Japan

^a cd20002@g.kogakuin.jp, ^b fukuoka@cc.kogakuin.ac.jp

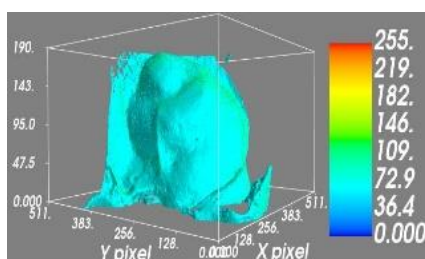
Abstract

Pendred syndrome, whose symptoms include bilateral hearing loss and recurrent dizziness, is caused by SLC26A4 gene mutation, and it is often reported that about 80% of cases have enlarged vestibular canal in the inner ear and Mondini type malformation in the cochlea^{[1][2]}. However, the exact structure of the cochlea malformation of a Pendred syndrome patient and its mechanism have not yet been elucidated^[3]. Hence, this study aims to develop a 3-dimensional (3D) analysis method of cochlea structure.

As a first step, we proposed an automatic 3D reconstruction of the cochlea based on micro-CT data (Fig.1). Cochlea images were obtained from a mouse genetically engineered to develop the Pendred syndrome and a mouse with natural genes (wild type).



(a) Het



(b) KO

Fig. 1. CT cochlear models of mice with natural genes (Het) and mice with Pendred syndrome (KO)

Then, the 3D images were analyzed through 1) image thresholding, 2) median filtering, 3) 3D

labelling, and 4) Hough transform (Fig. 2). These steps were employed to segment the cochlea by removing its surrounding tissues and to reduce noises.

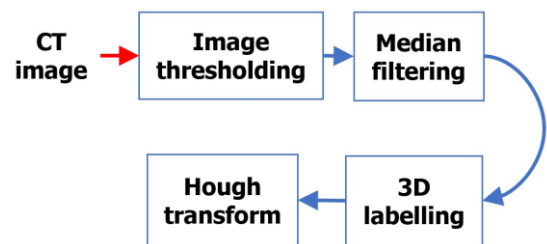
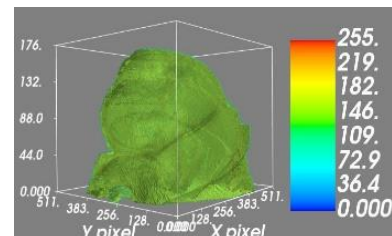
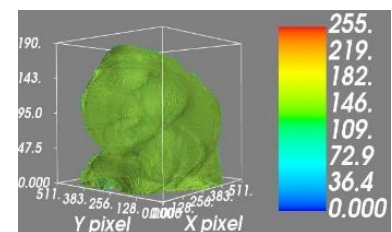


Fig. 2. A process that removes surrounding tissue and reduces noise

We need the exact structure that should be compared to an automatically constructed cochlea by the proposed method. Accordingly, we extracted the cochlea manually from the CT data. The manually extracted cochlea was deemed to be the exact model (Fig. 3), and it was used to calculate the error in the image processing.



(a) Het



(b) KO

Fig. 3. Manually extracted cochlea

Through the image processing, the cochlea was segmented automatically (Fig. 4). Then, the

* Poster paper presentation

automatically obtained structure was compared to its corresponding exact model (Fig. 3). We used Equation (1) to calculate the error rate between the manually extracted cochlea and the automatically extracted structure.

$$E = \frac{Num_{1\text{ or }255}[Img_{\text{manually}}(i,j,s) - Img_{\text{auto}}(i,j,s)]}{Num_{255}[Img_{\text{manually}}(i,j,s)]} \quad (1)$$

Here, $Img_{\text{manually}}(i,j,s)$ is a manually extracted cochlea image. $Img_{\text{auto}}(i,j,s)$ is the automatically extracted structure image. Num_x is the number of pixels that have values x in the calculated image.

An error rate of 6.69% and 8.53% was obtained for the malformed and the wild type cochlea, respectively (Table 1). Also, no apparent difference was found by visual inspection between the two models in both mice.

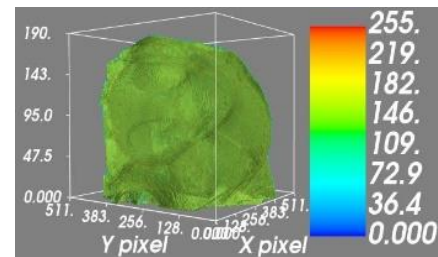
Table 1. Error rate with manual processing

| | Het | KO |
|------------|-------|-------|
| Error rate | 6.69% | 8.53% |

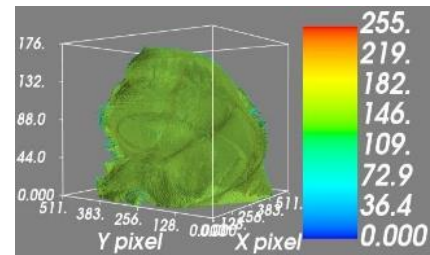
These results suggest that the proposed method is promising to analyze the 3D structure of the Mondini type malformation. In the future, we are planning to develop a method which can analyze structural differences between the Mondini-type malformation and the wild type cochlea to elucidate the pathophysiology of the malformation.

Keywords

Pendred syndrome, Mondini type malformation, cochlea, 3D image processing



(a) Het



(b) KO

Fig. 4. Automatically obtained structure by image

References

- [1] Johnsen T, Jørgensen MB, Johnsen S. 1986. Mondini cochlea in Pendred's syndrome. A histological study. Acta Otolaryngol (Stockh). 102: 239–47.
- [2] Ito T, Choi BY, King KA, Zalewski CK, Muskett J, Chattaraj P, Shawker T, Reynolds JC, Butman JA, Brewer CC, Wangemann P, Alper SL, Griffith AJ. 2011. SLC26A4 genotypes and phenotypes associated with enlargement of the vestibular aqueduct. Cell Physiol Biochem. 28(3):545-52.
- [3] Markova TG, Geptner EN, Lalayants MR, Zelikovich EI, Chugunova TI, Mironovich OL, Bliznetz EA, Polyakov AV, Tavartkiladze GA. 2016. The clinical definition and etiology of Pendred syndrome (a review of the literature and clinical observations). Vestnik Otorinolaringologii 81: 6, pages 25.

Using genetic algorithm and Gini coefficient neural network parameter optimization*

Okusu Yoshiyumi ^{1,a,*}, Naoya Takahashi ^{1,b}, Hidetoshi Saito ^{2,c}¹ Graduate School of Engineering, Kogakuin University² Dept of Electrical & Electronic Eng, Faculty of Engineering, Kogakuin University, Tokyo, Japan^a cm20011@ns.kogakuin.ac.jp, ^b cm19029@ns.kogakuin.ac.jp, ^c h-saito@cc.kogakuin.ac.jp**Abstract**

A Genetic Algorithm^[1] was used to optimize the parameters of the Artificial Neural Network^[2].

The error distribution was incorporated into the Neural Network update formula using the Gini coefficient^[3].

The dataset used is the Iris dataset. Of the total 150 data, we divided it into training 50 and test 100.

The Neural Network consists of an input layer 4, an intermediate layer 10, and an output layer 3. As the activation function, relu was used for the intermediate layer and softmax was used for the output layer.

The Genetic Algorithm was 100 for herd size, 20 for alternation of generations, roulette for the selection rule for the parent individual, ranking for the selection rule for alternation of generations, and uniform crossover for the crossover rule.

Each individual was trained 50 times with a neural network, and the generational change of the entire herd was repeated 50 times, which was repeated 20 times.

Equation [1] is a neural network parameter update equation. Equation [2] saves past updates

$$w_{t+1} = w_t - \text{eta} * \{(0.7 - \text{gini}) * \text{grad}W + (0.3 + \text{gini}) * h_t\} \quad (1)$$

$$h_{t+1} = \text{eta} * \{(0.7 - \text{gini}) * \text{grad}W + (0.3 + \text{gini}) * h_t\} \quad (2)$$

- The simulation results were evaluated by the correct answer rate in the test data and the magnitude of the error due to the cross entropy error. Table 1. is the result.

Table 1. Comparison with the case without using the Gini coefficient

| | Neural Network Only | Neural Network and Genetic Algorithm | Neural Network and Genetic Algorithm and Gini coefficient |
|----------------|---------------------|--------------------------------------|---|
| Error | 0.285639609 | 0.326653822 | 0.133349627 |
| Accuracy Train | 100% | 100% | 100% |
| Accuracy Test | 93% | 93% | 96% |

In Table 1, the vertical axis shows the cross entropy error, and the horizontal axis shows the number of Neural Network learnings. Since 50 learnings are repeated 20 times with a generation change in between, the total is 1000 times. For comparison, we prepared a neural network of the same scale using a single neural network and using the stochastic gradient descent method as the optimization method. One is the result of a flock that does not use the Gini coefficient, and the other is a single neural network that does not have a flock.

Keywords

Artificial neural networks (ANNs), backpropagation, genetic algorithms (GA), Gini index

* Poster paper presentation

References

- [1] John Henry Holland "Adaptation in Natural and Artificial Systems"(1975)
- [2] Rumelhart DE, Hinton GE and Williams RJ: Learning internal representations by error propagation. *Parallel Distributed Processing*, 1, MIT Press, MA, 318-362, (1986).sea cucumbers.
- [3] Corrado Gini. 1936.

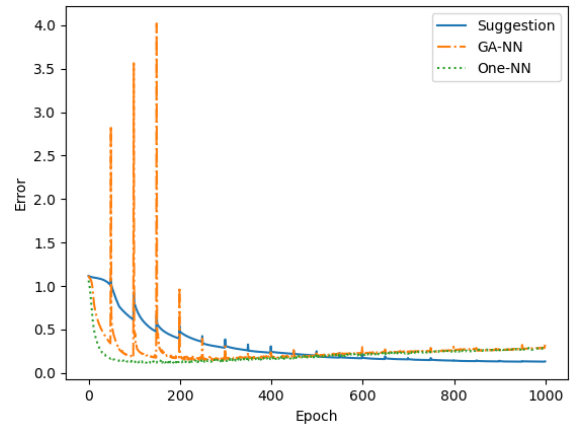


Fig. 1. Simulation result

Effects of variations in the parameters of EBMA in motion estimation accuracy*

Melvin C. Ilang-Ilang^{1,a}

¹Department of Electrical Engineering, College of Engineering & Agro-Industrial Technology, University of the Philippines Los Baños, Philippines

^amcilangilang3@up.edu.ph

Abstract

Motion estimation is an important part of any video processing system. Its applications include video compression, video sampling rate conversion, and video filtering. For video compression applications, the estimated motion vectors are used to produce motion-compensated prediction of a frame to be coded from a previously coded reference frame.

EBMA (Exhaustive Block Matching Algorithm), also referred to as full search, is the most computationally expensive among all block matching algorithms^[1] since a cost function is being calculated at each possible location in the search range. The cost function can be computed either through the mean absolute difference (Eq. 1) or the mean square error (Eq. 2) where N is the block size being used, A is the anchor frame, and T is the target frame.

$$MAD = \frac{1}{N^2} \sum_{i=0}^{N-1} \sum_{j=0}^{N-1} |A_{ij} - T_{ij}| \quad \text{Eq. 1}$$

$$MSE = \frac{1}{N^2} \sum_{i=0}^{N-1} \sum_{j=0}^{N-1} (A_{ij} - T_{ij})^2 \quad \text{Eq. 2}$$

The factors being considered when performing EBMA are block size, search range, and step size. For this study, the author used two levels each for the block size (8x8, 16x16) and step size (half-pel, integer-pel), and five levels for the search range (1, 2, 4, 8, 16).

While it is somehow obvious which combinations would yield the least computational time, evaluation in terms of video quality metrics is not yet fully known.

The foreman sequence^[2] with QCIF resolution (176x144) was used as the test sequence. Three frames from the said sequence were randomly chosen as anchor frames. The target frames

considered were the fifth frame from the anchor frame being considered.

Objective assessment on the test sequence was used to determine the effects of the above-mentioned factors when motion prediction is applied using PSNR (Peak Signal-to-Noise Ratio)^[3] and SSIM (Structural Similarity)^[4] as video quality metrics. In addition, computation time was also be measured. Full factorial design was utilized for this study in order to exhaust all possible combinations in the factors to give more definitive results.

Table 1 shows the summary of the best and worst computed PSNR and SSIM values per test frame while Table 2 shows the fastest and slowest measured computation time per test frame. Based on the results, it was confirmed that block size, step size, and search range all have significant effects in the PSNR and SSIM of a motion estimated frame using EBMA. For all the test frames, the block size – search range – step size combination that produced the best PSNR and SSIM values was 16x16 – 1 – half-pel. While the combination with the worst PSNR and SSIM values was 8x8 – 16 – integer-pel.

Table 1. Summary of best and worst computed PSNR and SSIM values per test frame.

| Test Frame | Block Size | Search Range | Step Size | PSNR (dB) | SSIM |
|------------|------------|--------------|-------------|-----------|--------|
| 1 | 16x16 | 1 | half-pel | 29.1516 | 0.9600 |
| 1 | 8x8 | 16 | integer-pel | 12.2866 | 0.4869 |
| 2 | 16x16 | 1 | half-pel | 27.2164 | 0.9424 |
| 2 | 8x8 | 16 | integer-pel | 12.0302 | 0.4610 |
| 3 | 16x16 | 1 | half-pel | 27.4844 | 0.9451 |
| 3 | 8x8 | 16 | integer-pel | 12.3038 | 0.4790 |

On the other hand, a generalized conclusion regarding the effect of the three parameters to the computation time cannot be determined since the

* Oral and poster paper presentation

data gathered does not follow the normal distribution. But for the considered test frames, it is advisable to use a 16x16 block size.

Table 2. Summary of fastest and slowest measured computation time per test frame.

| Test Frame | Block Size | Search Range | Step Size | Computation Time (μ s) |
|------------|------------|--------------|-------------|-----------------------------|
| 1 | 16x16 | 16 | integer-pel | 4.5333 |
| 1 | 8x8 | 4 | half-pel | 824437.1 |
| 2 | 16x16 | 16 | half-pel | 3.5333 |
| 2 | 16x16 | 1 | half-pel | 806528.8333 |
| 3 | 16x16 | 8 | half-pel | 3.7000 |
| 3 | 16x16 | 4 | half-pel | 826977.1333 |

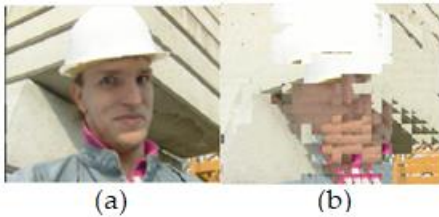


Fig. 1. Test Frame 1 predicted images using 16x16 - 1 - half-pel (a) and 8x8 - 16 - integer-pel (b) parameter combinations.

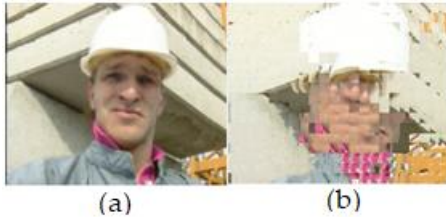


Fig. 2. Test Frame 2 predicted images using 16x16 - 1 - half-pel (a) and 8x8 - 16 - integer-pel (b) parameter combinations.

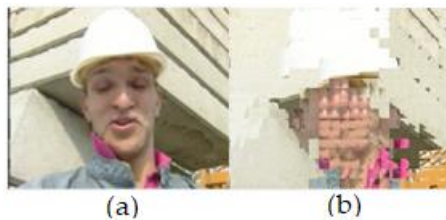


Fig. 3. Test Frame 3 predicted images using 16x16 - 1 - half-pel (a) and 8x8 - 16 - integer-pel (b) parameter combinations.

Keywords

EBMA, block matching, motion estimation

References

- [1] W. Hassen and H. Amiri, "Block Matching Algorithms for motion estimation," in 2013 7th IEEE International Conference on e-Learning in Industrial Electronics (ICELIE), Vienna, Austria, 2013.
- [2] "YUV Video Sequences," [Online]. Available: <http://trace.kom.aau.dk/yuv/index.html>. [Accessed 29 October 2019].
- [3] Z. Cheng, L. Ding, W. Huang, F. Yang and L. Qian, "Subjective QoE based HEVC encoder adaptation scheme for multi-user video streaming," in 2016 IEEE International Symposium on Broadband Multimedia Systems and Broadcasting (BMSB), Nara, Japan, 2016.
- [4] Z. Wang, L. Lu and A. Bovik, "Video quality assessment using structural distortion measurement," in International Conference on Image Processing, Rochester, NY, 2002.

Technical Presentations

Energy & Transportation

| | | |
|---------------------|--|---|
| Moderator | : | Dr. Rubenito M. Lampayan |
| Panelists | : | Dr. Marion Lux Y. Castro, Dr. Omar F. Zubia, Dr. Joan Cecilia C. Casila |
| Technical Assistant | : | Ms. Mary Ann M. Porlay |
| 01:30PM – 01:35PM | Welcome Remarks and Introduction of Panel Members | |
| 01:35PM – 02:35PM | Parallel Sessions for Water Resources Engineering | |
| 02:35PM – 02:50PM | A proposed self-powered data acquisition system for an agricultural pump testing rig | <u>John Paolo A. Ramoso*</u> , Dexter Jed S. Matibag, Thea Claire M. Chua, Lorwin Felimar B. Torrizo, Christian Paul R. Esteban, Erwin P. Quilloy, Arthur L. Fajardo, Romulo E. Eusebio (UPLB) |
| 02:50PM – 03:05PM | A Pilot Study on Using Rice Straw as Fuel for Paddy Drying | <u>Maria Victoria P. Migo-Sumagang*</u> , Monet Concepcion Maguyon- Detras, Martin Gummert, Catalino G. Alfafara, Myra G. Borines, Jewel A. Capunitan and Nguyen Van Hung (UPLB) |

A pilot study on using rice straw as fuel for paddy drying*

Maria Victoria P. Migo-Sumagang ^{1,2,a,*}, Monet Concepcion Maguyon-Detras ^{2,b}, Martin Gummert ^{1,c}, Catalino G. Alfafara ^{2,d}, Myra G. Borines ^{2,e}, Jewel A. Capunitan ^{2,f}, Nguyen Van Hung ^{1,g,*}

¹ International Rice Research Institute, Los Baños, Laguna, Philippines

² Dept of Chem Eng, College of Eng & Agro-Industrial Tech, Univ of the Philippines Los Baños, Philippines

^a mpmigo@up.edu.ph, ^b mmdetras@up.edu.ph, ^c m.gummert@irri.org, ^d cgalfafara@up.edu.ph,

^e mgborines@up.edu.ph, ^f jacapunitan@up.edu.ph, ^g hung.nguyen@irri.org

Abstract

Open-field burning and soil incorporation are the most common waste management options for rice straw. Both methods disregard the energy value of rice straw, which is a widely available resource. To tap its biomass energy potential, an alternative option is to use rice straw as fuel in paddy drying. In this study, a small-scale paddy dryer simulator using hot gases from a rice straw furnace was used to investigate whether the proposed alternative option is preferable in terms of energy balance and GHG emissions compared to open-field burning and soil incorporation. The effects of rice straw type (loose or baled), fuel feed rate, and drying airflow rate on thermal efficiency and increase in dryer temperature were initially investigated following a factorial experimental design. The optimum conditions that would result in the highest thermal efficiency with a sufficient increase in dryer temperature were then determined using Response Surface Methodology (RSM) designed experiments. The results of the experiments were then used in input-output energy analysis and GHG emissions balance from rice production to energy generation using the SimaPro software. Results show that the optimum

conditions are at a rice straw feed rate of 20.67 kg hr⁻¹ and a drying airflow rate of 3.03 m³ s⁻¹ using loose straw, which resulted in a thermal efficiency of 86.1% and 18.41°C increase in dryer temperature. Using literature data on rice production and the results of this study on energy generation, it was found that the energy ratio of the proposed alternative option was between 1.4 to 1.7, and the percent net energy was between 39 to 67%. The best-case offers a possibility of a net GHG avoided (-61 kg CO₂-eq Mg⁻¹), while the worst-case has a net GHG emission comparable with soil incorporation (856 kg CO₂-eq Mg⁻¹). Overall, using rice straw as fuel for paddy drying is better in terms of energy flow since it results in positive net energy, and has the potential to improve the GHG emissions of rice production systems compared to open-field burning and soil incorporation.

Keywords

Rice straw, bioenergy, energy efficiency, net energy balance, net GHG emissions

* Oral and poster presentation

Isolation, characterization, and screening of purple non-sulfur bacteria for biohydrogen production*

Floriebelle D. Querubin ^{1,a}, Saul M. Rojas ^{1,b}, Nacita B. Lantican ^{2,c}, Ruby Lynn G. Ventura ^{3,d}, Fidel Rey P. Nayve Jr. ^{4,e}, Jey-R S. Ventura ^{1,f,*}

¹ Dept of Eng Sci, College of Eng & Agro-Industrial Tech, Univ of the Philippines Los Baños, Philippines

² Microbio Div, Institute of Bio Sci, College of Arts & Sci, Univ of the Philippines Los Baños, Philippines

³ UP Rural High School, College of Arts & Sci, Univ of the Philippines Los Baños, Philippines

⁴ National Institute of Molecular Bio & Biotech, Univ of the Philippines Los Baños, Philippines

^a fdquerubin1@up.edu.ph, ^b smrojas@up.edu.ph, ^c nblantican@up.edu.ph, ^d rgventura@up.edu.ph,

^e fpnayve@up.edu.ph, ^f jsventura@up.edu.ph

Abstract

Photofermentation is one popular form of biohydrogen production because of its high substrate conversion efficiency. Among the microorganisms used in photofermentation, purple non-sulfur bacteria (PNSB) are considered good candidates because of their metabolic versatility and wide range of substrate utilization [1]. In this study, PNSB were isolated from mud slurry samples obtained from Molawin Creek, Laguna de Bay, and rice paddies in Los Baños, Laguna, Philippines using standard enrichment culture and anaerobic isolation methods. The isolates were characterized based on their colony formation and Gram stain reaction (Fig. 1).

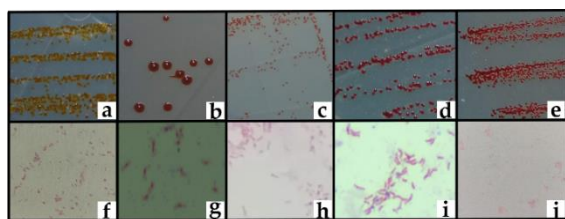


Fig. 1. Colony characteristics (a-e) and Gram stain reaction (f-j) of MAY2 (a, f), PR2 (b, g), IRR11 (c, h), MAL1 (d, i), and BG1 (e, j) from selected sites in Los Baños, Laguna

Based on cultural characteristics and cell morphology, all isolates were Gram-negative; had circular form, entire margin, and convex elevation; possessed brown to red colony pigmentation; and grew under anaerobic

condition – all of which are common characteristics of PNSB [2].

The 5 isolates were subjected to DNA isolation, amplification of the 16S rRNA gene and sequence analysis to determine their identities.

Table 1. Top 3 BLAST hits of the putative PNSB isolates

| Isolate Code | BLAST Hit | Identity (%) | Accession Code |
|--------------|---|--------------|----------------|
| MAY2 | <i>Rhodobacter sediminis</i> strain N1 | 97.56% | NR_151925.1 |
| | <i>Rhodobacter capsulatus</i> strain KC2137 | 97.40% | NR_115744.1 |
| | <i>Rhodobacter azollae</i> strain JA912 | 97.39% | NR_158007.1 |
| PR2 | <i>Rhodobacter johrii</i> strain JA192 | 98.84% | NR_115016.1 |
| | <i>Rhodobacter sphaeroides</i> strain 2.4.1 | 98.67% | NR_029215.1 |
| | <i>Rhodobacter sphaeroides</i> strain IFO12203 | 98.67% | NR_115532.1 |
| IRRI1 | <i>Rhodobacter sediminis</i> strain N1 | 98.84% | NR_151925.1 |
| | <i>Rhodobacter azollae</i> strain JA912 | 98.68% | NR_158007.1 |
| | <i>Rhodobacter capsulatus</i> strain KC2137 | 98.60% | NR_115744.1 |
| MAL1 | <i>Rhodopseudomonas palustris</i> strain ATCC 17001 | 96.69% | NR_112912.1 |
| | <i>Rhodopseudomonas thermotolerans</i> strain JA576 | 96.66% | NR_108528.1 |
| | <i>Rhodopseudomonas pentothetateixgens</i> strain JA575 | 96.71% | NR_108527.1 |
| BG1 | <i>Rhodopseudomonas faecalis</i> strain gc | 96.82% | NR_024971.1 |
| | <i>Rhodopseudomonas palustris</i> strain ATCC 17001 | 96.58% | NR_112912.1 |
| | <i>Rhodopseudomonas thermotolerans</i> strain JA576 | 96.61% | NR_108528.1 |

Results of the sequence analysis of the putative PNSB isolates using BLAST are summarized in Table 1. The 16S rRNA genes revealed that MAY2, PR2, and IRR11 showed 97-98% similarity to *Rhodobacter* sp. suggesting that these isolates belong to species under genus *Rhodobacter*. On the other hand, MAL1 and BG1 showed >96% similarity to *Rhodopseudomonas* sp. indicating that the two isolates are species under genus *Rhodopseudomonas*.

All isolates were screened based on their potential to produce biohydrogen using different volatile fatty acids (VFAs) namely acetate, butyrate, and

* Poster paper presentation

propionate, as carbon sources. These VFAs are the major fermentation by-products that are usually detected in dark fermentation liquors.

As presented in Fig. 3, isolates MAY2 and PR2 were found to produce biogas from butyrate and propionate. Minimal biogas production was observed from acetate. Isolate BG1, on the other hand, produced biogas from butyrate and acetate, while minimal from propionate. IRR1 and MAL1 were able to produce biogas from each individual acid substrates. Highest cumulative biogas production was attained by isolate PR2 with 2,242.37 mL/g, followed by IRR1 and MAY2 with 2,211.86 mL/g and 2,113.56 mL/g, respectively, after 15 days using propionate.

Finally, mixture of the three VFAs were also used to screen the potential of all the isolates to produce biohydrogen. Highest cumulative biogas production for mixed acids was observed in isolate MAY2 (1,644.57 mL/g) followed by isolate PR2 (1,622.83 mL/g), isolates IRR1 (1,490.22 mL/g), MAL1 (1,280.43 mL/g), and BG1 (701.09 mL/g).

Overall, the 5 PNSB isolated in this study were found to produce biogas using major fermentation

by-products. Theoretically, PNSB photo-fermentation utilizing VFAs as substrate can have more than 50% (mol) hydrogen in the biogas. Therefore, results of this study present the capability of the isolated PNSB to produce hydrogen. Gas analysis via gas chromatography will be conducted in the future to determine the actual hydrogen composition of the biogas.

Keywords

biohydrogen, photofermentation, PNSB, *Rhodobacter*, *Rhodopseudomonas*

References

- [1] Ventura RLG, Ventura JS, Oh YS. 2019. Photoheterotrophic Hydrogen Production of *Rhodobacter sphaeroides* KCTC 1434 under Alternating Ar and N₂ Headspace Gas. Philippine Journal of Science. 148(1): 63-72.
- [2] Madigan MT, Jung DO. 2008. Chapter 1 - An Overview of Purple Bacteria: Systematics, Physiology, and Habitats. In book: Advances in Photosynthesis and Respiration (Vol 28) – The Purple Phototrophic Bacteria. Springer, pp. 1-12.

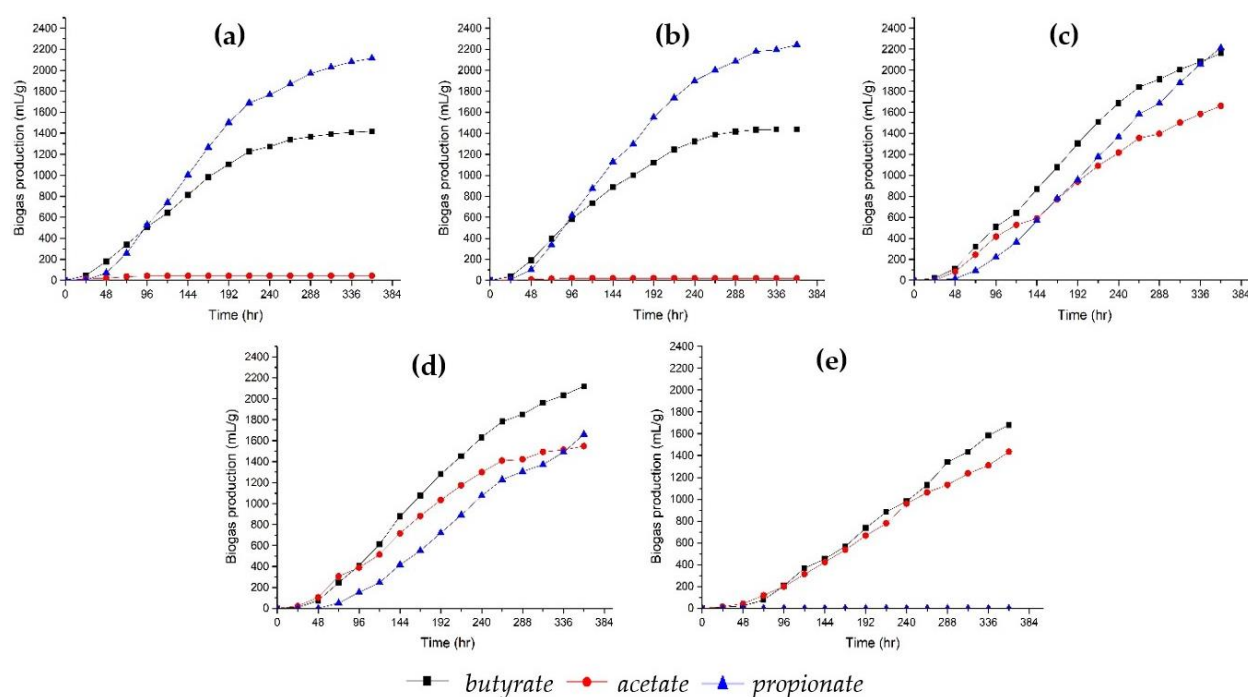


Fig. 3. Cumulative biogas production of isolates (a) MAY 2, (b) PR2, (c) IRR1, (d) MAL1, and (e) BG1 from butyrate, acetate, and propionate.

Comparison of temperature and relative humidity as exogenous variables for weekday load forecasting*

Michael Angelo A. Racelis ^{1,a}, Kim Jay R. Rosano ^{1,b,*}, Elvin D. Dulce ^{1,c}, Gabriela Monica M. Gonzales ^{1,d}, Raymond S. Mabilangan ^{1,e}

¹ Dept of Electrical Eng, College of Eng & Agro-Industrial Tech, University of the Philippines Los Baños, Philippines

^amaracelis@up.edu.ph, ^bkrrosano@up.edu.ph, ^ceddulce@up.edu.ph, ^dgmgonzales1@up.edu.ph, ^ersmabilangan@up.edu.ph

Abstract

Short-term demand forecasting provides the customers with information that could help them analyze their demand for resource allocation and power saving strategies and provide cost-effective and reliable power system operation through proper demand management^[1]. Time series analysis methods are usually used for demand forecasting, with numerous variations and techniques to incorporate various parameters like meteorological and temporal factors, which are some of the important factors affecting demand forecasts, among others^[2].

Studies were made to model the load as a function of the load's previous values. Autoregressive (AR) and Moving Average (MA) models were some of the most common techniques, among others. Using the 2017 energy consumption data of an academic institution, the effects of temperature and relative humidity to the forecast of energy demand was observed, with considerations of the daily seasonality of the data.

Seasonal Autoregressive Integrated Moving Average with Exogenous Variables (SARIMAX) was used on the 2017 data to forecast the first week energy demand of every month succeeding the forecasting month, comparing temperature- and relative humidity- integrated forecasts. For training, the weekends and holidays were removed from the dataset since the forecasts are to be modeled for weekdays only. An example of this is shown in Fig. 1 where the April 2017 weekday data serves as the

training data for forecasting the first weekdays of May.

Strong daily seasonality is observable in the model suggesting that the behavior of the demand has a season of 24-hours, or 1-day. ADF and KPSS tests were done for stationarity test. Using the stationary data, eleven models were generated for each forecasting month to forecast the first five days of the forecasted month (i.e. model trained using April 2017 data to forecast May 2017, May 2017 to forecast June 2017, and so on).

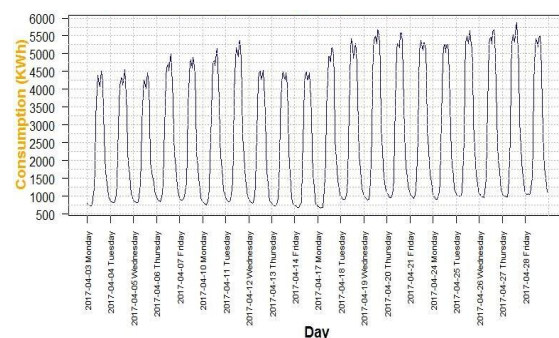


Fig. 1. April 2017 Weekday data

Comparing the forecast within days, as seen in Table 1, the Tuesday through Thursday forecasts on the average performed better than Monday and Friday forecasts for both models incorporating temperature (1.79% to 5.13% better on the average) and relative humidity (0.15% to 5.5% better on the average), suggesting that weekday forecast variation are generally affected by its proximity to the weekends.

Generally, forecast models with temperature as exogenous variable performed better than

* Poster paper presentation

forecast models with relative humidity, as seen in Table 2, with the months of May and June being the best performing forecasting months achieving 5-day average forecast MAPE of 3.59% and 4.36% for June and July, respectively^[3]. The rest of the months have a 5-day average forecast MAPE that varies from 5.7% to 14.47%^[3]. The results showed that SARIMAX has the capability of capturing the behavior of the demand, however, it resulted to significant errors in some days within the first week forecast. Other techniques may be explored to create longer forecasts with more exogenous variables on future work.

Table 1. Average MAPE for days categorized by its proximity to weekends

| Forecasted MONTH | SARIMAX with Temp | | SARIMAX with Rel Hum | |
|------------------|-------------------|----------|----------------------|----------|
| | MF Ave | TWTh Ave | MF Ave | TWTh Ave |
| February | 9.87 | 4.62 | 10.01 | 4.73 |
| March | 6.14 | 5.98 | 6.05 | 6.38 |
| April | 7.56 | 5.15 | 10.81 | 9.95 |
| May | 15.62 | 4.55 | 15.54 | 4.04 |
| June | 3.72 | 3.50 | 4.73 | 3.51 |
| July | 4.37 | 4.36 | 4.96 | 4.90 |
| August | 6.75 | 7.87 | 6.77 | 8.59 |
| September | 16.28 | 6.78 | 15.45 | 6.83 |
| October | 6.37 | 5.25 | 8.16 | 10.95 |
| November | 9.68 | 8.55 | 5.00 | 6.87 |
| December | 18.68 | 11.66 | 18.48 | 11.73 |

Keywords

Load forecast, weekday forecast, SARIMAX, temperature, relative humidity

Table 2. 5-day average MAPE for each forecasted month

| Forecasted MONTH | Average MAPE* (Temp) | Average MAPE* (Rel Hum) |
|------------------|----------------------|-------------------------|
| February | 6.7166 | 6.8389 |
| March | 6.0457 | 6.2465 |
| April | 6.1120 | 10.2910 |
| May | 8.9761 | 8.6397 |
| June | 3.5880 | 3.9961 |
| July | 4.3587 | 4.9253 |
| August | 7.4240 | 7.8604 |
| September | 10.5763 | 10.2780 |
| October | 5.7002 | 9.8329 |
| November | 9.0027 | 6.1193 |
| December | 14.4673 | 14.4308 |

*Average MAPE is computed as the 5-day average of the MAPEs of the forecasted month.

References

- [1] Zhao H, Tang Z, Wang Z. 2017. Study of short-term load forecasting in big data environment. 29th Chinese Control and Decision Conference (CCDC). China: IEEE.
- [2] Khatoon S, Ibraheem, Singh A, Priti. 2014. Effects of various factors on electric load forecasting: an overview. 6th IEEE Power India International Conference (PIICON). India: IEEE.
- [3] Racelis M. A. 2018. Short-term Energy Forecasting for Weekdays using Autoregressive Integrated Moving Average with Exogenous Variables (ARIMAX) and Seasonal ARIMAX (SARIMAX) for UPLB Power System. Undergraduate Thesis, DEE, CEAT, UPLB.

Evaluation of the capacity value of a solar power plant in the Visayas grid, Philippines*

Kyrstynne D. Ureta ^{1,a}, Elvin D. Dulce ^{1,b*}

¹Dept of Electrical Eng, College of Eng & Agro-Industrial Tech, Univ of the Philippines Los Baños, Philippines

^akdureta@up.edu.ph, ^beddulce@up.edu.ph

Abstract

In the Philippines, the total greenhouse gas (GHG) emissions from energy-related activities increased by 4.1 percent or 123.3 MtCO₂e in 2018. Power generation contributed more than half (51.7 percent) of the total GHG emissions, which is mainly due to the utilization of coal for power generation^[1]. To effectively prevent or reduce harmful emissions from conventional power plants, the Renewable Energy Act of 2008 promotes the development and utilization of renewable energy resources by providing incentives^[2]. The solar capacity in the country increased from only 1 MW in 2008 to 896 MW in 2018. Based on the Philippine Energy Plan 2018-2040, the solar capacity is expected to increase to 24,960 MW (around 27% grid penetration) by 2040^[1].

Globally, the use of solar photovoltaic (PV) continues to increase due to its lowering price, sustainability, and environmental benefits. The intermittent generation of solar PV, however, adds variability in the grid. This presents the need to quantify the contribution of solar PV generation in the system adequacy by calculating the Capacity Value (CV) - the ability of the PV plant to reliably meet demand^[3].

In this study, two reliability-based methods were used to calculate the CV of a solar PV plant - the Equivalent Conventional Power method and the Equivalent Load Carrying Capability method. The Equivalent Conventional Power (ECP) refers to the amount of dispatchable generation the solar PV plant could replace while the Equivalent Load Carrying Capability (ELCC) represents the amount of additional load that the system permits due to the presence of the solar PV plant^[3].

The 45 MW First Toledo Solar Energy Corp. (FTSEC) solar PV plant in the Visayas Grid, which was distinguished as the No. 1 Variable Renewable Energy (VRE) performer in 2017 by the Philippine Electricity Market Corporation (PEMC)^[4], was the solar PV plant considered in this study. The capacity values ELCC and ECP, were calculated based on a generation system reliability metric - the Loss of Load Expectation (LOLE).

The steps used to calculate the ECP of the 45 MW FTSEC solar PV plant are as follows:

1. With the solar PV plant in the system, the LOLE is calculated using Eq. 1^[3]:

$$LOLE_{PV} = \sum_{i=1}^T P(G_i + C_i < L_i) \quad (1)$$

where T is the total number of hours, G_i is the conventional capacity, C_i is the output of the solar PV plant, and L_i is the load level in hour i . $P(G_i + C_i < L_i)$ indicates the probability of the combined available generating capacity from the conventional plants and the solar PV plant being less than the load^[3].

2. The solar PV plant is removed and a conventional generator is added. The LOLE of the new system is computed using Eq. 2^[3]:

$$LOLE_{Gen} = \sum_{i=1}^T P(G_i + X_i < L_i) \quad (2)$$

where X_i is the generating capacity from the added conventional generator in hour i . The capacity of the conventional generator is increased until $LOLE_{Gen} = LOLE_{PV}$. The capacity of the conventional generator that achieves this equality is the calculated ECP of the solar PV plant^[3].

On the other hand, the steps used to calculate the ELCC of the 45 MW FTSEC solar PV plant are as follows:

* Poster paper presentation

- Without the solar PV plant in the system, the LOLE is calculated using Eq. 3^[3]:

$$LOLE_{base} = \sum_{i=1}^T P(G_i < L_i) \quad (3)$$

- With the solar PV plant in the system, a constant load D is added in each hour. The LOLE of the new system is calculated using Eq. 4^[3]:

$$LOLE_{Load} = \sum_{i=1}^T P(G_i < L_i + D) \quad (4)$$

The value of D is increased until $LOLE_{Load} = LOLE_{base}$. The value of the load D that achieves this equality is the calculated ELCC of the solar PV plant^[3].

After performing the methods discussed, the ECP results show that for a LOLE of 8.3 hours/year, the 45 MW FTSEC solar PV plant can replace a 15.6 MW geothermal plant, a 16.2 MW biomass plant, a 16.7 MW natural gas plant, a 16.7 MW coal plant, or a 19.4 MW diesel plant in the Visayas Grid, as shown in Fig. 1. Among these benchmark generators, geothermal and biomass plants have the lowest GHG emissions, natural gas and diesel plants have high GHG emissions, and coal plants have the highest GHG emissions^[5]. In power generation planning, this means that a 45 MW solar PV plant can be considered to replace a coal power plant with a minimum power output of 16.7 MW, to cut the GHG emissions.

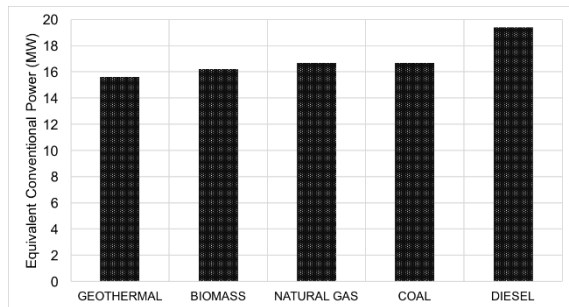


Fig. 1. ECP of FTSEC solar PV plant.

In addition, the ELCC results show that with the 45 MW FTSEC solar plant in the Visayas Grid at a LOLE of 9.5 hours/year, the system will allow an additional load of 15.3 MW or 34% of its rated capacity, which falls between 5% and 95% typical CV range for renewables. The penetration level of the 45 MW FTSEC solar PV plant in the Visayas Grid in 2017 is 1.6%.

When the solar penetration level is increased, the ELCC of the FTSEC solar PV plant decreases as

shown in Fig. 2. This is due to the increased variability in the grid caused by the intermittent supply from the solar PVs.

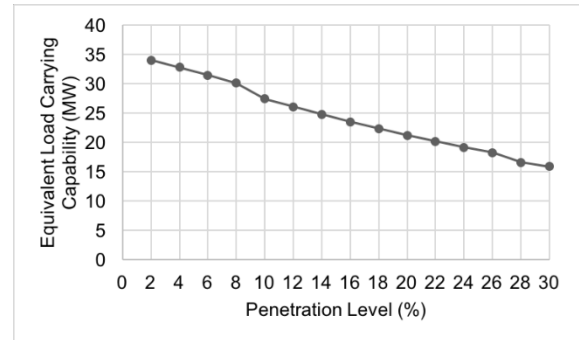


Fig. 2. ELCC of FTSEC solar PV plant at increasing penetration level.

Aside from solar PV plants, the CV of other emerging renewable, alternative, and non-conventional power plants such as tidal power plants and Battery Energy Storage Systems (BESS) can be considered for future work.

Keywords

Solar, capacity value, reliability

References

- [1] Department of Energy, "Philippine Energy Plan 2018-2040," 2018. [Online]. Available: <http://www.doe.gov.ph/sites/default/files/pdf/pep/pep-2018-2040-final.pdf>
- [2] Department of Energy, "Republic Act No. 9513," 2008. [Online]. Available: <http://www.doe.gov.ph/laws-and-issuances/republic-act-no-9513>
- [3] S. H. Madaeni, R. Sioshansi, and P. Denholm, "Comparison of capacity value methods for photovoltaics in the Western United States," National Renewable Energy Laboratory, Golden, Colorado, USA, July 2012. [Online]. Available: NREL/TP-6A20-54704.
- [4] Citicore Power Inc., "Citicore Power subsidiaries lauded as VRE Top Performers by PEMC." citicorepower.com.ph. <http://citicorepower.com.ph/citicore-power-subsiaries-lauded-vre-top-performers-pemc> (accessed October 21, 2018).
- [5] G. Heath, "Environmental impacts of renewable electricity generation technologies: a life cycle perspective," National Renewable Energy Laboratory, Golden, Colorado, USA, January 13, 2016. [Online]. Available: NREL/PR-6A20-65645.

A proposed self-powered data acquisition system for an agricultural pump testing rig*

John Paolo A. Ramoso ^{1,a*}, Dexter Jed S. Matibag ¹, Thea Claire M. Chua ¹, Lorwin Felimar B. Torrizo ¹, Christian Paul R. Esteban ¹, Erwin P. Quillooy ², Arthur L. Fajardo ³, Romulo E. Eusebio ³

¹Dept of Electrical Eng, College of Eng & Agro-Industrial Tech, UP Los Baños, Laguna, Philippines

²Institute of Agric & Biosys Eng, College of Eng & Agro-Industrial Tech, UP Los Baños, Laguna, Philippines

³Agricultural Machinery Testing and Evaluation Center, College of Eng & Agro-Industrial Tech, UP Los Baños, Laguna, Philippines

^ajaramoso@up.edu.ph

Abstract

INTRODUCTION: The need for faster and more precise measuring procedures of a testing facility gave rise to the design of a self-powered low-cost data acquisition system (DAS). An existing pump-testing rig system for axial flow pumps and centrifugal pumps at Agricultural Machinery Testing and Evaluation Center (AMTEC), as seen in Figure 1, was observed and was designed to be retrofitted with an automated DAS. To make the design sustainable, the sensor system was then selected to be powered by the unwanted vibrations from the pump that was being tested by the rig.

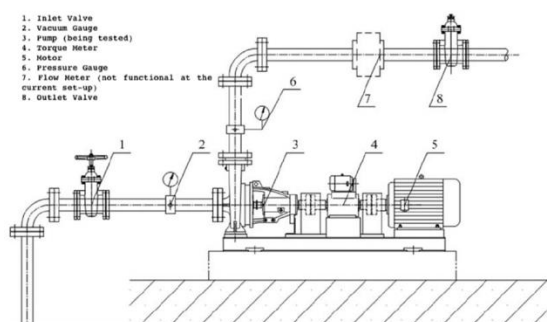


Fig. 1. Schematic diagram of the existing AMTEC pump test rig

SYSTEM ARCHITECTURE

Proposed data acquisition system (DAS) for the pump test rig: Referencing the existing set-up on the design, a VFD was connected to the induction motor to help in controlling its speed. The proposed DAS used a Raspberry Pi 3B+ as the

controller while locally available sensors and transducers were used to make sure the system was sustainable. Sensors were selected to pick up the ambient temperature, relative humidity, weight, relative pressure, vacuum pressure, and torque and vibrations of the motor. Signal conditioners were designed to interface the sensors and transducers to the controller. Figure 2 shows the block diagram of the automated DAS of the pump test rig. The digital signal was then acquired and recorded by the controller via an SD card or a flash drive and displayed with an LED or onboard monitor. The controller that was used in the design will allow the operator/technician to store the data as a CSV file and later on be transferred to a computer for further processing.

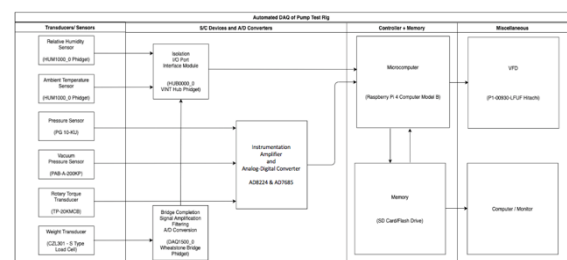


Fig. 2. Automated DAS of pump test rig

Energy Harvester Design: To power the DAS, a piezoelectric material was selected and simulated. Real vibration data from the existing pump rig was collected to characterize vibrations from the pump and testing rig while COMSOL Multiphysics was used to extrapolate possible energy that can be harvested from the transducer system. Electrical characteristics of the sensors, modules, and microcomputer were observed and

* Oral and poster paper presentation

tabulated to determine the load demand of the system. A cantilever mechanism (bimorph) was employed to simulate the energy harvesting. Figure 3 shows a model of the piezoelectric harvester. The in-software low-cost material of PZT-5A was selected for easier analysis and being commercially available. This was later compared to a modified PZT ceramics with $\text{Pb}[\text{Zn}_{0.4}\text{Ni}_{0.6}]_{1/3}\text{Nb}_{2/3}\text{O}_3$ (PZNN) [1] for higher maximum piezoelectric properties. The harvested simulated power was then (DC-DC) converted, figure 4, to the rated voltage level of 5V nominal rating needed by the DAS. SIMetrix/SIMPLIS software was used to design and observe the power conversion and supply output.

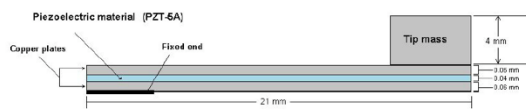


Fig. 3. Piezoelectric cantilever model

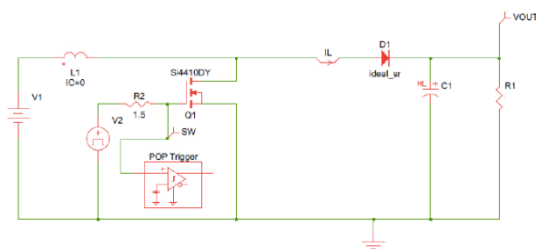


Fig. 4. Design of the boost converter in SIMPLIS

RESULTS AND CONCLUSION: The materials, list shown in Table 1, were designed to be as much as possible low-cost and locally sourced while targeting the range of values from the gathered data at AMTEC [2]. Vibrations were also determined to be the strongest at the motor base at 5 g to 7.83 g. The pump was observed to have the least vibrations at 0.39 g to 0.67 g of the intuitively vibrating parts of the test rig [3]. This lack of vibrations at the pump was expected because vibrations in the pump would lessen its efficiency.

Using the PZT-5A for the simulating material with a 20 mm by 10 mm (length by width) bimorph and 25 g tip mass, the mechanism achieved a 3.414 V voltage output at 2.331 mW maximum power point. This can, in theory, be bumped up to 231 mW/cm³ from the PZNN piezoelectric cantilever at 84 Hz under 1 g. A DC-DC boost converter was then designed to bring

Table 1. Summary of materials and estimated power dissipation

| Component | Model | Est. Power Dissipation [W] |
|---|----------------------------|----------------------------|
| Ambient Temperature Sensor | HUM1000_0 Phidget | |
| Relative Humidity Sensor | | 5.00E-06 |
| Pressure Sensor | PG 10-KU | 7.14E-02 |
| Vacuum Pressure Sensor | PAB-A-200KP | 5.34E-03 |
| Rotary Torque Transducer | TP-20KMCB | 7.14E-02 |
| Weight Transducer | CZL301 S Type Load Cell | 7.14E-02 |
| Isolation I/O port Interface Module | HUB0000_0 VINT Hub Phidget | 1.63E-01 |
| Instrumentation Amplifier | 3 x AD8224 | 3.00E+00 |
| Analog Digital Converter | 3 x AD7685 | 1.20E-02 |
| Wheatstone Bridge | DAQ1500_0 Phidget | 1.25E-04 |
| Microcomputer | Raspberry Pi 3B+ | 5.00E+00 |
| Miscellaneous | | 1.50 |
| Estimated Total Power Dissipation of the System in Watts: | | 9.89 |

it up to the 5 V needed by the DAS. The lack of power volume to drive the system can be addressed by having a system of piezoelectric bimorphs all in parallel. Roughly 5000 PZTs or only 50 PZNNs tiny 20 mm bimorphs are needed to drive the estimated power requirement of the system. The performance of the piezoelectric bimorphs can be further improved by increasing the length of the cantilever and weight of the tip mass.

In summary, the proposed self-powered DAS for an agricultural pump testing rig can be powered by harvesting its own unwanted vibrations using a system of piezoelectric bimorphs.

Keywords

Energy Harvest; Piezoelectric network; Data acquisition system; Machine testing;

References

- [1] Kang M-G., Jung W-S., Kang C-Y., and Yoon S-J. 2016. Recent Progress on PZT Based Piezoelectric Energy Harvesting Technologies. Actuators 5 (1) (2016), <https://doi.org/10.3390/act5010005>.
- [2] Chua, T.C.M. 2020. Development of a Raspberry Pi-based Pump Test Rig Data Acquisition System for the AMTEC-UPLB. Undergraduate Thesis, DEE, CEAT, UPLB.
- [3] Matibag, D.J.S. 2020. Design of a Piezoelectric energy harvester with a DC-DC boost converter for the pump test rig at AMTEC-UPLB. Undergraduate Thesis, DEE, CEAT, UPLB.

Technical Presentations

Food & Health

| | | |
|---------------------|--|--|
| Moderator | : | Dr. Arnold R. Elepaño |
| Panelists | : | Dr. Monet Concepcion M. Detras, Dr. Jerico Z. Alcantara, aProf Fidelina T. Flores |
| Technical Assistant | : | Engr. Mary Louise P. Pascual |
| 01:30PM – 01:35PM | Welcome Remarks and Introduction of Panel Members | |
| 01:35PM – 01:50PM | Ethanol Extraction of Bioactive Compounds from Waste Onion leaves by Conventional and Microwave-Assisted Methods | Audrey Dianne G. Mangilet, <u>Jewel A. Capunitan*</u> , Rex B. Demafelis, Myra G. Borines, Lisa Stephanie H. Dizon, Rona Joyce B. Landoy (UPLB) |
| 01:50PM – 02:05PM | Evaluation of Simulation Model for Constant Temperature Deep-bed drying of Hybrid Rice Seeds | <u>Luther John R. Manuel*</u> , Joanne P. Foliente, Mengke Lu and Kevin F. Yaptenco (UPLB) |
| 02:05PM – 02:20PM | Recirculating System with Gravel and Fluidized Sand Filter for Catfish Production | <u>John Paul A. Palillo*</u> , Aurelio A. Delos Reyes Jr. (UPLB) |
| 02:20PM – 02:35PM | Classification Skin Defect of Jujube by Using Spectral Images | Ngo Minh Tri Nguyen, Quoc Thien Pham and <u>Nai-Shang Liou*</u> (STUST) |
| 02:35PM – 02:50PM | Prediction of Moisture Content of Peanut Kernel Using Near-Infrared Hyperspectral Imaging Technique | <u>Jennyfer D. Rabanera*</u> , Jose D. Guzman, Kevin F. Yaptenco, Engelbert K. Peralta, Ma. Josie V. Sumague, April Shayne L. Sulabo (UPLB) |
| 02:50PM – 03:05PM | Disease Indexing for Mango (<i>Mangifera indica</i> L. cv. 'Carabao') Fruits Using Machine Vision | <u>Marijoree A. Sapigao*</u> , Kevin F. Yaptenco, Jessie C. Elauria, Delfin C. Suministrado, Erwin P. Quillooy (UPLB) |
| 03:05PM – 03:20PM | Effects of Thin-Layer Drying Temperature and Tempering on hybrid rice seed | <u>Rina A. Bawar*</u> , Joanne P. Foliente, Kevin F. Yaptenco (UPLB) |

Synthesis of modified chitosan containing multi-hydroxyl group for adsorption boron*

Quyen Hong Ho ^{1,a*}, Masashi Kurashina ^{2,b}, Mikito Yasuzawa ^{2,c}

¹ University of Science & Technology, The University of Danang, Vietnam

² Tokushima University, Japan

^a hhquyen@dut.udn.vn, ^b kurashina.masashi@tokushima-u.ac.jp, ^c yasuzawa@tokushima-u.ac.jp

Abstract

Although boron is crucial element for plants, animals and humans, it turns to poisonous when its concentration exceeds demand. Owing to wide-ranging application in numerous industries such as manufacture of glassware, ceramic, semiconductors, chemical, metallurgy, pharmaceuticals, cosmetic, construction, coal-fired power plants, waste of boron contaminates water sources, leading to environmental issues. Thus, the World Health Organization (WHO) has established the maximum boron concentration in drinking water to 2.4 mg/L whereas this value is limited to 1 mg/L in Japan, South Korea, Singapore, European Union. The exist of boron in aquatic environment is recorded in the form of boric acid and borax. Both these compounds can react with vis-diol group in polysaccharides to form stable borate complexes. In this study, gluconated chitosan particles (GChs) were synthesized by functionalization of chitosan with D-(+)-glucono-1,5 lactone (GL) in the simple process to provide vis-diol sections for boron adsorption. The adsorption mechanism of GChs was investigated in a batch system with initial boron concentration from 10 to 400 mg/L. The maximum boron adsorption capacity of GChs was

achieved at 5.80 mg/g. The adsorption isotherm data were well fitted to Langmuir model ($R^2 = 0.9993$). Boron adsorption capacity using GChs was similar to the result of commercial resin Amberlite IRA 743 (5.73 mg/g). The adsorption kinetics was tested from 0.5 to 24 h. The result showed that the adsorption equilibrium was reached after 700 min, and the adsorption kinetics of boron was following the pseudo-second order model ($R^2 = 0.9933$). The capacity of boron adsorption increased while pH rose from 5.6 to 9.8. Due to the slight increase in boron adsorption after the addition of NaCl salt, GChs could be applied for boron removal from saline water or seawater. The adsorbent was characterized by scanning electron microscopy (SEM). ¹H NMR and 2D-COSY NMR results indicated that GL was successfully introduced to the chitosan. Based on the colloidal titration result, the degree of gluconated units (DG%) in GChs made up 20.00%. This study presents that GChs is the material as a safe and environmentally friendly adsorbent for the removal of boron from aqueous solution.

Keywords

Boron removal, chitosan, adsorption, adsorbent, particles

* Poster paper presentation

Ethanol extraction of bioactive compounds from waste onion leaves by conventional and microwave-assisted methods*

Audrey Dianne G. Mangilet^{1,a}, Jewel A. Capunitan^{1,b*}, Rex B. Demafelis^{1,c}, Myra G. Borines^{1,d}, Lisa Stephanie H. Dizon^{1,e}, Rona Joyce B. Landoy^{1,f}

¹Dept. of Chemical Eng., College of Eng. & Agro-industrial Tech., University of the Philippines Los Baños, Philippines

^aagmangilet@up.edu.ph, ^bjacapunitan@up.edu.ph, ^crbdemafelis@up.edu.ph, ^dmgborines@up.edu.ph, ^elhdizon@up.edu.ph, ^frblandoy@up.edu.ph

Abstract

Onions (*Allium cepa* L.) are one of the most indispensable spices in the Filipino cuisine, with 124,170 metric tons of production in the Philippines from January to March of 2018^[1]. Approximately 25 % to 30 % of these are generated as waste, mainly in the form of its outer leaves, peel, and skin^[2]. Some studies have pointed out that waste onion leaves contain high value bioactive compounds^[3], one of which is quercetin, a well-studied flavonoid because of its anti-oxidant, anti-inflammatory, anti-microbial, and anti-cancer properties^[4].

This study was done to investigate the extraction of flavonoids and phenolics from waste onion leaves using aqueous ethanol as solvent via conventional solvent extraction (CSE) and microwave-assisted extraction (MAE). Ethanol was used as solvent because of its extraction efficiency and application on food systems (GRAS). Parametric studies via two-level factorial design of experiment were performed for each method to study the effects of ethanol concentration (50 %v/v and 80 %v/v), temperature (60 °C and 80 °C), and extraction time (1 hr and 4 hrs) for CSE, and those of ethanol concentration (50 %v/v and 80 %v/v), power level (10 % and 50 %), and extraction time (10 sec and 60 sec) for MAE, on the total flavonoid content (TFC) and total phenolic content (TPC) of waste onion leaves. TFC and TPC analyses were done using aluminum chloride (AlCl₃) colorimetric method and Folin-Ciocalteu reagent (FCR) colorimetric method, respectively. The maximum extractable flavonoid content, 8.61 mg quercetin equivalent

(QE)/g dry weight (DW), and phenolic content, 8.95 mg gallic acid equivalent (GAE)/g DW, from waste onion leaves were also determined through a 16-hr Soxhlet extraction.

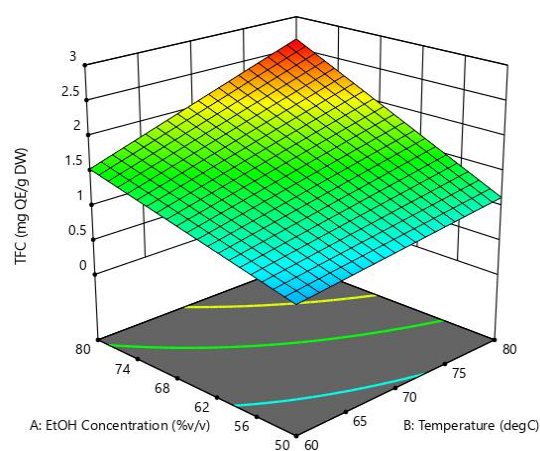
For CSE, ethanol concentration, extraction time and the interactions of the factors significantly affected the TFC. Fig. 1 shows that an increase in TFC yield was observed with increasing ethanol concentration and temperature at the low level of extraction time (1 hr). This could be attributed to the higher solubility of flavonoids in higher concentrations of ethanol and increased diffusivity of solute at higher temperatures^[5]. However, at the high level of extraction time (4 hrs), there was an observed decrease in TFC yield because the flavonoids within the plant matrix possibly degraded from prolonged exposures to such temperature level^[3].

On the other hand, all the three factors, ethanol concentration-temperature interaction, and ethanol concentration-extraction time interaction significantly affected the TPC. At low ethanol concentration, increasing the temperature and extraction time had no effect on TPC yield; while at high ethanol concentration, a decrease in TPC yield was observed with increasing temperature and extraction time. A higher temperature should increase the diffusivity of the solute. However, some phenolic compounds are less thermally stable than flavonoids and start to decompose at around 60 °C^[3]. They can also be easily oxidized or decomposed by light^[4].

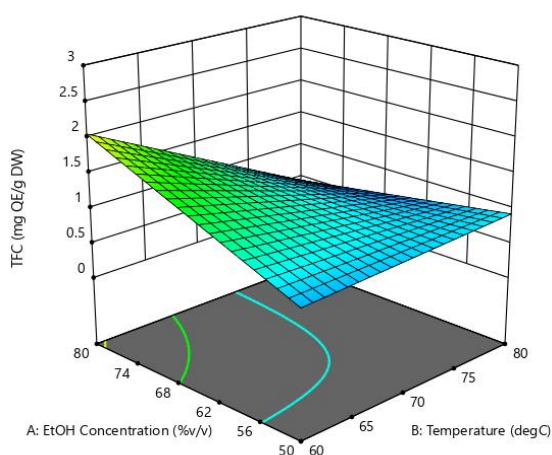
For MAE, increasing the ethanol concentration and power level significantly increased the TFC yield from the extracts, as higher ethanol

* Oral paper presentation

concentration was more favorable for flavonoid extraction and a higher power level promotes the disintegration of the cellular structures within the plant matrix due to the rapid increase of both temperature and pressure from dielectric heating^[5]. Finally, only the ethanol concentration significantly affected the TPC yield from the extracts, since extraction recovery and efficiency of MAE greatly depends on the solubility of the target compounds to the type of solvent used and on the solvent's ability to absorb microwave energy, which is aided by the presence of water in the solvent^[5].



(a)



(b)

Fig. 1. 3D surface plot for TFC by conventional solvent extraction at (a) low and (b) high extraction time.

In conclusion, it was found that waste onion leaves could be utilized as a potential source of flavonoids and phenolics. For CSE, high level of ethanol concentration (80 %v/v) and low level of extraction time (1 hr) resulted in higher values of TFC (2.63 mg QE/g DW) and TPC (6.15 mg GAE/g DW). As for MAE, higher values of TFC (2.98 mg QE/g DW) and TPC (4.24 mg GAE/g DW) were obtained at the high level of ethanol concentration (80 %v/v ethanol), high power level (50 %), and high level of extraction time (50 sec). MAE was also found to be a more advantageous extraction method than CSE because of its comparable flavonoids and phenolics yields at a shorter extraction time.

Keywords

onion leaves, flavonoids, phenolics, extraction, ethanol

References

- [1] Philippine Statistics Authority. 2018. Performance of Philippine Agriculture January to March 2018. Quezon City. https://psa.gov.ph/sites/default/files/PAR_January_to_March_2018.pdf
- [2] Sagar NA, Pareek S, Sharma S, Yahia E, Lobo MB. 2018. Fruit and vegetable waste: bioactive compounds, their extraction, and possible utilization. *Comprehensive Reviews in Food Science and Food Safety*. 17: 512-531.
- [3] Miean KH, Mohamed S. 2001. Flavonoid (myricetin, quercetin, kaempferol, luteolin, and apigenin) content of edible tropical plants. *Journal of Agriculture and Food Chemistry*. 49(6): 3106-3112.
- [4] Dmitrienko SG, Kudrinskaya VA, Apyari VV. 2012. Methods of extraction, preconcentration, and determination of quercetin. *Journal of Analytical Chemistry*. 67(4): 299-311.
- [5] Orsat V, Routray W. 2017. Microwave-assisted extraction of flavonoids. *Water Extraction of Bioactive Compounds from Plants to Drug Development*. 221-244. Elsevier Inc.

Utilization of waste onion leaves for food applications*

Rona Joyce B. Landoy ^{1,a}, Myra G. Borines ^{1,b}, Rex B. Demafelis ^{1,c}, Wilson T. Tan ^{2,d},
Jewel A. Capunitan ^{1,e}, Lisa Stephanie H. Dizon ^{1,f}, Raymund C. Rodriguez ^{1,g}

¹ Department of Chemical Engineering, College of Engineering & Agro-Industrial Technology, University of the Philippines Los Baños, Laguna, Philippines

² Institute of Food Science and Technology, University of the Philippines Los Baños, Laguna, Philippines

^a rblandoy@up.edu.ph, ^b mgborines@up.edu.ph, ^c rbdemafelis@up.edu.ph, ^d wttan@up.edu.ph,
^e jacapunitan@up.edu.ph, ^f lhdizon1@up.edu.ph, ^g rcrodriguez5@up.edu.ph

Abstract

Onion is considered as one of the most important crops produced worldwide due to its indispensability as a culinary ingredient. According to Hanci [2], the worldwide total onion production in 2016 was around 93 million tons, with a total onion production area of about five million hectares [3]. China tops the world's largest onion producer followed by India and the United States. In the Philippines, the production areas for onion are estimated to be 17,905 hectares in 2018. With this total area, the country registered a production of 172,666 metric tons of onion [2]. Realizing the need to develop and expand its local production and provide solutions to specific problems on competitiveness for each stage in its value chain, producing high-value products from onion waste is targeted, thereby minimizing agricultural wastes in onion farming and providing additional income for farmers. In this study, several packages of technology were developed for the processing of waste onion leaves into different food products. The sample waste onion leaves were obtained from two of the top onion producers in the Philippines, namely Nueva Ecija and Occidental Mindoro. Although drying is a preservation technique for herbs such as onions, it is often accompanied by loss of volatiles and bioactive compounds. Hence, the changes in bioactive components of waste onion leaves in terms of total phenolic content (TPC) and total flavonoid content (TFC), using various dehydration techniques were also evaluated. Results revealed that waste onion leaves possess flavor, aroma, and bioactive components similar to onion bulb, making it a potential alternative

spice. The waste onion leaves have a moisture content (MC) of $92.58 \pm 1.00\%$ while its bioactive components such as TPC and TFC were found to be 633.99 ± 4.90 mg Gallic acid equivalent per g dry weight and 10.44 ± 0.26 mg Quercetin per g dry weight, respectively. These findings were much higher compared to the TPC and TFC of onion bulb, which are 13.71 mg GAE per g dry weight and 3.456 mg Quercetin per g dry weight, respectively, as reported in the study of Sharma & Jameda [5]. Different dehydration techniques such as sun drying, convection drying, vacuum drying, and freeze drying were also found to have significant effects on preserving bioactive compounds (Table 1). Vacuum drying is the most efficient drying technique in terms of moisture reduction and TFC preservation but not with TPC retention. Conventional drying showed favorable results on the preservation of TPC and TFC but failed to reduce the moisture of onion leaves below 15% which is the critical factor for the postharvest management of herbs [1]. Heating had a positive effect on TFC of dried onion leaves except for sun drying. Sun drying showed comparable performance with freeze drying in preserving TPC, however, the color and appearance of sun-dried samples were not retained, and the desired moisture was not attained. Longer drying time and increasing pressure resulted in a more favorable retention of TPC while blanching significantly reduced the TPC. A decrease in TFC was observed at increasing temperature and shorter drying time. Sulfur-containing compounds like alk(en)yl mono-, di-, and tri-sulfides onions, which

* Poster paper presentation

contribute to the aroma of onion, were detected in all the dried samples.

Table 1. MC, TPC and TFC of waste onion leaves after drying of waste onion leaves using different methods

| Drying technique | Moisture content (%) | Total phenolic content [mg GAE (g dry weight) ⁻¹] | Total flavonoid content [mg quercetin (g dry weight) ⁻¹] |
|--------------------------|----------------------|---|--|
| Fresh Waste Onion Leaves | 92.58 ± 1.00 | 633.99 ± 4.90 | 10.44 ± 0.26 |
| Conventional Drying | 19.57 ± 0.06 | 652.08 ± 82.14 | 15.89 ± 2.54 |
| Vacuum Drying | 10.46 ± 0.03 | 67.54 ± 17.29 | 76.47 ± 23.20 |
| Freeze Drying | 16.58 ± 0.14 | 430.30 ± 51.83 | 11.54 ± 1.71 |
| Sun Drying | 49.46 ± 13.56 | 438.53 ± 55.63 | 9.95 ± 2.38 |

Since waste onion leaves are targeted for food applications, pesticide residues in waste onion leaves were also analyzed. Results showed that the detected pesticide traces in waste onion leaves obtained from Occidental Mindoro were below the limit of quantification (< LOQ). Consequently, traces of cypermethrin and lambda-cyhalothrin of about 0.06 mg/kg and 0.02 mg/kg, respectively, were detected in the samples obtained from Nueva Ecija. These findings revealed that pesticide residues in waste onion leaves were below the specified maximum residue level (MRL) for cypermethrin and lambda-cyhalothrin in onions or shallots which are 0.1 mg/kg and 0.2 mg/kg, respectively based on the European Union (EU) Pesticide Database [2]. Additionally, the packages of technology (POTs) developed for the processing of waste onion leaves were drying, powdering, pickling, vacuum frying, and juicing of onion leaves. These POTs produced different food products such as dehydrated onion leaves, powdered onion leaves, pickled onion leaves, vacuum-fried onion leaves, and onion leaves extract. Consequently, these products were further processed to produce onion leaves-flavored pandesal (bread), kropek (cracker), noodles, tea, puree, juice, garnish, and seasoning (Fig 1). With the proven potential of waste onion

leaves for food applications, not only the problem of agricultural waste disposal is addressed but also its possible significant impact on the profitability of farmers and the onion industry in general.



Fig 1. Products derived from waste onion leaves

Keywords

bioactives, dehydration/drying, food, package of technology, waste onion leaves

References

- [1] Díaz-Maroto MC, Pérez-Coello MS, Cabezudo MD. 2002. Effect of different drying methods on the volatile components of parsley (*Petroselinum crispum* L.). *European Food Research and Technology*, 215: 227–230.
- [2] EU Pesticides Database. 2020. Food Safety - European Commission.
- [3] Hanci F. 2018. A Comprehensive Overview of Onion Production: Worldwide and Turkey. *IOSR Journal of Agriculture and Veterinary Science (IOSR-JAVS)*.11(9):17-27. Doi: 10.9790/2380-1109011727
- [4] Philippine Statistics Authority. 2019. Crops Statistics of the Philippines (2014-2018) National and Regional. Quezon City, Philippines: Author
- [5] Sharma V, Jameda P. 2014. Extraction, isolation, and identification of flavonoid from *Euphorbia neriifolia* leaves. *American Journal of Chemistry*. 10: 509-514.

Evaluation of simulation model for constant temperature deep-bed drying of hybrid rice seeds*

Luther John R. Manuel ^{1,a}, Joanne P. Foliente ^{1,b}, Mengke Lu ^{2,c}, Kevin F. Yaptenco ^{1,d}

¹ Institute of Agric & Biosys Eng, University of the Philippines Los Baños, Philippines

² BayerAG, Germany

^alrmanuel1@up.edu.ph, ^bjpfoliente@up.edu.ph, ^cmengke.lu@bayer.com, ^dkfyaptenco@up.edu.ph

Abstract

Currently, drying practices for drying seeds are based on studies of drying rice for milling and consumption. Aside from difference on drying practice for different purpose, difference on the variety of seeds could result to different drying rates which could lead significant difference on drying practice. There are lots of studies on deep-bed drying of rice using simulation models. Page [1], Wang and Singh [2, 3], Thompson [4], and Logarithm and Equilibrium [4] models had performed satisfactory results when they are used in simulation model of deep-bed drying of inbred rice. Mean relative error between the experimental and predicted data regards 10-15% as satisfactory results. However, none of these literatures have looked on the effect of drying to the seed condition. Also, most of them predicted only grain moisture. Since grain temperature is important in drying seeds, it is vital to predict also this parameter during the drying process. Thus, this study aims to improve the drying practice of hybrid rice seeds by determining grain moisture and temperature while drying. Preliminary results showed that Page Model posed the most accurate prediction result and thus, the simulation model based on it for predicting grain moisture and temperature at different level on a deep-bed drying set-up was developed. To evaluate this, hybrid rice seeds were dried in a laboratory dryer with a 50-cm depth test cell. Two drying temperatures (45°C and 55°C) were used. During drying, grain moisture and temperature were measured at specified intervals until the grain moisture reaches about 11%. Grain samples were extracted and stored from top, middle and bottom layers of the deep-bed. After 4 months, germination test was performed on the seed

samples. It was found out that though using 55°C drying air temperature has faster drying time, the final moisture content between the top and bottom layer seeds have large gradient (see Fig. 1).

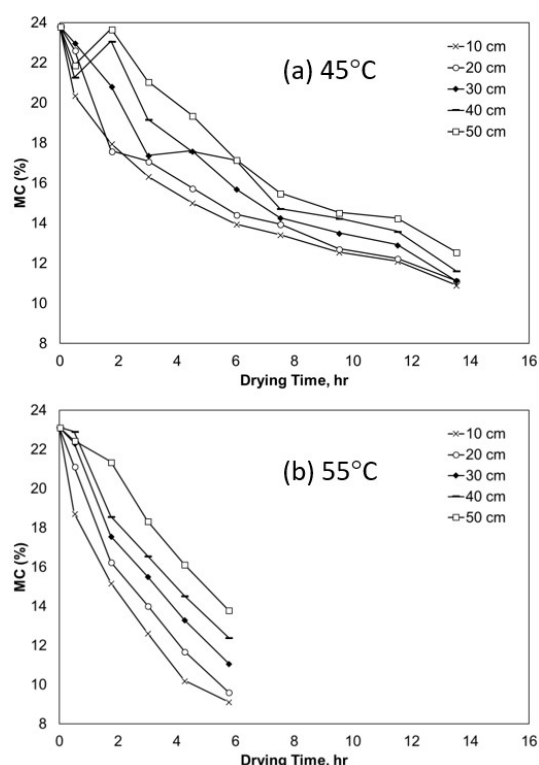


Fig. 1. Grain moisture distribution across the deep-cell

Grain temperature reduction of those dried using 55°C drying air has almost twice value than that of 45°C drying air (Fig. 2). However, germination test of the samples between the two drying temperature and the top and bottom layer seeds showed no significant difference.

The grain moisture and temperature were also compared to the predicted drying parameters of the simulation model based on Page Model (see Fig. 2). It was found that the mean relative error

* Oral paper presentation

between the experimental and predicted grain moisture values across the grain layer of 45°C and 55°C drying temperature setting is 3.4% and 2.4%, respectively. The mean relative error for grain temperature across the grain layer for 45°C and 55°C is 1.8% and 5.7%, respectively. This proves that the Page model could well predict grain moisture and temperature while drying hybrid rice seed in a deep-bed set-up. Based on these results, drying the hybrid rice seeds using 45°C drying air temperature could produce seeds with uniform moisture across the depth of the deep-bed. Results from this study could optimize the drying operation by using the optimal drying condition with the greatest seed germination rate.

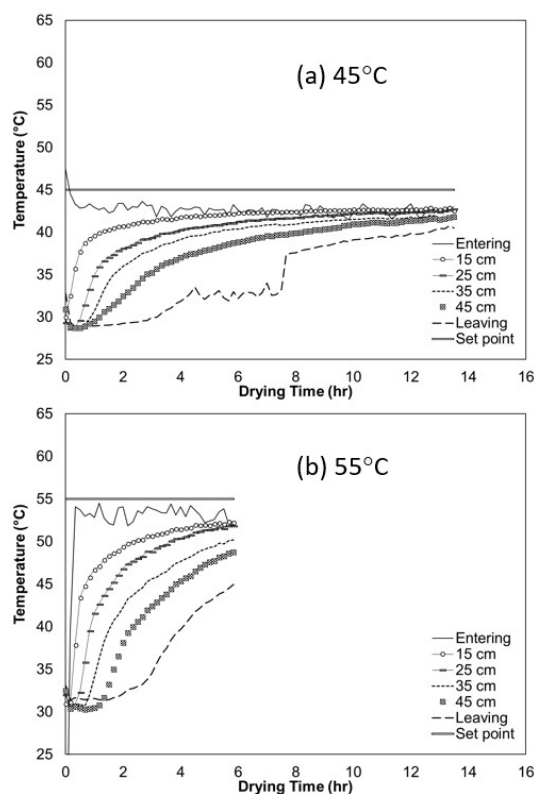


Fig. 2. Air and grain moisture at different levels of deep-cell.

Keywords

Hybrid rice, deep-bed drying, Page Model, grain moisture, grain temperature, germination test

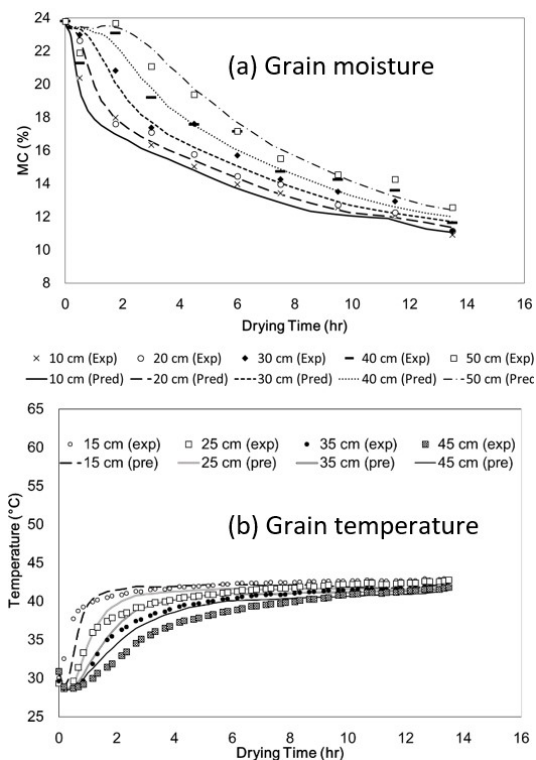


Fig. 3. Simulation results for 45°C drying parameters.

REFERENCES

- [1] Wongwises S and Thongprasert M. (2000). Thin layer and deep bed drying of long grain rough rice. *Drying Technology* 18(7), 1583-1599.
- [2] Zare D and Chen G. (2009). Evaluation of a simulation model in predicting the drying parameters for deep-bed paddy drying. *Computers and Electronics in Agriculture* 68, 78-87.
- [3] Torki-Harchegani M, Sadeghi M, Moheb A, Naghavi Z. (2014). Investigation on rough rice drying kinetics at various thin layers of a deep bed. *Heat Mass Transfer* 50, 1717-1725.
- [4] Hung N, Martinez R, Tuan T, Gummert M. (2019). Development and verification of a simulation model for paddy drying with different flatbed dryers. *Plant Production Science* Vol. 22, 119-130.
- [5] Lopes D, Neto A, Santiago J. (2014). Comparison of equilibrium and logarithmic models for grain drying. *Biosystems Engineering* 118, 105-114.

Prediction of moisture content of peanut kernel using near-infrared hyperspectral imaging technique*

Jennyfer D. Rabanera ^{1,a,*}, Kevin F. Yaptenco ^{2,b}, Jose D. Guzman ^{1,c}, Engelbert K. Peralta ^{2,d}, Ma. Josie V. Sumague ^{3,e}, April Shayne L. Sulabo ^{3,f}

¹Dept. of Agric & Biosys Engineering, Cagayan State University, Cagayan, Philippines

²Institute of Agric & Biosys Engineering, College of Engineering & Agro-Industrial Technology, University of the Philippines Los Baños, Philippines

³Institute of Food Sci & Tech, College of Agric & Food Sci, Univ of the Philippines Los Baños, Philippines

^ajdmarantan@up.edu.ph, ^bkfyaptenco@up.edu.ph, ^cjoguz1129@gmail.com,

^dengelbert.peralta@gmail.com, ^emvsumague@up.edu.ph, ^falsulabo@up.edu.ph

Abstract

Moisture content (MC) is a basic and significant indicator of quality and storage stability in peanuts ^[1]. Different methods in peanut moisture content determination such as oven drying ^[2, 3], NIR reflectance spectroscopy ^[4, 5], electronic moisture analyzer (CI meter) ^[6] and capacitance sensor ^[7] are all reliable but time-consuming, destructive, tedious and cannot be implemented for online detection ^[1], thus a technique that would address these problems is needed. This study used a rapid and non-destructive way of predicting the moisture content of peanut kernels using hyperspectral imaging technique in the near-infrared (NIR) region (900 nm to 1700 nm).

Image of two hundred (200) peanut kernels (BPI-Pn9 variety) with MC from 7.6 to 33.22 % wb were taken using a typical push-broom NIR hyperspectral imaging system (Specim Spectral Imaging Ltd.). The hyperspectral images were calibrated and pre-processed using the ENVI Classic software. Spectral data was extracted from the chosen region of interest (ROI). The mean reflectance from band 1 to 256 was used to develop the spectral signature of each kernels. These were subjected to partial least square regression (PLSR) using Unscrambler X 10.5 by CAMO Software to develop the MC prediction model. The model was evaluated using the values of the determination coefficients of calibration (R^2_c), validation (R^2_v), and prediction (R^2_p) and root mean square error of calibration (RMSEC), validation (RMSEV), and prediction (RMSEP). Optimization of the prediction model was done by

identifying wavelengths with the highest absolute regression coefficients (correlation coefficient or beta coefficients) ^[1,8,9,11]. These were used to develop the optimized MC prediction model. This model was applied to the hyperspectral images at a pixel-wise level using Matlab R2013a software to develop the moisture content distribution map of each peanut kernel.

Results showed that the peanut kernels having different levels of MC exhibit the same shape of spectral signatures (Fig. 1) varying only on the amplitudes ^[4]. It can be noted that the reflectance of the kernels is inversely proportional to the moisture content. This is mainly attributed to the effect of water in the peanut kernel because water shows strong absorption at the NIR region indicating lower reflection ^[10]. The MC PLSR model developed at full spectrum displayed good performance as shown (Table 1). To reduce the data processed thus simplify the model, optimization was done resulting to a model that can predict MC using only 20 key wavelengths. The optimized model showed better performance. Applying this model to the peanut kernel hyperspectral images in a pixel-wise manner resulted in the peanut kernel moisture content distribution map (Fig. 2).

Results show promising potential of the hyperspectral imaging technique in the near infrared region combined with partial least square regression for rapid and non-destructive prediction of moisture content of peanut kernels.

* Oral paper presentation

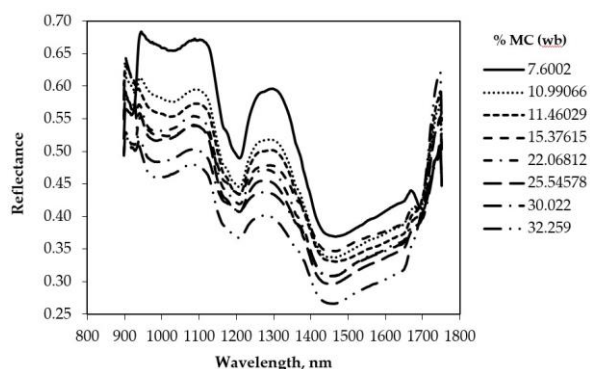


Figure 1. Spectral signature of sample peanut kernels at different levels of moisture content

Table 1. Summary of the evaluation performance of the two MC prediction models.

| No. of WL* | Calibration | | Validation | | Prediction | |
|------------|-----------------------------|--------|-----------------------------|--------|-----------------------------|--------|
| | R ² _c | RM SEC | R ² _v | RM SEV | R ² _p | RM SEP |
| 256 | 0.9309 | 1.7 | 0.9083 | 1.96 | 0.9368 | 1.87 |
| 20 | 0.9357 | 1.64 | 0.9133 | 1.90 | 0.9445 | 1.78 |

*WL = wavelengths

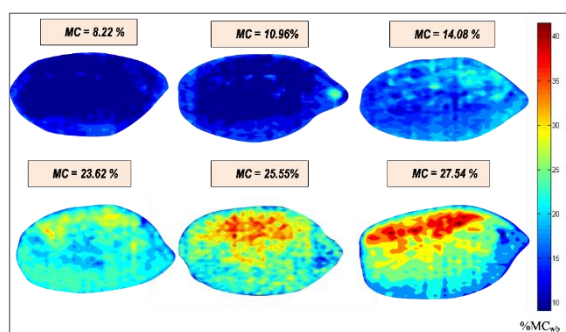


Figure 2. Moisture content distribution map of sample peanut kernels

Keywords

Near-infrared hyperspectral imaging, optimal wavelength, partial least square regression, peanut kernel, peanut moisture content

References

- [1] Jin H, Li L, Cheng J. 2015. Rapid and non-destructive determination of moisture content of peanut kernels using hyperspectral imaging technique. *Food Analytical Methods*. 2524-2532.
- [2] ASABE Standards. 2010. S410.2 Moisture Measurements-Peanuts. St. Joseph, Michigan.

American Society of Agricultural and Biological Engineers.

- [3] Butts C, Lamb M, Sorensen R, Chen S. 2014. Oven drying times for moisture content determination of single peanut kernels. *Transactions of the ASABE*. 57: 579-584.

- [4] Govindarajan K, Kandala C, Subbiah J. 2009. NIR reflectance spectroscopy for nondestructive moisture content determination in peanut kernels. *Transactions of the ASABE*. 1661-1665.

- [5] Sundaram J, Kandala C, Govindarajan K, Subbiah J. 2012. Sensing of moisture content of in-shell peanuts by NIR reflectance spectroscopy. *Journal of Sensor Technology*. 2: 1-5.

- [6] Kandala C, Butts C, Lamb M. 2008. Moisture content determination for in-shell peanuts with a low-cost impedance analyzer and capacitor sensor. *Transactions of the ASABE*. 51: 1377-1381.

- [7] Kandala C, Sundaram J. 2010. Nondestructive measurement of moisture content using a parallel-plate capacitance sensor for grain and nuts. *IEEE Sensors Journal*. 10: 1282-1287.

- [8] Wang W, Heitschmidt G, Ni X, Windham W, Hawkins S, Chu X. 2014. Identification of aflatoxin B1 on maize kernel surfaces using hyperspectral imaging. *Food Control*. 78- 86.

- [9] Kandala C, Sundaram J. 2012. Determination of moisture content using NIR reflectance spectroscopy with single calibration for both Valencia and Virginia in-shell peanuts. *Transactions of the ASABE*. 55: 609-612.

- [10] Achata E, Esquerre C, O'Donnell C, Gowen A. 2015. A study on the application of near infrared hyperspectral chemical imaging for monitoring moisture content and water activity in low moisture systems. *Molecules*.

- [11] Elmasry G, Kamruzzaman M, Sun D, Allen P. 2012. Principles and applications of hyperspectral imaging in quality evaluation of agro-food products: a review. *Critical Reviews in Food Science and Nutrition*. 999-10123.

Visible and near-infrared spectroscopy for rapid prediction of sugarcane quality*

Jeric H. Rosales ^{1,a*}, Mary Jane L. Quindoy ¹, Kevin F. Yaptenco ¹

¹ Agricultural, Food & Bio-Process Engineering Division, Institute of Agricultural & Biosystems Engineering, College of Engineering & Agro-Industrial Technology, University of the Philippines Los Baños, Philippines

^a jhrosales@up.edu.ph

Abstract

Development of a rapid, non-destructive, and efficient mode of measurement which can be performed directly on sugarcane stalk samples is necessary, most especially when dealing with in-field conditions. The potential of visible (Vis) and near-infrared (NIR) spectroscopy to measure °Brix, moisture and fiber contents of sugarcane at different maturity levels was investigated. Sugarcane stalks of ten different high yielding varieties were harvested – considering 10th, 11th and 12th month maturity. The diffuse reflectance spectra of whole sugarcane stalks at three different internodes [1] – top, middle and bottom sections – were acquired by directly scanning their skin using two spectrometer units that consider different wavelength range: (a) 900nm to 1700nm for NIR, and (b) 340nm to 1040nm for Vis-NIR. Reference data of sugarcane quality such as °Brix and moisture content (%MC) were measured using digital refractometer and oven-drying method, respectively. Fiber content (FC, %) was computed from these reference values using Equation 1[2]:

$$FC = \frac{(100^2 - 100 \times \%MC - 97 \times ^\circ\text{Brix})}{(100 + ^\circ\text{Brix})} \quad (1)$$

The data were modified by excluding the first and last 50 nm of the spectra to remove spectral noises. Preprocessing and multivariate statistical analysis employed are shown in Fig. 1. Spectral data were partitioned to calibration and validation data sets using random sampling technique. Multiplicative scatter correction and mean-centering were applied to preprocess the data prior to principal component analysis

(PCA) and partial least squares regression (PLSR).

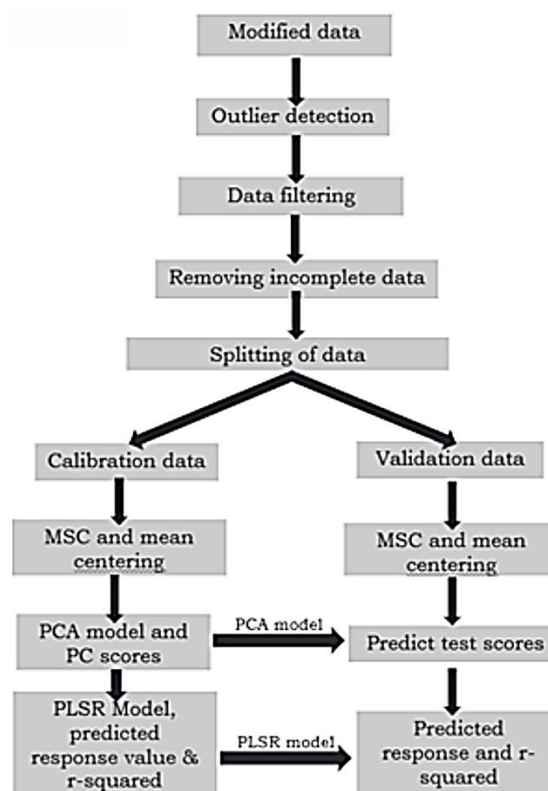


Fig. 1. Multivariate statistical analysis employed

Results of the PCA-PLSR modelling of reference data and the obtained Vis-NIR and NIR spectral data are summarized in Table 1. The PLSR model derived from PCA scores of NIR spectral data yielded good predictive performance for °Brix ($R^2=0.7150$) and %MC ($R^2=0.7266$) and a poor fit for the model of %FC ($R^2=0.3256$). The same trend can be observed from results derived from Vis-NIR data which yield to 0.6249, 0.6264, and 0.2996 values of R^2 for °Brix, %MC and %FC, respectively.

* Poster paper presentation

Table 1. Coefficient of determination (R^2) of PLSR models based from filtered NIR and Vis-NIR data sets.

| Data Set | Coefficient of correlation (R^2) | | |
|----------------------------------|--------------------------------------|--------|--------|
| | °Brix | %MC | %FC |
| NIR data filtered at 1.7 nm | | | |
| Calibration | 0.7266 | 0.7402 | 0.3444 |
| Validation | 0.7150 | 0.7266 | 0.3256 |
| Vis-NIR data filtered at 1.65 nm | | | |
| Calibration | 0.6673 | 0.6590 | 0.3298 |
| Validation | 0.6249 | 0.6264 | 0.2996 |

Coefficients of determination of PLSR models based on NIR data were higher than those from Vis-NIR. The prediction accuracy of the models based on NIR data were reasonably good, especially for °Brix and %MC where R^2 values are above 0.70. The model's poor predictive performance of %FC (relatively low R^2 for %FC) is expected since data was not obtained directly via laboratory method, instead, through calculation involving measured values of °Brix and %MC. Correlation plots of observed and predicted sugarcane parameters based on PLSR modelling of NIR validation data are shown in Fig. 2.

Results showed that visible and near-infrared spectroscopy has great potential for rapid determination of sugarcane quality, particularly °Brix and %MC. However, it also suggests the need to explore other preprocessing methods such as data filtering to further improve the performance of the model. Other parameters related to the sugarcane productivity such as Polarity may also be considered for future research.

Keywords

sugarcane; sugarcane quality; Vis-NIR; spectroscopy; PCA-PLS

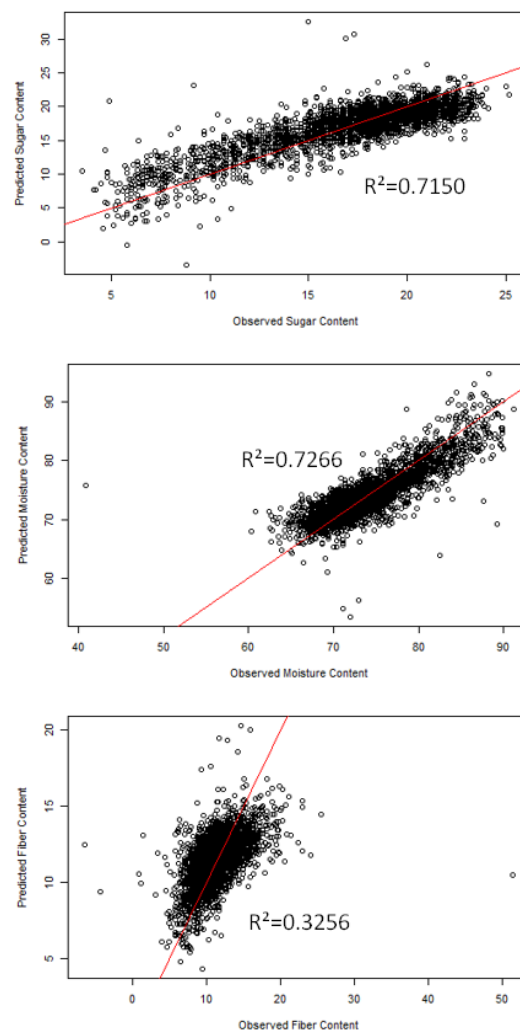


Fig. 2. Correlation between observed and predicted °Brix, %MC and %FC.

References

- [1] Phuphaphud A, Saengprachatanarug K, Posom J, Maraphum K and Taira E. 2019. Prediction of the fibre content of sugarcane stalk by direct scanning using visible-shortwave near infrared spectroscopy. *Vibrational Spectroscopy*. 101: 71-80.
- [2] Matt NN, Rowshon KM, Guangnan C, Troy J. 2014. Prediction of sugarcane quality parameters using visible-shortwave near infrared spectroradiometer. *Agriculture and Agricultural Science Procedia*. 2: 136 – 143.

Disease indexing for mango (*Mangifera indica* L. cv. 'Carabao') fruits using machine vision*

Marijoree A. Sapigao ^{1,2,a*}, Kevin F. Yaptenco ^{2,b}, Jessie C. Elauria ^{2,c}, Delfin C. Suministrado ^{2,d}, and Erwin P. Quilloy ^{2,e}

¹Department of Resource Engineering & Agricultural Mechanization, Pampanga State Agricultural University, Pampanga, Philippines

²Institute of Agricultural & Biosystems Engineering, College of Engineering & Agro-Industrial Technology, University of the Philippines Los Baños, Laguna, Philippines

^amasapigao@up.edu.ph, ^bkfyaptenco@up.edu.ph, ^cjcelauria@up.edu.ph, ^ddcsuministrado@yahoo.com,

^eepquilloy@up.edu.ph

Abstract

Disease indexing was done to observe and monitor the disease growth and its behavioral pattern. The disease index result is used for the development of control measures for certain diseases. Therefore, proper disease diagnosis and indexing should be applied in order to create efficient and effective control measures. Disease detecting and severity quantification are done visually or by machine-aided technologies^[1]. Though visual methods are still widely used, studies in improvement and development of higher technologies involving disease identification and assessment are inevitably increasing. In the Philippines, the traditional method of disease indexing which is through visual 'hedonic' scales^[2] is still practiced. This method relies on the estimations and personal judgments of the evaluator. The method also requires experienced and skilled laboratory staffs that are knowledgeable about the diseases and disease-causing agents because of the similarity of disease symptoms. The method is also time consuming and demands costly affairs due to the availability of the experts. Thus, a machine vision system was designed and developed to perform non-destructive and accurate disease indexing that may assist in disease assessment practice in the country.

METHODOLOGY

The machine vision system consists of a hardware setup and a software application named Mango Disease indexing Software (MDIS). The MDIS is designed for automatic disease identification and

severity quantification limited for anthracnose and stem end rot infection in carabao mango fruits. The general process flow of MDIS is summarized in Fig. 1.

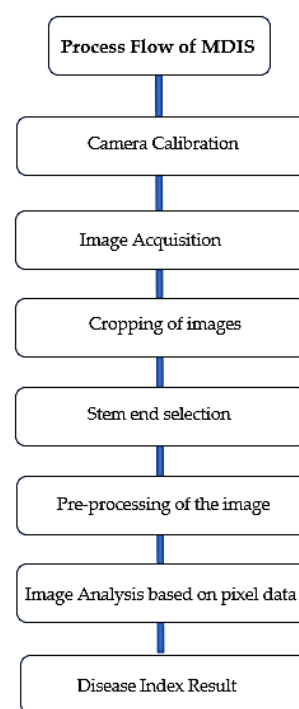


Fig 1. General process flow of MDIS

The hardware setup was designed to fit with the environment required by MDIS to capture the desired image for easier image analysis. The hardware setup is shown in Fig 2. It is composed of a setup table, sampling platform, lighting chamber, and the camera box.

* Oral and poster paper presentation

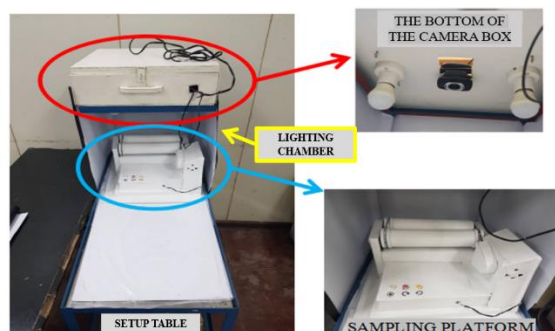


Fig. 2. The hardware setup and its components.

The accuracy of MDIS' disease indexing performance for both anthracnose and stem end rot was evaluated by comparing its predicted value (MDIS disease indexing result) to the measured value of ImageJ. ImageJ is an open-source program commonly used in image processing. Twenty-five mango samples infected with anthracnose and stem end rot was observed for nine days. The images of the samples were taken daily within nine days using MDIS. The data gathered were compared and analyzed using regression analysis [1].

RESULTS AND DISCUSSION

Results showed that the MDIS system achieved an assessment accuracy of 97.53% for anthracnose (Fig. 3) and 95.23% for stem end rot (Fig. 4) disease indexing.

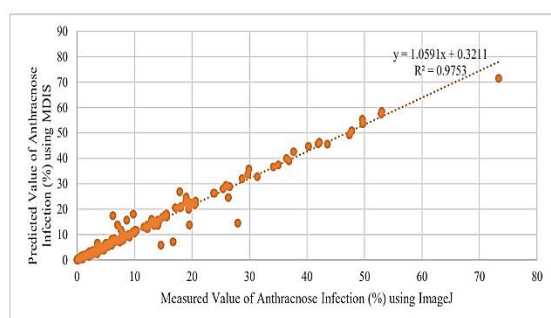


Fig.3. Line Fit Plot of Measured Value using ImageJ and Predicted Value using MDIS for Anthracnose Infection (%).

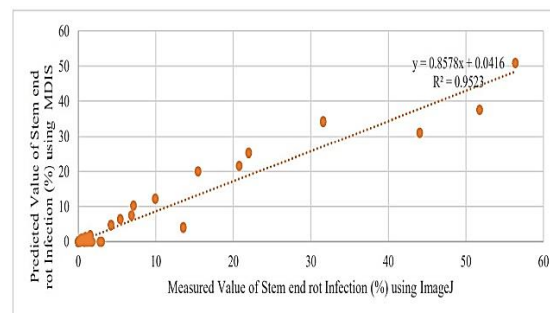


Fig.4. Line Fit Plot of Measured Value using ImageJ and Predicted Value using MDIS for Stem end rot Infection (%).

The technology took 24.30 seconds for an overall disease indexing process. Overall disease indexing includes all the process starting from image acquisition up to the disease index result. Generally, the result showed that as the severity of each disease increased, the MDIS prediction's accuracy decreased.

Keywords

machine vision, disease indexing, mango postharvest diseases, image processing, color analysis

References

- [1] BOCK, C. H., & NUTTER, F. W. (2011). Detection and measurement of plant disease symptoms using visible-wavelength photography and image analysis. CAB Reviews: Perspectives in Agriculture, Veterinary Science, Nutrition and Natural Resources, 6.
- [2] HOLMES, R., HOFMAN, P., & BARKER, L. (2009). Mango quality assessment manual A guide to assessing the post-harvest quality of Australian mangoes.

Recirculating system with gravel and fluidized sand filter for catfish production*

John Paul A. Palillo ^{1,a*}, Aurelio A. Delos Reyes Jr. ^{1,b}

¹Land and Water Resources Engineering Division, Institute of Agricultural & Biosystems Engineering
College of Engineering and Agro-Industrial Technology, University of the Philippines Los Baños,
Philippines

^ajapalillo@up.edu.ph, ^baadelosreyes2@up.edu.ph

Abstract

A 1-m³ recirculating African catfish (*Clarias gariepinus*) system having an 11-L gravel bed for solids removal and 1-L fluidized sand filter for biological filtration was evaluated (Fig. 1 and 2). The application of gravel bed filter [1] and fluidized sand filter [2] to an aquaculture system were derived from previous studies. Commercially available sand of 1.2-2.0 mm diameter was used but of similar properties with river sand [2].

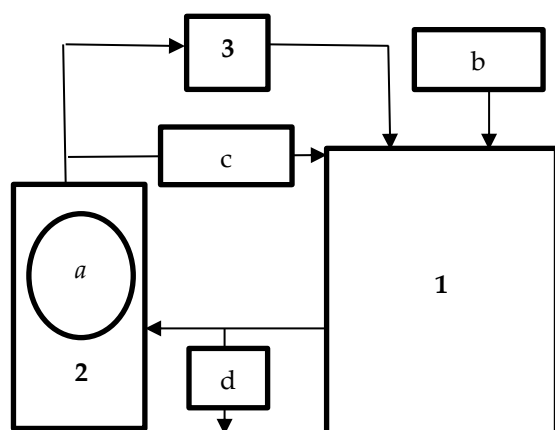


Fig. 1. Schematic Diagram of the Recirculating Catfish System in the study composed of: (1) Fish Tank; (2) Gravel Bed Filter; (3) Fluidized Sand Filter; with supporting components of: (a) Submersible Pump; (b) Aerator; (c) By-Pass; (d) Drain.

The well-aerated system operated at an average flow of 12.95 Lpm, and the hydraulic flux of 2,085.52 Lpm/m² resulted to 40.0% fluidization of the sand filter.

Desirable water quality parameters including total ammonia-nitrogen (TAN), nitrite-nitrogen

(NO₂-N), nitrate-nitrogen (NO₃-N), pH, dissolved oxygen, electrical conductivity, total dissolved solids and color were attained [3, 4, 5]. The volumetric TAN conversion rate (VTR) and volumetric NO₂-N conversion rate (VNR) were computed using Eq. 1 and 2, respectively, with k_c as conversion factor, Q for flow rate, V for gravel filter media volume, TAN_i and TAN_e for TAN concentrations of influent and effluent, respectively, and NO_{2i} and NO_{2e} as NO₂-N concentrations of influents and effluent, respectively.

$$VTR = k_c(TAN_i - TAN_e) \frac{Q}{V} \quad (1)$$

$$VNR = VTR + k_c(NO_{2i} - NO_{2e}) \frac{Q}{V} \quad (2)$$



Fig. 2. Recirculating African Catfish Culture System.

The gravel bed filter, which was provided mainly for solids removal, attained an equivalent volumetric TAN conversion rate (VTR) and volumetric NO₂-N conversion rate (VNR) of 153.33 g TAN/ m³-day and 53.61 g NO₂-N/ m³-day, respectively. Biological filtration was mostly achieved in the fluidized sand filter

* Oral paper presentation

which attained a VTR of 1396.39 g TAN/m³-day and a VNR of 1148.11 g NO₂-N/m³-day (Table 1).

The Areal TAN Conversion Rate (ATR) and Areal Nitrite Conversion Rate (ANR), which are the removal rates per media surface area, were computed by dividing VTR and VNR, respectively, with the specific surface area (SSA) of gravel bed of 298.05 m²/m³ [1] and 4528.19 m²/m³ for fluidized sand filter. ATR and ANR values for gravel bed filter were 0.52 g TAN/m²-day and 0.18 g NO₂-N m²-day, respectively while for fluidized sand filter were 0.31 g TAN/m²-day and 0.25 g NO₂-N m²-day, respectively (Table 1).

Two to three gravel filter backwashing resulted to at most 55 L or about 5% daily water replacement. The filter proved more than adequate in supporting the 20 kg catfish load which had 100 % survival rate, 1.21 feed conversion ratio, 0.43% specific growth rate, and 2.44 protein efficiency ratio in a 30-day evaluation period.

Cost and returns analysis showed that the system would not be profitable at only 20kg/m³ stocking density but would be break-even at about 46 kg/m³. Noting that a stocking density of 150 kg/m³ is attainable for African catfish [5] indicates that the project has high potential for profitability. Observed TAN and NO₂-N levels of less than 1 mg/L indicated that higher stocking can still be handled by the gravel and fluidized sand filter system.

Keywords

Recirculating Aquaculture System (RAS); Biofiltration; Water Quality; African Catfish (*Clarias gariepinus*); Fluidized Sand Filter.

References

- [1] Labinghisa, R. S. (2009). *Performance Evaluation of Charcoal, Charcoal-Gravel, and Gravel Biofilters for Aquaculture Applications*. Los Banos, Laguna: University of the Philippines Los Banos.
- [2] Escala, R. F. (2016). *Performance Evaluation of Fluidized Sand Filter with Different Grades of River Sand*. Los Banos, Laguna, Philippines: University of the Philippines Los Banos.
- [3] Bregnballe, J. (2015). *A Guide to Recirculation Aquaculture: An introduction to the new environmentally friendly and highly productive closed fish farmig systems*. Retrieved May 7, 2019, from Food and Agriculture Organization of the United Nations: <http://www.fao.org/3/a-i4626e.pdf>
- [4] Malone, R. (2013, October). *Recirculating Aquaculture Tank: A Review of Current Design Practice*. Retrieved May 21, 2019, from Southern Regional Aquaculture Center: <http://fisheries.tamu.edu/files/2013/09/SRAC-Publication-No.-453-Recirculating-Aquaculture-Tank-Production-Systems-A-Review-of-Current-Design-Practice.pdf>
- [5] Somerville, C., Cohen, M., Pantanella, E., Stankus, A., & Lovatelli, A. (2014). *Small-Scale Aquaponic food Production: Integrated Fish Farming*. Retrieved May 6, 2019, from Food and Agriculture of the United Nations: <http://www.fao.org/3/a-i4021e.pdf>

Table 1. The average TAN and NO₂-N removal rates of the gravel bed and fluidized sand filter

| Filter | VTR (g TAN/ m ³ -day) | VNR (g NO ₂ -N/m ³ -day) | ATR (g TAN/ m ² -day) | ANR (g NO ₂ -N/m ² -day) |
|----------------|-------------------------------------|---|-------------------------------------|---|
| Gravel Bed | 153.95 | 53.61 | 0.52 | 0.18 |
| Fluidized Sand | 1396.39 | 1148.11 | 0.31 | 0.25 |

Efficacy of pomegranate peel extracts against urothelial carcinoma *in vitro* and *in vivo**

Ching-Ping Chang ^{1,a}, Yu-Yi Chan ^{2,b}, Chien-Feng Li ^{3,c}, Lan-Hsiang Chien ^{1,d}, Song-Tay Lee ^{2,e} and Ting-Feng Wu ^{2,f}*

¹Department of Medical Research, Chi-Mei Medical Center, Tainan 710, Taiwan

²Department of Biotechnology, Southern Taiwan University of Science and Technology, Tainan 710, Taiwan

³Department of Pathology, Chi-Mei Medical Center, Tainan 710, Taiwan

^ajessica.cpchang@gmail.com, ^byuyichan@stust.edu.tw, ^cangelo.p@yahoo.com.tw,

^dm96h0207@stust.edu.tw, ^esongtlee@stust.edu.tw, ^fwutingfe@stust.edu.tw

Abstract

Urothelial carcinoma is the most frequent lesion among various bladder tumor types, contributing to more than 90% of bladder cancer cases[1]. Pomegranate (*Punica granatum* L.) fruit has been reported to have inhibitory activities to many types of tumors[2,3]. Pomegranate pericarp (peel) is a rich resource of phenolics, flavonoids, ellagitannins (predominantly punicalagin), and proanthocyanins compounds[4]. This study investigated the molecular mechanism underlying the inhibitory impacts of Taiwanese local pomegranate fruit on urinary bladder urothelial carcinoma. We implemented two bladder cancer cell lines and xenografted mice to examine the effects of pomegranate. MTT, Western immunoblotting, and immunohistochemical staining were used for research in this study. The findings of the 3-(4,5-dimethylthiazol-2-yl)-2,5-diphenyltetrazolium bromide assay showed that the ethanol extract of pomegranate peel demonstrated better inhibitory activities to human urinary bladder urothelial carcinoma T24 and J82 cells than those of pulp. The ethyl acetate part of peel ethanol extract possesses the best suppressive efficacy against urinary bladder urothelial carcinoma cells. The PEPE2 fraction of eight fractions (PEP1 to PEP8) obtained from the ethyl acetate part with Diaion HP-20 column chromatography had the best inhibitory effects. The flow cytometry and apoptotic examinations' data implied that the repressive impacts of PEPE2 fraction resulted from the bladder cancer cell apoptosis. Besides, xenografted human bladder tumors were created

in nude mice to translate the cell line results. The results of animal studies demonstrated that the ethyl acetate part (2, 5, 10, and 100 mg/kg) could dwindle the volume and weight of T24 tumors. The findings of tumor specimens with terminal deoxynucleotidyl transferase-mediated deoxyuridine triphosphate nick end-labeling assay showed that xenografted tumors underwent apoptosis. This study implicated the possibility that the non-edible pomegranate peel waste may be re-used to produce an affordable and hopeful chemopreventive nutraceutical to prevent the incidence or recurrence.

In this study, the peels of fresh pomegranate fruits were extracted with ethanol to produce peel extract (PEP). The MTT measurement findings showed that PEP demonstrated inhibitory activities to urinary bladder urothelial carcinoma (UBUC) T24 and J82 cells (Figure 1), both high grades.

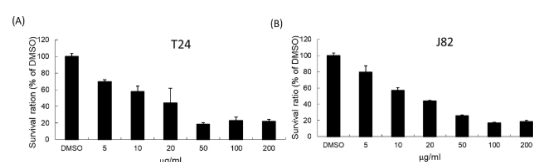


Fig. 1 The inhibitory effects of pomegranate peel ethanol extract on UBUC cells. (A) T24 cells; (B) J82 cells.

PEP was further partitioned successively between H₂O/EtOAc and between H₂O/n-BuOH, respectively, to yield three layers of EtOAc, n-BuOH, and H₂O. MTT assay results showed that IC₅₀ of EtOAc layer from PEP was 5 µg/ml toward T24 cells while for J82 cells, IC₅₀ was 20 µg/ml

* Oral paper presentation

(Figure 2). Thus, the EtOAc layer had the best inhibitory activity against UBUC cell lines.

The EtOAc layer was further fractionated to 8 fractions. The results of Fig. 3 indicated that the PEP2 fraction exhibited the best inhibitory efficacy to T24 and J82 cells.

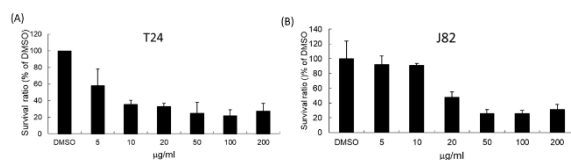


Fig. 2 The inhibitory effects of the EtOAc layer of PEP on UBUC cells. (A) T24 cells; (B) J82 cells.

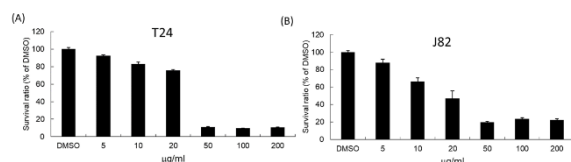


Fig. 3 The repressive activities of PEP2.

The above data implicated that pomegranate peel had ingredients that could inhibit UBUC cell proliferation. Thus mice were xenografted with human T24 cells to demonstrate that PEP possessed the inhibitory activities to UBUC in vitro. The findings of Fig. 4 demonstrated that oral consumption of 5, 10, and 100 mg/kg EtOAc layer could inhibit the UBUC growth.

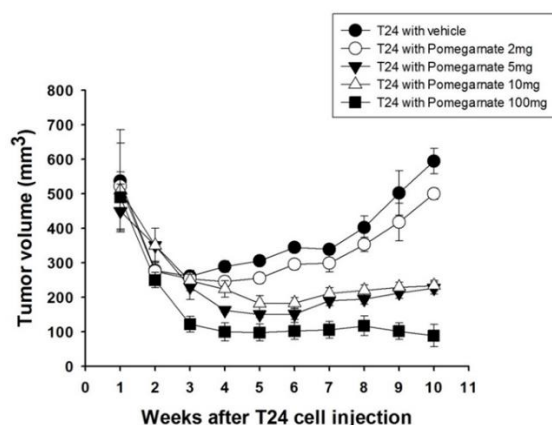


Fig. 4 The impacts of EtOAc layer on the UBUC

Keywords

Urinary bladder urothelial carcinoma, pomegranate, bladder cancer, apoptosis, tannins

References

- [1] Siegel RL, Miller KD, Jemal A. Cancer Statistics, 2017. CA Cancer J. Clin. 2017, 6, 7–30
- [2] Khan N, Hadi N, Afaq F, Syed D-N 2007. Pomegranate fruit extract inhibits prosurvival pathways in human A549 lung carcinoma cells and tumor growth in athymic nude mice. Carcinogenesis 28: 163-173.
- [3] Malik A, Afaq F, Sarfaraz S, Adhami V-M. 2005. Pomegranate fruit juice for chemoprevention and chemotherapy of prostate cancer. Proc. Natl. Acad. Sci. USA 102: 14813-14818.
- [4] Sharma P, McClees S-F, Afaq F. Pomegranate for prevention and treatment of Cancer: An update. Molecules 2017, 22, 177-194.

Modeling the effect of vitamin D intake on mortality in Vietnamese men*

Thi Huynh Anh, Le ^{1,a}, Thi Thao Nguyen, Nguyen ^{1,b*},

¹ Faculty of Project Management, The University of Danang, University of Science and Technology

^a lthanh@dut.udn.vn, ^b ntnguyen@dut.udn.vn

Abstract

Mortality is a vital measure of a population's health status, thus it provides information regarding the patterns in the contributing causes of death by population groups over time. Analyzing death patterns could explain the differences and changes in the health status, evaluating health strategies, as well as guiding the plan of policy-making. The purpose of this study is to analyze factors that affecting mortality of men in regards to their Vitamin D (V25d) level and provide suitable recommendations. This study uses the data from Ministry of Health in Vietnam, with the factors considered such as femoral neck Bone Mineral Density (fnBMD), Body Mass Index (BMI), Smoking Habit, V25d and Dietary Calcium Intake (Ca). The result shows that insufficient intake of V25d, low BMI and normal Ca level lead to the higher risk of getting low femoral neck BMD. Additionally, the person having either deficit, severe deficiency or insufficient intake of V25d with a high risk of femoral neck BMD has a higher probability of death. Furthermore, it is also known that smoking habit may not have any significant impact on mortality, as the probability of smoking and nonsmoking are equal. Another finding is that Femoral neck BMD is proven to be significantly mediating the effect of vitamin D to death of Vietnamese men.

METHODOLOGY

The study is conducted about the factors effect to mortality using Bayesian Method. First, by conducting data pre-processing to convert the continuous data to categorical data. Secondly with structure learning, DAG was created using expert judgment and model evaluation using conditional table test and BIC. Last, Inference Making, learning the parameter and using

mediation analysis for making inferences. Each of factors were categorized as : BMI (normal, underweight, obese and overweight); Ca (normal, high, low); fnBMD (normal, low risk, high risk), V25d (sufficient, insufficient, toxicity, deficit, and severe deficiency).

The data from Ministry of Health in Vietnam is utilized with 413 men.

RESULTS

Table 1. Conditional Probability Table of fnBMD

| Variable | Value | Categorical Description |
|---------------|-------------|-------------------------|
| BMI (kg/cm2) | <18.5 | Underweight |
| | 18.5 – 24.9 | Normal weight |
| | 25 – 29.9 | Overweight |
| | 30 | Obese |
| fnBMD (g/cm2) | > 0.95 | Low Risk |
| | 0.77 – 0.95 | Normal |
| | 0.76 | High Risk |
| V25d (mmol/l) | 25 | Severe Deficit |
| | 25-50 | Deficit |
| | 75-250 | Sufficient |
| Ca (md/d) | > 250 | Toxicity |
| | < 500 | Low |
| | 500-1500 | Normal |
| | > 1500 | High |
| Smoking | | Yes, No |
| Death | | Yes, No |

The result shows that insufficient intake of V25d, underweight (BMI) and normal Ca level lead to higher risk of fnBMD, with 50% chance. Additionally, either deficit, severe deficiency and insufficient intake of V25d or high risk of fnBMD has higher probability on impacting to

* Poster paper presentation

mortality rate. Meanwhile, the experiment finds that smoking habit may not have any significant impact to the mortality, as the probability of smoking and nonsmoking are equal (50%). Moreover, the vitamin D level has not direct effect on death because the level of vitamin D increases, the probability of death should be lower, but it is not in our result. However, the mediation effect of vitamin D is significant. Furthermore, other research found that the association between vitamin D and mortality was inconsistent (Alison M. Mondul 2017). (TS. Tran 2018) also determined that femoral neck BMD has significant impact to mortality in men with 67%. In 2014, (Nicola Napoli 2014) showed that vitamin D deficiency causes bone loss and increases bone turnover. Therefore, we can conclude that vitamin D level has significant indirectly impact to the mortality rate. The result is helpful for medical treatment and healthy life.

Table 2. Conditional Probability Table of *fnBMD*

| Variable | Factor | <i>FnBMD</i> "High_risk" |
|-------------|---------------------|--------------------------|
| V25d | Deficit | 0.34 |
| BMI | Underweight | |
| Ca | Normal | |
| V25d | Insufficient | 0.5 |
| BMI | Underweight | |
| Ca | Normal | |
| V25d | Toxicity | 0.34 |
| BMI | Underweight | |
| Ca | High | |
| V25d | Toxicity | 0.33 |
| BMI | Overweight | |
| Ca | High | |
| V25d | Toxicity | 0.34 |
| BMI | Obese | |
| Ca | High | |

Keywords

Bayesian network, femoral neck BMD, mortality, vitamin D level

Table 3. Conditional Probability Table of Death

| | Factor | Death "Yes" |
|--------------|------------------|-------------|
| V25d | Deficit | 0.67 |
| | Insufficient | 0.49 |
| | Toxicity | 0.49 |
| Smoking | Yes | 0.51 |
| | No | 0.49 |
| <i>fnBMD</i> | High Risk | 0.72 |
| | Normal | 0.46 |
| | Low Risk | 0.44 |

Table 4. Conditional Probability Table of Death from the Combination

| V25d | <i>fnBMD</i> | Smoking | Death | Pro |
|--------------------------|------------------|---------|-------|--------------|
| Deficit | High Risk | No | Yes | 0.8 |
| Insufficient | High Risk | No | Yes | 0.75 |
| Sufficient | High Risk | No | Yes | 0.6 |
| Toxicity | High Risk | No | Yes | 0.333 |
| Deficit | High Risk | Yes | Yes | 0.667 |
| Insufficient | High Risk | Yes | Yes | 0.75 |
| Severe Deficiency | High Risk | Yes | Yes | 0.667 |
| Deficit | Normal | Yes | Yes | 0.692 |
| Toxicity | Normal | Yes | Yes | 0.333 |

References

- [1] Alison M. Mondul, Stephanie J. Weinstein, Tracy M. Layne, Demetrius Albanes. Vitamin D and Cancer Risk and Mortality: State of the Science, Gaps, and Challenges. *Epidemiologic Reviews*, (2017) 28-48
- [2] Nicola Napoli, Rocky Strollo, Delia Sprini, Ernesto Maddaloni, Giovam Battista Rini, and Enrico Carmina. Serum 25-OH Vitamin D in relation to Bone Mineral Density and Bone Turnover. *International Journal of Endocrinology* (2014).
- [3] TS. Tran, TV. Nguyen. Association Between Alendronate and All-Cause Mortality and Cardiovascular Mortality Among Hip Fracture: An Alternative Explanation. *Journal of Bone and Mineral Research*, (2018).

Synthesis of modified chitosan containing multi-hydroxyl group for adsorption boron*

Quyen Hong Ho^{1, a*}, Masashi Kurashina^{2, b} and Mikito Yasuzawa^{3, c}

¹University of Science and Technology, The University of Da Nang, Viet Nam

²Tokushima University, Tokushima 770-8506, Japan

^ahhquyen@dut.udn.vn, ^bkurashina.masashi@tokushima-u.ac.jp, ^cyasuzawa@tokushima-u.ac.jp

Abstract

Although boron is a crucial element for plants, animals and humans, it turns to poisonous when its concentration exceeds demand. Owing to wide-ranging application in numerous industries such as the manufacture of glassware, ceramic, semiconductors, chemical, metallurgy, pharmaceuticals, cosmetic, construction, coal-fired power plants, waste of boron contaminates water sources, leading to environmental issues [1]. Thus, the World Health Organization (WHO) has established the maximum boron concentration in drinking water to 2.4 mg/L whereas this value is limited to 1 mg/L in Japan, South Korea, Singapore, European Union [2]. The exist of boron in the form of boric acid and borax can react with *vis*-diol group in polysaccharides to form stable borate complexes. In this study, gluconated chitosan particles (GChs) were synthesized by functionalization of chitosan with D-(+)-glucono-1,5 lactone (GL) in the simple process to provide *vis*-diol sections for boron adsorption.

Firstly, the mixture of chitosan flakes (5 g) and acetic acid solution 1% (v,v) (500 mL) was stirred vigorously for 12 h. Next, 27.63 g of GL was added to the solution, and the reaction mixture was refluxed by heating in an oil bath at 115 °C for 24 h. Then, NaOH 1 M was added dropwise to form the precipitate, and this compound was separated by filtration. Residuals of free acetic acid and unreacted GL were removed by dialysis against Mili-Q water using dialysis membrane. Finally, the obtained product was collected by filtration and dried completely in the vacuum at room temperature. The synthesis of GChs is shown in Fig. 1.

The adsorption mechanism of GChs was investigated in a batch system with initial boron concentration from 10 to 400 mg/L (Fig. 2). The maximum boron adsorption capacity of GChs was achieved at 5.80 mg/g. The adsorption isotherm data were well fitted to Langmuir model ($R^2 = 0.9993$). From the results of Table. 1, boron adsorption capacity using GChs was similar to the result of commercial resin Amberlite IRA 743 (5.73 mg/g).

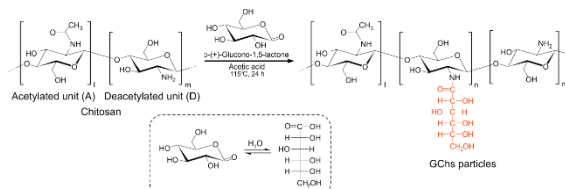


Fig. 1. Illustration of the preparation of GChs.

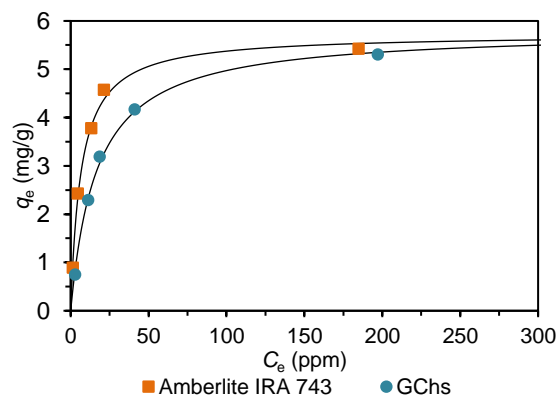


Fig. 2. Adsorption isotherm of boron on GChs and Amberlite IRA 743 by fitting Langmuir (C_i from 10 to 400 ppm, the mass of adsorbent 0.2 g in the samples of 10 and 50 ppm and 0.8 g in the samples of 100 to 400 ppm, V 20 mL, temperature 25 °C and contact time 24 h).

The adsorption kinetics was tested from 0.5 to 24 h. As shown in Fig. 3, the adsorption equilibrium was reached after 700 min, and the adsorption kinetics of

* Poster paper presentation

boron was following the pseudo-second order model ($R^2 = 0.9933$).

The effect of pH on boron uptake was investigated from 5.6 to 9.8. As shown in Fig. 4, The capacity of boron adsorption increased from 5.0 to 6.2 while pH rose from 5.6 to 9.8.

Fig. 5 displays the impact of ionic strength on the adsorption of boron into GChs particles. There is a slight increase in boron adsorption after the addition of NaCl salt from 10 to 1000 mmol/L.

To conclude, chitosan-based adsorbent (GChs), GChs exhibited the maximum adsorption capacity at 5.80 mg/g after 700 min. The boron adsorption capacity enhanced with the increase in initial pH. There was a slight increase in boron adsorption in the presence of NaCl salt; therefore, GChs may be applied for boron removal from saline water or seawater.

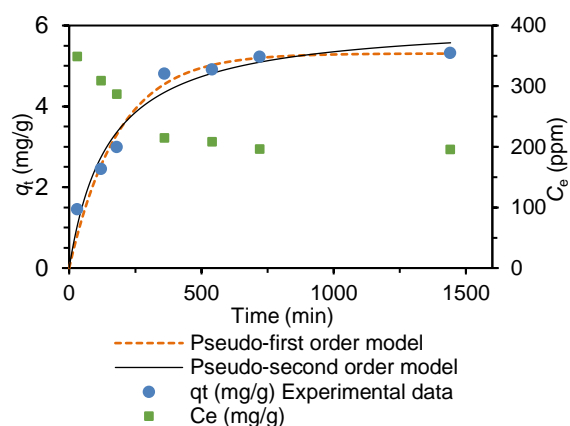


Fig. 3. Adsorption kinetics of boron on GChs (Ci 400 ppm, the mass of adsorbent 0.8 g, pH 5.6, V 20 mL, temperature 25 °C and contact time 24 h).

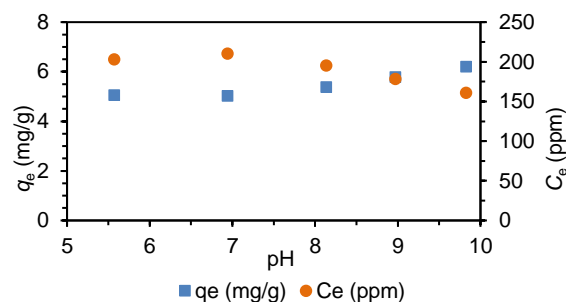


Fig. 4. Effect of pH on boron adsorption by using GChs (Ci 400 ppm, the mass of adsorbent 0.8 g, V 20 mL, temperature 25 °C and contact time 24 h).

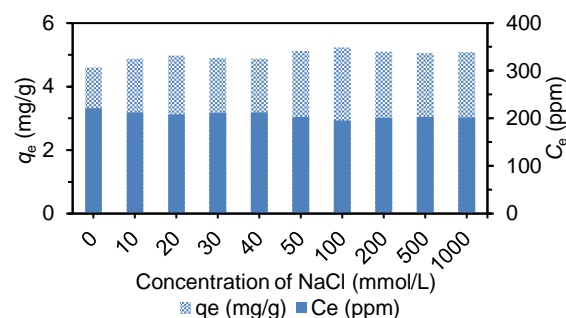


Fig. 5. Effect of NaCl salt on boron adsorption by GChs (Ci 400 ppm, the mass of adsorbent 0.8 g, V 20 mL, temperature 25 °C and contact time 24 h).

Keywords

Boron, chitosan, removal, adsorption, Amberlite 743.

References

- [1] J.A. Ober, Mineral commodity summaries 2018, Mineral Commodity Summaries Reston, VA, 2018, pp. 204.
- [2] Guidelines for Drinking-water Quality, World Health Organization WHO 4th Edition 2011

Table 1. Langmuir and Freundlich isotherm parameters and correlation coefficient at 25 °C for adsorption of boron by GChs.

| | Langmuir model | | | | Freundlich model | | |
|---------------|----------------------|-------------|--------|---------------|------------------|-------|--------|
| | q_{\max} (mg/g) | b (L/mg) | R^2 | R_L range | K_F | n | R^2 |
| GChs | 5.80 | 0.060 | 0.9993 | 0.071 - 0.748 | 1.141 | 3.309 | 0.8506 |
| Amberlite 743 | 5.73 | 0.151 | 0.9997 | 0.016 - 0.385 | 1.826 | 4.522 | 0.7764 |

Classification skin defect of jujube by using spectral images*

Ngo Minh Tri Nguyen ^{1,a}, Quoc Thien Pham ^{1,b}, Nai-Shang Liou ^{1,c*}

¹ Southern Taiwan University of Science and Technology, Taiwan R.O.C.

^a Da81y206@stust.edu.tw, ^b pthien0288@gmail.com, ^c nliou@stust.edu.tw

Abstract

Appearance is an important factor which influences fruit price. Because manual sorting of fruits sorting is money and time consuming, computer and machine vision technologies have been used for postharvest processing of fruits [1-3]. Hyperspectral imaging (HSI), with the capability of collecting data in both spatial and spectral domains, becomes an emerging method used for postharvest processing of fruits in recent years [3, 4].

In this study, a hyperspectral system with an effective range of 468-950 nm was used to obtain the reflection spectra of jujubes for the application of surface defect detection. Hyperspectral image data were used for classification of 6 common skin defects (decay, rusty, flesh, black fungus, white fungus, over ripen) of jujube. Three classification models were developed to classify defect surfaces, normal surface and glare area on jujube surface. The skin defects were investigated by using traditional classification methods (e.g. band ratio, vegetation index and spectrum angle mapper or SAM) used for remote sensing hyperspectral images, and supervised machine learning methods (support vector machine or SVM, artificial neural network or ANN). The classification results of aforementioned methods show that the validation accuracies of band ratio and vegetation index methods are low and thus not suitable for skin defect detection of jujube. The validation accuracies of SAM, SVM and ANN are 77.4%, 97.3% and 97.7% respectively.

Compared to SVM and ANN, SAM is simple, fast. However, the prediction accuracy is lower than those of SVM and ANN model. In Fig. 1, the prediction results of SAM model shows that the area near the center of the specimen (3) was misclassified as Flesh while the other two

methods can correctly predict that area as over ripen or rusty. Furthermore, the flesh area of specimen (2) was misclassified by SAM model.

The classification accuracy and speed of ANN model are better than those of SVM model. The high accuracy and computation efficiency of ANN model makes ANN model having the potential to be used for on-line sorting of jujubes.

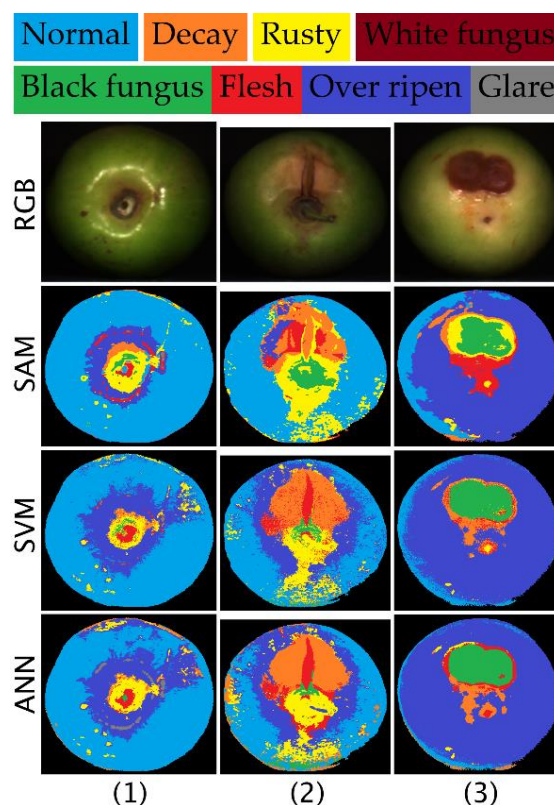


Fig. 1. RGB images and prediction results of SAM, SVM, ANN models

Keywords

Postharvest Processing, Hyperspectral imaging, Skin Defect Detection, Supervised Classification

References

[1] I. Kavdir and D. E. Guyer, "Apple sorting using artificial neural networks and spectral

* Oral paper presentation

imaging," Transactions of the Asae, vol. 45, pp. 1995-2005, Nov-Dec 2002.

[2] J. Naranjo-Torres, M. Mora, R. Hernandez-Garcia, R. J. Barrientos, C. Fredes, and A. Valenzuela, "A Review of Convolutional Neural Network Applied to Fruit Image Processing," Applied Sciences-Basel, vol. 10, May 2020.

[3] Y. Z. Lu, W. Saeys, M. Kim, Y. K. Peng, and R. F. Lu, "Hyperspectral imaging technology for

quality and safety evaluation of horticultural products: A review and celebration of the past 20-year progress," Postharvest Biology and Technology, vol. 170, Dec 2020.

[4] Z. Gao, Y. Shao, G. Xuan, Y. Wang, Y. Liu, and X. Han, "Real-time hyperspectral imaging for the in-field estimation of strawberry ripeness with deep learning," Artificial Intelligence in Agriculture, vol. 4, pp. 31-38, 2020/01/01/ 2020

Effects of thin-layer drying temperature and tempering on hybrid rice seed*

Rina A. Bawar ^{1,a}, Joanne P. Foliente ^{1,b}, Kevin F. Yaptenco ^{1,c}

¹ Agricultural and Bio-Process Division, Institute of Agricultural Engineering, College of Engineering & Agro-Industrial Technology, University of the Philippines Los Baños, Philippines

^arabawar@up.edu.ph, ^bjpfoliente@up.edu.ph, ^ckfyaptenco@up.edu.ph

Abstract

This laboratory research conducted thin-layer drying tests for rice seeds for two hybrids (H1 and H2). Hybrid rice has been developed to address the decline in Philippine rice production since it is a type of rice that has been produced from two different parents which can significantly out-yield other rice varieties [1].

The independent parameters included drying air temperature (45, 55, and 65°C) and tempering duration (1, 2 and 4 hours) that evaluated the effects on seed quality, particularly germination and vigor rates and on its thin-layer drying characteristics such as drying curves, drying rate and effective operation time.

At present, thin-layer drying curves for hybrid rice seeds are limited and need to be established, especially for varieties produced in the Philippines. Drying protocols, on which drying temperature and tempering duration would result to optimal drying rates and germination rates, can also be established.

The study was divided into thin-layer drying and tempering experiments (Fig. 1) followed by germination tests after three months of ambient storage.

Results showed that dried H2 samples stored for three months achieved the required 85% germination rate [2] only with continuous drying temperature of 45°C. However when tempered for 2 or 4 hours, H2 samples dried at 65°C resulted to germination rate of more than 90% as shown in Fig. 2.

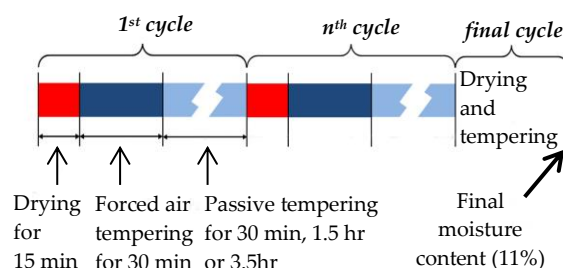
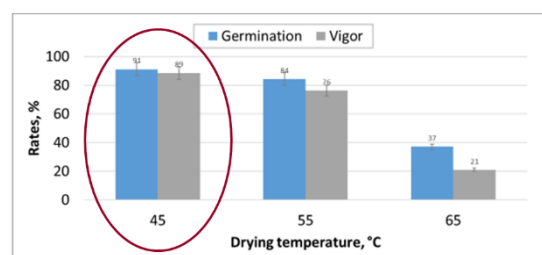
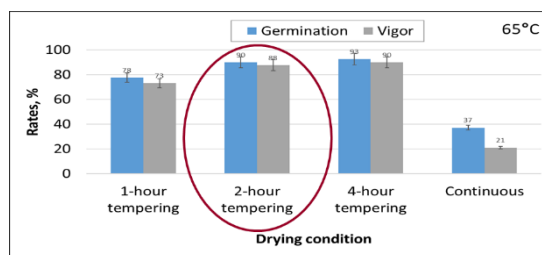


Fig. 1. Experimental details for tempering during the drying process



(a) continuously dried



(b) dried at 65°C and tempered

Fig. 2. Germination rates of (a) continuously dried at different drying temperatures compared to (b) dried at 65°C with different drying conditions

Drying rate was also significantly affected by the drying temperature and tempering duration, as it increased with higher air temperature and with tempering. Tempered samples for 2 hours have significant increase in drying rate compared with those continuously dried and tempered for 1 hour,

* Oral and poster paper presentation

but have no significant difference compared with those treated with 4-hour tempering.

Samples dried at 65°C and tempered for 2 hours had comparable total operation time with those continuously dried at 45°C. However, the effective operation time was shorter. From 6.5 hours that the dryer is turned on during 45°C continuous drying, it is just 1 hour open when dried at 65°C and tempered for 2 hours (Fig. 3).

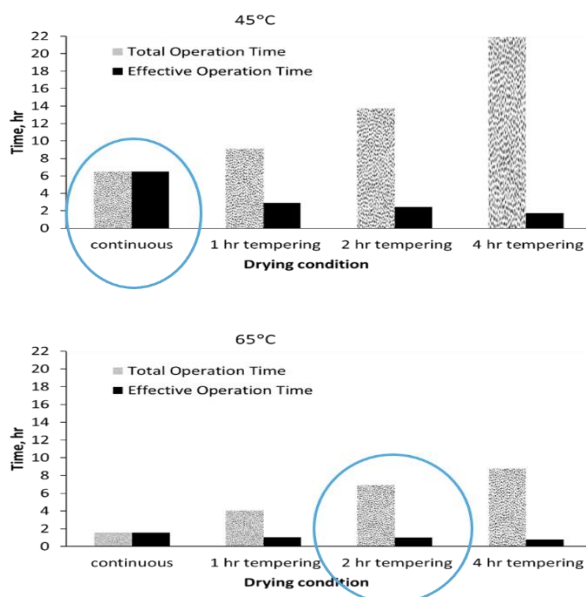


Fig. 3. Total operation time vs effective operation time with different drying conditions at 45 and 65°C

Through the thin-layer drying process, thin-layer drying curves were obtained. This actual drying curves have been fitted to several known Drying Models [2]. The values of R^2 were the highest (ranging from 0.99 to 0.999) and the values of RMSE were the lowest (ranging from 0.006 to 0.030) for the Midilli and Two-Term Models, based on all data points. All corresponding R^2 values were consistently higher and the RMSEs were lower compared with the other models. For the purpose of simulation and scale up, the Two term model is recommended. Although, the Midilli Model would be the best according to the R^2 values, a general model is needed wherein the parameters are linearly related to the drying temperature and the extrapolation is better in lower temperature ranges. Only the Two-Term Model with parameters linearly related to temperatures can fit the experimental data well.

It could be concluded that the drying rate and seed quality were significantly affected by the

drying temperature and tempering duration. It is also possible to have shorter effective drying time and acceptable germination rate by combining high temperatures with tempering.

1. Continuously dried samples at drying temperature of 45°C and stored in ambient for 3 months achieved the required 85% germination rate.
2. H2 samples dried at 65°C and tempered for 2 hours and stored for 3 months at ambient had comparable total operation time and seed quality and significantly shorter effective operation time compared with those continuously dried at 45°C
3. Among the eight models considered, Midilli and Two-Term Models resulted to the best goodness-of-fit with the actual drying process.

There is potential improvement of drying characteristics and seed quality of hybrid rice seeds by including tempering treatments. Simulation of deep-bed drying with intermittent drying can be explored. With proper economic analysis, results generated on this study may be used to encourage stakeholders to introduce automated tempering treatments to large-scale drying of rice seeds.

Keywords

hybrid rice seeds, continuous drying, tempering, germination, drying curves

References

- [1] Barclay, A. (2007). A hybrid history. *Rice Today*. 6(4): 23-24. Retrieved November 15, 2019 from <https://tinyurl.com/ybuqs6ha>
- [2] Department of Agriculture. (2010). Administrative Order No. 04. Retrieved May 27, 2020 from <https://tinyurl.com/y8yz64qy>
- [3] Hacıhafizoglu, O., A. Cihan & K. Kahveci. (2008). Mathematical modelling of drying of thin layer rough rice. *Food and Bioprocess Processing*. 268-275.

Technical Presentations

Human Engineering

| | | |
|----------------------|---|---|
| Moderator | : | Dr. Rossana Marie C. Amongo |
| Panelists | : | Dr. Ralph Kristoffer B. Gallegos, Dr. Diana Marie R. de Silva, aProf Erwin P. Quillo |
| Technical Assistants | : | aProf. Adrian A. Borja, aProf. Romel A. Arrobang |
| 01:30PM – 01:35PM | Welcome Remarks and Introduction of Panel Members | |
| 01:35PM – 01:50PM | Motion analysis of infants using musculoskeletal model | <u>Tomoaki Ichikawa*</u> , Shigeo Yamashita, Shinichiro Morichi, Hisashi Kawashima, Gaku Yamanaka, Yoshikazu Kobayashi, Ayuko Saito (KUTE) |
| 01:50PM – 02:05PM | A study on motion measurement for early screening for neurological disease | <u>Tatsuro Sato*</u> , Shigeo Yamashita, Shinichiro Morichi, Hisashi Kawashima, Gaku Yamanaka, Satoru Kizawa, Ayuko Saito (KUTE) |
| 02:05PM – 02:20PM | A study on the view factor in sensory evaluation of human movement | <u>Jun Muramatsu*</u> , Shogo Takeuchi, Ayuko Saito (KUTE) |
| 02:20PM – 02:35PM | Ergonomic Keyboard for English and Tagalog Languages | <u>Angelica Louise P. San Juan*</u> , Josefa Angelie D. Revilla, Angelo C. Ani, Clarissa M. Pesigan, Alan Marco S. Mercado (UPLB) |
| 02:35PM – 02:50PM | Construction of a Kalman filter for real time motion measurement | <u>Yutaka Tanzawa*</u> , Satoru Kizawa, Ayuko Saito (KUTE) |
| 02:50PM – 03:05PM | Development of infants suits for motion measurement | <u>Yu Amagasaki*</u> , Shigeo Yamashita, Shinichiro Morichi, Hisashi Kawashima, Gaku Yamanaka, Satoru Kizawa, Ayuko Saito (KUTE) |
| 03:05PM – 03:20PM | Experiment on selecting evaluation words for sensory evaluation of beautiful gait | <u>Shogo Takeuchi*</u> , Jun Muramatsu, Masaki Tamura, Ayuko Saito (KUTE) |

Ergonomic keyboard for English and Tagalog languages*

Angelica Louise P. San Juan ^{1,a*}, Josefa Angelie D. Revilla ^{1,b}, Angelo C. Ani ^{1,c}, Clarissa M. Pesigan ^{1,d}, Alan Marco S. Mercado ^{1,e}

¹Department of Industrial Engineering, College of Engineering & Agro-Industrial Technology, University of the Philippines Los Baños, Philippines

^aapsanjuan@up.edu.ph, ^bjdrevilla@up.edu.ph, ^cacani2@up.edu.ph, ^dcmpesigan@up.edu.ph,

^easmercado1@up.edu.ph

Abstract

The use of computers, especially for school-works or office-related activities, has been vital in the recent years. Nowadays, English and Tagalog languages are alternately used for formal writing, while Taglish is often used for informal writing. Either means of type-written communication is highly dependent on the use of computer keyboards. The most used keyboard layout today is the QWERTY layout, which was designed to address the problem of adjacent typebars jamming the typewriter when tapped quickly ^[1]. It is also known to some as not ergonomically designed because it overburdens the left hand and pinky fingers and has an uneven load distribution ^[2]. Various keyboard layouts were also developed in different countries in order to fit their comfortability in typing. These keyboards are the AZERTY and QWERTZ, however since both were variations of the QWERTY layout, it only addresses the mechanical problems of the keyboard and not the comfortability of the users ^[3]. Hence, this study aims to develop ergonomic keyboard layouts that is more fit, in terms of utilizing finger strength and encouraging finger and hand alternation, for typing in English, Tagalog, and Taglish than the QWERTY layout, with the use of Python programming language.

Letter frequencies from 1,000 most common English and Tagalog words for letter sequence and a weighted pointing system generated from rankings of previous studies' identified factors (finger strength, finger alternation, and hand alternation^{[3][4][5]}), were the primary considerations for the development of possible layouts. Based on the importance of the factors

from previous studies, for this study, the factors were ranked as: 1 – hand alternation, 2 – finger alternation, and 3 – finger strength. There were 12 keyboard layouts developed using decisions such as prioritizing either sides or different rows whenever there are equal values from the pointing system. However, due to time constraint, this paper was able to present the development and evaluation of two (out of the 12) layouts and the QWERTY layout. Moreover, the layout was based on right-handed people and a touch-typing scheme. Also, only the letters were rearranged. Layout 1, which prioritizes the left side and middle row, is shown in Fig. 1, and Layout 2, which prioritizes the left side and top row, is shown in Fig. 2.

| | | | | | | | | | | | |
|---|---|---|---|---|---|---|---|---|---|---|---|
| J | X | D | S | Y | M | T | B | C | F | * | * |
| H | U | E | N | O | I | A | G | K | * | * | |
| Z | Q | W | R | V | P | L | * | * | * | | |

Fig. 1. Keyboard Layout 1

| | | | | | | | | | | | |
|---|---|---|---|---|---|---|---|---|---|---|---|
| J | X | H | E | D | M | I | B | C | F | * | * |
| Y | U | O | N | S | T | A | G | K | * | * | |
| Z | Q | W | R | V | P | L | * | * | * | | |

Fig. 2. Keyboard Layout 2

The three layouts were evaluated using text analysis (TA) approach. In this approach, the points determined in each keyboard using 500,000 letters from 10 genres per language were compared. TAs were calculated using the distance of letters from one another, and penalties from consecutive usage of same finger and hand. In addition, to accurately compute for the TAs, they were also programmed using Python. Essentially, higher TA points meant more hand movement, therefore less ergonomic.

Two-way ANOVA followed by the Bonferroni test was used to test which keyboard layouts are

* Oral paper presentation

significantly different from each other based on their TA points. For preliminary results, only 50,000 texts were used with 5 genres per language (English and Tagalog). Table 1 (L1 – Layout 1, L2 – Layout 2, Q-QWERTY, T-Tagalog, E-English) shows the statistical values based on the preliminary TA results for the three layouts. Two-way ANOVA was conducted that reveals the effect of layout and language on TA points. There was a statistically significant interaction between the effects of layout and language on TA points with a p-value of 0.000, therefore pairwise comparison was examined. Bonferroni test was used to determine which of the layout-language pairs were significantly different from each other.

Table 1. Bonferroni simultaneous tests for differences of means results

| Difference of layout*language | Difference of Means | T-Value | Adjusted P-Value |
|-------------------------------|---------------------|---------|------------------|
| (L1 T) - (L1 E) | -5155 | -5.71 | 0.000 |
| (L2 E) - (L1 E) | 9769 | 10.83 | 0.000 |
| (L2 T) - (L1 E) | -6022 | -6.67 | 0.000 |
| (Q E) - (L1 E) | 5979 | 6.63 | 0.000 |
| (Q T) - (L1 E) | -2510 | -2.78 | 0.155 |
| (L2 E) - (L1 T) | 14924 | 16.54 | 0.000 |
| (L2 T) - (L1 T) | -867 | -0.96 | 1.000 |
| (Q E) - (L1 T) | 11134 | 12.34 | 0.000 |
| (Q T) - (L1 T) | 2645 | 2.93 | 0.109 |
| (L2 T) - (L2 E) | -15791 | -17.5 | 0.000 |
| (Q E) - (L2 E) | -3790 | -4.2 | 0.005 |
| (Q T) - (L2 E) | -12279 | -13.61 | 0.000 |
| (Q E) - (L2 T) | 12001 | 13.3 | 0.000 |
| (Q T) - (L2 T) | 3512 | 3.89 | 0.010 |
| (Q T) - (Q E) | -8489 | -9.41 | 0.000 |

Based on the difference of means, it shows that typing English in Layout 1 is better than typing English in Layout 2 ($p < 0.01$, Table 1 Row 2) and QWERTY ($p < 0.01$, Table 1 Row 4). Typing Tagalog in Layout 1 is better than typing English in Layout 1 ($p < 0.01$, Table 1 Row 1), Layout 2 ($p < 0.01$, Table 1 Row 6), and QWERTY ($p < 0.01$, Table 1 Row 8). Typing Tagalog in Layout 2 is better than typing English in Layout 1 ($p < 0.01$, Table 1 Row 3), Layout 2 ($p < 0.01$, Table 1 Row 10), and QWERTY ($p < 0.01$, Table 1 Row 13), and

typing Tagalog in QWERTY ($p < 0.01$, Table 1 Row 14). However, it also shows that typing English in QWERTY is better than typing English in Layout 2 ($p < 0.01$, Table 1 Row 11). Furthermore, typing Tagalog in QWERTY is better than typing English in Layout 2, and QWERTY ($p < 0.01$, Table 1 Row 12). In conclusion, based on the initial findings, it can be stated that Layout 2 seemed to ease hand movement when typing in Tagalog, while Layout 1 when typing in English. The study will continue the development and evaluation of the other 10 layouts and more texts will be used for comparison. Nevertheless, it can be inferred from the initial results that there are opportunities for improving the traditional QWERTY keyboard.

Keyboards

ergonomics, keyboard, qwerty, typing

References

- [1] Kay NM. 2013. The QWERTY problem. Paper presented at the 35th DRUID Celebration Conference 2013, Barcelona, Spain, June 17- 19.
- [2] Noyes J. 1998. QWERTY - the immortal keyboard. *Computing & Control Engineering Journal*, 9(3), 117-122. doi:10.1049/cce:19980302
- [3] Wagner MO, Yannou B, Kehl S, Feillet D, Eggers J. 2003. Ergonomic modelling and optimization of the keyboard arrangement with an ant colony algorithm. *Journal of Engineering Design*, 14(2), 187-208. doi:10.1080/0954482031000091509. hal-00748740
- [4] Walker CP. 2003. Evolving a more optimal keyboard. Course project: Introduction to evolutionary computation, Missouri University of Science & Technology.
- [5] Deshwal P, Deb K. 2006. Ergonomic Design of an Optimal Hindi Keyboard for Convenient Use. 2006 IEEE International Conference on Evolutionary Computation. doi:10.1109/cec.2006.1688577

Construction of a Kalman filter for real time motion measurement*

Yutaka Tanzawa^{1, a*}, Satoru Kizawa² and Ayuko Saito^{1, b}

¹ Department of Mechanical Science and Engineering, School of Advanced Engineering,
Kogakuin University, Tokyo, Japan

² Department of Mechanical Engineering and Robotics, National Institute of Technology (KOSEN), Akita
College, Akita, Japan.

^as517033@ns.kogakuin.ac.jp, ^bsaito@cc.kogakuin.ac.jp

Abstract

1. Introduction

Small and light-weight 9-axis sensor modules have been developed with the MEMS technology progresses. 9-axis sensor modules have been used for pose estimation in a wide range of fields such as medical welfare, sports, and entertainment [1]. The Kalman filter is often used for pose estimation using 9-axis sensor modules because of its low computational load and excellent noise resistance [2]. However, it is not easy to determine the noise covariance in the Kalman filter by accurately detecting the dynamic characteristic of the measurement target and the noise characteristics of a 9-axis sensor module. The Kalman filter is often used for the offline pose estimation by utilizing the measurement information after the 9-axis sensor modules measured human motion. The offline process, nevertheless, takes a while for the pose estimation. Applying the Kalman filter for the real-time pose estimation in clinical practice requires determining the noise covariance in real-time to increase the estimation accuracy.

Therefore, in this study, we constructed a Kalman filter that could be used for accurate pose estimation in real time utilizing the noise covariance matrix based on the 9-axis sensor module outputs. The pitch angle estimation was performed in this study, as the first step of real time 3D pose estimation.

2. Method

2.1 Initial pitch angle

The initial pitch angle was calculated from Eq. (1) using the acceleration sensor output at rest [3].

$$\theta_A = \text{atan2} \frac{-A_x}{\sqrt{A_y^2 + A_z^2}} \quad (1)$$

where A_x , A_y and A_z are the accelerometer output for x , y , and z axes, respectively

2.2 Kalman filter algorithm using noise covariance based on sensor output

A linear Kalman filter for pitch angle estimation was constructed. The state and observation equations are shown in Eqs. (2) and (3), respectively.

$$x_{t+1} = Ax_t + Bu_t + w_t \quad (2)$$

$$y_t = Cx_t + v_t \quad (3)$$

$$x_t = [\theta_t], y_t = \left[\text{atan2} \frac{-A_{x,t}}{\sqrt{A_{y,t}^2 + A_{z,t}^2}} \right]$$

where x_t is the pitch angle, u_t is the gyro sensor output, w_t is the process noise, v_t is the observation noise, and $A=B=C=1$. Then, the prediction step (Eqs. (4) and (5)) and the filtering step (Eqs. (6), (7), and (8)) were calculated using the linear discrete-time system represented by Eqs. (2) and (3).

$$x_{t+1}^- = Ax_t + Bu_t \quad (4)$$

$$P_{t+1}^- = AP_t A^T + BQ_t B^T \quad (5)$$

$$K_{t+1} = P_{t+1}^- C^T (C P_{t+1}^- C^T + R_t)^{-1} \quad (6)$$

$$x_{t+1} = x_{t+1}^- + K_{t+1} (y_{t+1} - C x_{t+1}^-) \quad (7)$$

$$P_{t+1} = (I - K_{t+1} C) P_{t+1}^- \quad (8)$$

where P represents the error covariance matrix, K denotes the Kalman gain, and Q and R respectively denote the covariance matrices of the process noise and observation noise. Q and R are based on the gyro sensor output and accelerometer output, respectively, as shown in Eqs. (9) and (10).

* Oral paper presentation

$$Q_t = 0.0001\sqrt{\omega_{x,t}^2 + \omega_{y,t}^2 + \omega_{z,t}^2} \quad (9)$$

$$R_t = 0.0001\sqrt{A_{y,t}^2 + A_{z,t}^2} \quad (10)$$

where $\omega_{x,t}$, $\omega_{y,t}$, $\omega_{z,t}$ respectively stand for the gyroscope output for x , y and z axes. A_y and A_z respectively express the accelerometer outputs for the y and z axes.

3. Experiment

The 9-axis sensor module used in this study (BMX055 from Bosch) includes a three-axis gyro sensor, a three-axis acceleration sensor, and a three-axis geomagnetic sensor. The experiments were conducted with the measurement range of ± 2 G for the acceleration sensor and ± 1000 degree/sec for the gyro sensor. The size of the sensor is $14 \times 10 \times 5$ mm and the weights 5 g. The microcontroller board used in the experiment was STM32F401RE. Measurement data acquisition and setting for the 9-axis sensor module was performed through I2C communication. The maximum communication speed of the I2C communication was set to 400 kbps. The 9-axis sensor module was attached to a two-link mechanism controlled by a servomotor. The mechanism moved in a range of 90 degrees from the initial posture of 0 degree.

4. Result

The results are shown in Fig. 1. The horizontal axis is the normalized time from starting the operation of the robot to the end of that as 100%.

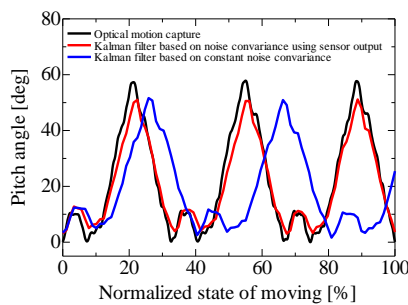


Fig.1. Measurement results

The vertical axes are the pitch angle results. The black solid line represents the result obtained from the optical motion capture system, which is used as the true value in the experiment. The red solid line represents the result obtained from the Kalman filter using the proposed method. The blue solid line shows the result from the Kalman filter, which used the constant process and observation noise covariances. The constant process and observation noise covariances were determined to maximize the log-likelihood using 100 sample data before the measurement. The proposed method result is generally consistent with the result obtained from the optical motion capture system. On one hand, the result using the constant process and observation noise covariances show a time-delay result.

5. Conclusion

The proposed method could estimate the pitch angle in real time utilizing the noise covariance matrix based on the 9-axis sensor module outputs. The method is expected to be useful for estimating motion in sports and healthcare applications.

Keywords

Kalman filter, Noise covariance, Pose estimation, Real-time, 9-axis sensor module

References

- [1] Nazarahari et al, Sensor-to-body calibration procedure for clinical motion analysis of lower limb using magnetic and inertial measurement units, *Journal of Biomechanics*, Vol.85, No. 6 (2019), pp.224–229.
- [2] Zheng et al, Data fusion based multi-rate Kalman filtering with unknown input for on-line estimation of dynamic displacements, *Measurement*, Vol.131 (2019), pp.211–218.
- [3] Jurman et al, Calibration and data fusion solution for the miniature attitude and heading reference system, *Sensors and Actuators A: Physical*, Vol.138, No. 2 (2007), pp.411–420.

A study of the folding umbrella stick with solar-powered LED lighting*

Zhi-Fang Xu ^{1,a}, Hsinn-Jyh Tzeng ¹

¹ Department of Mechanical Engineering, Southern Taiwan University of Science & Technology, Tainan, Taiwan

^a 4A612051@stust.edu.tw

Abstract

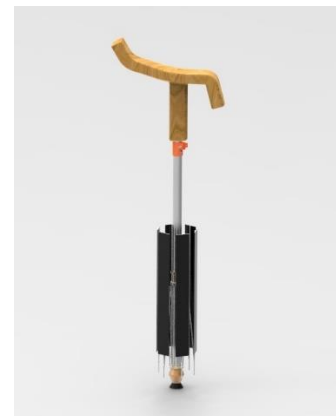
To solve the living environment of the elderly, the research aims at modifying the walk aid and ameliorate the quality of their physical activities. The core concept of research is also focus on safety, environmental protection, health, convenience and thoughtful care. In the consideration of elderly walking, a solar-powered LED folding cane umbrella is designed to combine with the functions of trekking poles and folding umbrellas. A flexible solar panel power generation mechanism is installed at the end of the umbrella surface to generate electricity from solar energy. The power is supplied with safety warning lights and GPS attached. The system takes into consideration satellite positioning, green energy, environmental protection, positioning functions, and night safety factors. Even if the elderly or demented people are lost, they can be found efficiently from their family members, relatives and friends.

Considering that the PM2.5 level in Taiwan is becoming more and more serious, the design grip part is equipped with a portable PM2.5 sensor to monitor the air quality at any time when you go out. In addition, it is with a folding function to easily carry. It also has the effect of beautifying the appearance and achieving safely away from home.

Internal components for crutch grips:



The main shape of the walking stick (folded state):



The main shape of the walking stick (expanded state):



* Poster paper presentation

Keywords

Solar-powered, LED, PM2.5

References

Mountaineering stick having warning and lighting means and capable of being dismantled and assembled rapidly, Jy-Tsair Lin, USPTO, 1992.

Walking cane, Nikolai B. Riemer, USPTO, 2013.

Illuminatable umbrella, Phyllis Carver, USPTO, 1976.

V. P. Onbattuvelli, R. K. Enneti, S. minum Nitride, Int. Journal of Refractory Metals and Hard Materials 36, pp.77-84, 2013.

W. K. You, J. P. Choi, S. M. Yoon, J. S. Lee, Low Temperature Powder Injection Molding of Iron Micro-Nano Powder Mixture, Powder Technology 228, pp.199-205, 2012.

Yanwei, Huyong, Processing Parameter Optimization for Injection Molding Products in

Agricultural Equipment Based on Orthogonal Experiments and Analysis, International Conference on Computer Distributed Control and Intelligent Environmental Monitoring, pp560-564, 2011.

M. S. Huang, H. C. Hsu, Effect of backbone polymer on properties of 316L stainless steel MIM compact, Journal of Materials Processing Technology 209, pp. 5527-5535, 2009.

Babur Ozcelik, Ibrahim Sonat "Warping and structural analysis of thin shell plastic in the plastic injection molding", Journal of Materials and Design 30, pp.367-375, 2009.

Wan, W.A., L. T. S., Abdul R. R., Injection moulding simulation analysis of natural fiber composite window frame, in journal of materials processing technology, pp.22-30, 2008.

K. M. B. Jansen, D. J. V. Dijk, M. H. Huesselman, "Effect of processing conditions on shrinkage in injection molding", Polymer Engineering and Science, Vol.38, No.5, pp.838-846, 1998.

Development of infants suits for motion measurement*

Yu Amagasaki^{1, a*}, Shigeo Yamashita², Shinichiro Morichi³, Hisashi Kawashima³,
Gaku Yamanaka³, Satoru Kizawa⁴ and Ayuko Saito^{1, b}

¹Department of Mechanical Science and Engineering, School of Advanced Engineering,
Kogakuin University, Tokyo, Japan

²nac Image Technology Inc., Tokyo, Japan

³Department of Pediatrics and Adolescent Medicine, Tokyo Medical University

⁴Department of Mechanical Engineering and Robotics, National Institute of Technology (KOSEN),
Akita College, Akita, Japan

^as518003@ns.kogakuin.ac.jp, ^bsaito@cc.kogakuin.ac.jp

Abstract

INTRODUCTION: Measuring postures and movements of infants and discovering a pattern for their typical characteristics is useful for early screening of infants at developmental risk. An optical 3D motion analysis device is widely used in human motion measurement [1][2]. The device, however, requires 30 to 40 reflective markers to be attached to the body when using the conventional motion analysis model. Therefore, an optical 3D motion analysis using the conventional motion analysis model requires a long time and is not suitable for measuring the movement of infants. Nevertheless, the optical 3D motion analysis device has the advantage of high accuracy compared with other motion measurement methods such as inertial sensors. The optical 3D motion analysis using quite very few reflective markers can be expected to be applied to the measurement of infants because reducing the number of reflective markers to be attached to the body contribute to reducing the burden on the subject. In this research, we developed a measurement suit for infants using 2D reflective stickers that could be used to measure the motion by an optical 3D motion analysis device. Since the 2D reflective stickers would not make the subject feel uncomfortable during wearing the measurement suit, it could reduce the burden on infants. We measured the movement of a healthy infant using 2D reflective stickers and conventional reflective markers. Finally, we evaluated the measurement accuracy of the suit developed by using 2D reflective stickers.

MOTION MEASUREMENT SUIT FOR INFANTS:

Fig.1 shows the motion measurement suit for infants proposed in this study. Hook and loop fasteners were attached to the surface of the suit, which enabled to attach and detach reflective stickers to fit the joint positions.



Fig.1 Motion measurement suit for infants

EXPERIMENTS

SUBJECT AND MEASURING DEVICE: A 2-year-old healthy boy participated in the experiment. Following an explanation of the purpose and requirements of the study, the participant's parent gave her written informed consent to the participation of her child in the study. Study approval was obtained from the Research Ethics Board, Kogakuin University. During the experiment, kinematic data were collected using an optical three-dimensional motion analysis device (MAC3D, MOTION ANALYSIS Co. Ltd.).

CONDITIONS: Fig. 2 shows a reflective sticker and a reflective marker. The sticker and marker positions were decided referring to the Helen Hayes marker set (Fig. 3) [3]. After starting the measurement, the infant started walking at his own timing.

* Oral paper presentation

The sampling frequency of the optical three-dimensional motion analyzer was 100 Hz.



(a) Reflective sticker



(b) Reflective marker

Fig.2 Reflective sticker and reflective marker

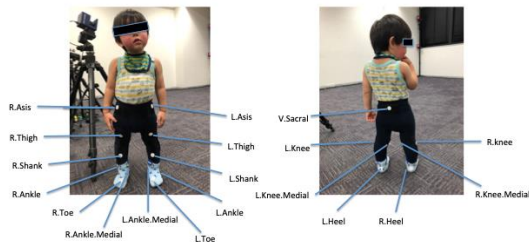
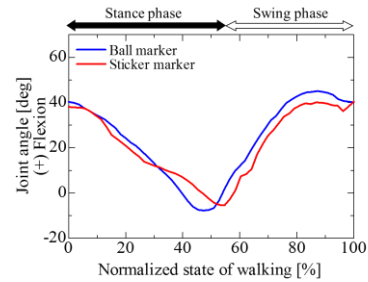


Fig.3 Marker positions

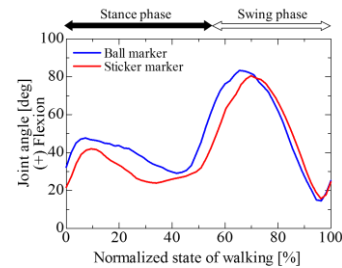
RESULTS: Fig. 4 shows the results of the lower limb joint angles. The horizontal axis shows the normalized time with one gait cycle including one stance phase and one swing phase as 100%. The vertical axes are the joint angles, in which the positive values are the hip and knee joints' flexion, and the ankle joint's dorsiflexion. The blue solid curves represent the results obtained using the conventional reflective markers, and the red solid curves represent the results obtained using the reflective stickers. The results for the knee and hip joint angles obtained using the stickers and markers were almost the same, and the same tendency was shown for the ankle joint angles.

Keywords

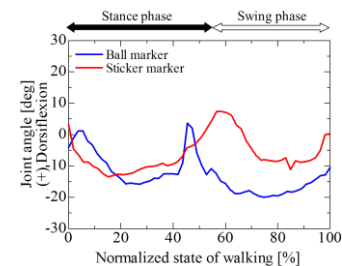
Infant, motion analysis, reflective marker, reflective sticker, suit



(a) Hip joint angles



(b) Knee joint angles



(c) Ankle joint angles

Fig.4 Results of the lower limb joint angles

References

- [1] Stief F., et al., Reliability and accuracy in three-dimensional gait analysis: A comparison of two lower body protocols, *Journal of Applied Biomechanics*, 29-1, pp.105-111, 2013.
- [2] Nazareth A., et al., Effect of Tibia Marker Placement on Kinematics in Pathological Gait, *Journal of applied biomechanics*, 32-6, pp.603-607, 2016.
- [3] Thomas, D. C. et al., A six degrees-of-freedom marker set for gait analysis: Repeatability and comparison with a modified Helen Hayes set, *Gait & Posture*, 30(2), pp.173-180, 2009.

Motion analysis of infants using musculoskeletal model*

Tomoaki Ichikawa ^{1, a*}, Shigeo Yamashita ², Shinichiro Morichi ³, Hisashi Kawashima ³,
Gaku Yamanaka ³, Yoshikazu Kobayashi ⁴, Ayuko Saito ^{1, b}

¹Department of Mechanical Science and Engineering, School of Advanced Engineering, Kogakuin University, Tokyo, Japan

² nac Image Technology Inc., Tokyo, Japan

³Department of Pediatrics & Adolescent Medicine, Tokyo Medical University, Japan

⁴Department of Mechanical Engineering and Robotics, National Institute of Technology, Akita College, Akita, Japan.

^a s518008@ns.kogakuin.ac.jp, ^b saito@cc.kogakuin.ac.jp

Abstract

INTRODUCTION: Spastic gait caused by central nervous system disease in infants is difficult to distinguish from internal rotation gait, making it difficult to detect central nervous system disease by methods other than MRI brain imaging. A safer and simpler examination method is desired because sedatives may be administered in infant examinations using MRI, and serious complications such as respiratory arrest due to administration have been reported [1]. Excessive muscle tension in the ankle plantar flexors muscles occurs at the end of the swing phase in patients with spastic hemiplegia during walking [2]. Therefore, a safer and simpler examination method for screening spastic gait is desired. In this study, we attempted to analyze the motions of infants using a musculoskeletal model as a first step to construct a method for analyzing behavior that can be used to screen for central nervous system disorders. We analyzed the tension in the muscle of the infant's lower limbs during walking using the musculoskeletal model software OpenSim. The two scaling patterns for a healthy infant model were performed in the analysis.

METHODOLOGY: A 2-year-old healthy boy participated in the experiment (height: 100 cm, weight: 12 kg). Following an explanation of the purpose and requirements of the study, the participant's parent gave her written informed consent to the participation of her child in the study. Study approval was obtained from the Research Ethics Board, Kogakuin University. During the experiment, kinematic data were

collected using an optical 3D motion analyzer (MAC3D, MOTION ANALYSIS Co. Ltd.) and a 6-axis force sensor (FFS080F102M10106IO, Leptrino Co. Ltd.). The sampling frequencies of the optical 3D motion analyzer and the 6-axis force sensor were 100 Hz. For the gait measurement, 19 reflective markers were attached to the subject's lower limbs, referring to the Helen Hayes marker set [3]. Marker positions are shown in Fig. 1. Markers attached to subject are shown in Fig. 2. The subject started walking at his own timing, after starting the measurement.

The software OpenSim3.3 [4] was used to estimate the lower limb muscle tension during walking. The model used in the analysis was Gait2392, which has 23 degrees of freedom and 92 musculotendon actuators. The two scaling patterns were performed: Pattern A, which scaled the whole body parts based on height, and Pattern B, which scaled each bone with reference to the subject's body dimensions. Then, muscle tension was calculated by Static Optimization.

RESULTS: The results for the rectus femoris muscle which is agonist for hip flexion, and the biceps femoris LH muscle which is antagonist for hip flexion, are shown in Fig. 3 and 4, respectively. The horizontal axis shows the normalized time, where one stance phase is 100%, and the vertical axis is the result of the muscle tension calculated by OpenSim. Black solid curves present results obtained using the scaling pattern A, and black dashed curves present results obtained using the scaling pattern B. Fig. 3 shows that the rectus femoris muscle tensions calculated by scaling

* Oral paper presentation

patterns A and B are both activated throughout the stance phase. In toddler gait, many lower limb muscles are generally involved and fired simultaneously. Therefore, the rectus femoris muscle that is the antagonistic muscle of the biceps femoris LH may not have developed completely.

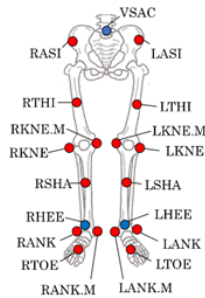


Fig. 1 Marker positions



(a) Front

(b) Back

Fig. 2 Markers attached to subject

Fig. 4 shows that the biceps femoris muscle tensions calculated by scaling patterns A and B both have the largest peak in the early stance phase. The results are similar muscle activities in adult walking. Since the development of antagonism differs from muscle to muscle to muscle [5], the results indicated that the biceps femoris muscle may have developed its antagonism earlier than the rectus femoris muscle. Focusing on the results of scaling patterns A and B, muscle tensions obtained by pattern A changed in a wide range and had a larger number of changes compared to pattern B. It is considered that infants have different proportions of body dimensions than adults. Hence, a more rigorous scaling method is required to calculate appropriate muscle tensions.

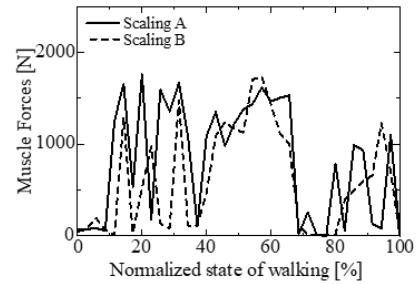


Fig. 3 Rectus femoris

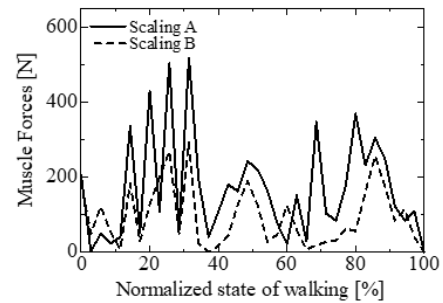


Fig. 4 Biceps femoris LH

Keywords

Infant, muscle tension, OpenSim, scaling, spastic gait

References

- [1] Katsumori, H. et al., Survey on sedation management of pediatric patients undergoing MRI examination, Journal of the Japan Pediatric Association, 117(7), pp.1167-1171, 2013(in Japanese).
- [2] Tsushima Y. et al., Association between ankle joint function and muscle activity during gait in patients with spastic hemiplegia, Rigakuryohokagaku, 34(1), pp.37-40, 2019(in Japanese).
- [3] Thomas, D. C. et al., A six degrees-of-freedom marker set for gait analysis: Repeatability and comparison with a modified Helen Hayes set, Gait & Posture, 30(2), pp.173-180, 2009.
- [4] Delp, S. L. et al., OpenSim: Open-source software to create and analyze dynamic simulations of movement, IEEE transactions on biomedical engineering, 54(11), pp.1940-1950, 2007.
- [5] Okamoto T., Gait learning in infants, Clinical Electroencephalography, 15, pp.145-154, 1980.

A study on motion measurement for early screening for neurological disease*

Tatsuro Sato ^{1, a*}, Shigeo Yamashita ², Shinichiro Morichi ³, Hisashi Kawashima ³
Gaku Yamanaka ³, Satoru Kizawa ⁴, Ayuko Saito ^{1, b}

¹Department of Mechanical Science & Engineering, School of Advanced Engineering,
Kogakuin University, Tokyo, Japan

²nac Image Technology Inc., Tokyo, Japan

³Department of Pediatrics & Adolescent Medicine, Tokyo Medical University, Japan

⁴Department of Mechanical Engineering & Robotics, National Institute of Technology,
Akita College, Japan.

^as518025@ns.kogakuin.ac.jp, ^bsaito@cc.kogakuin.ac.jp

Abstract

Movement disorders in pediatric patients with cerebral palsy would change due to growing up. Cerebral palsy is occasionally diagnosed by detecting gait abnormalities [1]. Evaluation of gait abnormalities including spastic gait from the viewpoints of kinematics and kinetics enables to determine the presence or absence of disease [2]. However, spastic gait caused by central nervous system diseases in infants is not easy to distinguish from internal rotation gait. A simple motion measurement that detects the characteristics of spastic gait can provide more children early screening of diseases.

Therefore, in this study, we caused a humanoid robot that was driven by servomotors to reproduce the characteristic motion of lower limb joints in the spastic gait. We developed an analytical method that could relatively easily extract the characteristics of spastic gait using the information obtained from the robot's motion measurement. Specifically, the characteristics of spastic gait were obtained from the trajectory of a small number of reflective markers attached to

the robot. The proposed method is useful for giving opportunities for screening for children with central nervous system diseases and is expected to contribute to early treatment.

METHODOLOGY: The humanoid robot (JD Humanoid, EZ-Robot Inc.) was used in the experiment. The robot motion was measured using a three-dimensional optical motion analysis

device (MAC3D System, MOTION ANALYSIS Inc.).

Fig. 1 shows the reflective marker positions. The markers were attached to the shoulder, upper arm, and forearm of the robot. In the experiment, the shoulder joint and elbow joint of the robot were treated as human knee joint and ankle joint (Fig. 2). The robot reproduced the joint movements in the normal gait and spastic gait shown in Fig. 3 by referring to the previous study [3]. The knee joint angle and ankle joint angle of the sagittal surface in spastic gait of paralyzed patients were reproduced. The horizontal axis in Fig. 3 shows the normalized time, where one gait cycle including a stance phase and swing phase is 100%. The black solid curves show motions in the normal gait, and the red solid curves show motions in the spastic gait of patients with hemiplegia. The sampling frequency of the three-dimensional optical motion analysis device was 100 Hz.

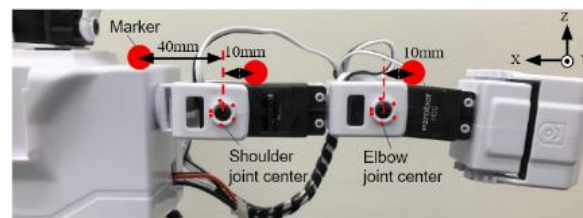


Fig.1 Reflective marker positions and laboratory coordinate system.

* Oral paper presentation

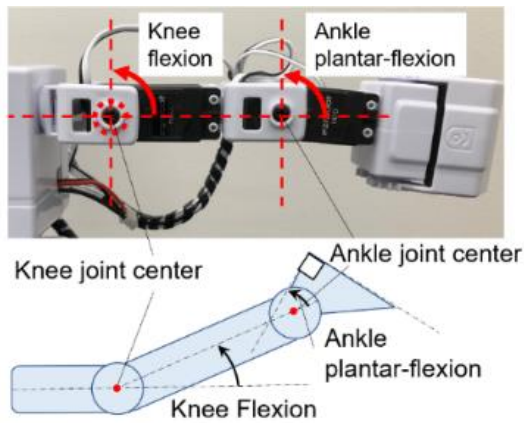
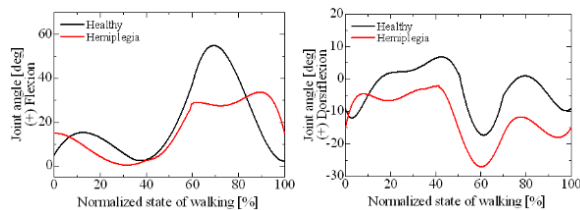


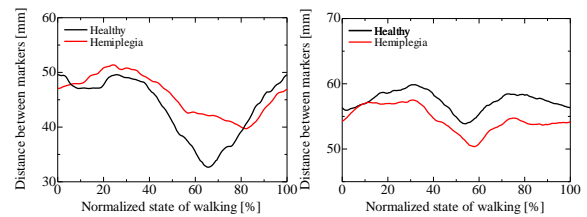
Fig. 2. Correspondence between robot and human lower limb joints.



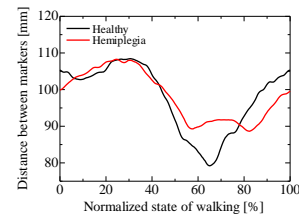
(a) Knee joint angles (b) Ankle joint angles

Fig. 3. Joint angles reproduced by the robot.

RESULTS: Fig. 4 shows the results of time series changes of the distances between markers. Fig. 5 (a) shows the distances between the robot's shoulder marker and upper arm marker, Fig. 5 (b) shows the distances between the upper arm marker and the forearm marker, and Fig. 5 (c) shows the distances between the forearm marker and the shoulder marker. The horizontal axis shows the normalized time, where one gait cycle including a stance phase and swing phase is 100%. The black solid curves show motions in the normal gait, and the red solid curves show motions in the spastic gait of patients with hemiplegia. The results indicate that the variation in the distance of the pelvis marker and the tibia marker, and the pelvis marker, and the foot marker may be significantly different between normal gait and spastic gait. Fig. 5 shows the trajectory of the midpoint between the markers. From the result, the trajectory of the midpoint between markers obtained from the spastic gait data has a shorter range than that obtained from the normal gait data, although the shapes of the trajectories of the midpoints between markers of the two types gait data are similar.



(a) Shoulder and upper arm (b) Upper and lower arm



(c) Lower arm and shoulder

Fig. 4 Time-series changes between markers.

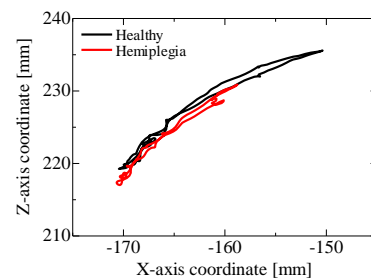


Fig. 5 Locus of the midpoint between markers.

Keywords

Cerebral palsy, motion measurement, neurological disease, robot, spastic gait

References

- [1] Nakajima M. et al., Developmental changes in the Collis horizontal reaction analyzed using a three-dimensional video motion analysis system, Japanese society of child neurology, 37(6), pp. 479-485, 2005 (in Japanese).
- [2] Suzuki E. et al., Evaluation on spastic gait caused by cervical myelopathy with gait analysis, Proceedings of Annual Meeting of Japanese Society for Clinical Biomechanics and Related Research, 23, pp. 447-451, 2002 (in Japanese).
- [3] Yanagizono, T. Pediatric abnormal gait by gait analysis, MB Medical Rehabilitation, 156, pp. 15-23, 2013 (in Japanese).

Experiment on selecting evaluation words for sensory evaluation of beautiful gait*

Shogo Takeuchi ^{1, a, *}, Jun Muramatsu ¹, Masaki Tamura ², Ayuko Saito ^{1, b}

¹ Department of Mechanical Science & Engineering, School of Advanced Engineering, Kogakuin University, Tokyo, Japan

² Department of Architecture, School of Architecture, Kogakuin University, Tokyo, Japan

^a 518037@ns.kogakuin.ac.jp, ^b saito@cc.kogakuin.ac.jp

Abstract

INTRODUCTION: "Beautiful gait"[1] which is an elegant walk with correct posture has been popular mainly among women. In addition to the exercise effect during walking, a beautiful gait has the effect of improving mental health by being seen to be beautiful by others. Therefore, it can be expected to be accepted by many people as an exercise style that supports physical and mental health. However, the standard of beauty is not definite. Therefore, in this study, as the first step to clarify the relation between biomechanical factors, such as joint angles and joint moments, during walking [2] and psychological factors when a person evaluates beauty, we examined the evaluation criteria of "beautiful" for "beautiful gait" by deriving the correlation coefficient[3] between the evaluation words that the evaluators who watched "beautiful gait" answered in the questionnaire.

METHODOLOGY: We collected about 400 adjectives with reference to the literature [1] and dictionaries on "beautiful gait." Seven participants evaluated whether the collected adjectives were appropriate for evaluating "beautiful gait" using three choices (1: Applicable 2: Neither 3: Not applicable). Then, the number of selected adjectives were narrowed down from about 400 words to 146 words by deleting adjectives with an average evaluation score of 2.5 or higher. Furthermore, 146 adjectives were separated into 13 groups. The adjectives belonging to the same group had similar meanings. An adjective with the lowest evaluation score in each group was used as the representative word. We excluded the adjectives such as "Dirty" and "Hard" which were

not appropriate words to evaluate "beautiful gait" from the 13 representative words. In addition, we added "Like", "Fast", and "Wide stride" as evaluation words. "Like" indicates a personal preference. "Fast" and "Wide stride" indicate physical quantities. Finally, the thirteen words including "Like", "Beautiful", "Couth", "Fast", "Wide stride", "Sharp", "Bright", "Gentle", "Stable", "Without strain", "Soft", "Calm," and "Elegant" were selected. We decided the antonyms on the selected 13 words and constructed each evaluation word pair.

We asked 34 evaluators including men and women to watch the video [4] of "beautiful gait" and conducted a questionnaire survey on the "beautiful gait" using the selected evaluation words. The evaluators answered 1 to 5 for each evaluation word (1: Very XXX 2: Slightly XXX 3: Neither 4: Slightly ○○○ 5: Very ○○○). Fig.1 shows the evaluation sheet used in the experiment.

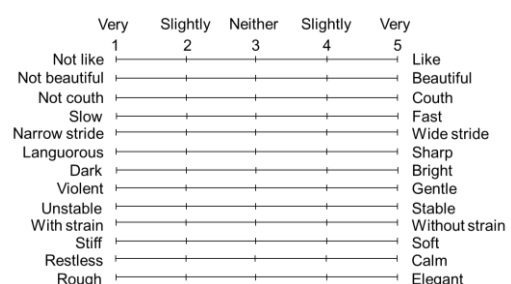


Fig.1 Evaluation sheet

RESULTS: Fig. 2 shows the boxplot of questionnaire results. The average value for all evaluation words was 3.49. We assumed that 3.8 or more was a high valuation and less than 3.0 was a low valuation. The evaluation words with an average value of 3.8 or more were "Beautiful",

* Oral paper presentation

"Couth", "Bright", and "Elegant". The differences between the averages and medians of these four words were less than 0.5. In addition, the standard deviations of "Beautiful", "Bright", and "Elegant" were less than 1.0. The results indicate that most of the evaluators felt "Beautiful", "Bright", and "Elegant" when they watched the beautiful gait video.

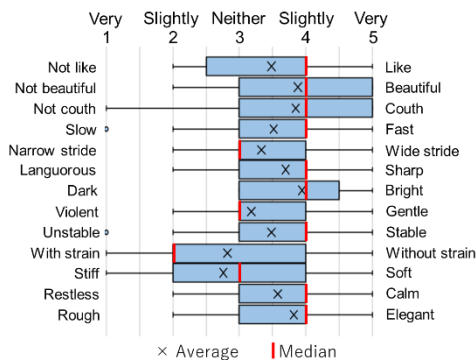


Fig.2 Boxplot of questionnaire results

Table 1 shows the correlation coefficients between evaluation words. Focusing on the results having correlation coefficients of 0.6 or more, there were positive correlations between "Beautiful" and "Like", "Couth", "Stable", "Calm". Because the differences between the averages and medians of "Beautiful" and "Calm" were less than 0.5 and their deviations were less than 1.0, most of the evaluators might have felt "Beautiful" at the same time as they felt "Calm". There were positive correlations between "Like" and "Couth", "Stable". There were also positive correlations between

"Couth" and "Stable". Although not all the evaluators felt "Like" and "Stable" when they felt "Couth", the result suggests that "Like" and "Stable" might be closely related to "Couth".

CONCLUSION: In this study, we concluded that "Like", "Couth", "Stable", and "Calm" are related to "Beautiful". We will verify what postures and movements are related to "Like", "Couth", "Stable", and "Calm" in terms of biomechanical factors in future work.

Keywords

Adjectives, beautiful, correlation coefficient, gait, health

References

- [1] Kobayashi K., The most beautiful and correct gait in the world, Japanese society of child neurology, NIHONBUNGEISHA Co.,Ltd., 2018 (in Japanese).
- [2] Yamasaki A., Gait biomechanics (1) Kinematics and biomechanics of normal gait, The Japanese Journal of Physical Therapy, 47(5), pp. 429-437, 2013 (in Japanese).
- [3] Soeta Y. et al., Effects of temperature of oshibori on kansei evaluation:- Investigation over four seasons (Differences of room temperature and sexual specificity), Transactions of Japan Society of Kansei Engineering, 13(1), pp. 239-245, 2014 (in Japanese).
- [4] <https://www.youtube.com/watch?v=wTjVHHCy7T4>

Table 1. Correlation coefficients between the evaluation words

| | Like | Beautifu l | Cout h | Fast | Wide strid e | Shar p | Bright | Gentl e | Stabl e | Withou t strain | Soft | Cal m | Elegan t |
|----------------|-----------|---------------|-----------|-----------|--------------------|-----------|--------|------------|------------|--------------------|-----------|----------|-------------|
| Like | 1 | - | - | - | - | - | - | - | - | - | - | - | - |
| Beautiful | 0.67 1 | 1 | - | - | - | - | - | - | - | - | - | - | - |
| Couth | 0.68 3 | 0.667 | 1 | - | - | - | - | - | - | - | - | - | - |
| Fast | 0.23 8 | 0.432 | 0.294 | 1 | - | - | - | - | - | - | - | - | - |
| Wide stride | 0.38 6 | 0.545 | 0.375 | 0.62 8 | 1 | - | - | - | - | - | - | - | - |
| Sharp | 0.49 4 | 0.397 | 0.177 | 0.30 3 | 0.256 | 1 | - | - | - | - | - | - | - |
| Bright | 0.39 2 | 0.381 | 0.256 | 0.35 3 | 0.151 | 0.587 | 1 | - | - | - | - | - | - |
| Gentle | 0.38 7 | 0.345 | 0.402 | 0.24 2 | 0.509 | 0.263 | 0.290 | 1 | - | - | - | - | - |
| Stable | 0.73 2 | 0.772 | 0.639 | 0.43 7 | 0.570 | 0.383 | 0.228 | 0.470 | 1 | - | - | - | - |
| Without strain | 0.62 8 | 0.545 | 0.498 | 0.25 0 | 0.386 | 0.356 | 0.367 | 0.706 | 0.612 | 1 | - | - | - |
| Soft | 0.34 7 | 0.250 | 0.214 | 0.19 6 | 0.386 | 0.349 | 0.268 | 0.333 | 0.314 | 0.628 | 1 | - | - |
| Calm | 0.46 3 | 0.660 | 0.568 | 0.19 5 | 0.452 | 0.097 | 0.299 | 0.563 | 0.622 | 0.708 | 0.41 5 | 1 | - |
| Elegant | 0.30 9 | 0.395 | 0.510 | 0.35 8 | 0.351 | 0.217 | 0.279 | 0.286 | 0.267 | 0.333 | 0.20 6 | 0.423 | 1 |

Reducing bias and improving contrast of parametric images in positron emission tomography*

Paulus Kapundja Shigwedha ^{1,a*}, Takahiro Yamada ², Kohei Hanaoka ², Kazunari Ishii ^{2,3},
Yuichi Kimura ⁴, Yutaka Fukuoka ¹

¹Dept. of Electrical Eng. & Electronics, Graduate School of Eng., Kogakuin University, Tokyo, Japan

²Div. of Positron Emission Tomography, Inst. of Adv. Clinical Medicine, Kindai University, Osaka, Japan

³Dept. of Radiology, Faculty of Medicine, Kindai University, Osakasayama, Osaka, Japan

⁴Dept. of Computational Systems Biology, Kindai University, Wakayama, Japan

^acd18001@g.kogakuin.jp

Abstract

Logan graphical analysis (LGA) [1,2] is a method for analyzing positron emission tomography (PET) data. LGA linearize PET data, and the slope of the resulting linear relationship, is a physiological quantity, distribution volume ratio (DVR), which quantifies receptor availability. LGA suffers from the effects of noise in PET data, which causes an underestimation of DVR [3,4,5]. Various studies have been conducted to reduce the bias in DVR estimates. However, these methods have been found to reduce the bias while increasing the variance in the estimates [3,5]. Earlier, we employed a different linear regression method called least-squares cubic (LSC) [6], to estimate the LGA slope. LSC was shown to reduce the bias in LGA estimates [7]. However, LSC estimates also showed slightly increased variances compared to OLS estimates [7]. Increased variance may hinder image contrast. In this study, we combined LSC with principal component analysis (PCA) denoising technique to reduce the variance in LSC-based DVR estimates in order to improve the quality of parametric images, measured as the contrast between gray and white matter. PCA has been previously used for PET data denoising, in which one particular finding — which is of interest to this study — was variance reduction [8]. The number of principal components used to denoise the data were set to account for 97% of variance in the data. We denote the LSC and PCA combination as LSC-PCA. LSC-PCA was evaluated for both simulation and clinical data, against LSC-, and OLS-based LGA.

Simulation results in Fig. 1 shows that LSC-PCA has reduced the variance in DVR estimates, in comparison to LSC estimates.

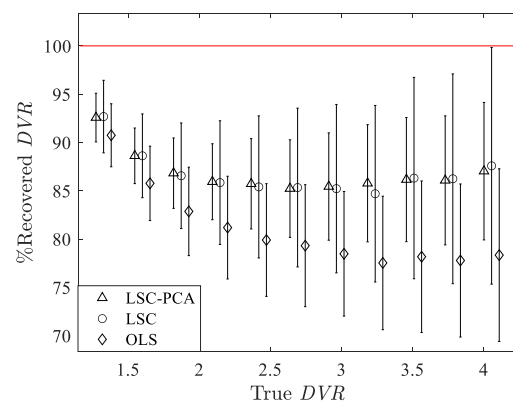


Fig. 1. Percentage recovered of the average DVR values estimated from noisy tTACs using LSC-PCA, LSC, and OLS. The error bars denote standard deviations.

Clinical data results showed LSC-PCA to have significantly (p value < 0.05 , compared to LSC) improved the contrast between gray and white matter. As expected, LSC-PCA DVR images also showed reduced variances across voxels, compared to both LSC and OLS images, enabling better contrasting between brain regions. In conclusion, LSC-PCA reduced the variance in DVR estimates, in turn improving the contrast of parametric images. These findings will contribute to improved interpretability of in-vivo receptor analysis.

* Poster paper presentation

Keywords

Positron emission tomography, distribution volume ratio, least-squares cubic, principal component analysis

References

- [1] J. Logan, J. S. Fowler, N. D. Volkow, A. P. Wolf, S. L. Dewey, D. J. Schlyer, R. R. MacGregor, R. Hitzemann, B. Bendriem, S. J. Gatley and D. R. Christman, "Graphical Analysis of Reversible Radioligand Binding from Time—Activity Measurements Applied to [N-11C-Methyl]-(-)-Cocaine PET Studies in Human Subjects," *Journal of Cerebral Blood Flow & Metabolism*, vol. 10, no. 5, pp. 740-747, 1990.
- [2] J. Logan, J. S. Fowler, N. D. Volkow, G.-J. Wang, Y.-S. Ding and D. L. Alexoff, "Distribution volume ratios without blood sampling from graphical analysis of PET data," *Journal of Cerebral Blood Flow & Metabolism*, vol. 16, no. 5, pp. 834-840, 1996.
- [3] Y. Kimura, M. Naganawa, M. Shidahara, Y. Ikoma and H. Watabe, "PET kinetic analysis—Pitfalls and a solution for the Logan plot," *Annals of nuclear medicine*, vol. 21, no. 1, pp. 1-8, 2007.
- [4] M. Slifstein and M. Laruelle, "Effects of statistical noise on graphic analysis of PET neuroreceptor studies," *Journal of Nuclear Medicine*, vol. 41, no. 12, pp. 2083-2088, 2000.
- [5] J. Logan, "A review of graphical methods for tracer studies and strategies to reduce bias," *Nuclear medicine and biology*, vol. 30, no. 8, pp. 833-844, 2003.
- [6] D. York, N. M. Evensen, M. L. Martinez and J. De Basabe Delgado, "Unified equations for the slope, intercept, and standard errors of the best straight line," *American Journal of Physics*, vol. 72, no. 3, pp. 367-375, 2004.
- [7] P. K. Shigwedha, T. Yamada, K. Hanaoka, K. Ishii, Y. Kimura and Y. Fukuoka, "A strategy to account for noise in the X-variable to reduce underestimation in Logan graphical analysis for quantifying receptor density in positron emission tomography," *BMC medical imaging*, vol. 20, no. 1, pp. 1-8, 2020.
- [8] A. Joshi, J. A. Fessler and R. A. Koeppe, "Improving PET receptor binding estimates from Logan plots using principal component analysis," *Journal of Cerebral Blood Flow & Metabolism*, vol. 28, no. 4, pp. 852--865, 2008.
- [9] J. Logan, J. S. Fowler, N. D. Volkow, Y. S. Ding, G.-J. Wang and D. L. Alexoff, "A strategy for removing the bias in the graphical analysis method," *Journal of Cerebral Blood Flow & Metabolism*, vol. 21, no. 3, pp. 307-320, 2001.
- [10] M. Ichise, J.-S. Liow, J.-Q. Lu, A. Takano, K. Model, H. Toyama, T. Suhara, K. Suzuki, R. B. Innis and R. E. Carson, "Linearized reference tissue parametric imaging methods: application to 11C DASB positron emission tomography studies of the serotonin transporter in human brain," *Journal of Cerebral Blood Flow & Metabolism*, vol. 23, no. 9, pp. 1096-1112, 2003.

A study on the view factor in sensory evaluation of human movement*

Jun Muramatsu ^{1,a*}, Shogo Takeuchi ¹, Ayuko Saito ^{1,b}

¹ Dept. of Mechanical Sci. & Eng., School of Advanced Engineering, Kogakuin University, Tokyo, Japan

^a s518063@ns.kogakuin.ac.jp, ^b saito@cc.kogakuin.ac.jp

Abstract

Introduction

Movements that fascinate people such as traditional dance and figure skating include "elements of beauty" which are expressed by multiple adjectives, for instance, "supple" and "elegant". Because elements that are perceived as beautiful in the movements are based on personal sensibility, clarifying "elements of beauty" quantitatively requires analyzing the cognitive structure of individuals who perceived beautiful and why they evaluated as beautiful.

An element of beauty is involved in human movements which are expressed by kinematic data such as joint angles and joint moments [1]. However, the appearance, clothes, and background of a person who performs movements may affect the viewers' evaluation criteria. This study examined the influence of the background in the evaluation of human movements as a first step to indicate a relation between kinematic data and evaluation words such as beautiful. We clarified the influence of the background on the psychology of the evaluator when they evaluated human movements by performing factor analysis on the results of the questionnaire.

Methodology

We prepared two types of videos in which the same person walked at the same walking speed with the same stride (Fig. 1). The background of video A was downtown and that of video B was nature. The time length of each video was about 10 seconds. 30 people including men and women participated in the questionnaire survey.

We selected the appropriate evaluation words for the evaluation of pedestrian movements and background to create the questionnaire items. Six

evaluation words including "Fast", "Calm", "Monotonous", "Cheerful", "Gentle", and "Soft" were selected to evaluate the movements. The evaluation words related to the background were eight words "Like", "Beautiful", "Bright", "Quiet", "Relieved", "Natural", "Calm", and "Friendly"[3]. This study used the SD method. Therefore, we prepared the antonyms on the selected 14 words and created each evaluation word pair.

Thirty people including men and women participated in the questionnaire survey. The participants watched the two videos and answered the questionnaire. They answered 1 to 4 for each evaluation word (1: Very XX, 2: Slightly XX, 3: Slightly OO, 4: Very OO) [2].



Fig.1. Two types of videos

Factor analysis

Table 1 shows the results of factor analysis. The evaluation words, which had factor loadings of more than 0.5 in factor 3 of video A (contribution rate 11%) and factor 1 of video B (contribution rate 22%), were only related to the background. We

* Oral paper presentation

have determined that these two factors were related to the evaluation of the background. Because the contribution rate of factor 1 of video B is twice that of factor 3 of video A, the evaluators might have been more interested in the background of video B than that of video A. This results indicate that the evaluator might not have been interested in the familiar scenery of Video A and might have concentrated on watching the pedestrian. On one hand, we have determined the evaluators might have mainly looked at the background as they were interested in the natural scenery of video B.

Both factor 1 of video A (contribution rate 19%) and factor 2 of video B (contribution rate 17%) include "calm" and "monotonous" which are the evaluation words of the movement, and "calm" which is the evaluation word of the background. This results indicate that the evaluators might evaluate the movement as "monotonous" and "calm" when they watched the calm background.

Conclusion

This study examined the influence of the background in the evaluation of human movements. The results indicated that the

evaluator's impression of the movement might change when they would be interested in the background. It is necessary to use the background in which the evaluators would not show strong interest when examining the influence of the background in the evaluation of human movement.

Keywords

Background, cognitive structure, factor analysis, movement, sensory

References

- [1] A. Yamasaki, Gait biomechanics (1) Kinematics and biomechanics of normal gait, The Japanese Journal of Physical Therapy, 47(5), pp. 429-437, 2013 (in Japanese).
- [2] Y. Soeta et al., Effects of temperature of oshibori on kansei evaluation:- Investigation over four seasons (Differences of room temperature and sexual specificity), Transactions of Japan Society of Kansei Engineering, 13(1), pp. 239-245, 2014 (in Japanese).
- [3] I. Shinmura, Kojien, Iwanami Shoten, Publishers, 2008.

Table 1 Results of factor analysis

| Evaluation words | Factor1 | | Factor2 | | Factor3 | |
|-----------------------|---------|--------|---------|--------|---------|--------|
| | A | B | A | B | A | B |
| Movement: Fast | -0.196 | -0.522 | -0.059 | 0.183 | 0.026 | 0.308 |
| Movement: Calm | 0.747 | 0.132 | 0.231 | 0.618 | 0.158 | -0.095 |
| Movement: Monotonous | 0.742 | -0.194 | -0.055 | 0.728 | 0.150 | -0.030 |
| Movement: Cheerful | -0.524 | -0.473 | 0.231 | -0.087 | 0.169 | 0.718 |
| Movement: Gentle | 0.780 | -0.004 | 0.066 | 0.765 | -0.067 | -0.202 |
| Movement: Soft | -0.057 | -0.058 | 0.575 | 0.298 | 0.023 | -0.077 |
| Background: Like | -0.027 | 0.465 | 0.142 | 0.445 | 0.722 | 0.413 |
| Background: Beautiful | 0.133 | 0.273 | -0.039 | -0.227 | 0.334 | 0.872 |
| Background: Bright | -0.336 | -0.042 | -0.060 | -0.184 | 0.665 | 0.669 |
| Background: Quiet | 0.098 | 0.667 | 0.707 | -0.183 | -0.176 | -0.062 |
| Background: Relieved | 0.507 | 0.490 | 0.236 | 0.010 | 0.347 | 0.018 |
| Background: Natural | 0.139 | 0.929 | 0.542 | -0.043 | 0.510 | 0.075 |
| Background: Calm | 0.494 | 0.601 | 0.519 | 0.526 | -0.024 | 0.095 |
| Background: Friendly | 0.124 | 0.624 | 0.740 | 0.482 | 0.332 | 0.031 |

Technical Presentations

Information & Communications Technology

| | | |
|---------------------|---|--|
| Moderator | : | Prof. Jaderick P. Pabico |
| Panelists | : | aProf Annie Liza C. Pintor, Dr. Maria Art Antonette D. Clariño, Engr. Lorwin Felimar B. Torrizo |
| Technical Assistant | : | Ms. Mary Jane F. Gallardo |
| 01:30PM – 01:35PM | Welcome Remarks and Introduction of Panel Members | |
| 01:35PM – 01:50PM | Enhancement of Network Infrastructure for security and communication at Danang General Hospital | <u>Quang Long Bui*</u> , Anh Nghia Bui, Ngoc Hung Le (DUT) |
| 01:50PM – 02:05PM | A Research on New Type of Local Information Dissemination System (D-ZEV System) | <u>Hodaka Tokita*</u> , Yusuke Nakajima (KUTE) |
| 02:05PM – 02:20PM | Tx Power Optimization of Pico-eNB for Multiband Heterogeneous Mobile Networks | <u>Ayumi Yoneyama*</u> , Fumiya Kemmochi, Hiroyuki Otsuka (KUTE) |
| 02:20PM – 02:35PM | Transmission Performance against Subcarrier Spacing of OFDM in Multipath Fading Channels | <u>Daisuke Kosuge*</u> , Hiroyuki Otsuka (KUTE) |
| 02:35PM – 02:50PM | Performance of Adaptive Control CRE in Multi-band Heterogeneous Mobile Networks | <u>Kento Fujisawa*</u> , Hiroyuki Otsuka (KUTE) |
| 02:50PM – 03:05PM | Field and Virtual Assessment for Recurring Hurricane Reconnaissance in U.S. Gulf Coast | <u>Do Quang-Trung*</u> (DUT) |
| 03:05PM – 03:20PM | Heterogeneous Mobile Networks Using Millimeter Wave with Three-dimensional Beamforming | <u>Fumiya Kemmochi*</u> , Hiroyuki Otsuka (KUTE) |
| 03:20PM – 03:35PM | A Study on Dynamic Path Establishment Method using Superposition Coding in EON | <u>Hiroyasu Sato*</u> , Ken-ichi Baba (KUTE) |
| 03:35PM – 03:50PM | User Throughput Improvement by Three-dimensional Beamforming in Mobile Systems | <u>Yuji Omura*</u> , Hiroyuki Otsuka (KUTE) |
| 03:50PM – 04:05PM | Telemedicine using TVWS Technology for Rural Consultations in the Philippines | Aaron Raymond See, Jolo Gerald Miel Tolentino, <u>Welsey Daniel Advincula*</u> , Chun-Ping Hsieh, Renann Baldovino, Nilo Bugtai (STUST) |

A research on new type of local information dissemination system (D-ZEV System)*

Hodaka Tokita ^{1,a}, Yusuke Nakajima ^{2,b}

¹ Graduate Student, Kogakuin University, Tokyo, Japan

² School of Architecture, Kogakuin University, Tokyo, Japan

^a dm20037@ns.kogakuin.ac.jp, ^b yusuke@cc.kogakuin.ac.jp

Abstract

INTRODUCTION: Around large railway station areas, after a disaster or other emergency, it is important to quickly collect damage information around the station and to properly guide the many people who are staying in the area. It is additionally considered that the construction of a system that collects that information and transmits it is necessary. Furthermore, previous research has shown that such a system must be utilized during times of normalcy for them to be applicable at the time of emergency. The quality of the lighting and air conditioning of the access point environments in evacuation shelters and emergency sheltering facilities decreases owing to their malfunction during power outages, and thus, improvements are deemed necessary. The present study develops a system that rapidly and accurately collects real-time information and transmits it at the time of emergency, and this information is transmitted to regions where such a system is not present as a pre-existing tool during normal times. Furthermore, this year, we conducted surveys on the current status of the energy and thermal environments in buildings designated as emergency sheltering facilities for the objective of improving the latter, and we built an environmental / disaster-prevention information system that incorporates these surveys.

D-ZEV SYSTEM: The collection and transmission of disaster information, admission of local residents and travelers having trouble returning home, and emergency rescue are important issues at local disaster prevention centers (e.g., evacuation shelters and emergency sheltering facilities) during a disaster. Therefore, we built an information transmission system based on the "Disaster-robust Zero Energy Vehicle" (D-ZEV); this system rapidly reaches local disaster prevention centers at the time of a disaster while providing information transmission, minimum energy supply, and emergency rescue support.

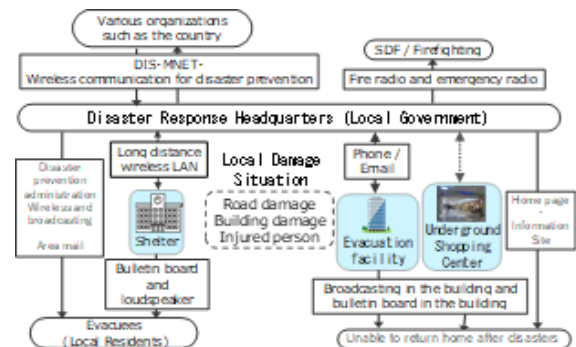


Fig. 1. Current information transmission system

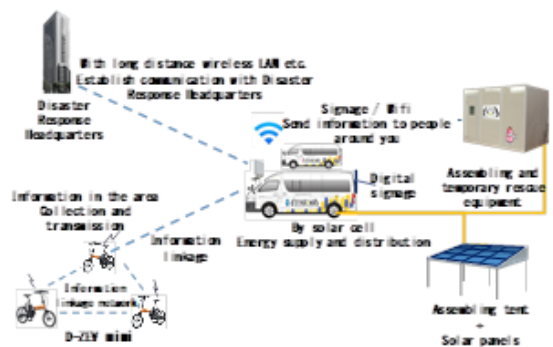


Fig. 2. D-ZEV system

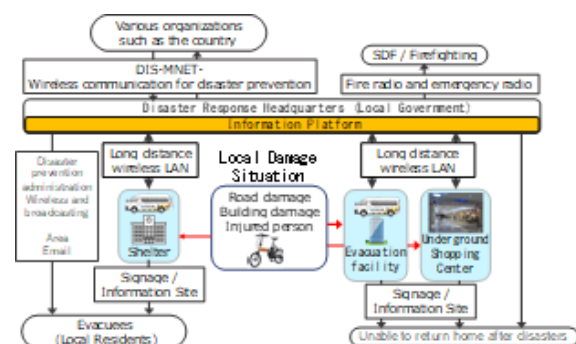


Fig. 3. Environmental and disaster prevention information system including D-ZEV system

* Oral paper presentation

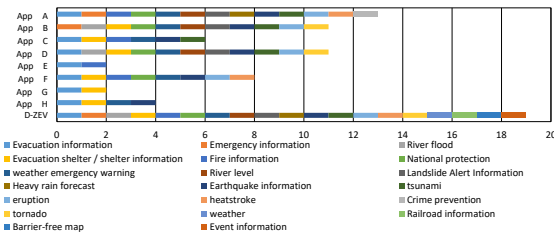


Fig. 4 Comparison with existing apps

URBAN RENAISSANCE SAFETY SECURITY PLAN AND ITS IMPLEMENTATION BY THE LOCAL GOVERNMENTS: 25 local governments developing the Urban Renaissance Safety Security Plans. This plan is requested by the government to be created in the area around the station, which is presumed to have many evacuee those who have given up on returning home. Questionnaire surveys were conducted to understand the current status of plan implementation. As a result, the introduction of information transmission means to residents around stations has not progressed during power outages and non-power outages.

CURRENT STATUS OF ENERGY AND INFORMATION TRANSMISSION MEANS FOR EVACUATION FACILITIES: We conducted a survey of local governments for building managers who have agreed to an urban renaissance security plan. Of the 263 copies, 83 were answered. As a result, it was found that many facilities have emergency generators installed in the basement and lower floors, and few facilities distribute surplus energy to other facilities in the event of a power outage.

VARIOUS SURVEYS AROUND SHINJUKU STATION: About energy, given the current scenario where municipalities do not know the capacity of emergency generators in each emergency shelter, it may be important to understand the energy sources available in the event of a disaster. Therefore, referring to the data from the Tokyo Fire Department, we mapped the emergency generator near Shinjuku Station and the storage battery equipment (not under the jurisdiction of the Fire Service Act). Many buildings without emergency generators were also exhibited. It is shown in Fig. 5.

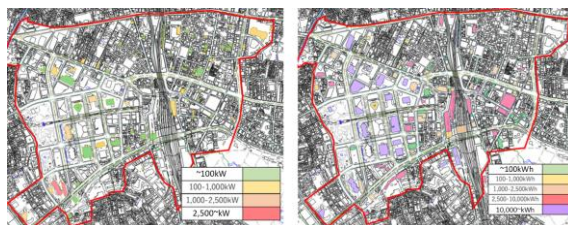


Fig 5. Emergency generator and storage battery equipment

Regarding the visualization of the summer thermal environment, the local government is conducting evacuation guidance without knowing the air conditioning equipment, and information on the summer outdoor thermal environment is indispensable. Regarding the thermal environment in the immediate vicinity of the building designated as an emergency evacuation facility in the event of a disaster, the indoor and outdoor measurement results at 1:00 pm show that the air conditioning temperature fluctuates depending on the building. Despite the air conditioning, there is not much difference in temperature between indoors and outdoors.



Fig 6. Thermal environment map at 13:00 on August 7, 2019

DEMONSTRATION SURVEY OF D-ZEV SYSTEM: In November 2019, a demonstration survey on D-ZEV systems was conducted. In the overall D-ZEV system, more than 90% of the positive. In the free description, many voices demanded the "immediateness and accuracy of information", and voices such as "damage information such as power outages at the time of disaster" and "Worrying that you may not be able to operate in a situation where there are few operators" were also mentioned.

CONCLUSION: From the results of this survey, it is clear that many evacuation facilities lack energy such as air conditioning in the event of a power outage and lighting of power receiving devices, and an information system for promptly transmitting information on evacuation facilities has not been established. became. The results of the thermal environment survey around Shinjuku Station also confirmed that there are differences in air conditioning temperature depending on the facility. A questionnaire on the D-ZEV system confirmed the need. In the future, we plan to conduct an interview survey on the contents of the "D-ZEV system" of local governments and make further improvements.

Keywords

Local information dissemination system; evacuation center; evacuee

Enhancement of network infrastructure for security and communication at Danang General Hospital*

Quang Long Bui ^{1, a}, Anh Nghia Bui ^{1, b}, Ngoc Hung Le ^{1, c}

¹Faculty of Advanced of Science and Technology, University of Danang-University of Science and Technology, Vietnam

^a quanglongbui153@gmail.com, ^b banhnghia234@gmail.com, ^c lengochung299@gmail.com

Abstract

Currently, the state of network infrastructure and information storage servers has been built for a long time. Hence, the devices as well as the operating system have become outdated, so during the process of operation will have problems, which will endanger the communication at the hospital. In addition, techniques and physical devices that have been designed and implemented in hospitals have many problems in securing the network and also have not been deployed synchronously, which are critical in critical places like hospitals. Improving the network infrastructure here, therefore, is one of the most important things in the current situation of COVID-19 translation.

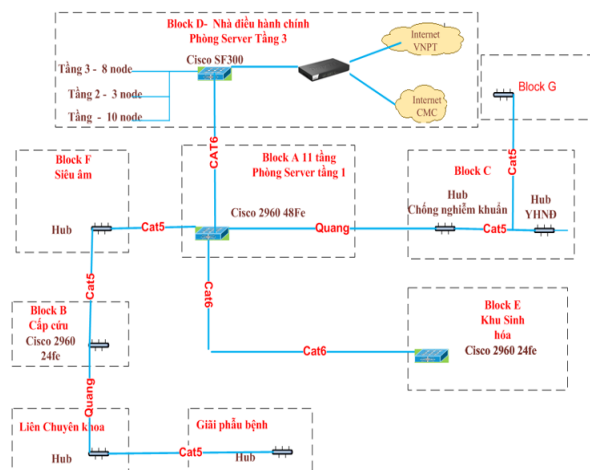


Fig. 1. Previous network infrastructure at Da Nang General Hospital

TESTING, DEPLOYING AND EVALUATION THE UPGRADE INFRASTRUCTURE

1. Testing and Deployment

The software which has been used and tested are VMware Workstation for creating the Virtual

Servers, OSs and EVE-NG for creating network infrastructure which supports a huge vendor's devices and firewall devices. In this study, the system has been upgraded with a CISCO which is the largest brand of network devices.

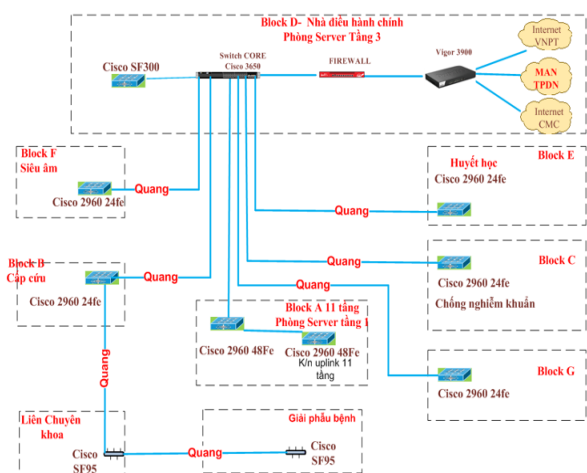


Fig. 2. Topology of upgrading network system at the Danang General Hospital

The system has been upgraded with a core switch, which is a centralized device to manage separate VLANs for departments. In addition, this device is capable of controlling traffic, entering and leaving between the hospital ward areas, preventing unauthorized access. Another important upgrade is the deployment of a firewall between the intranet and the internet so that it can control access and protect LAN. The system has been added to a server system to monitor the status of devices. The system is capable of sending warnings to the administrator in case of equipment or infrastructure problems.

2. Evaluation

Because the system has been updated from the old system, there will still be problems while the

* Oral paper presentation

system is working. Therefore, it is important to conduct performance evaluation of the system.

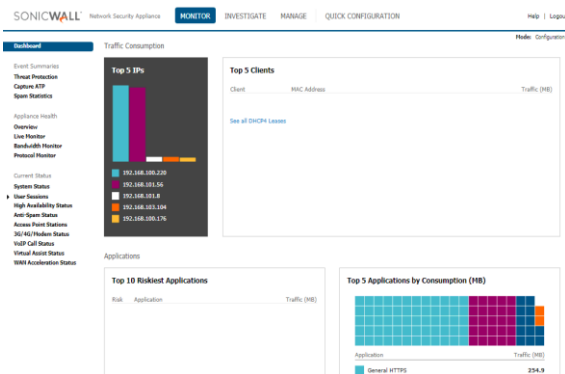


Fig. 3. Monitoring network activities users from LAN to the internet

Testing and evaluating the system based on the above mentioned factors which are connectivity, reliability, stability and security. Monitoring the user's external networking activity can be controlled through the firewall device. It is clear that the administrator can be monitored IP addresses that access the internet as well as the destination addresses that users access. This helps to control the internet access of users on the local network more closely and thus ensures better safety than before.

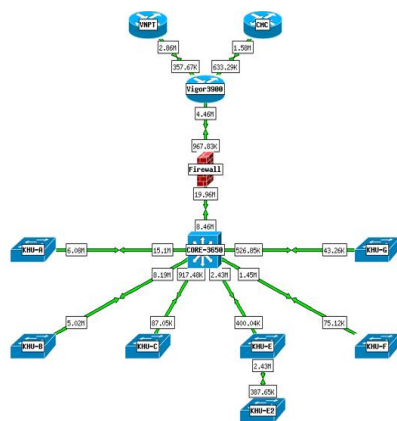


Fig. 4 Operational status of the connection

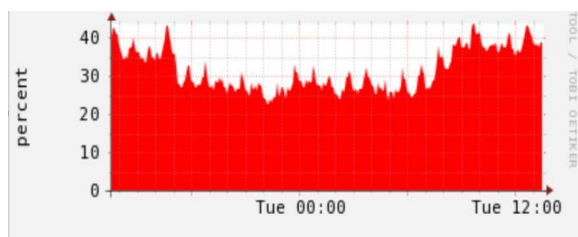


Fig. 5 Monitoring CPU of devices

It is clear that administrators can easily monitor the status of devices as well as connections between devices, so they can easily troubleshoot and ensure connectivity in a timely manner. lowest possible latency.

CONCLUSION: In conclusion, the new system has been deployed and has shown greater advantages than the previous system. Firstly, the new system is completely compatible with the old system, in addition the system is ready and compatible with future expansion solutions. Secondly, the system has high stability. The new system devices are from CISCO, ensuring 24x7 continuous and stable operation. Last but not least, the system is highly secure. The new system is built with tools for flexible management and decentralization. The system is capable of protecting users' data, documents, intrusion protection, and virus attacks on the internal network of Danang General Hospital. However, Technology is evolving at a dizzying rate, so the risks associated with cybersecurity are increasing. The system, therefore, will be updated to more security features in the future to avoid network security incidents.

Keywords

Network infrastructure, local area network (LAN), metropolitan area network (MAN), backup redundancy and network monitoring

References

- [1] Mustafa Almahdi Algaet, Zul Azri Bin Muhamad Noh, Ali Ahmad Milad, A. S. Shibghatullah, Quality of Service in Integrated Networking System at the Hospital Scenarios: A Review.
- [2] Muhammad Raza, Vellanki Pavan Kumar, Ali Nafareih, William Robertson, An Analysis of the Effects of Network Implementation Choices on Healthcare Applications.
- [3] Hong Zhou, Hesham Ali, Jon (Jong-Hoon) Youn, Zhongwei Zhang, A Hybrid Wired and Wireless Network Infrastructure to Improve the Productivity and Quality Care of Critical Medical Applications.

Radiation patterns of MgO and AlN evaluated by angle-resolved cathodoluminescence measurements*

Y. Igari ^{1,a}, K. Kudo ¹, W. Kosaka ², K. Kaneko ^{3,4,5}, T. Yamaguchi ^{1,2}, T. Honda ^{1,2}, S. Fujita ^{3,5}, T. Onuma ^{1,2,b}

¹Department of Electrical Engineering and Electronics, Graduate School of Engineering, Kogakuin University, Tokyo, Japan

²Department of Applied Physics, School of Advanced Engineering, Kogakuin University, Tokyo, Japan

³Department of Electronic Science and Engineering, Kyoto University, Kyoto, Japan

⁴Engineering Education Research Center, Kyoto University, Kyoto, Japan

⁵Photonics and Electronics Science and Engineering Center, Kyoto University, Kyoto, Japan

^a cm20006@ns.kogakuin.ac.jp, ^b onuma@cc.kogakuin.ac.jp

Abstract

Deep ultraviolet (DUV) and vacuum ultraviolet (VUV) light emitters have a variety of applications, such as in ozone cleaners and UV sterilization. Especially, recent attention is focusing on the alternative use of 222-nm-light from the XeCl excimer lamp instead of conventionally-used 254-nm-DUV-light to sterilize human skin with suppressing DNA lesions^[1]. However, most of the commercially available DUV and VUV light sources are discharge-type lamps. We are focusing on rocksalt-structured (RS) $\text{Mg}_x\text{Zn}_{1-x}\text{O}$ alloys as alternative candidate materials for DUV and VUV emitters by virtue of their wide variation of bandgap E_g from 4.5 eV for RS-ZnO to 7.8 eV for RS-MgO. Recently, successful growths of atomically-flat single crystalline RS- $\text{Mg}_x\text{Zn}_{1-x}\text{O}$ films on (001) MgO substrates by the mist chemical vapor deposition method and observation of cathodoluminescence (CL) peak at around 199-210 nm were demonstrated ^[2,3]. In this study, electron-beam incidence-angle-resolved CL (IAR-CL) spectra were measured for an (0001) AlN film on Al_2O_3 and (001) MgO single crystalline substrates to comparatively study their radiation patterns.

The samples investigated were an AlN film on (0001) sapphire substrate and a (001) MgO single crystalline substrate. As shown in Fig. 1, our IAR-CL setup consists of an electron gun operating at 8-10 kV with an emission current of 66-74 μA , a

rotational sample holder, and a monochromator. The monochromator was purged with nitrogen gas during operation. The CL spectra were measured at 6 K. The detection angle θ_D was changed from 0° to 90° with a 15° step by varying the electron-beam incidence angle θ_I , where $\theta_D = 90^\circ - \theta_I$.

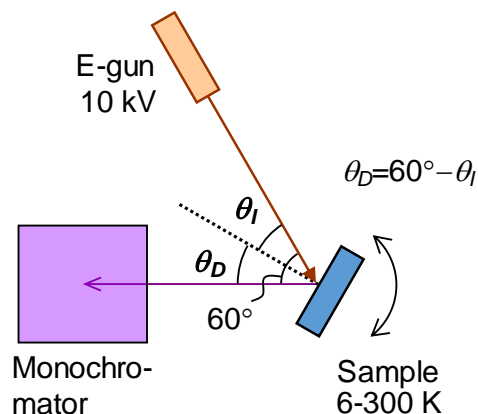


Fig. 1. Schematic diagram of our electron-beam incidence-angle-resolved cathodoluminescence (IAR-CL) setup.

The IAR-CL spectra of the AlN film and MgO crystal at 6 K are shown as a function of θ_D in Fig. 2. The spectra exhibited sharp near-band-edge emission peaks at 6.02 eV (206 nm) for AlN and 7.63 eV (162 nm) for MgO, respectively. Spectrally integrated NBE CL intensities (I_{CL}) are plotted as a function of θ_D in Fig. 3, where I_{CL} is normalized to the maximum intensity. To compensate an electron beam spot elongation on the surface, the raw data was divided by $\cos(\theta_D - 60^\circ)$ to give the

* Poster paper presentation; this work was supported in part by Grants-in-Aid for Scientific Research No. 20H00246 from MEXT, Japan

corrected data points. The AlN showed a maximum intensity at 45° and the MgO had a maximum at 0° . For comparison, the Lambertian shape radiation pattern, dipole radiation pattern, and their combination are shown by blue, green, and red solid lines, respectively. For AlN, the wurtzite structure lowers its crystal symmetry [4], and its optical anisotropy reduces the light extraction efficiency. The results demonstrate a superior emission property of RS-MgO.

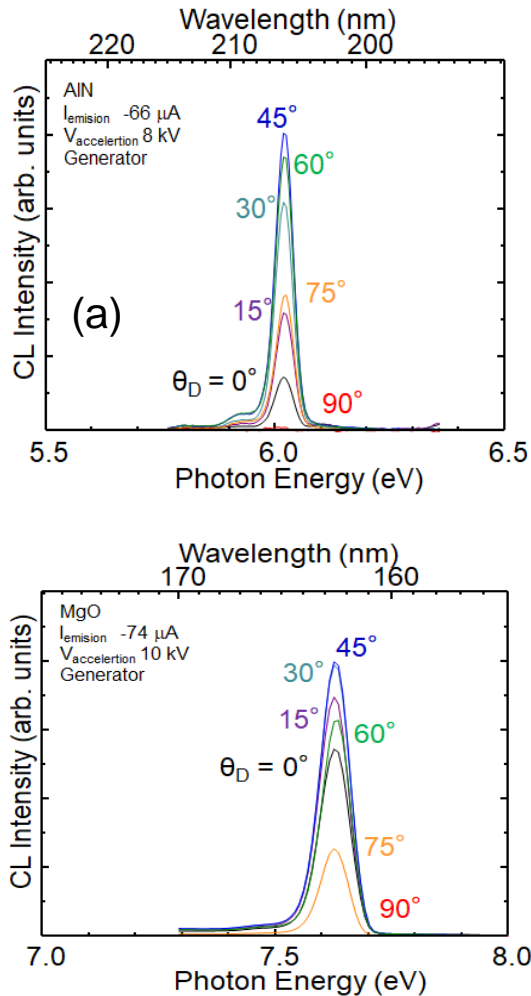


Fig. 2. IAR-CL spectra of (a) AlN film and (b) MgO crystal at 6 K as a function of θ_D .

Keywords

Vacuum and deep UV light source, Magnesium zinc oxide (MgZnO), cathodoluminescence, radiation pattern

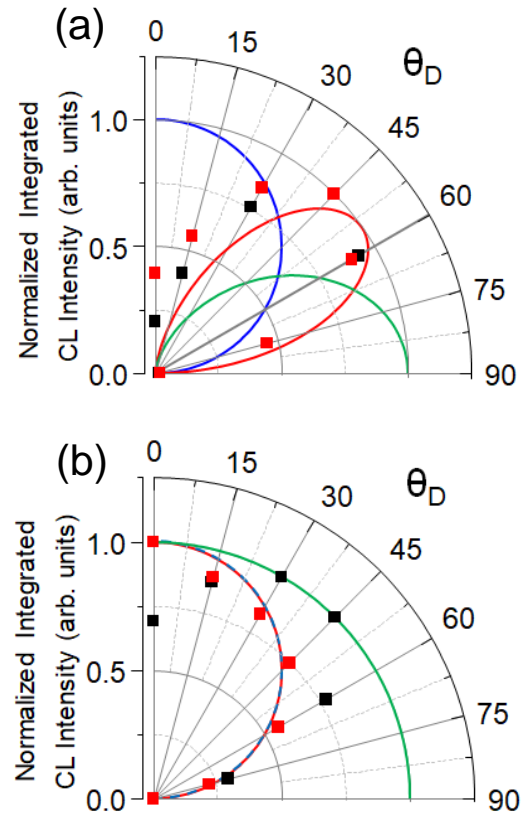


Fig. 3. Spectrally integrated CL intensities of (a) AlN film and (b) MgO crystal as a function of θ_D . Black and red closed squares represent raw and corrected data, respectively. Blue, green, and red solid lines represent the Lambertian shape radiation pattern, dipole radiation pattern, and their combination, respectively.

References

- [1] D. Welch *et al.*, Scientific Reports **8**, 2752 (2018).
- [2] K. Ishii *et al.*, Appl. Phys. Express **12**, 052011 (2019).
- [3] M. Ono *et al.*, J. Appl. Phys. **125**, 225108 (2019).
- [4] Y. Taniyasu and M. Kasu, Appl. Phys. Lett., **96**, 221110 (2010).

Performance of adaptive control CRE in multi-band heterogeneous mobile networks*

Kento Fujisawa ^{1,a,*}, and Hiroyuki Otsuka ^{1,b}

¹ Graduate School of Engineering, Kogakuin University, Tokyo, Japan

^a cm19040@ns.kogakuin.ac.jp, ^b otsuka@cc.kogakuin.ac.jp

Abstract

Fifth-generation (5G) mobile systems are being developed, notably in the third-generation partnership project (3GPP) standards body. The primary objectives of 5G are to increase system capacity and improve data rates.

A heterogeneous mobile network (HetNet) is a noteworthy ultra-dense network in which picocells with a low-power eNB (pico-eNB) are installed within the coverage area of a macrocell. HetNets can offload traffic from macrocell to picocells because the radio resources of the pico-eNB are independent of those of the macro-eNB. In HetNets deployments, cell range expansion (CRE) technique plays an important role as it can virtually expand picocell coverage.

A higher-order modulation scheme is also a promising technique for increasing data rates within a limited bandwidth. In Release 8 of the Third Generation Partnership Project (3GPP) standards, 64-quadrature amplitude modulation (QAM) was described as the highest modulation in a modulation and coding scheme (MCS). Later, 3GPP Release 12 recognized the introduction of 256-QAM. Recently, 3GPP Release 15 introduced 1024-QAM support [2].

In [3]–[5], an adaptive control CRE using two different CSOs, in which a CRE zone for user equipment (UE) is adaptively changed, has been proposed. In this paper, we evaluate the user throughput of the adaptive control CRE in a multi-band HetNets using the carrier frequencies of 2 and 3.4 GHz regarding the condition of UE layout. In particular, we investigate the user throughput of that against the cluster size for UE layout defined as the radius of circle centered at

each pico-eNB, using modulation and coding scheme incorporating 1024-QAM.

ADAPTIVE CONTROL CRE: Figure 1 shows the principle of an adaptive control CRE and how to determine the two different CSOs. The SINR threshold (i.e., SINR_{th}) is determined using the cumulative distribution function (CDF) value of α , where the CDF is for the downlink SINR measured at the UE from the macrocell (i.e., $\text{SINR}_{\text{macro}}$). The macro-eNB first determines α , SINR_{th} and two different CSOs (CSO_{high} and CSO_{low}) based on the results of the CDF. Then, the macro-eNB commands all UE within the macrocell in which CSO_{high} is assigned to UE with $\text{SINR}_{\text{macro}}$ lower than SINR_{th} , and CSO_{low} is assigned to UE with $\text{SINR}_{\text{macro}}$ greater than SINR_{th} .

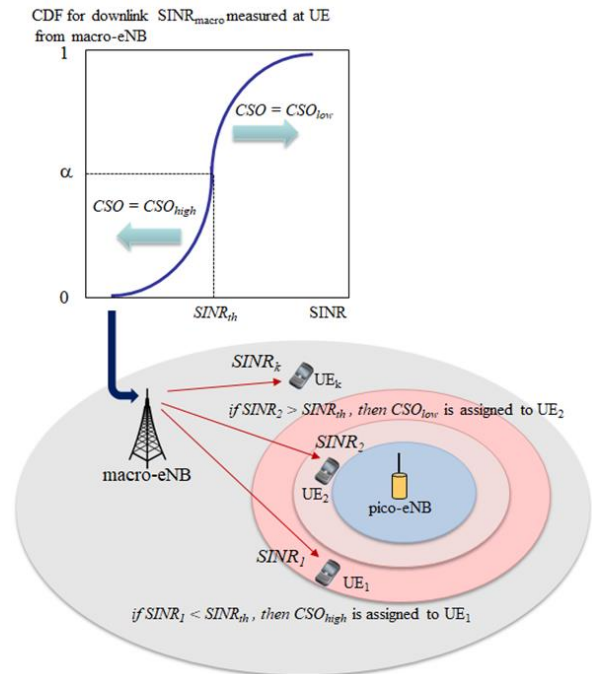


Fig. 1. Adaptive control CRE

* Oral paper presentation

SIMULATION CONDITIONS AND RESULTS:

The primary simulation parameters are listed in Table 1. We use 25 types of MCS indexes included five types of modulation scheme are used QPSK, 16-QAM, 64-QAM, 256-QAM, and 1024-QAM in the downlink. In the simulations, we define the cluster size for UE layout, which is the radius of circle centered at each pico-eNB. UE layout is based on the form of the cluster distribution around the pico-eNB. The ratio of UE cluster distribution is defined as the ratio of the number of UE within the circle to the number of UE outside the circle.

Table 1. Primary Simulation Parameters

| Parameter | Assumption | |
|----------------------------------|--|--------------------|
| | macro-eNB | pico-eNB |
| Cell layout | Hexagonal grid, 19 cell sites, 3 sectors per site | 4 picos per sector |
| Cell radius (ISD) | 289 m (500 m) | - |
| Tx power | 46 dBm | 30 dBm |
| Tx Antenna height | 32 m | 10 m |
| eNB Tx antenna gain | 14 dBi | 5 dBi |
| Carrier frequency | 2.0 GHz | 3.4 GHz |
| System bandwidth | 10 MHz | 10 MHz |
| UE distribution | 30 UEs per sector, uniform distribution, 2/3 cluster distribution | |
| Cluster size for UE distribution | from 20 m to 70 m | |
| CSO | 3 dB | |
| Adaptive control CRE | $CSO_{low} = 3 \text{ dB}$, $CSO_{high} = 12 \text{ dB}$, $\alpha = 0.4$ | |
| Link adaptation | 25 MCS (QPSK to 1024-QAM) | |

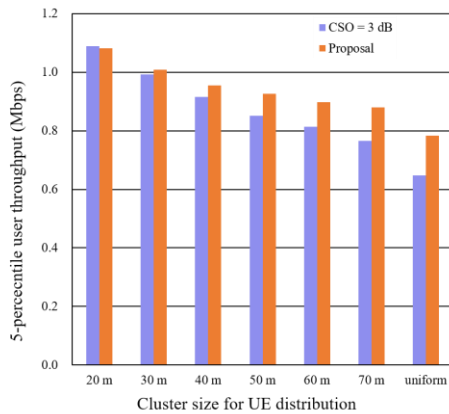


Fig. 2. 5-percentile user throughput of adaptive control CRE against cluster size

CONCLUSION: We clarified that the proposed adaptive control CRE can improve the 5-percentile user throughput by 20.9% and 4% compared with conventional CRE for uniform distribution and a cluster size of 40 m. We also confirm that a cluster size of 20 m can improve the 5-percentile user throughput by 74% respectively compared with uniform distribution.

Keywords

mobile communication, heterogeneous networks, cell range expansion, cell selection offset, UE layout

References

- [1] I. Guvenc, "Capacity and Fairness Analysis of Heterogeneous Networks with Range Expansion and Interference Coordination," IEEE Commun. Letters, vol. 15, issue 10, Oct. 2011.
- [2] 3GPP TR 36.783, "Evolved Universal Terrestrial Radio Access (E-UTRA); Introduction of 1024 Quadrature Amplitude Modulation (QAM) in LTE downlink (Release 15)," 2017.
- [3] K. Kikuchi and H. Otsuka, "Parameter optimization for adaptive control CRE in HetNet," in Proc. PIMRC2013, NET47, Sept. 2013.
- [4] S. Nakazawa, S. Matsuoka, and H. Otsuka, "Adaptive control CRE and its throughput performance in HetNet," IEICE ComEX, vol. 4, no. 4, pp. 117-122, 2015.
- [5] K. Fujisawa, F. Kemmochi, and H. Otsuka, "Personal-Cell Scheme Using Adaptive Control CRE for Multicarrier HetNets," in Proc. VTC2019-Fall, 8B-5, Sept. 2011

Heterogeneous mobile networks using millimeter wave with three-dimensional beamforming*

Fumiya Kemmochi ^{1,a*} and Hiroyuki Otsuka ^{1,b}

¹ Graduate School of Engineering, Kogakuin University, Tokyo, Japan

^a cm19016@ns.kogakuin.ac.jp, ^b otsuka@cc.kogakuin.ac.jp

Abstract

Fifth-generation (5G) mobile systems have been partially launched and are expected gradually to being diffused worldwide [1]. Heterogeneous mobile networks (HetNets) can offload traffic from macrocell to picocells by adding picocells whose radio resources are independent of the radio resources of the macrocell when the traffic in the macrocell enormously increases. From the carrier frequency perspective, the use of high carrier frequencies such as millimeter wave (mmWave) has been investigated worldwide. In particular, the multiband HetNets with picocells operating at mmWave have attracted a lot of attention to achieve higher user throughput because of the enormous amount of signal bandwidth. Three-dimensional beamforming (3D-BF), in which antenna beams can be individually tailored to each user equipment (UE) in the azimuth and elevation domains through the use of a massive multiple-input multiple-output (MIMO) antenna architectures, is key technology for achieving 5G requirements [2]. 3D-BF is effective to overcome large propagation loss in higher carrier frequency bands. Thus far, typical picocell is formed by an omni antenna in HetNets, and also the performance evaluation for the picocell using 3D-BF technology has not been investigated. We propose HetNets using sectorized picocells with three-dimensional beamforming operating at a carrier frequency of 28 GHz under the assumption that the signal bandwidth of the picocells is 10 times wider than that of the macrocell.

THREE-SECTOR PICOCELL WITH 3D-BF AT 28 GHz BAND: Figure 1 shows a multiband HetNet combined with a macrocell using 2 GHz band, and picocells covered by low-power pico-

eNB operating at 28 GHz band. In HetNets, the cell selection procedure which allows UE to camp on to a cell is executed by measuring a downlink reference signal from the macro-eNB and pico-eNB. Pico-eNB has a sector antenna which is assumed to be a type of directional mmWave antenna with a sector-shaped radiation pattern. Figure 2 shows the fundamental beam management procedure for the downlink 3D-BF between pico-eNB and UE. The sector antenna consists of massive MIMO to form 3D-BF. The pico-eNB transmit reference signal (RS) for channel state information (CSI) for each beam, i.e., sweeps transmission (Tx) beam and UE measures the received SINR and RSRP of each beam, and then reports the results of the CSI to the pico-eNB. The CSI includes the channel quality indicator (CQI) to decide the downlink modulation and coding sets, the rank indicator (RI) to decide the number of streams, and precoding matrix indicator (PMI) to decide the precoding for Tx beams. Then, the pico-eNB decides best Tx beam among 36 beams.

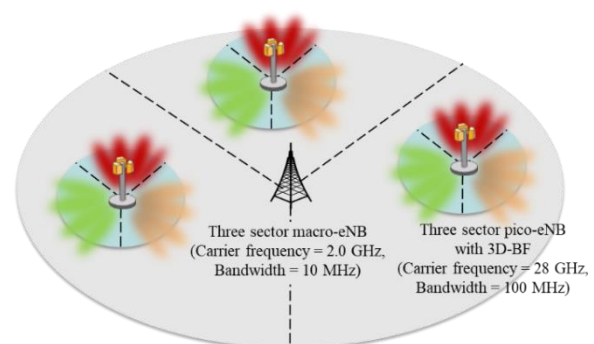


Fig. 1. HetNet using three-sector picocells with 3D-BF at 28 GHz band.

SIMULATION CONDITION AND RESULTS: We investigate the average and 5-percentile user throughput of the HetNet using three-sector

* Oral paper presentation

picocells with 3D-BF in comparison with that using conventional omni picocells. The primary simulation parameters are listed in Table I. Two-thirds of the UE are deployed near the pico-eNB, i.e., within the cluster size of the pico-eNB, and the remaining one-third UE are located outside it. The Tx power and the Tx antenna gain are obtained from [3], [4]. The path-loss model is obtained from [5]. We assume that macro-eNB that uses 2 GHz band installs a three-sector Tx antenna and UE has omni receiver antenna. Figure 3 shows the average and 5-percentile user throughput of the proposed HetNet as well as that of conventional omni picocell. Here, "Proposal" means the HetNet using three-sector picocells with 3D-BF, whereas "Conventional" is the HetNet using conventional omni picocell. It is shown that the proposed scheme can improve the average and 5-percentile user throughput by approximately 2.1 and 1.8 times compared with that conventional, respectively.

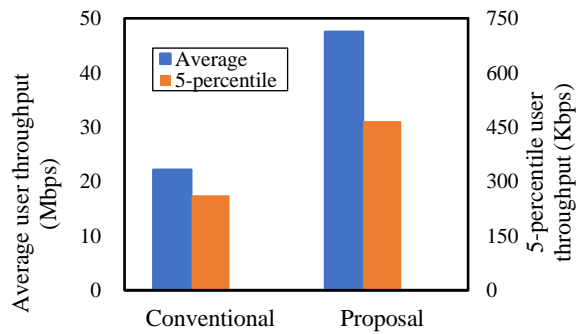


Fig. 2. Average and 5-percentile user throughput.

CONCLUSION: We confirmed that the proposed HetNet using sectorized picocells with 3D-BF can improve the average and 5-percentile user throughput by approximately 2.1 and 1.8 times compared with that conventional, respectively.

Keywords

mobile networks, millimeter wave, 3D-beamforming, system-level simulation

References

- [1] 3GPP, "Heterogeneous networks in LTE," online, <http://www.3gpp.org/technologies/keywords-acronyms/1576-hetnet>.
- [2] M. Giordani, M. Polese, A. Roy, D. Castor, and M. Zorzi, "A Tutorial on beam management for 3GPP NR at mmWave frequencies," *IEEE Communications Surveys & Tutorials*, vol. 21, pp. 173-196, Sept. 2018.
- [3] ITU Radiocommunication study groups, "Impact of IMT systems on to inter-satellite service in 25.25-27.5 GHz," Sept. 2017.
- [4] F. Kemmochi, K. Fujisawa, and H. Otsuka, "Potential design for modulation and coding scheme in mmWave multicarrier HetNets," in *Proc. VTC2019-Fall*, 3P-12, Sept. 2019.
- [5] 3GPP TR 38.901 version 14.2.0 Release 14, "Study on channel model for frequencies from 0.5 to 100 GHz," Oct. 2017.

Table 1. Simulation parameters

| Parameter | Assumption | |
|------------------------|---|---|
| | Macro-eNB | pico-eNB |
| Cell layout | Hexagonal grid, 19 cell sites, 3 sectors per site | 4 picos per macro sector, 3 sectors per site |
| Cell radius | 289 m | — |
| Carrier frequency | 2 GHz | 28 GHz |
| System bandwidth | 10 MHz | 100 MHz |
| Tx power | 46 dBm | 22 dBm per beam |
| Tx antenna gain | 14 dBi | 23 dBi |
| The number of beams | — | 36 12 beams in azimuth plane 3 beams in elevation plane |
| 3 dB beamwidth | Horizontal | 70 deg. |
| | Vertical | 10 deg. |
| Antenna downtilt angle | 15 deg. | 15 deg. |
| UE distribution | 30 UEs per macro-sector, 2/3 clustered distribution | |
| Link adaptation | 22 MCS (QPSK to 256-QAM) | |
| MIMO | 2 × 2 SU-MIMO | |
| Traffic model | Full buffer | |

Field and virtual assessment for recurring hurricane reconnaissance in U.S. Gulf Coast*

Do Quang-Trung^{1,2 a}

¹The University of Danang-University of Science & Technology, Danang City, Vietnam

²Visiting Assistant Professor, University of Louisiana at Lafayette, USA

^adqtrung@dut.udn.vn; trung.do@louisiana.edu

Abstract

Hurricane was identified among the most frequent and costliest natural hazard damage to the Gulf States such as Texas and Louisiana. In 2020, two major disaster events, Hurricane Delta [1] and Hurricane Laura [2] made land fall to the same area in Louisiana with approximately 10 miles (16 km) away from each other within 6 weeks. In order to obtain a curated dataset and event briefing for these special recurring hurricanes, the Structural Extreme Event Reconnaissance Network (StEER), under the banner of Natural Hazard Engineering Research Infrastructures (NHERI) program funded by the U.S. National Science Foundation (NSF), deployed the Field Assessment Structural Teams (FAST) for regionally accessing the hurricane direct and aftermath impacts. The direct impacts include structural and non-structural damage to buildings, transportation system, and other infrastructure system such as transmission network, water network, etc. However, the aftermath impacts including social and business disruption and additional health consequences during the COVID-19 pandemic require further research to document. The FAST teams were equipped with high-end technology survey instruments such as drones and street cameras with GPS encryption. In the meantime, Virtual Assessment Structural Teams (VAST) responded for gathering additional data from social media, processing satellite images, producing the wind and surge maps, and directing the FASTs. Data collected from the two recurring hurricanes was combined to produce a longitudinal data capturing for the same area which already been documented for the

previous event (Hurricane Laura) and the later event (Hurricane Delta).

Data collected for assessment includes overall photos from the FAST team, aerial photos from satellite image or drone, and photos before damage from online sources. Each building structure was virtual damage assessment as shown in Table 1 which include building address, number of stories, first floor elevation, occupancy, years of built, roof shapes.

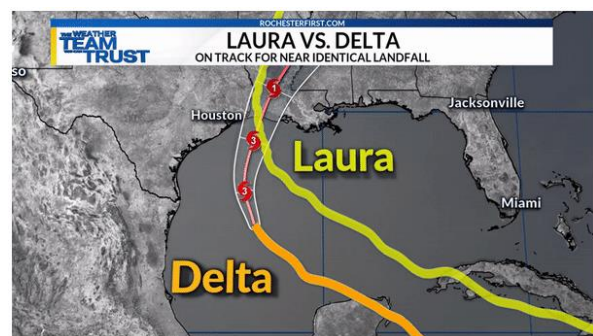


Fig. 1. Tracks and landfall locations of Hurricane Laura and Hurricane Delta in Louisiana in 2020
(Source: <https://www.rochesterfirst.com/>)

Lessons learned from field and virtual data collecting methodology in this study can be applied for longitudinal study of typhoon impacts in Asia Pacific region. Event briefing and typhoon loss estimated based on field and virtual reconnaissance are valuable for improving resilience of coastal communities.

Keywords

Hurricane / typhoon reconnaissance, field/virtual assessment, event briefing

References

- [1] Roueche, D. Kameshwar, S. Marshall, J. Bandaru, S. Do, T. Kijewski-Correa, T. Cortes, M.

* Oral paper presentation

Crawford, S. Javadinasab Hormozabad, S. Strader, S. Prevatt, D. (2020) "Event Briefing", in StEER - Hurricane Delta. DesignSafe-CI. <https://doi.org/10.17603/ds2-y2gc-xj10>.

[2] Roueche, D. Kameshwar, S. Rodriguez, L. (2020) "Hybrid Preliminary Virtual Reconnaissance Report-Early Access Reconnaissance Report (PVRR-EARR)", in StEER - Hurricane Laura. DesignSafe-CI. <https://doi.org/10.17603/ds2-ng93-se16>.

Table 1. Building damage classification for Hurricane Laura for 418 structural samples

| Damage states | Describe | Number of structures |
|---------------|--|----------------------|
| DS 0 | Undamaged: No visible damage from outside | 122 |
| DS 1 | Minor: No more than 1 broken window, door or garage door. Less than 15% roof cover or wall cladding damage. | 172 |
| DS 2 | Moderate: Between 15% and 50% roof cover or wall cladding damage OR <5% roof substrate failure. | 87 |
| DS 3 | Severe: >50% roof cover / wall cladding damage OR 20-50% windows/doors damaged OR 5-25% roof sheathing loss OR <15% roof structure damage. | 23 |
| DS 4 | Destruction: 15% roof structure failure OR failure of wall structure OR >25% roof deck loss OR >50% window/door damage | 14 |

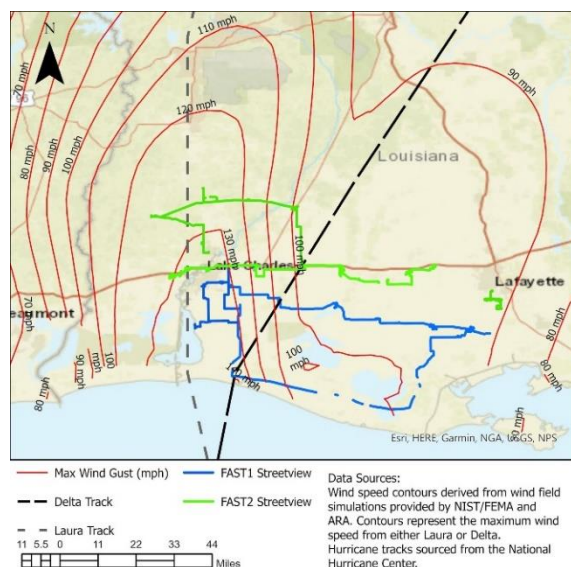


Fig. 2. Street view routes by FAST within context of maximum gust wind speeds from both Laura and Delta [1]

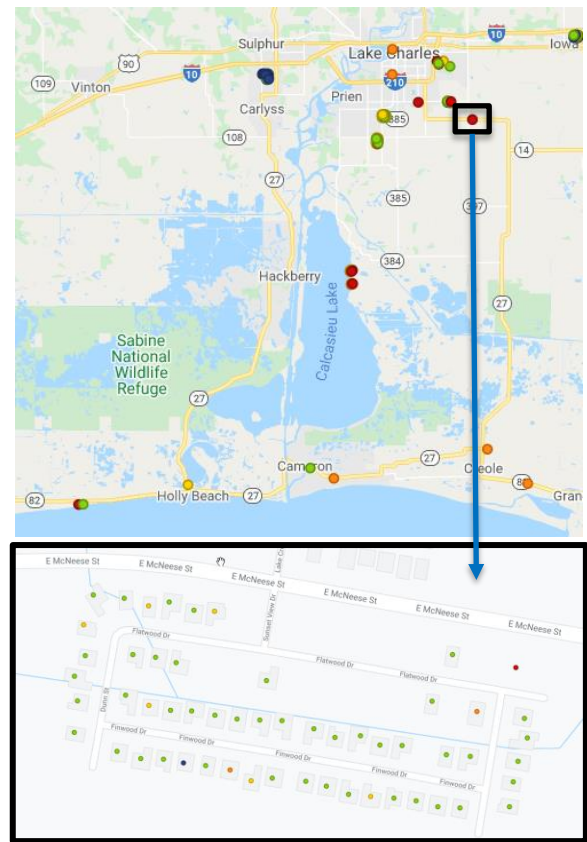


Fig. 3. Data input using Fulcrum app.



Fig. 4. Example of before and after damage

A study on dynamic path establishment method using superposition coding in EON*

Hiroyasu Sato ^{1,a,*}, Ken-ichi Baba ^{1,b}

¹ Advanced Network System Laboratory, Graduate School of Engineering, Kogakuin University, Tokyo, Japan

^a cm20025@ns.kogakuin.ac.jp, ^b baba@cc.kogakuin.ac.jp

Abstract

INTRODUCTION: In recent years, Elastic Optical Network (EON) is studied energetically and provides increasing traffic to admit efficiently to core network. In the field of EON, various methods to increase frequency utilization efficiently is researched. The method which applies the superposition coding used the wireless communication field to EON is also one of their methods. In the wireless communication filed, the capacity is improved on the downlink in multiple access by NOMA that applies Successive Interface Cancellation [1]. *Fig. 1* shows an overview of superposition coding in EON and its merits. The superposition coding makes it possible to share frequency slots and send both of optical signals under several conditions.

In this paper, we aim to improve the efficiency of frequency resource utilization and propose a path establishment method and routing control dynamically using superposition coding. Superposition coding in EON is studied and it shows usefulness for efficiency resources, but the study targets at the design problem given traffic matrix [2]. That is out of consideration for dynamic request generation to say.

PROPOSED METHOD: Our proposed method has several conditions to apply that to EON. Superposition coding in EON, both of candidate paths need to satisfy the following conditions: 1) Source nodes are the same, 2) Destination nodes are not the same, 3) One connection completely contains the other connection, 4) There is a difference in path length according to network node performances.

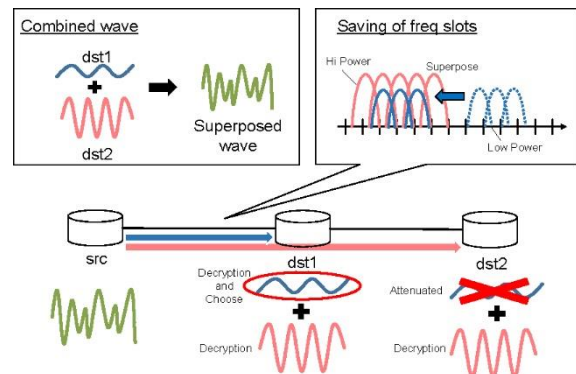


Fig. 1. Overview of Superposition coding in EON and its merits on frequency slots

It is checked the conditions when the path request arrives. If all conditions are satisfied, the request is superposed on the target path. On the other hands, if the conditions are not satisfied, the path is assigned to frequency slots as a normal path. This method makes it possible to give priority to the number of superpositions in this simulation. The algorithm from request generation to frequency slots allocation is shown below.

1. A request is generated.
2. Calculate the K-shortest paths and select the first path.
3. Determine the modulation method based on the path lengths.
4. Check if there is a path in the optical fiber that satisfies the 4 applicable conditions. If it exists, proceed to step 5, and if it does not exist, proceed to step 6.
5. Superpose with the target existing path, share the frequency slots, accommodate the request, and end the processing.

* Oral paper presentation

6. If the K th candidate route has not been selected, select the next candidate route, and return step 3. If the K th candidate route has been selected, proceed to step 7.
7. Check whether normal path establish is possible in order from the first candidate of paths. If it can establish, slots are assigned, and if neither is possible, it is rejected, and the process ends.

PERFORMANCE EVALUATION: To evaluate the frequency resource utilization efficiency of the proposed method, we adopt call blocking probability and the number of superpositions as performance measures. The network model to be used is JPN12, 320 frequency slots per link, and the number of candidate routes K is 3. There are three types of modulation methods used, and we define the path lengths that each modulation method can operate them. In this method, it is selected the highest degree of modulation in three levels. We defined the modulation scheme and number of dedicated slots as a call according to lengths of the pass as shown in the following *Table 1*. In addition, the requests that occur follow the Poisson distribution with an average arrival rate of λ , and the duration follows an exponential distribution with an average of 30 seconds.

Table 1. The modulation scheme and number of dedicated slots according to path lengths

| Path Lengths [km] | Modulation Method | Dedicated Slots |
|----------------------|----------------------|--------------------|
| ~800 | 16-QAM | 3 |
| 801~1200 | QPSK | 4 |
| 1201~ | BPSK | 5 |

As a result, *Fig. 2* shows the call blocking probability at the arrival rate of 6.5 is reduced by about 54.6% as compared to the conventional method. The number of superpositions is increased with increasing arrival rate in shown as *Fig. 3*. It can be said that efficiently is improved in high arrival rate because there are many target paths in the situation where the line is busy.

CONCLUSION: We proposed path establishment method using superposition

coding in EON. By the proposed method, it was confirmed that the utilization efficiency of frequency resources was improved. As a future work, we speculate this method is more effective by considering detour paths and verify that.

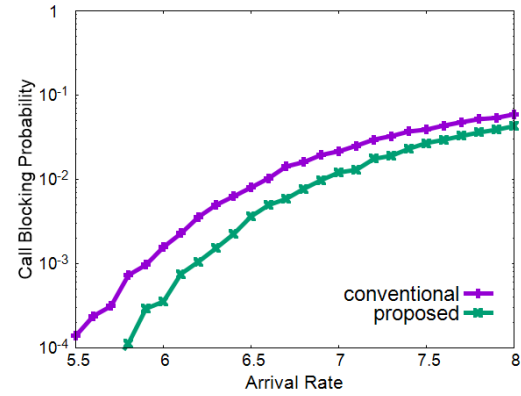


Fig. 2. Call blocking Probability on JPN12

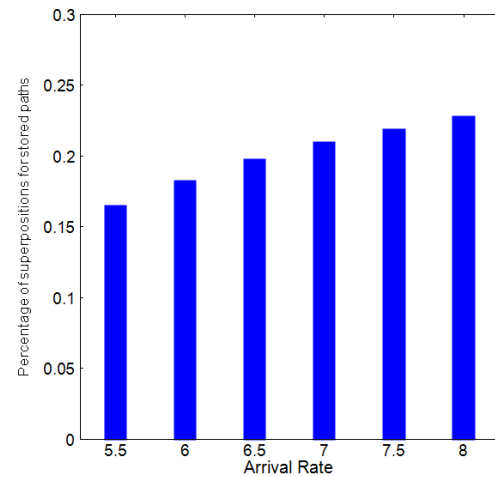


Fig. 3. Percentage of Superpositions for stored paths

Keywords

Elastic optical network, path establishment method, superposition coding

References

- [1] Yuya Saito et al., "Non-Orthogonal Multiple Access (NOMA) for Cellular Future Radio Access", in *Proc. of IEEE VTC Spring 2013*, pp. 1-5, 2013.
- [2] Yusuke Hirota and Takashi Watanabe, "Examination of Frequency Resource Saving Using 1-to-2 Communication in EON", *IEICE Technical Report (PN2016-105)*, vol. 116, no. 498, pp. 125-130, 2017

GPS positioning accuracy improvement by using drone in relay type GPS*

Kouhei Yoshida ^{1,a}, Takatoshi Sugiyama

¹ Graduate School of Engineering, Kogakuin University, Tokyo, Japan

^a cm20054@ns.kogakuin.ac.jp

Abstract

INTRODUCTION: In recent years, GPS (Global Positioning System) [1] has become one of the most important systems for our lives because it assists in position information, navigation, etc. However, it is difficult to receive GPS signals from GPS satellites directly in urban area because GPS signals are blocked by buildings [2]. In order to solve this problem, relay type GPS [3, 4] has been previously proposed. It calculates the target GPS receiver's positions by the assistance of the many mobile terminals around them. The mobile terminals, called G-MTs (Mobile terminals transmitting GPS signals), transmit their own position information via the same GPS signal format. Therefore, the target GPS receiver's calculated distance error can be improved by the information from G-MTs.

PROPOSED SCHEME: In the conventional scheme, the calculated distance error performances of the G-MTs are degraded, especially in urban area, by reflected GPS signals. This leads worse target GPS receiver's calculated distance errors. To solve this problem, relay type GPS by using drone, called G-Drone is proposed to improve the calculated distance error performances of the target GPS receivers in urban areas [5]. The system conceptual diagram of the proposed scheme is shown in Fig. 1. G-Drone can receive GPS signals at higher position than G-MTs and receive GPS signals directly from GPS satellites. In this paper, we evaluate the calculated distance error performances of the target GPS receiver by the proposed scheme.

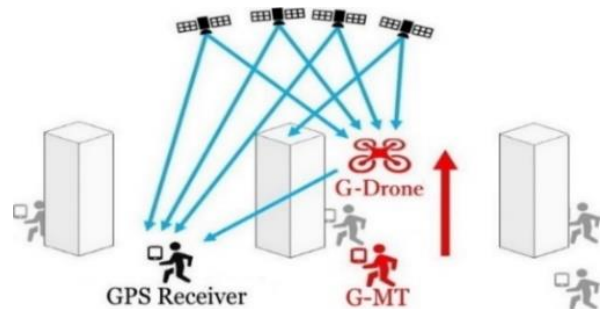


Fig. 1 The system conceptual diagram of the relay type GPS by using G-Drone.

SIMULATION PARAMETERS: The simulation parameters are shown in Table 1. The simulation time is 24 hours and the position calculation interval is set to be 5 minutes. The simulation model is shown in Fig. 2. In the model to simulate the urban area, we have created dimensions of 40 m × 40 m × 100 m sixteen buildings with concrete material.

SIMULATION RESULTS: The CCDF (Complementary Cumulative Distribution Function) of the calculated distance error is shown in Fig. 3. The computer simulation results indicate the proposed relay type GPS by using G-Drone improves the calculated distance error performances compared to those of the conventional scheme. For example, the proposed scheme obtains 20.01m improvement at CCDF of 50%.

Table 1. The major simulation parameters

| Parameter | Value |
|--------------------------------|------------|
| Number of G-Drone | 1 |
| Height of G-Drone | 100 meters |
| Simulation time | 24 hours |
| Position calculation interval | 5 minutes |
| The total number of satellites | 32 |

* Poster paper presentation

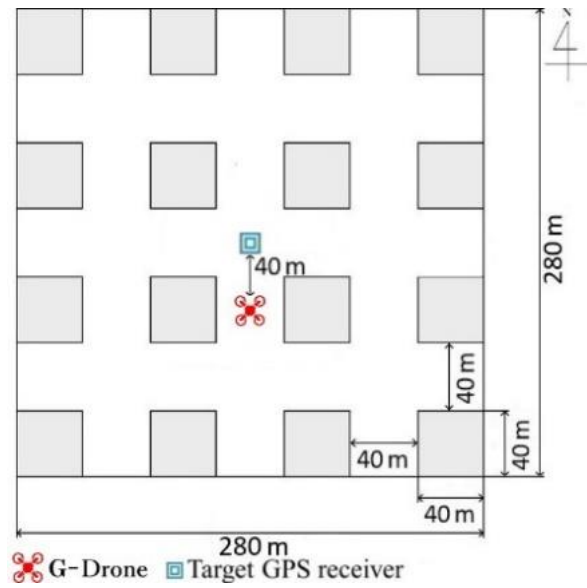


Fig. 2 The simulation model.

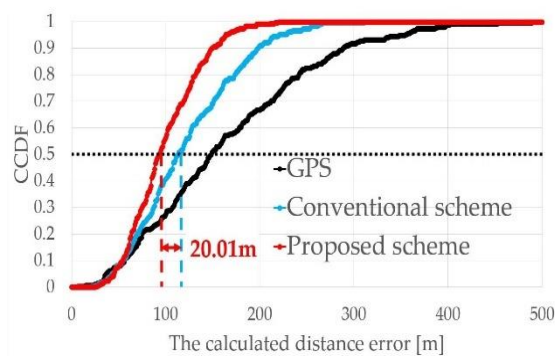


Fig. 3 CCDF of the calculated distance error.

CONCLUSION: We have evaluated the calculated distance error performances of the target GPS receiver by the relay type GPS by using drone. The proposed relay type GPS by using drones improves the calculated distance

error performances of the target GPS receivers compared to those of the conventional scheme. For example, the proposed scheme obtains 20.01m improvement at CCDF of 50% in an urban building model.

Keywords

GPS, position calculation, urban area, drone

References

- [1] Pratap Misra and Per Enge, "Global Positioning System: Signals, Measurements, and Performance", Syoyo Bunko, 2004.
- [2] Bradford W. Parkinson, "Introduction and Heritage of NAVSTAR, the Global Positioning System", Global Positioning System: Theory and Applications, Vol. I, AIAA, 1996.
- [3] Norifumi Murai and Takatoshi Sugiyama, "Proposal of Relay Type GPS Using Many Mobile Terminals", KICS ICTC2017, V-1.3, Sept. 2017.
- [4] Norifumi Murai, Takatoshi Sugiyama, "Distance Error Improvement by Relay Type GPS Using Many Mobile Terminals", P146, ISAT-16, Nov. 2017.
- [5] Kouhei Yoshida and Takatoshi Sugiyama, "Calculated Distance Error Improvement by Using Drones in Relay Type GPS", KICS ICTC2020, VI-6.4, Oct. 2020.f

Electrical characterization of Zr-based ReRAM with a sandwiched resistive switching layer*

Keito Toyama ^a, Daiki Naniwa, Shinya Aikawa ^{b,*}

Kogakuin University, 2665-1 Nakano-machi, Hachioji, Tokyo 192-0015, Japan

^acm20037@ns.kogakuin.ac.jp, ^baikawa@cc.kogakuin.ac.jp

Abstract

Nonvolatile memories with high capacity and low power consumption demand for next generation information technologies^[1]. Several nonvolatile memory devices have been considered as candidates for post flash memory. Among them, resistive random access memory (ReRAM) has many advantages, including low power consumption, large on-off current ratio, multi-level and, high-speed operation, as well as atomic-scale miniaturization^[2]. In general, ReRAM has a simple structure, however, Pt is often used for electrode because of its stability^[3]. Pt is a noble and expensive metal, thus conventional transition metals can be adopted for ReRAM electrode because of cost reduction. Here, we fabricated ReRAM free from noble materials as electrode using sandwiched $\text{SiO}_x/\text{ZrO}_x/\text{SiO}_x$ resistive switching layer. Cu and Mo were chosen for top and bottom electrode, respectively because they are compatible with CMOS technology.

A Si substrate was used as a substrate. At first, the substrate was washed in acetone and IPA, then the surface was cleaned by UV irradiation. Mo was deposited at 50 nm using an electron beam evaporator as a bottom electrode. Next, a sandwiched resistive switching layer was formed sequentially deposition of SiO_x , Zr and SiO_x . The SiO_x layer (10nm) was formed using SiO_2 tablet. After 25nm of Zr deposition, the SiO_x/Zr stacked layer was annealed in O_2 at 600 °C for 30 min. Furthermore, the top SiO_x layer(10nm) was prepared by the same method of the bottom SiO_x layer. Finally, top Cu electrode was deposited at 50nm through a shadow mask [Fig. 1(a)]. As a comparison sample, ReRAM without a SiO_x layer between Zr/Cu was also fabricated, as shown in Fig. 1(b).

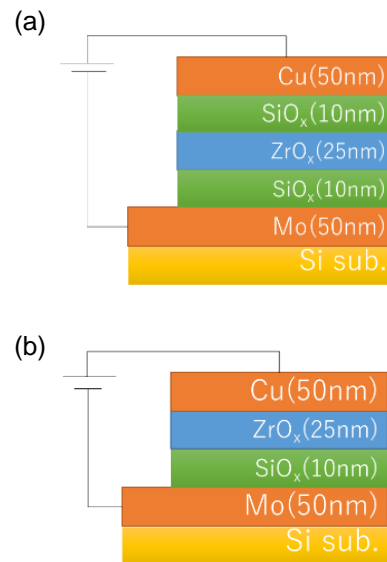


Fig.1 Schematic image of the fabricated ZrO_x -based ReRAM (a) with and (b) without SiO_x layer.

Fig. 2(a) and 2(b) show I - V characteristics of the fabricated ReRAM with and without top SiO_x layer, respectively. Both ReRAM were well operated in memory device such as large on/off current ratio and set/reset behavior, however, the controlled sample, which is ReRAM without top SiO_x , was worked in memory operation only few cycles. On the other hand, the ReRAM with the top SiO_x layer was continuously operated more than 15 cycles. This difference is attributed to the suppression of Cu ion migration from top electrode. Since Cu ions form conductive filament in ZrO_x layer playing an electron path, blocking SiO_x layer is required when transition metal was used as electrode.

In summary, we fabricated Zr-based ReRAM free from noble Pt electrode using sandwiched $\text{SiO}_x/\text{ZrO}_x/\text{SiO}_x$ resistive switching layer and

* Poster paper presentation

compared the electrical properties of ReRAM with and without top SiO_x layer. For the sandwiched structure, better ReRAM performances with a more than 3 order of magnitude on/off ratio and repeatable operation was obtained. This might be caused by the insertion of the SiO_x , acting as a blocking layer. However, further improvements are required for realization of reliable memory devices.

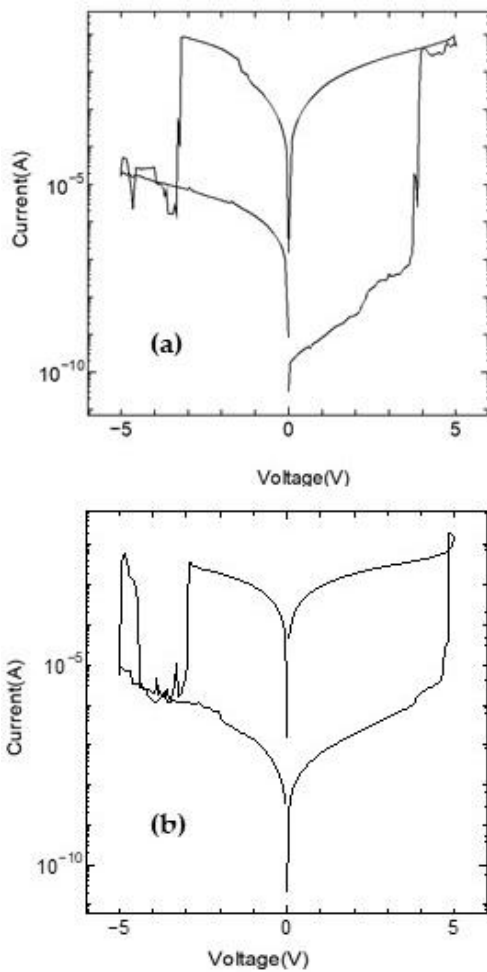


Fig.2. Typical I-V characteristics of the fabricated ZrO_x -based ReRAM (a) with and (b) without SiO_x layer.

KEYWORDS

ReRAM, sandwiched resistive switching layer, noble metal free, SiO_x as ion blocking layer

REFERENCES

- [1] S. Raoux, G. W. Burr, M. J. Breitwisch, C. T. Rettner, Y.-C. Chen, R. M. Shelby, M. Salinga, D. Krebs, S.-H. Chen, H.-L. Lung, and C. H. Lam, IBM J. Res. Dev. **52**, 465 (2008).
- [2] H. Zhai, J. Kong, J. Yang, J. Xu, Q. Xu, H. Sun, A. Li, and D. Wu, J. Mater. Sci. Technol. **32**, 676 (2016).
- [3] D. Takashima and I. Kunishima, IEEE J. Solid-State Circuits **33**, 787 (1998).

Transmission performance against subcarrier spacing of OFDM in multipath fading channels*

Daisuke Kosuge ^{1,a,*}, Hiroyuki Otsuka ^{1,b}

¹ Graduate School of Engineering, Kogakuin University, Tokyo, Japan

^a cm20019@ns.kogakuin.ac.jp, ^b otsuka@cc.kogakuin.ac.jp

Abstract

In 5G, the use of high frequency bands is being considered to meet the requirements of high speed and high capacity. For high-bandwidth transmission using high-frequency bands, OFDM signals must support multiple subcarrier spacing, and the subcarrier spacing must be increased, especially when higher carrier frequencies such as millimeter wave are used. The authors have previously evaluated the transmission performance of 256/1024/4,096-QAM under LTE-based subcarrier spacing conditions [1].

In this paper, we discuss the transmission performance of OFDM signals using 256-QAM under multipath fading conditions against four different types of subcarrier spacings.

TRANSMISSION MODELS AND SIMULATION CONDITIONS: Table 1 shows the OFDM models. Model A has a bandwidth of 10 MHz and a subcarrier spacing of 15 kHz, while Models B, C and D have a bandwidth of 100 MHz and subcarrier spacing of 30, 60 and 120 kHz, respectively. Figure 1 shows the OFDM signals for models A and B. The overhead ratio of the cyclic prefix (CP) is fixed at 4.76, 2.38, 1.19, 0.595 μ s for models A, B, C, and D, respectively. The modulation scheme is 256-QAM, and there are two coding ratios, 1/3 and 3/4.

Table 1. OFDM models

| Model | A | B | C | D |
|---------------------------|------|------|------|-------|
| Subcarrier interval (kHz) | 15 | 30 | 60 | 120 |
| Bandwidth (MHz) | 20 | 100 | 100 | 100 |
| Cyclic prefix (μ s) | 4.76 | 2.38 | 1.19 | 0.595 |

Figure 2 shows the transmission model. A pilot signal is inserted at the transmitter side to estimate the channel characteristics between transmitter and receiver. At the receiver side, channel equalization is performed based on the channel estimation. In this paper, we assume that the number of pilots is the same for models A, B, C and D. Table 2 shows main simulation parameters.

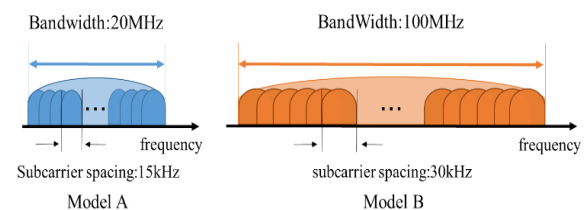


Fig. 1. OFDM signals for models A and B

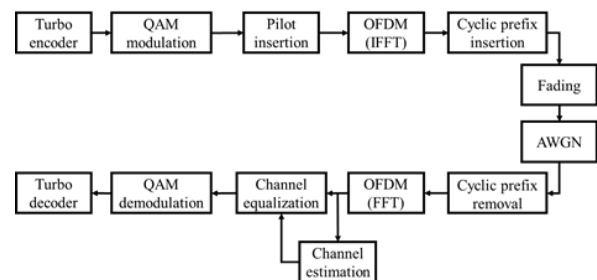


Fig. 2. Transmission

In this paper, the number of pilots is the same for models A, B, C and D. Table 3 shows multipath fading channels used in the simulation, which is based on the EPA (Extended Pedestrian A) model defined in 3GPP, however the reflected path with a longer delay is added to the EPA model.

SIMULATION RESULTS: Figure 3 shows the BER performance for models A, B, C and D. For

* Oral paper presentation

models A and B, when $CR = 1/3$, the required SNR to satisfy $BER = 10^{-4}$ increases by about 3 dB during fading, and for model C, it increases by 7 dB. This is due to the fact that the delay of the reflected wave exceeds the CP length.

Table 2. Main simulation parameters

| Parameter | Values |
|-------------------|---------------|
| Symbol modulation | 256-QAM |
| Signal mapping | Gray code |
| Turbo encoder | $CR=1/3, 3/4$ |
| Turbo decoder | Soft decision |

Table 3. Multipath fading channels used in the simulation

| | |
|-----------------|--|
| Doppler shift | 5 Hz |
| Path delay (ns) | 0, 30, 70, 90, 110, 190, 410, 1400 |
| Path gain (dB) | 0, -1, -2, -3, -8, -17.2, -20.8, -26.8 |

When $CR=3/4$, the characteristics of models B and C are much worse than those of model A. This is because the number of pilots is the same. This is probably due to the fact that the subcarrier spacing is increased under the same condition of the number of pilots.

For model D, when $CR=1/3$, BER did not satisfy the 10^{-4} point. When $CR=3/4$, the BER did not satisfy the 10^{-2} point. This indicates that if the CP length is extremely small compared to the delay of the reflected wave, no matter how good the propagation environment is, the BER characteristics will not improve.

CONCLUSION: In this paper, we clarified the transmission performance against the subcarrier spacing of OFDM in multipath fading channels.

Keywords

Mobile communications, OFDM, Multipath fading, EPA models, Subcarrier Spacing

References

- [1] H. Otsuka, R. Tian, and K. Senda, "Transmission Performance of an OFDM-Based Higher-Order Modulation Scheme in Multipath Fading Channels," *Journal of Sensor and Actuator Networks*, no. 8(2), vol. 19, March 2019.
- [2] D. Kosuge and H. Otsuka, "Transmission Performance of 256-QAM for Subcarrier Spacing of OFDM under Fading Environment," *IEICE Communications Society Conference*, B-5-2, Sept. 2020.

User throughput improvement by three-dimensional beamforming in mobile systems*

Yuji Omura ^{1,a,*}, Hiroyuki Otsuka ^{1,b}

¹ Graduate School of Engineering, Kogakuin University, Tokyo, Japan

^a cm20012@ns.kogakuin.ac.jp, ^b otsuka@cc.kogakuin.ac.jp

Abstract

INTRODUCTION: One of the objectives of fifth-generation (5G) mobile systems is to increase system capacity and data rates [1]. Three-dimensional beamforming (3D-BF), in which antenna beams can be individually tailored to each user equipment (UE) in the elevation domain through the use of a massive MIMO antenna architectures, is key technology for achieving 5G. This enables directs signal transmission toward a target UE, potentially increasing the signal-to-interference plus noise ratio (SINR) while reducing the interference directed to adjacent cells and other UE [2].

PROPOSED SCHEME: In the beam management for 3D-BF, eNB transmit reference signals for beam measurement, i.e., sweeps Tx beam and UE measures the received SINR of each beam, and then reports the results to the eNB. Then, the eNB decides best Tx beam and optimal MCS based on the results from UE. Table 1 shows the antenna gain, azimuth 3 dB beamwidth, and elevation 3 dB beamwidth as parameters of the number of beams for the eNB Tx sector antenna, assuming that the maximum azimuth-plane and elevation-plane beams are eight and three, respectively. We use 25 different MCS indexes in downlink assigned to the UE, as listed [3], where five types of modulation scheme are used: QPSK, 16-QAM, 64-QAM, 256-QAM, and 1024-QAM.

Table 1. Beam Parameters in 3D-BF

| Number of beams per sector | 1 (Non BF) | 3 | 6 | 9 | 12 | 15 | 18 | 21 | 24 |
|--------------------------------|------------|------|------|------|------|------|------|------|------|
| Max. Tx antenna gain (dBi) | 14 | 18.8 | 21.8 | 23.5 | 24.8 | 25.8 | 26.7 | 27.2 | 27.8 |
| Azimuth 3 dB beamwidth (deg.) | 70 | 70 | 35.0 | 23.3 | 17.5 | 14.0 | 11.7 | 10.0 | 8.8 |
| Elevation 3dB beamwidth (deg.) | 10 | 3.3 | | | | | | | |

SIMULATION RESULTS: Figure 1 shows the average and 5-percentile user throughput versus the number of Tx beams. Both the average and 5-percentile user throughput increase as the number of Tx beams increases. For example, 15 beams can improve the average and 5-percentile user throughput by approximately 2.0 and 1.7 times compared with the non-BF, respectively. Similarly, 24 beams can improve the average and 5-percentile user throughput by approximately 2.2 and 1.8 times compared with the non-BF, respectively. Figure 2 is the analysis of the use rate of each modulation scheme in downlink MCS versus the number of Tx beams. The use of 15 and 24 beams can increase the use rate of 1024-QAM by 12% and 17% for all UEs, respectively.

CONCLUSION: Using system-level computer simulations, we provided the transmission performance of mobile networks that use a MCS incorporating 1024-QAM and a beam-based transmission in downlink 3D-BF. We also clarified the use rate of each modulation scheme in the downlink MCS versus the number of beams in 3D-BF.

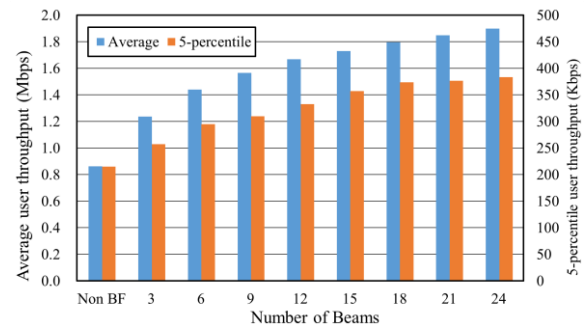


Fig. 1. Average and 5-percentile user throughput versus the number of Tx beams.

* Oral paper presentation

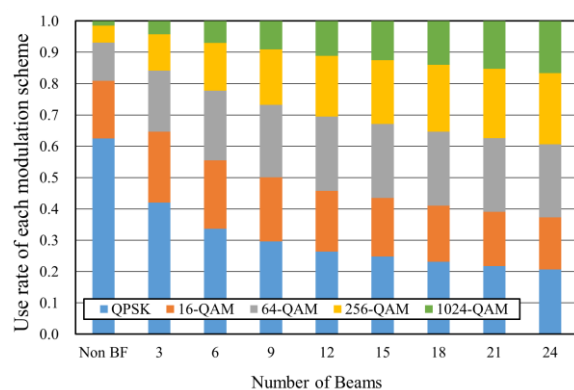


Fig. 2. Modulation scheme ratio used in MCS versus the number of Tx beams.

Keywords

mobile communication, 3D beamforming, beam based transmission, 1024-QAM, user throughput

References

- [1] S.Satoshi, T.Okuyama, Y.Inoue and Y.Kishiyama, "5G Multi Antenna," NTT DOCOMO Technical Journal, Vol.23, No.4, pp.33-39, Jan. 2016. (in Japanese)
- [2] Y. Omura, F. Kemmochi, H. Utatsu, S. Satoshi and H. Otsuka, "User Throughput as a Function of Number of Beams using 3D-BF and 1024-QAM," IEICE General Conference, B-5-20, March 2020. (in Japanese)
- [3] Y. Omura, F. Kemmochi, K. Fujisawa and H. Otsuka, "Implementation of MCS Incorporating 1024-QAM and Beam-Based Transmission in 3D-BF," in Proc. VTC2020-Spring, 1D-2, May 2020.

Realization of monolithic blue μ -LED pixels and their color conversion by phosphors*

H. Chikui ^{1,a*}, S. Takeda ¹, T. Abe ¹, T. Onuma ¹, T. Yamaguchi ¹, T. Honda ^{1,b}

¹ Department of Elect. Eng. & Electronics, Grad. School of Eng., Kogakuin University, Tokyo, Japan

^a cm20036@ns.kogakuin.ac.jp (Chikui), ^b ct11761@ns.kogakuin.ac.jp

Abstract

Micro-LED (μ -LED) displays are considered as promising technologies for developments of next generation displays. The display with high-brightness LED pixels is expected to be used for outdoor equipment [1]. Most of commercially developed μ -LED displays are built by integrating the flip-chip type μ -LED chips on the TFT or CMOS circuits. However, there still exists critical issues on cost-effective mass-transfer techniques to precisely handle huge numbers of μ -LED chips. A monolithic integration method realizes simultaneous miniaturization and mounting the μ -LEDs by etching the LED wafer. The use of phosphors makes it possible to produce full-color μ -LED display with low time costs. In this study, blue μ -LED pixels are fabricated using the inductively-coupled-plasma reactive-ion-etching (ICP-RIE) and color conversion was demonstrated using green and red phosphors.

The blue LED structure was grown on (0001) sapphire substrate by metalorganic vapor phase epitaxy. It consists of a 2.5- μ m-thick unintentionally-doped (UID) GaN, 1.0- μ m-thick Si-doped n-type GaN, a total of 100-nm-thick five periods of GaInN/GaN multiple quantum-well emission layer, and a 100-nm-thick Mg-doped p-type GaN. The fabrication processes for μ -LED pixels are schematically shown in Fig. 1. After annealing the LED wafer in a nitrogen atmosphere to activate acceptors in the p-type GaN, a 200-nm-thick Ni metal was deposited by an electron beam (EB) evaporation method. After patterning the Ni metal by photolithography and wet chemical etching, the LED wafer was selectively etched for 1 min. and 20 sec. by ICP-RIE. Then, to make n-GaN contacting layer, the LED wafer was patterned by photolithography and Ni mask was selectively wet etched followed

by the ICP-RIE etching for 16 sec. Then, to form the n-type electrode, the LED wafer was patterned by photolithography and a total of 110-nm-thick Ti/Al/Ni/Au metal were deposited by the EB evaporation. The initial Ni mask was used as a p-type electrode. The μ -LED mesa structure was evaluated by field emission-scanning electron microscope (FE-SEM), current-voltage (I-V) characteristics, and emission spectrum.

As shown in Fig. 2, well-defined 100 \times 70 μ m² size square-shape blue μ -LED mesa structure was fabricated without forming etching damage on the surface. The current-voltage characteristics showed a rectifying property with a threshold voltage of 3 V as shown in Fig. 3(a). The μ -LED showed a vivid blue light with a peak wavelength at 463 nm though the Ni p-electrode interrupts the light extraction and the light came out only from the side walls as shown in Fig. 3(b) and 3(c). As a preliminary study, green and red color phosphors were coated on a 200 \times 300 μ m² blue LED chips. The external quantum efficiency was evaluate using the integrated sphere. The color conversion efficiencies for the green and red color phosphors were respectively extracted as 43.0 and 2.26%. The study clarifies future realization of full-color μ -LED pixels by combining the phosphors with the μ -LEDs.

Keywords

micro-LED, display, ICP-RIE, monolithic, pixel

References

- [1] G. Biwa, The Institute of Image Information and Television Engineers **73**, pp.939~942 (2019).

* Poster paper presentation; this work was supported in part by Takahashi Industrial & Economic Research Foundation

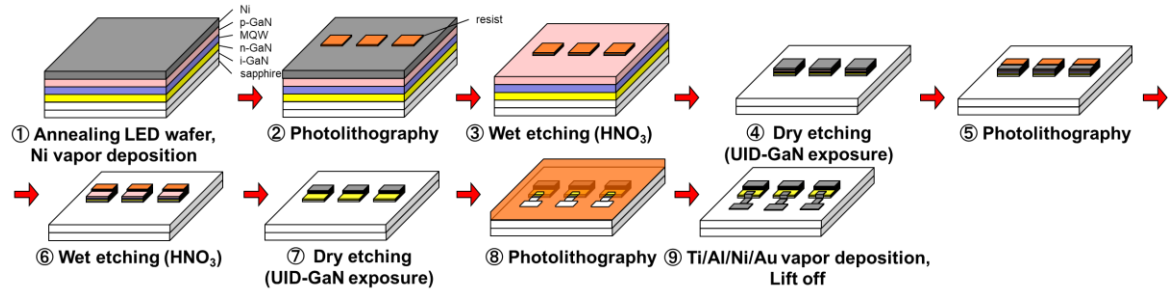


Figure 1: Schematic diagram of fabrication processes for μ -LED pixels.

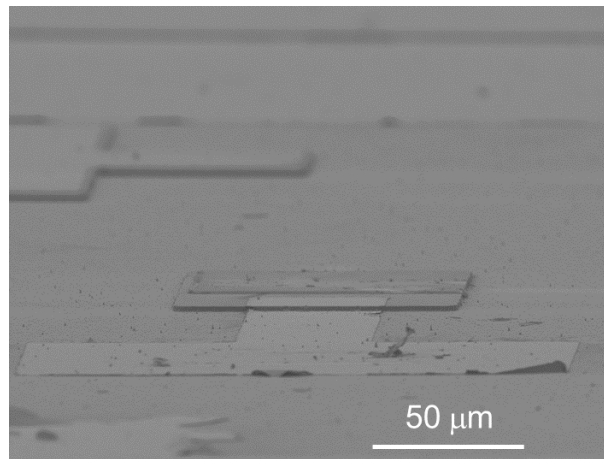


Figure 2: (a) Bird's-eye view SEM image.

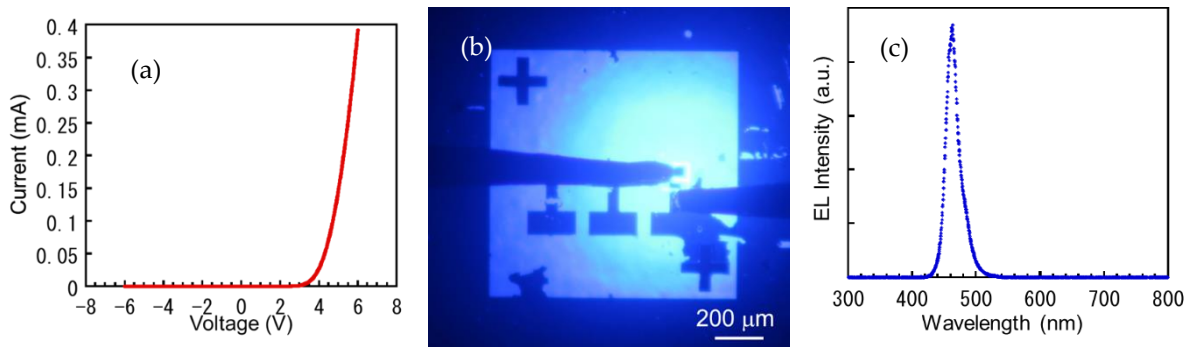


Figure 3: (a) Current-voltage characteristics of μ -LED, (b) Emission image operated at 6 V and 0.75 mA, (c) Emission spectrum of μ -LED operated at 6 V and 0.75 mA.

Parametric study of fabrication processes of micro-LED array and characterization of emission properties*

Shoma Takeda ^{1,a*}, Hiroyoshi Chikui ¹, Tomohiro Yamaguchi ¹, Takeyoshi Onuma ¹, Tohru Honda ¹

¹ Department of Electrical Engineering & Electronics, Graduate School of Engineering, Kogakuin University, Tokyo, Japan

^a cm19031@ns.kogakuin.ac.jp

Abstract

In recent years, micro-LED display is expected to be applied to smart phones, wearable devices and virtual-reality devices, since LED has favorable characteristics such as high brightness, high contrast, low power consumption and long life-time [1]. However, the display manufacturing technology still has challenging issues in mass production because it requires a large number of micro-LEDs and is difficult to place accurately. The monolithic integration technology widely used in the industry since it enables miniaturization and pattern transfer. It is expected to bring a solution to solve the issues in micro-LED manufacturing [2]. In this study, fabrication of monolithic micro-LED arrays ($30 \times 30 \mu\text{m}^2$) is demonstrated by etching the LED wafer using the inductively-coupled-plasma reactive-ion-etching (ICP-RIE) method. Electroluminescence (EL) properties are measured to evaluate the processes.

The blue LED structure was grown on (0001) sapphire substrate by metalorganic vapor phase epitaxy. It consists of a conventional structure, i.e., 2.5- μm -thick unintentionally-doped (UID) GaN, 1.0- μm -thick Si-doped n-type GaN, a total of 100-nm-thick five periods of GaInN/GaN multiple quantum well (MQW) emission layer, and a 100-nm-thick Mg-doped p-type GaN contacting layer. As schematically shown in Fig. 1, a 3-nm-thick nickel and a 100-nm-thick ITO stack layers were deposited on top of the LED wafer using electron beam (EB) evaporation method to form a current spreading layer for the p-type GaN contacting layer. Then, the Ni/ITO was patterned by photolithography followed by

wet etching with hydrochloric acid and nitric acid. And, the partially exposed LED structure was etched down to the n-type GaN layer using ICP-RIE. The ICP-RIE was conducted using chlorine, boron trichloride, and argon gases with a mixture ratio of 9:1:2. The structure was further patterned by photolithography to partially expose the n-type GaN contacting layer on the micro-LEDs, and simultaneously to isolate the micro-LEDs by etching down to the UID GaN layer. Finally, line electrodes were formed on the n-contacting layer by depositing Ti (20 nm) / Al (20 nm) / Ni (20 nm) / Au (50 nm) and lift-off. The processes were evaluated by measuring the current-voltage (I-V) characteristics and EL spectra at room temperature.

I-V characteristic is shown in Fig. 2. The micro-LED showed blue emission at the operating voltage higher than 3.5 V. As shown in Fig. 3, well-aligned $30 \times 30 \mu\text{m}^2$ micro-LED arrays are monolithically formed, and distinct EL emission was observed from the micro-LED by virtue of selective hole injection through the Ni/ITO current spreading layer formed on the p-GaN surface. As shown in Fig. 4, EL with a peak wavelength of 463 nm was observed from the micro-LED. The observations ensure that the etching rate is precisely controlled and the etching depth is enough to isolate the micro-LEDs. The observation of EL from the well-aligned monolithic micro-LED arrays also ensures the effective manufacturing the micro-LED display by the monolithic integration technology, resulting in a significant reduction in time cost.

* Poster paper presentation; this work was supported in part by Takahashi Industrial & Economic Research Foundation

In summary, fabrication of monolithic micro-LED arrays ($30 \times 30 \mu\text{m}^2$) was demonstrated by etching the LED wafer using the ICP-RIE method. The results indicate a possibility to fabricate the micro-LED display using monolithic integration technology.

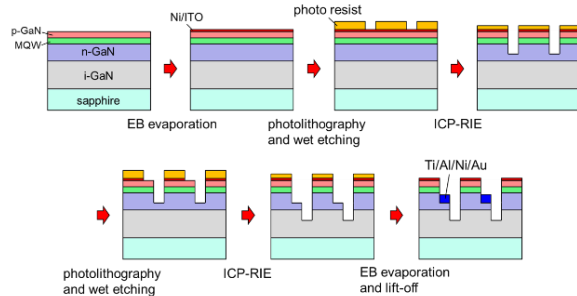


Fig. 1. Schematic diagram of fabrication process.

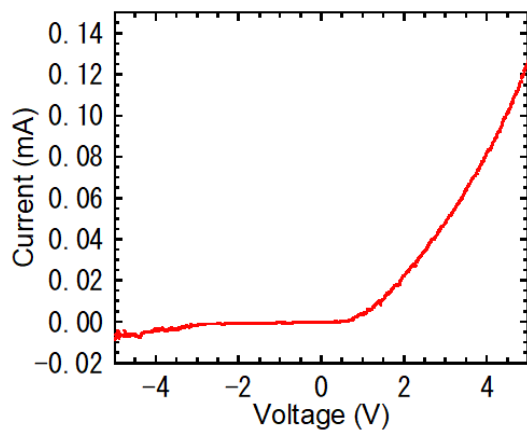


Fig. 2. I-V characteristic of micro-LED.

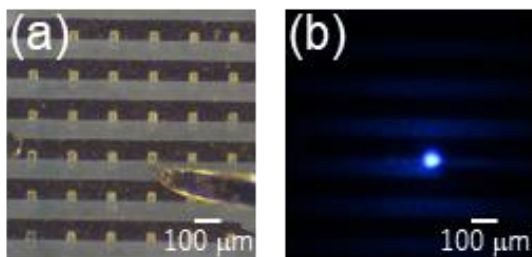


Fig. 3. Optical microscope images of (a) micro-LED array and (b) EL emission operated at 5 V and 0.13 mA.

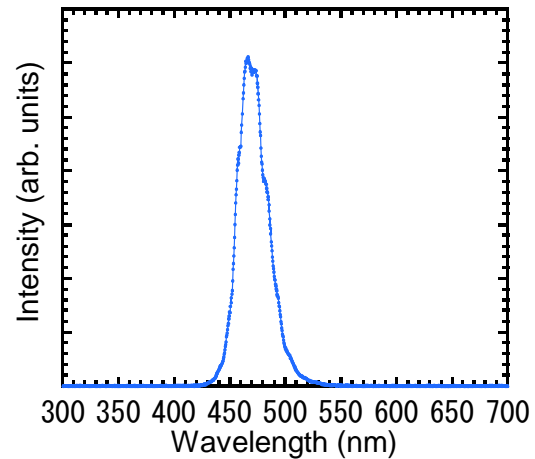


Fig. 4. EL spectrum of micro-LED operated at 5 V and 0.13 mA.

Acknowledgement

This work was supported in part by Takahashi Industrial and Economic Research Foundation

KEYWORDS

micro-LED, ICP-RIE, monolithic integration, display, electroluminescence

REFERENCES

- [1] Tingzhu Wu *et al.*, 2018. Mini-LED and Micro-LED: Promising Candidates for the Next Generation Display Technology. *Appl. Sci.* **8**, 9.
- [2] Wei Guo *et al.*, 2020. Wafer-Level Monolithic Integration of Vertical Micro-LEDs on Glass. *IEEE Photon. Technol. Lett.* **32**, 12.

Improving belief propagation decoding performances of polar codes using permuted factor graphs*

Naoya Takahashi ^{1, a*}, Hidetoshi Saito ^{2, b}

¹Graduate School of Electrical & Electronic Engineering, Kogakuin University, Tokyo, Japan

²Department of Electrical & Electronic Engineering, Kogakuin University, Tokyo, Japan

^acm19029@ns.kogakuin.ac.jp, ^bh-saito@cc.kogakuin.ac.jp

Abstract

INTRODUCTION: Arikan's polar codes are designed by the theory of channel polarization [1]. It is well known that polar codes can be strictly proven to achieve the theoretical Shannon limit for a binary input discrete memoryless channels. For the typical decoding algorithms of polar codes, both of successive cancellation (SC) and belief propagation (BP) decoding algorithms are known [1],[2]. Moreover, derived from SC decoding, SC list (SCL) decoding is proposed and cyclic redundancy check (CRC) aided SCL (CA-SCL) decoding exhibits the superior decoding performance in comparison with SC or BP decoding [3]. On the other hand, the SCL decoding algorithm still suffers from the low throughput performance. However, the BP decoding algorithm can be executed in parallel, which allows the BP decoder to achieve the high throughput performance. Moreover, the over representation of the FG employed post BP iteration is improve the error correction performance [5]. Although, the error correction performance of polar BP decoding is inferior to the performance of the conventional CA-SCL decoding. Thus, to improve the error correction performance of polar BP decoding, we show the new polar BP decoding method by using multiple FG and amplifying the minimum value of log-likelihood ratio (LLR) of an estimated codeword symbol. Our simulation results show that the block error rate (BLER) performance of a CRC aided polar code with the codeword length of 1024 is superior to the BLER performance of the conventional polar BP decoding [5] about 0.5 dB at the BLER of 10^{-4} . When increasing the number of FG, the BLER of the proposed polar BP decoding method shows the almost same BLER performance of the CA-SCL with a list of size $L = 4$.

POLAR CODES: The concept of channel polarization transforms independent channels into polarized channels by channel combining and splitting [1]. The code rate is $R = K/N$, where K is information bits and N is the codeword length (or block length). From the idea of channel polarization, the K reliable channels

are used to transmit information bits, while the other $N - K$ channels are used for frozen bits and set to zeros. For a given polar code with the rate $R = K/N$, the K information bits and the other $N - K$ frozen bits are determined by Bhattacharyya parameters [4]. The block length of a polar code is given by $N = 2^m$ and the generator matrix \mathbf{G}_N of this (N, K) polar code which can be recursively defined as

$$\mathbf{G}_N = \mathbf{F}^{\otimes m}, \mathbf{F} = \begin{bmatrix} 1 & 0 \\ 1 & 1 \end{bmatrix},$$

where $\mathbf{F}^{\otimes m}$ denotes the m^{th} Kronecker power of \mathbf{F} . The message \mathbf{u} is composed of K information bits and encoded to a codeword $\mathbf{x} = \mathbf{u} \cdot \mathbf{G}_N$. In this research, the codeword is modulated by binary phase shift keying (BPSK) and transmitted over additive white Gaussian noise (AWGN) channels.

BELIEF PROPAGATION DECODING: BP decoding iteratively propagate messages in parallel and can be estimate the codeword $\hat{\mathbf{x}}$ and the message $\hat{\mathbf{u}}$. The messages are passed along the factor graphs in an iterative manner from right to left and from left to right until the maximum number of iterations N_{\max} is reached, or an early termination condition is satisfied in decoding. Two examples of early termination conditions shown as below [6]:

1. \mathbf{G} -based: $\hat{\mathbf{x}} = \hat{\mathbf{u}} \cdot \mathbf{G}_N$ is satisfied.
2. CRC-based: the parity checks of the concatenated CRC calculation are satisfied.

BP DECODING ON PERMUTED FACTOR GRAPHS: The permutation of FG are a way to provide multiple representations of a single BP decoder. $((\log_2 N)!$ permutations in codeword length N polar codes [5]). Different FG representations of a polar code are given by the permutation of FG layers. In [5], parallel BP decoders are applied to a set of randomly selected FG for a given polar code concatenated with a CRC. This BP decoding scheme [5] improves the error correction performance. However, the permutation of FG layers results in different BP scheduling and requires the design of different BP decoders for each permutation.

* Poster paper presentation

Further, to achieve the reasonable error-correction performance, the optimal selection from a large number of permutations of makes this decoding scheme too complex for practical applications.

PROPOSED BP DECODING: The most common causes of BP decoding failures are decided by the minimum sizes of the stopping sets and trapping set. There are several ways to mitigate these causes. One way uses a permuted FG introduced in [4]. The other way uses BP bit flip (BPF) decoding that amplifies the LLR value of the error prone estimated information bit index [7]. Therefore, we propose a decoding method to amplify an estimated codeword symbol with the minimum LLR value obtained in the decoding process using a way of suppressing the BP decoding failures caused by the stopping and trapping sets. Unlike conventional BPF decoding, the minimum LLR value of a symbol in an estimated message is amplified to positive or negative infinity fold in the decoding result. However, if the amplified correction LLR value doesn't indicate a correct sign value, an error will be detected. Thus, the sign of the LLR value is reversed and corrected in predetermined iterations N_{it} . After all the steps of proposed decoding method were completed, the other FG are selected and the next BP decoding process is performed. Here, we define the symbol $N_{it,max}^p$ as the maximum iterations for each FG and q_{max} as the total number of FG. If $N_{it,max}^p > N_{it}$, the overall maximum number of iterations $N_{max} = N_{it} \cdot q_{max}$. Table 1 shows the setting parameters in this research.

Table 1 The setting parameters for BP decoding.

| | |
|----------------|-----------|
| N_{it} | 100 |
| $N_{it,max}^p$ | 300 |
| q_{max} | 10,32 |
| N_{max} | 3000,9600 |

SIMULATION RESULTS: Fig. 1 shows the BLER performances of (1024, 512) polar codes concatenated with the 10 CRC bits (CRC-10) and $q_{max} = 10$. Both of \mathbf{G} -based and CRC-based conditions are used for early decoding termination. The BLER performance of the proposed BP decoding method is slightly superior to that of the original BP decoding method at a high signal-to-noise ratio (SNR). If we use the proposed BP decoding method with MPFG, we improve SNR about 0.5 dB compared to the conventional BP decoding method [5] at the BLER of 10^{-4} . Moreover, Fig. 2 shows the BLER performances of the proposed BP decoding methods with MPFG and the conventional CA-SCL decoding methods for (1024, 512) polar codes. From Fig. 2, it is found that the BLER performance of the proposed BP decoding methods with MPFG and Permuted-32 is almost same

performance of the conventional CA-SCL decoding method with CRC-8 and $L = 4$.

CONCLUSION: In this research, we propose the new effective modified BP decoding method. As a result, proposed decoding method is able to improve the SNRs in both of the BLER performances of the conventional decoding methods [3], [5] by computer simulation.

References

- [1] E. Arıkan, *IEEE Trans. Inf. Theory*, vol. 55, no. 7, pp. 3051-3073, June 2009.
- [2] E. Arıkan, in *Proc. ISBC 2010*, Melaka, Malaysia, July 11-14, 2010.
- [3] I. Tal and A. Vardy, *IEEE Trans. Inf. Theory*, vol. 61, no. 5, pp. 2213-2226, May 2015.
- [4] N. Doan, et al., *GLOBECOM 2018*, WCS-I2, Abu Dhabi, United Arab Emirates, 9-13 Dec. 2018.
- [5] K. Niu and K. Chen, *IEEE Commun. Lett.*, vol. 16, no. 10, pp. 1668-1671, Oct. 2012.
- [6] B. Yuan and K. K. Parhi, *IEEE Trans. Sig. Process.*, vol. 62, no. 24, pp. 6496-6506, Dec. 2014.
- [7] Y. Yu, Z. Pan, N. Liu, and X. You, *IEEE Access*, vol. 7, pp. 10937-10946, 2019.

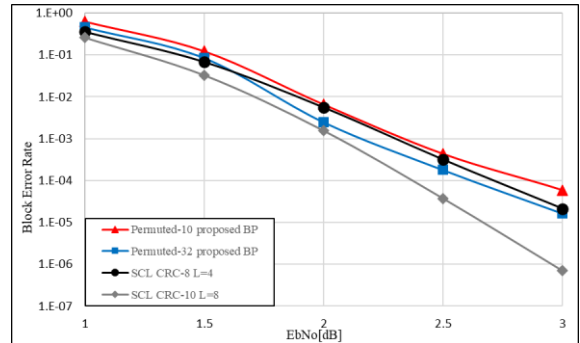


Fig. 1 BLER performances of (1024, 512) polar codes.

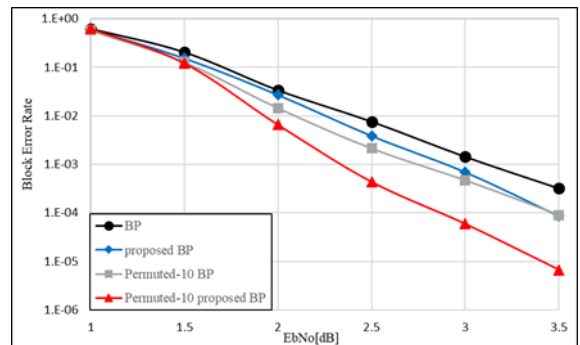


Fig. 2 The BLER performances of proposed BP and CA-SCL decoding methods

Fundamental research for full duplex communications*

Rion Okazaki ^{1, a*}, Hiroyuki Otsuka ^{1, b}

¹ Graduate School of Engineering, Kogakuin University, Tokyo, Japan

^a cm20013@ns.kogakuin.ac.jp, ^b otsuka@cc.kogakuin.ac.jp

Abstract

INTRODUCTION: Full duplex communications (FD) can improve the system capacity of mobile systems significantly compared with traditional frequency division duplex (FDD) or time division duplex (TDD), in which FD enables simultaneous transmission and reception in the same carrier frequency^{[1], [2]}. The application of FD to fifth-generation (5G) mobile systems has been discussed worldwide, however, the FD has challenge issue to suppress self-interference which is signal leakage from the transmitter to its own receiver. First, we analyze the signal power of self-interference for the distance between transmitter and receiver antennas at a base station such as evolved node B (eNB) in LTE mobile system. Then, we propose the two-stage self-interference canceller in which transversal filter is used in the baseband domain after the self-interference is approximately removed in radio frequency domain. In this paper, we show the configuration and principle of the proposed cancellation technique.

MECHANISM OF SELF-INTERFERENCE: When the down and uplinks use same carrier frequency (f_1) simultaneously (t_1) between base station (BS) and user equipment (UE), the transmission in the downlink interferes with the reception in the uplink as shown in Fig. 1. This type of interference is called “self-interference”. In this case, the self-interference signal power generated at the BS receiver could easily exceed the power of desired signal from UE. Therefore, it is important for FD to cancel or eliminate the self-interference.

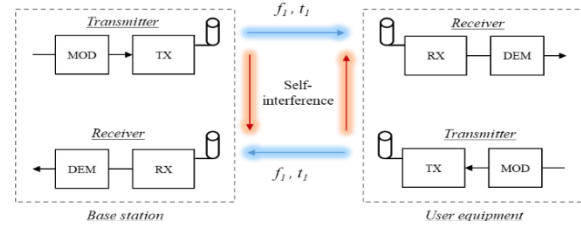


Fig. 1. Mechanism of self-interference

ANALYSIS OF SELF-INTERFERENCE: We investigate the signal power of self-interference for the distance between transmitter and receiver antennas at BS. Table 1 shows the primary parameters used in the analysis. The carrier frequencies, f_c , are 2 and 28 GHz. The transmission power of BS, W , are +46 and +22 dBm for $f_c = 2$ and 28 GHz, respectively. The path loss (PL) between the transmitter antenna and receiver antenna is specified in Eq. 1, where, d is the distance between the transmitter antenna and receiver antenna.

$$PL(dB) = 20 \log_{10} \left(\frac{4\pi d f_c}{c} \right) \quad (1)$$

The signal power of self-interference, P , is calculated as shown in Eq. 2, where, I_{so} is spatial isolation with respect to transmitter and receiver antennas considering antenna gain and radiation direction.

$$P(dBm) = W - PL + I_{so} \quad (2)$$

This is assumed to be 12 dB in this paper. Figure 2 shows the P versus d for the two kinds of f_c . The power of thermal noise in the receiver is also shown in Fig. 2 by the dashed line, assuming that the noise bandwidth is 10 MHz and the noise figure is 3 dB. In the case of $f_c = 2$ GHz, when $d = 1$ m, P becomes -4.5 dBm. If d becomes 10 m the signal power of self-interference can be reduced by -24.5 dBm. For example, the self-interference must reduce by 76.5 dB to be the same power of thermal noise. When $f_c = 28$ GHz,

* Poster paper presentation

the self-interference must reduce by 29.6 dB to be the same power of thermal noise for $d = 10$ m.

Table 1. Primary parameters used in the analysis

| | | |
|--|----------|----------|
| Carrier frequency : f_c | 2.0 GHz | 28.0 GHz |
| BS Tx power : W | 46 dBm | 22 dBm |
| Antenna isolation between TX and RX: Iso | 12 dB | |
| Distance between BS Rx and BS Tx: d | 1 ~ 10 m | |

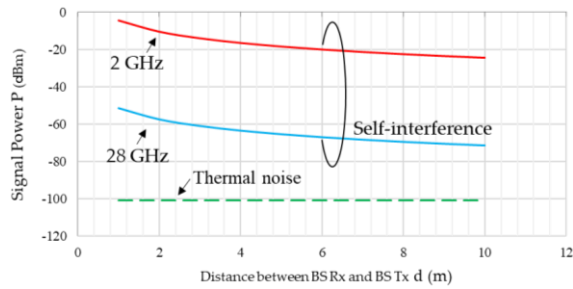


Fig. 2. Signal power P of self-interference versus d

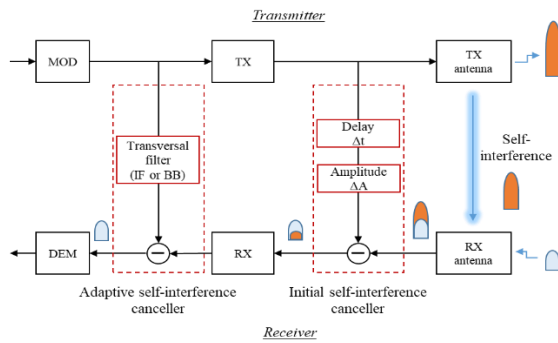


Fig. 3. Proposed self-interference canceller

FUTURE WORK: We propose the two-stage self-interference canceller in which transversal filter is used in the baseband domain, i.e., by the

use of adaptive self-interference canceller, after the self-interference is approximately eliminated in radio frequency domain, i.e., by the use initial self-interference canceller. Figure 3 shows the configuration of the self-interference canceller. The adaptive self-interference canceller in the latter stage can eliminate the residual self-interference due to the spatial channel fluctuation between the transmitter and receiver antennas.

CONCLUSIONS: We analyzed the signal power of self-interference with respect to the distance between the transmitter and receiver antennas in full-duplex communications. We also described the concept of the two-stage self-interference canceller using transversal filter.

Keywords

Mobile communications, full duplex, self-interference, transversal filter

References

- [1] J. II. Choi, M. Jain, K. Srinivasan, P. Levis, and S. Katti, "Achieving single channel, Full duplex wireless communication," in Proc. MobiCom2010, pp. 1-12, Sept. 2010.
- [2] K. Yamazaki, Y. Sugiyama, Y. Kawahara, S. Saruwatari, and T. Watanabe, "Preliminary evaluation of simultaneous data and power transmission in the same frequency channels," in Proc. WCNC2015, pp. 1237-1242, March 2015.

Telemedicine using TVWS technology for rural consultations in the Philippines*

Aaron Raymond See ^{1*}, Jolo Gerald Miel Tolentino ¹, Welsey Daniel Advincula ¹,
Chun-Ping Hsieh ¹, Renann Baldovino ², Nilo Bugtai ²

¹Department of Electrical Engineering, Southern Taiwan University of Science & Technology, Taiwan

²Manufacturing Engineering & Management Department, De La Salle University – Manila, Philippines

^a aaronsee@stust.edu.tw, ^b ma92b202@stust.edu.tw

Abstract

Access to proper healthcare is an especially rampant problem in the Philippines [1]. Limited by the geographic constraints found in provinces, most Filipinos must go through such lengths just to consult with medical professionals. The difficulty to seek medical help in these areas is a deterrent factor for Filipinos that have mild ailments [2]. Being able to discern whether your ailments are serious or mild, is a fine line that most Filipinos gamble to avoid unnecessary trips to the doctor. To address the problem, one can suggest internet consultation although fast stable internet connections are still considered to be a luxury in the country.

Recent studies have postulated the idea of Television White Space (TVWS) frequencies as a substitute for internet connectivity. According to Noguet et. Al, the affordability of White Space Devices (WSDs) in the market paves a way for free data transmission through the TVWS spectrum [3]. It was noted in a research done by Khalil et. Al, TVWS systems have an advantage over similar technology such as WiMAX, WiLD and Satellite communication [4]. Delving into remote consultation research, telemedicine via TVWS is conducted in far flung regions explored in developing countries such as Botswana [5]. TV whitespace pertains to the unoccupied TV frequency bands found in the VHF/UHF range. These frequency ranges serve as “guard bands” to prevent cross talk between adjacent occupied channels. Not only does it create a distinction between used channels, but it also serves as a medium for WSDs to

broadcast and receive data [6]. This paper explores the possible use of TVWS systems for real time consultation, circumventing the internet connection stability problem.

The data used for the setup, are ultrasound images obtained from a phantom model with a tumor inside. Subsequently, the images were used to test the data transmission of the experimental TVWS system in Tainan, Taiwan. Base station was set up within Southern Taiwan University of Science and Technology and the client station was at the Disaster Prevention Research Center to evaluate the data transmission setup. The system made use of a TVWS module (TDM-633S-base and TDM-633S-cpe by Hotware International Co., Ltd.) and video over internet protocol for video streaming as shown in Figure 1.



Fig 1. Video over internet protocol GUI

To evaluate the system, different metrics such as file size, transmission speed, total transmission time were observed in our analysis found in Table 1 and 2. It was noted that the

* Oral paper presentation

TVWS systems' transmission rate varied with distance.

Table 1. Base station to client station

| STUST to DPRC = 8.43 km | | | | |
|-------------------------|-----------|----------------|---------------------------|-------------------|
| Bandwidth (MHz) | Size (Mb) | Delay Time (s) | Transmission Speed (Mb/s) | Complete Time (s) |
| 5 | 5.97 | 25.29 | 0.67 | 34.21 |
| 5 | 11.98 | 23.53 | 0.53 | 46.27 |
| 5 | 89.97 | 23.67 | 0.66 | 160.97 |
| Average Speed | 0.62 Mb/s | | | |

Table 2. Client station to base station

| DPRC to STUST = 8.43 km | | | | |
|-------------------------|-----------|----------------|---------------------------|-------------------|
| Bandwidth (MHz) | Size (Mb) | Delay Time (s) | Transmission Speed (Mb/s) | Complete Time (s) |
| 5 | 5.97 | 0 | 0.26 | 22.91 |
| 5 | 11.98 | 0 | 0.29 | 41.83 |
| 5 | 246.97 | 0 | 0.29 | 841.65 |
| Average Speed | 0.28 Mb/s | | | |

Given the delay in data transfer in the system, the researchers believe that delay during consultation is inevitable. The research recommends incorporating image data compression techniques to improve the latency of consultation in telemedicine via TVWS. If internet problems persist, a TVWS systems can provide an inexpensive 2-way communication system for rural and urban sites, which resolves the problem regarding long distance travels for doctor consultation, although latency in data transfer must always be accounted for.

Keywords

Rural areas, telemedicine, television white space (TVWS), remote consultation, data transfer

References

- [1] Alipio, M., & Pregoner, J. 2020. Determinants of Healthcare Utilization among Senior Citizens in Davao City, Philippines. JPAIR Multidisciplinary Research Vol. 39 No. 1
- [2] Balangcod, T., & Balangcod, A. 2011. Ethnomedical knowledge of plants and healthcare practices among the Kalanguya tribe in Tinoc, Ifugao, Luzon, Philippines. Indian Journal of Traditional Knowledge 10(2):227-238
- [3] Noguet, D., Gautier, M. & Vincent, B. 2011. Advances in opportunistic radio technologies for TVWS. EURASIP Journal On Wireless Communications And Networking, 2011(1). doi: 10.1186/1687-1499-2011-170
- [4] M. Khalil, J. Qadir, O. Onireti, M. A. Imran and S. Younis. 2017. "Feasibility, architecture and cost considerations of using TVWS for rural Internet access in 5G,". 20th Conference on Innovations in Clouds, Internet, and Networks (ICIN), Paris, 2017, pp. 23-30,
- [5] Chavez A, Littman-Quinn R, Ndlovu K, Kovarik CL. 2016. Using TV white space spectrum to practise telemedicine: A promising technology to enhance broadband internet connectivity within healthcare facilities in rural regions of developing countries. J Telemed Telecare. 260-3.
- [6] L. Simić, M. Petrova and P. Mähönen, "Wi-Fi, but not on Steroids: Performance analysis of a Wi-Fi-like Network operating in TVWS under realistic conditions," 2012 IEEE International Conference on Communications (ICC), Ottawa, ON, 2012, pp. 1533-1538.

Printed 8-port MIMO antennas for 5G C-band access point applications*

Pin-Feng Chen ^{1,a}, Wen-Shan Chen ^{1,b*}

¹Department of Electronic Engineering, Southern Taiwan University of Science & Technology, Taiwan, R.O.C.

^aMA830216@stust.edu.tw, ^bchenws@stust.edu.tw

Abstract

INTRODUCTION: 5th Generation Mobile Networks^[1] has become the currently trend. The fast transmission speed and short transmission distance of 5G is also increasing. Therefore, MIMO technology is need for 5G. Some designs for 5G access point antennas^[2-3] have been published. In paper^[2], the microstrip line to excite the 4 slot elements, A T-shaped is cut in the middle of the slot element to increase isolation between the two input ports to more than 10 dB. In paper^[3], the three monopole strips, proposed antenna is formed by integrating have Broadband consequent. In the paper, a design of 8-port MIMO slot-loop antennas with a reflector of four bent slit will be proposed and examined. The design with broadband (3.4 - 4.2GHz) and good antenna gain could be applied to the application for 5G access point.

ANTENNA DESIGN AND APPLICATION BANDS: Fig. 1 shows the overall view of the design. And the Fig. 2 shows the detail antenna geometry and structure of the design. The proposed design consists of an antenna part and the part of reflector. The antenna part is composed of four slot-loop antennas, four slots, and eight ports feeding by microstrip lines. The reflector with four bent slit is also presented as the part of reflector. The two parts are implemented on the 1.6mm thickness FR4 substrate of dielectric constant 4.4, loss tangent of 0.0245. The sizes of the proposed MIMO antennas and the reflector are 75 mm × 75 mm × 1.6mm. The antenna uses the slot-loop feeding by microstrip line vertically to excite the required modes. The four slits printed on the ground plane of the MIMO antennas to increase

the isolation effect of the design. The four bent slits printed on the reflector reduce the mutual coupling between antennas.

The reflector is placed below the MIMO antennas at 9.8 mm, which is about one-eighth wavelength. The reflector could enhance the antenna gains of the design. Table 1 lists the detailed dimensions of the antenna.

Table 1. Detailed dimensions of the proposed antenna

| Parameter | W1 | W2 | W3 | W4 | W5 | W6 | |
|-----------|----|----|----|----|-----|------|----|
| Unit(mm) | 75 | 15 | 36 | 17 | 8.5 | 5.5 | |
| Parameter | L1 | L2 | L3 | L4 | L5 | L6 | L7 |
| Unit(mm) | 75 | 13 | 15 | 13 | 8.5 | 13.5 | 12 |

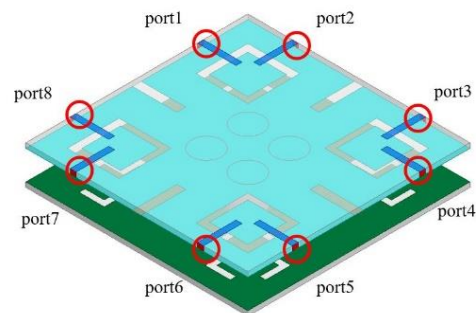


Fig. 1. Overall view of the proposed design

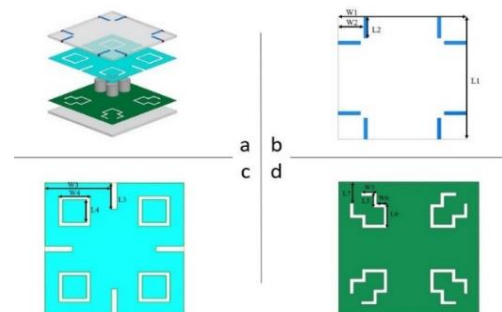


Fig. 2. Detail Antenna geometry and structure

* Poster paper presentation

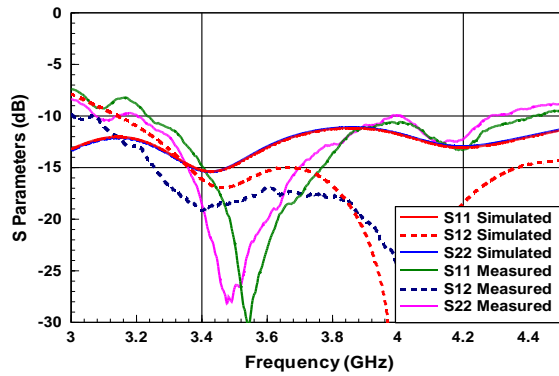


Fig. 3. Simulated and measured S_{11} , S_{12} , S_{22} of the design

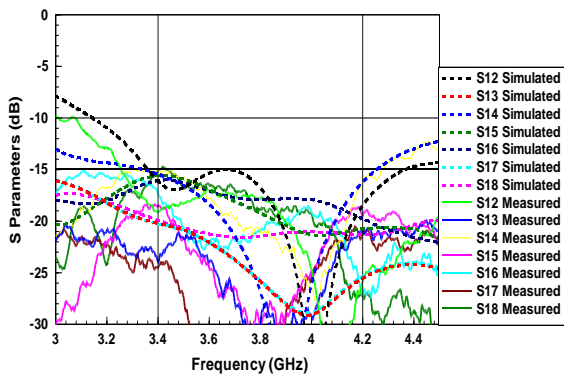


Fig. 4. Simulated and measured S_{ij} (when i is not equal to j) of the proposed design

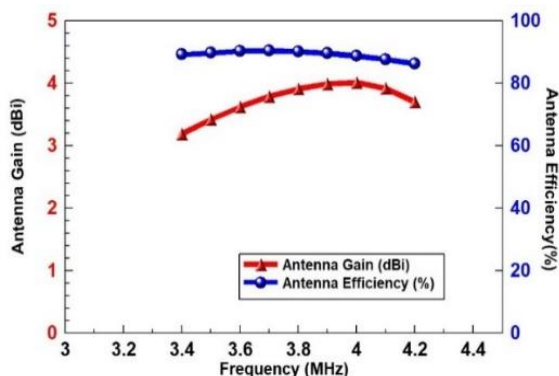


Fig. 5. Simulated gain and efficiency of the MIMO antennas at port1

SIMULATED AND MEASURED RESULTS: Fig. 3 shows the simulated and measured S_{11} , S_{12} , and S_{22} of the proposed design. It could be found the simulated and measured results could meet the frequency band of 5G C-band (3.4 -

4.2GHz). Fig. 4 shows the S_{ij} when i is not equal to j of the proposed design. The simulated and measured isolation is large than 15dB within the operating band. Fig. 5 shows the simulated gain and efficiency of the antenna at port1. The gain of the design is ranging from 3.19 to 4.01 dBi, and the efficiency of the design is ranging from 86 to 90.4%.

CONCLUSION: The design of 8-port Slot loop MIMO antennas for 5G C-band access point application has been proposed. The design uses the slot-loop antenna feeding by microstrip line. For improving the isolation of the design, four slits printed on the antenna ground plane and four bent slits on the reflector are introduced. The reflector used in the design could enhance the antenna gains. According to the simulated and measured results, the design with good performances and simulated antenna gains and efficiencies will be suitable for applications of access point antennas.

Keywords

MIMO antennas, access point, 5G C-band, 8-port, slot-loop, reflector with slits.

References

- [1] T. Tuovinen, N. Tervo and A. Parssinen, "Analyzing 5G RF System Performance and Relation to Link Budget for Directive MIMO," IEEE Transactions on Antennas and Propagation, vol. 65, no. 12, pp. 6636- 6645, 2017.
- [2] X. Hua, D. Wu, S. W. Cheung and Q. L. Li, "A Planar 8-port MIMO Antenna for 2.4GHz WLAN Applications," IEEE International Symposium on Antennas and Propagation & USNC/URSI National Radio Science Meeting, 2017.
- [3] Y. Li, B. Yu, H. Shen, L. Zhu and G. Yang, "An 8-Port Planar UWB MIMO Antenna for Future 5G Micro Wireless Access Point Applications," International Applied Computational Electromagnetics Society Symposium (ACES), 2017.

Four-port MIMO antennas on USB device for 5G C-band applications*

Guan-Hua Huang^{1,a}, Wen-Shan Chen^{1,b*}

¹Department of Electronic Engineering, Southern Taiwan University of Science & Technology, Tainan City, Taiwan

^aMA830122@stust.edu.tw, ^bchenws@stust.edu.tw

Abstract

The four-port MIMO antennas of USB device for 5G C-band is proposed and investigated. The overall size of the design is 35mm × 28mm × 5mm. The design is implemented on the substrate with permittivity of 4.4 and thickness of 0.8 mm. There are four antennas on the design and the antenna return loss and isolations are all larger than 10dB with the operating band. From the results, the design could be applied the band of 5G C-band (3.4 - 3.6 GHz). And compact size, good performances and The function with 4×4 MIMO antennas is good for application of USB dongle devices.

INTRODUCTION: With the rapid development of wireless communications, speed of wireless products continues to increase. Using multiple-input multiple-output antennas^[1-3] is a promising method to achieve the goal. It can offer improvement in transmission rate and distance without additional bandwidth. However, designing multiple antennas in a limited space will make the antennas affect each other, so it is necessary to design isolation mechanism to reduce interference between them. For isolation design for MIMO antennas in dongle devices, most design used designs with neutral line^[1] or T-bar^[2], or through special design, the isolation effect can be reduced without isolation mechanism^[3]. The next section will be describes antenna geometry and detailed dimensions.

ANTENNA DESIGN AND APPLICATION BANDS: Fig. 1 shows the overall view of the design. The overall dimensions of the design are 35mm × 28mm × 5mm. The design is implemented on the substrate with permittivity of 4.4 and thickness of 0.8 mm. There are four antennas on the design. Antennas 1 and 2 are

coupled PIFA antennas with a grounded T-shaped isolation structure. They are placed on the top edge of the ground plane, and the bend PIFAs are adjusting to reach a broadband frequency of 3.3 - 4 GHz. The antenna 3 and 4 are open slots fed by microstrip lines. They are vertically placed to the ground plane, and adjusted to match the band of 3.4 -3.6 GHz. By proper adjusting the dimensions of the design, a design of 4×4 MIMO antennas for USB devices could be achieved. Fig. 2 shows the geometry of the design. In Table 1, the antenna detailed dimensions are also listed in the paper.

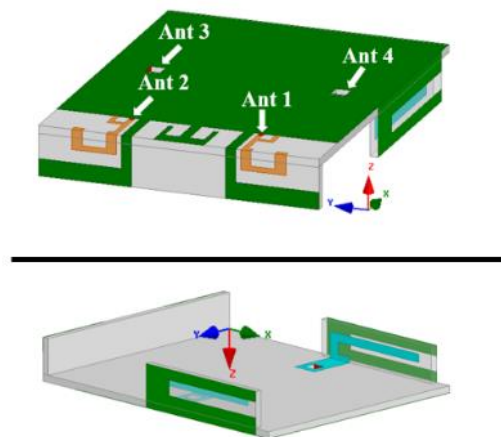


Fig. 1. Overall view of proposed design

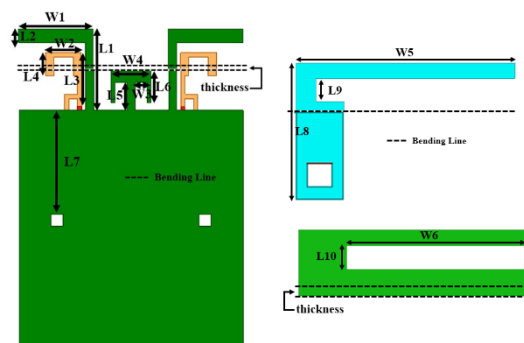


Fig. 2. Antenna configuration and geometry

* Poster paper presentation

Table 1 Detail dimensions of the proposed design

| Parameters | W1 | W2 | W3 | W4 | W5 | W6 | L1 | L2 |
|------------|-----|-----|-----|----|-------|------|------|-----|
| Unit (mm) | 9.3 | 4.5 | 1.5 | 5 | 13.75 | 13.4 | 10 | 1.7 |
| Parameters | L3 | L4 | L5 | L6 | L7 | L8 | L9 | L10 |
| Unit (mm) | 6.5 | 2.6 | 3.5 | 4 | 13 | 8.45 | 1.45 | 1.8 |

SIMULATED AND MEASURED RESULTS: Fig. 3 shows the simulated and measured S -parameters of the design. From the results, The S_{11} to S_{44} are all less than -10 dB over the 5G C-band. Fig. 4 shows the simulated and measured S_{ij} when i is not equal to j of the design. The isolation is all larger than 10 dB within the operating band.

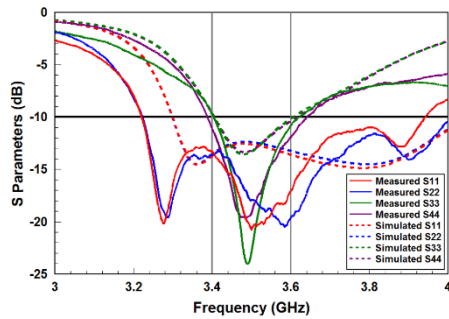
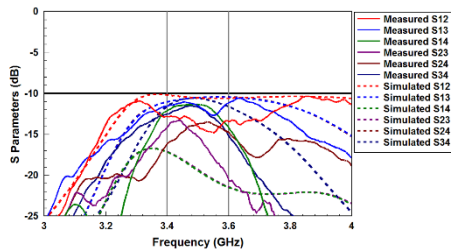
Fig. 3. Measured and simulated S_{11} - S_{44} of the proposed design

Fig. 4. Measured and simulated isolation of the proposed design

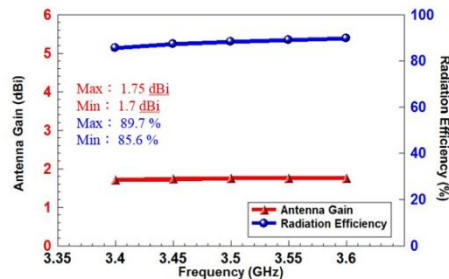


Fig. 5. Simulated gains and efficiencies of the design at port 1

The simulated antenna gains and efficiencies of the design at port 1 are shown in Fig. 5. From the results, the gain of the frequency band is ranging from 1.7 to 1.75 dBi, and the efficiency of the frequency band is ranging from 85 to 89% .

CONCLUSION: The design of the four-port MIMO antennas of USB device for 5G C-band has been proposed. Antennas 1 and 2 are designed as coupled PIFAs. In order to improve isolation, T-type isolation mechanism is adopted. The antenna 3 and 4 are open slots fed by microstrip lines. From the results, The isolations between them are all larger than 10 dB within the operating band. The design with 4×4 MIMO antennas, compact size, and good performances is suitable for USB dongle devices.

Keywords

USB dongle, four-port, MIMO, 5G C-band

References

- [1] W.-S. Chen, Y.-C. Lai and C.-Y.-D. Sim, "MIMO dongle antenna design for next generation mobile communication system," 2017 IEEE International Conference on Computational Electromagnetics (ICCEM), March, 2017.
- [2] W.-S. Chen, C.-S. Lin and H.-M. Liu, "MIMO antennas with U-shaped ground and three protruded strips for WLAN applications," 2015 International Workshop on Antenna Technology (iWAT), March, 2015.
- [3] W.-S. Chen, H.-J. Hsu, and K.-C. Liao, "Spiral-type Monopole Antennas for WLAN MIMO Systems," 2016 IEEE 5th Asia-Pacific Conference on Antennas and Propagation (APCAP), Feb., 2016.

MIMO antennas of coupled-fed PIFAs for laptop computers*

Ching-Hsiang Yang ^{1,a}, Yue-Ying Lin ^{1,b}, Wen-Shan Chen ^{1,c*}

¹ Department of Electronic Engineering, Southern Taiwan University of Science & Technology, Taiwan, R.O.C.

^a 4a636032@stust.edu.tw, ^b 4a636014@stust.edu.tw, ^c chenws@stust.edu.tw

Abstract

INTRODUCTION: 5G application and MIMO technology are all need at laptop computer. Therefore, the MIMO antennas operating at 5G frequency band is implemented in antenna design of laptop computers. There are some published papers^[1-4] for antennas for laptop computers. In these papers, couple-fed PIFA/IFA^[1], loop antennas^[2], IFAs^[3] and monopole^[4] were adopted to design the MIMO antennas. To reduce the height of the antennas and maintain the multi-band operation, a new design of MIMO antennas will be presented in the paper.

ANTENNA DESIGN AND APPLICATION BANDS: Fig. 1 shows the geometry of the design: (A-1) is the full view of the design; (A-2) is the side view of antennas; (A-3) is the detailed geometry of the proposed MIMO antennas. The overall size of the antenna is 4.2 mm × 45 mm × 3.2 mm (L×W×H). A copper sheet of 200 mm × 260 mm (L×W) is used to act as a ground of 13-inch laptop computer. The antenna uses an inverted L-shaped strip with bending and a couple-fed monopole connected to the ground. The metal patch with an L-strip connected to the ground is feed to the RF input. The design is printed on an FR4 substrate with a dielectric constant of 4.4, a loss tangent of 0.0245, and a thickness of 0.8mm. The detailed dimensions are also listed in Table 1. The design could be operated at the frequency bands of WLAN2.4GHz (2.4 - 2.484 GHz), WLAN5.2GHz (5.15 - 5.35 GHz), WLAN5.8GHz (5.725 - 5.825 GHz), 5G C-Band (3.4 - 3.6 GHz). The low frequency band (WLAN2.4GHz) is excited by the longest path of inverted L-shaped strip with bending, and the

intermediate frequency band (5G C-Band) is excited by the strip from the feed point to the strip on the back side by via hole. The high frequency band (WLAN5.2GHz and WLAN5.8GHz) is formed by the high-order mode of the low frequency band and the mode excited by the metal patch with an L-strip connected to the ground and a 2.7nH inductor.

SIMULATED AND MEASURED RESULTS: Fig. 3 shows the simulated and measured S₁₁, S₂₂, S₁₂ and S₂₁ of the proposed design. The results of the simulation and measurement are almost the same. The results indicates that the operating bands could meet the requirement of the bands of WLAN2.4GHz, WLAN5.2GHz, WLAN5.8GHz, and 5G C-Band (3.4 - 3.6 GHz). The isolation is large than 15dB with the operating bands. Fig. 4 shows the simulated and measured antenna gains and efficiencies of the bands for Ant. 1 of the proposed design. The radiation performances of the design are good for applications.

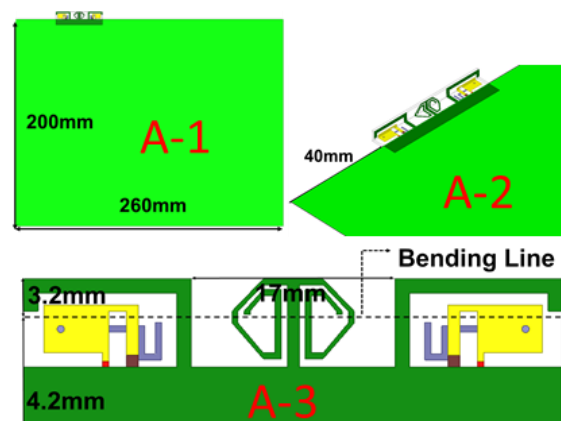


Fig. 1. Antenna geometry: (A-1) full view of the design, (A-2) side view of antennas and (A-3) detailed geometry of the proposed MIMO antennas.

* Poster paper presentation

Table 2. Dimensions of the antenna design

| Parameter | L1 | L2 | L3 | L4 | L5 | L6 | L7 | L8 | L9 | ϕ | Inductor |
|-----------|-----|-----|-----|-----|----|-----|----|------|------|--------|----------|
| Unit(mm) | 7.4 | 3.2 | 0.7 | 2.7 | 1 | 1 | 1 | 2.35 | 3.15 | 0.6 | 2.7nH |
| Parameter | W1 | W2 | W3 | W4 | W5 | W6 | W7 | W8 | W9 | W10 | AB |
| Unit(mm) | 14 | 1.5 | 7.9 | 1.2 | 1 | 1.5 | 6 | 0.9 | 1.9 | 0.5 | 25 |

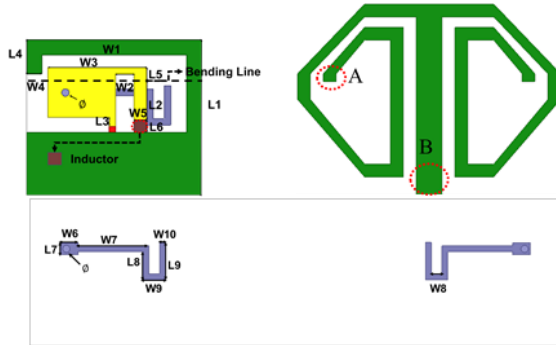


Fig. 2. Antenna part of the design

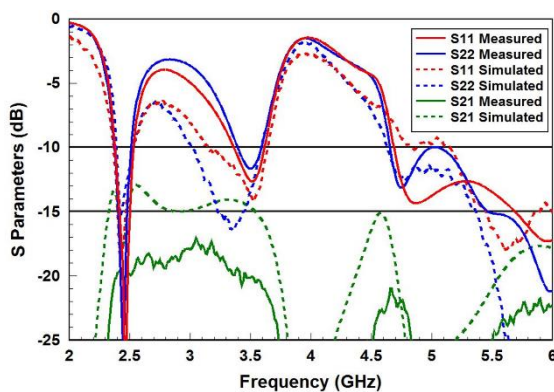
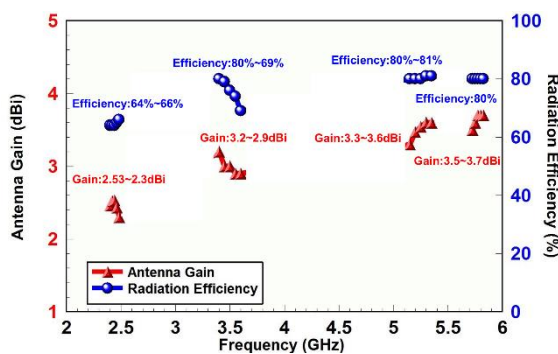
Fig. 3. Measured and simulated S -parameters for the proposed design.

Fig. 4. Simulated gains and efficiencies of the bands for Ant.1

CONCLUSION: A design of MIMO antennas of coupled-fed PIFAs for laptop computers has been proposed. A bending T-shaped strip placed between them to enhance the isolation of the design. From the measurement results, the S_{11} and S_{22} is less than -10 dB in the operating bands and the isolation is large than 15 dB. The design with good performances is suitable for MIMO antennas for laptop computer applications.

Keywords

Couple-fed PIFA, C-band, laptop, MIMO antennas

References

- [1] W. S. Chen and Y. L. Chen, "Small-Size 5G C-Band/WLAN 5.2/5.8GHz MIMO Antenna for Laptop Computer Applications," *2018 IEEE iWEM*, pp.1-2, Aug. 2018.
- [2] J. Y. Deng, J. Y. Li, L. Zhao and L. Guo, "A Dual-Band Inverted-F MIMO Antenna with Enhanced Isolation for WLAN Applications," *IEEE Antennas and Wireless Propagation Letters*, Aug. 2017.
- [3] C. T. Lee and S. W. Su, "Small-Sized, Tri-Band, Two-Antenna System Aimed for 4×4 Gbps Notebook Applications," *2018 ISAP*, Aug. 2018.
- [4] M. H. Liang, Y. R. Chen and W. S. Chen, "Design of MIMO Antennas for 5G C-band/WLAN Operation in the Laptop Computer," *2019 IEEE CAMA*, Aug. 2019.

Tx power optimization of pico-eNB for multiband heterogeneous mobile networks*

Ayumi Yoneyama ^{1,a,*}, Fumiya Kemmochi ^{1,b} and Hiroyuki Otsuka ^{1,c}

¹ Graduate School of Engineering, Kogakuin University, Tokyo, Japan

^a cm20056@ns.kogakuin.ac.jp, ^b cm19016@ns.kogakuin.ac.jp, ^c otsuka@cc.kogakuin.ac.jp

Abstract

Fifth-generation (5G) mobile systems have been partially launched and are being gradually used worldwide. Two types of 5G mobile systems have been approved by the third-generation partnership project (3GPP) standards body. One type of system is 5G New Radio (NR) with non-standalone (NSA) operation which enables 5G NR deployments using existing the fourth-generation (4G) mobile systems. Another type of mobile system is 5G NR with standalone (SA) operation, which provides a complete 5G NR with a 5G core network. The initial phase of 5G NR with NSA focuses on enhanced mobile broadband (eMBB) using both 5G NR and 4G long-term evolution (LTE) [1]-[3].

In heterogeneous mobile networks (HetNets) that combine with macrocells and picocells in the same coverage area, picocells operating with high carrier frequencies are typically overlaid on macrocells using low carrier frequencies [4],[5]. A key technology for increasing data rates includes higher-order modulations such as the 256 – and 1024 – quadrature amplitude modulation (QAM).

In this study, we investigate the optimal transmission (Tx) power of a pico-evolved node B (eNB) for multiband HetNets combined with macrocell using 2 GHz and picocells using 4.5 GHz band.

SIMULATION SETUP: We investigate the average and 5-percentile user throughput as a function of the Tx power of the pico-eNB. The primary simulation parameters are listed in Table 1. The carrier frequencies used in the macro- and pico-eNB are 2 GHz and 4.5 GHz, respectively. The signal bandwidth for the macro- and pico-eNB are 10 MHz and 100 MHz,

respectively. The Tx power of the pico-eNB varies from 28 to 46 dBm. The path-loss model and other assumptions are obtained from [6].

Table 1. Primary Simulation Parameters

| Parameter | Macro-eNB | Pico-eNB |
|------------------------|---|--------------------|
| Cell layout | Hexagonal grid, 19 cell sites, 3 sectors per site | 4 picos per sector |
| Carrier frequency | 2.0 GHz | 4.5 GHz |
| System bandwidth | 10 MHz | 100 MHz |
| Cell radius (ISD) | 289 m (500 m) | - |
| Tx Antenna height | 32 m | 10 m |
| Tx power | 46 dBm | From 28 to 46 dBm |
| Tx antenna gain | 14 dBi | 5 dBi |
| Tx antenna downtilt | 15 deg. | 10 deg. |
| UE distribution | 30 UE per sector, 2/3 cluster distribution | |
| Traffic model | Full buffer | |
| Link adaptation | 25 MCS (QPSK to 1024-QAM) | |
| Link to system mapping | EESM | |
| MIMO | 2 × 2 SU-MIMO | |

SIMULATION RESULTS: Figure 1 shows the average and 5-percentile user throughput as a function of the Tx power of the pico-eNB. Based on these results, we confirmed that the Tx power of the pico-eNB of 37 dBm can provide the best performance when the Tx antenna height is 10 m and the number of pico-eNB is four per macro-sector. Furthermore, Figure 2 shows that the use rate of both 256- and 1024-QAM in the

* Oral paper presentation

downlink MCS reaches 11% when the Tx power is 37 dBm.

CONCLUSION: We clarified the optimal Tx power of pico-eNB for multiband HetNets combined with macrocell using 2 GHz and picocells using 4.5 GHz band. We also analyzed the use rate of each modulation method in the downlink MCS.

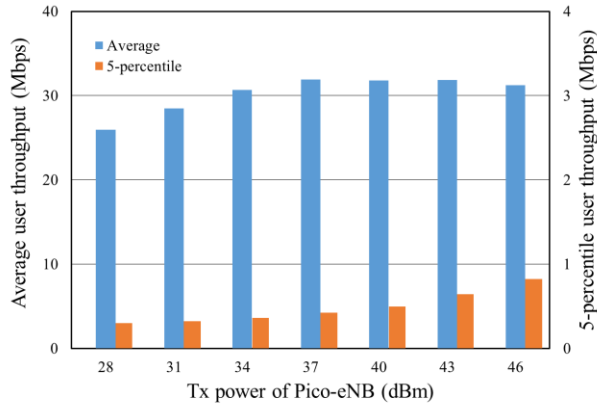


Fig. 1. Average and 5-percentile user throughput as a function of pico-eNB Tx power

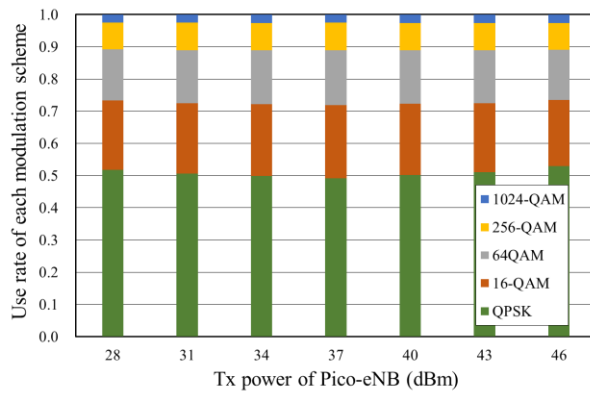


Fig. 2. Analysis of use rate of modulation method used in downlink MCS as a function of pico-eNB Tx power

Keywords

mobile communication, heterogeneous network, multiband, pico-eNB Tx power, 1024-QAM

References

- [1] D. Soldani and A. Manzalini, "Horizon 2020 and beyond; On the 5G operating system for a truly digital society," *IEEE Veh. Tech. Mag.*, vol. 10, no. 1, pp. 32-42, March 2015.
- [2] T. Nakamura, A. Benjebbour, Y. Kishiyama, S. Suyama, and T. Imai, "5G radio access: Requirements, concept and experimental trials," *IEICE Trans. on Commun.*, vol. E98-B, pp. 1397-1406, Aug. 2015.
- [3] T. E. Bogale and L. B. Le, "Massive MIMO and mmWave for 5G wireless HetNet," *IEEE Veh. Tech. Mag.*, vol. 11, no. 1, pp. 64-75, March 2016.
- [4] R. Baldemair, T. Irnich, K. Balachandran, E. Dahlman, G. Mildh, Y. Selen, S. Parkvall, M. Meyer, and A. Osserian, "Ultra-dense networks in millimeter-wave frequencies," *IEEE Commun. Mag.*, vol. 53, no. 1, pp. 202-208, Jan. 2015.
- [5] K. Chandra, A. S. Marcano, S. Mumtaz, R. V. Prasad, and H. L. Christiansen, "Unveiling capacity gains in ultradense networks," *IEEE Veh. Tech. Mag.*, vol. 13, no. 2, pp. 64-83, June 2018.
- [6] ITU Report M.2135-1, "Guidelines for evaluation of radio interface technologies for IMT-Advanced," Dec. 2009.

Technical Presentations

Materials, Mechanical & Manufacturing Engineering

| | | |
|---------------------|---|---|
| Moderator | : | Dr. Manolito E. Bambase Jr. |
| Panelists | : | Dr. Ramon Christian P. Eusebio, Dr. Arthur L. Fajardo, Dr. Victor A. Rodulfo Jr. |
| Technical Assistant | : | Engr. Kristel M. Gatdula |
| 01:30PM – 01:35PM | Welcome Remarks and Introduction of Panel Members | |
| 01:35PM – 01:50PM | Structure of Jet with Velocity Oscillation at Slot | <u>Chisato Ichihara*</u> , Kotaro Sato (KUTE) |
| 01:50PM – 02:05PM | Fabrication of core-shell structures using TiO ₂ and PANI for methyl orange removal | <u>Marco Miguel P. Parel*</u> , Ivy R. Colambo, Marvin U. Herrera (UPLB) |
| 02:05PM – 02:20PM | Compositional analysis of black carbon aerosols by means of TOF-SIMS and SNMS | <u>Kentaro Sakai*</u> , Ryota Koiwai, Masato Morita, Tetsuo Sakamoto (KUTE) |
| 02:20PM – 02:35PM | Ferroelectric Characteristics of SrBi ₂ Ta ₂ O ₉ Thin Film and Application | <u>Wen-Cheng Tzou*</u> and Cong Cheng Li (STUST) |
| 02:35PM – 02:50PM | Structure of Jet Deflected by Secondary flow | <u>Yu Tamanoi*</u> , Kotaro Sato (KUTE) |
| 02:50PM – 03:05PM | Development of a Portable Carrot Harvester | <u>Zion Jemillinium S. Tam-awen*</u> , Rossana Marie C. Amongo, Fernando O. Paras Jr., and Engelbert K. Peralta (UPLB) |
| 03:05PM – 03:20PM | To Enhance Mechanical Property of PBI Thin-Film by E-Beam Irradiation | <u>Hsiao-Wu Lai*</u> (STUST) |
| 03:20PM – 03:35PM | Development of Cassava (Manihot esculenta Crantz) Mechanical Planter | <u>Ruel R. Guardarama*</u> , Rossana Marie C. Amongo, Delfin C. Suministrado, Engelbert K. Peralta (UPLB) |
| 03:35PM – 03:50PM | Flow Control using Interaction between Synthetic and Continuous Jets | <u>Yodai Suzuki*</u> , K. Sato, K. Nishibe, K. Yokota (KUTE) |
| 03:50PM – 04:05PM | Performance Evaluation of a Locally designed Water Pump | <u>Aga-Angelica S. Pascual*</u> , Arthur L. Fajardo, Omar F. Zubia, Roger A. Luyun Jr (UPLB) |
| 04:05PM – 04:20PM | Aerodynamic characteristics of soccer balls focusing on drag crisis | <u>Yuki Sakamoto*</u> , Shinichiro Ito, Masaki Hiratsuka (KUTE) |

Synthesis of polyhydroxybutyrate / cellulose / calcium carbonate bioplastic composites using heat-assisted solution casting method*

Joemer A. Adorna Jr ^{1,a}, Ruby Lynn G. Ventura ^{2,b}, Van Dien Dang ^{3,c}, Ruey-An Doong ^{4,d},
Jey-R S. Ventura ^{1,e,*}

¹ Biomaterials & Environmental Engineering Laboratory, Department of Engineering Science, College of Engineering & Agro-Industrial Technology, University of the Philippines Los Baños, Philippines

² UP Rural High School, College of Arts and Science, University of the Philippines Los Baños, Philippines

³ Institute of Environmental Engineering, National Chiao Tung University, Taiwan

⁴ Institute of Analytical & Environmental Sciences, National Tsing Hua University, Taiwan

^ajaadorna@up.edu.ph, ^brlgventura@up.edu.ph, ^cdiendang.envi@gmail.com, ^dradoong@mx.nthu.edu.tw, ^ejsventura@up.edu.ph

Abstract

Biodegradable plastics derived from polyhydroxybutyrate (PHB), a microbially produced polymer, have gained attention as possible replacement for fossil-based commodity polymers due to their biodegradability and properties that are similar to commercial plastics. However, their applications are limited due to a relatively high production cost.

The incorporation of cheap biomass fillers can significantly reduce the production cost of the resulting bioplastic [1]. In this study, cheap and widely available biomass fillers such as cellulose (CL) and calcium carbonate (CC) were incorporated to PHB at 90 PHB/10 CL, 90 PHB/10 CC, and 80 PHB/10 CL/10 CC w/w compositions, via a heat-assisted solution casting method. Morphological, mechanical, physicochemical, and biodegradation tests were performed to characterize the composite films. The schematic diagram of the methodology is shown in Figure 1.

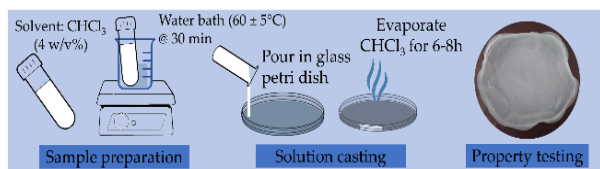


Fig. 1. Synthesis of PHB/CC/CL composites

Figure 2 (SEM results) indicates that the biomass fillers utilized have introduced different extent of heterogeneity on the surface of pure PHB (Fig. 2a). 90 PHB/10 CC (Fig. 2b) displayed a larger

agglomeration of filler particles mainly due to large surface area of calcium carbonate. For 90 PHB/10 CL (Fig. 2c), the resulting bioplastic composite appears to be smoother, however, cellulose fibrils with an average length of 3.0 μm can be observed on the polymeric surface. This effect has considerably increased for 80 PHB/10 CC/10 CL (Fig. 2d), suggesting co-agglomeration of CaCO_3 and cellulose particles on the polymer surface matrix [2,3].

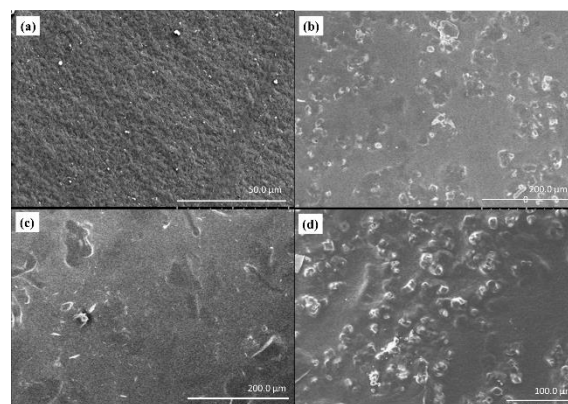


Fig. 2. Scanning electron microscope (SEM) images of (a) PHB 100, (b) 90 PHB/10 CC, (c) 90 PHB/10 CL, and (d) 80 PHB/10 CC/10 CL.

The XRD results (Fig. 3a) revealed that PHB exists in orthorhombic plane, while the biomass fillers CL and CC are present as cellulose I and calcite with no other impurity peaks present, implying the purity of the materials used for the composite [3]. The FTIR spectra shown in Fig. 3b showed an absence of the intermolecular bonding of the carboxyl group around 1645 cm^{-1} , which suggests

* Poster paper presentation

that esterification most likely occurred during the incorporation of the biomass fillers with PHB [4].

Thermogravimetric analysis performed at ambient temperature to 800°C showed improved thermal stability, as the thermodegradative peaks of the composites has shifted to the left (Fig. 3c). The stress-strain diagram acquired through UTM testing (Fig. 3d) illustrates that the Young's modulus of the bioplastic film increased with the introduction of CC, while the mechanical property slightly decreased upon the addition of CL. This may be mostly attributed to the aggregation of fillers thus creating distinct effects on the polymer-filler matrix [4,5].

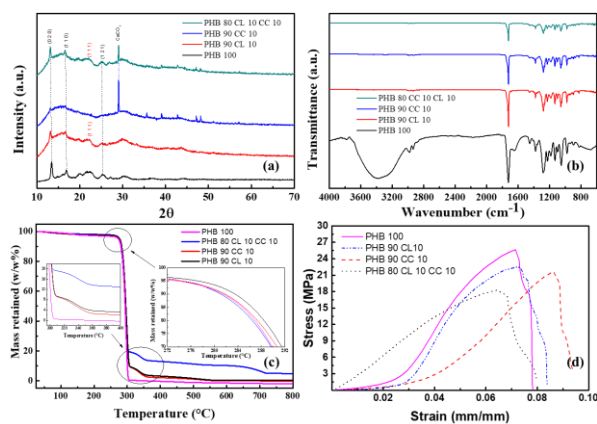


Fig. 3. Characterization of PHB/CC/CL composites. (a) XRD results. (b) FTIR results. (c) TGA results. (d) Stress-strain (UTM) results.

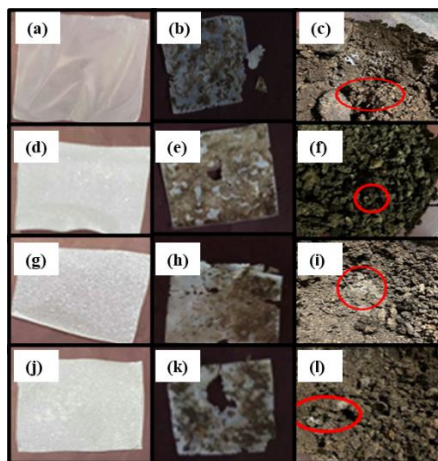


Fig. 4. Simulated compost biodegradation results of PHB/CC/CL composites. PHB 100 at (a) Day 0, (b) Day 5, and (c) Day 15; 90 PHB/10 CC at (d) Day 0, (e) Day 5, and (f) Day 15; 90 PHB/10 CL at (g) Day 0, (h) Day 5, and (i) Day 15; and 80 PHB/10 CC/10 CL at (j) Day 0, (k) Day 5, and (l) Day 15.

The bioplastic composites were subjected to simulated compost biodegradability tests under thermophilic conditions (55°C). Figs. 4b, 4e, 4h, and 4k showed significant degradation along with biofilm accumulation on the bioplastic film surface which denotes very high biological activity. From Figs. 4c, 4f, 4i, and 4l, all samples have almost completely degraded and are irretrievable from the compost matrix in less than 2 weeks.

The incorporation of CC and CL alters some properties of PHB as presented in the study. Improving the biocomposites through reactive polymerization, or the addition of nucleating agents and/or plasticizers would be investigated to further improve composite properties for further applications.

Keywords

bioplastics, polyhydroxybutyrate, biomass filler, composite, solution casting

References

- [1] Adorna JA, Aleman CKA, Gonzaga ILE, Pangasinan JN, Sisican KM, Dang VD, Doong R-A, Ventura RLG, Ventura JS. 2020. Effect of Lauric Acid on the Thermal and Mechanical Properties of Polyhydroxybutyrate (PHB)/ Starch Composite Biofilms, *International Journal of Polymer Science*. 7947019: 1–11.
- [2] Srithep Y, Ellingham T, Peng J, Sabo R, Clemons C, Turng L-S, Pilla S. 2013. Melt compounding of poly (3-hydroxybutyrate-co-3-hydroxyvalerate)/ nanofibrillated cellulose nanocomposites. *Polymer Degradation and Stability*. 98(8): 1439–1449.
- [3] Supaphol P, Harnsiri W, Junkasem J. 2004. Effects of calcium carbonate and its purity on crystallization and melting behavior, mechanical properties, and processability of syndiotactic polypropylene. *Journal of Applied Polymer Science*. 92(1): 201–212.
- [4] Zhang L, Deng X, Zhao S, Huang Z. 1997. Biodegradable polymer blends of poly (3-hydroxybutyrate) and starch acetate. *Polymer International*. 44: 104–110.
- [5] Zhang B, Huang C, Zhao H, Wang J, Yin C, Zhang L, Zhao Y. 2019. Effects of cellulose nanocrystals and cellulose nanofibers on the structure & properties of polyhydroxybutyrate nanocomposites. *Polymers*. 11(12): 2063.

Design thinking driven requirements elicitation method based on role-based prototyping*

Senju Nakajima ^{1, a*}, Takayuki Kitagawa ^{2, b}, Tadahisa Kondo ^{1, c}, Mari Inoki ^{1, d}

¹ Kogakuin University, Tokyo, Japan

² Toshiba Digital Solutions Corporation, Tokyo, Japan

^a em20013@ns.kogakuin.ac.jp, ^b Kitagawa.Takayuki@toshiba-sol.co.jp

^c tkondo@cc.kogakuin.ac.jp, ^d m_inoki@cc.kogakuin.ac.jp

Abstract

People have high hopes from design thinking as a suitable approach for eliciting true customer requirements. Design thinking is a way of thinking devised by Tim Brown and a methodology for solving problems creatively [1]. The process of the design thinking approach involves five steps: Empathize, Define, Ideate, Prototype, and Test; all these steps are repeated to put this methodology into practice for solving problems [2].

In case of the conventional requirements elicitation methods, stakeholder analysis, scenario analysis, and use case modeling are utilized for developing the specifications of the requirements of the software products [3]. In conventional methods, the development is driven by engineers. This poses a risk as, in such methods, the truly desired functional and non-functional requirements of the customer may not be realized by the software product.

Accordingly, in this study, a requirements elicitation method based on design thinking has been proposed in order to substantiate customer empathy by combining design thinking and requirements engineering.

An overview of the proposed method is shown in Fig. 1, where:

- Fig. 1 (a) illustrates the process of problem-solving using design thinking.
- Fig. 1 (b) exhibits the role-based prototyping process, which involves the

combination of design thinking and requirements engineering.

- Fig. 1 (c) illustrates the process of developing a customer journey map.
- Fig. 1 (d) provides examples of artifacts created by the proposed requirements elicitation method based on role-based prototyping.

In the proposed method, the problem-solving process using the design thinking approach, as shown in Fig. 1 (a), involves repeating the prototyping three times while inheriting the created prototype shown in Fig. 1 (b). Each prototyping process includes the following tasks: customer journey map creation, use case modeling, and prototyping. As shown in Fig. 1 (c), the process of creating the customer journey map consists of the following subtasks (c1)–(c5):

- (c1) defining the target persona and the scenario.
- (c2) extracting actions of the persona, assuming the behavior of the persona in that scenario.
- (c3) eliciting opponents, which the persona contacts in the scenario.
- (c4) imagining the thoughts and feelings of the persona in that scenario.
- (c5) identifying the problems that the persona faces, evaluating why they occur, how to solve them, and what other analysts have noticed.

* Poster paper presentation; this research was supported by the MEXT enPiT-Pro Smart SE: Smart Systems and Services Innovative Professional Education Program and the Research Organization of Information and Systems at Inter-University Research Institute Corporation

During the creation of the customer journey map, the insights derived from the customers are identified in order to comprehend the thinking and feeling of the persona. Accordingly, the subsequent results are used for identifying the problems that the customers face and for developing suitable solutions for the same. Through this method, the insights ascertained through the customer journey map are substantiated via prototyping in order to define the software requirements.

While carrying out the prototyping using this method, the prototypes were classified into the following three roles based on the level of the state of requirements elicitation method: The first role involves substantiating ideas and confirming what customers truly desire. The second role of prototyping is to confirm the direction of the customers' requirements in order to evaluate whether the improvement in the idea is appropriate. The final role is to support the decision on the ultimate resolution.

The state of the type of workshop with respect to Fig. 1 (a), (b), and (c) is illustrated in Fig. 1 (d1). Specific examples of the deliverables created by Fig. 1 (a), (b), and (c) are shown in (d2)–(d6) of Fig. 1 (d). Fig. 1 (d2) exhibits examples of persona definitions. Fig. 1 (d3) is a low-level customer journey map charted during

the first prototyping. Fig. 1 (d4) is a high-level customer journey map created during the third stage of prototyping. Meanwhile, Fig. 1 (d5) is a use case model, and Fig. 1 (d6) is a prototype created by the third prototype.

The authors practiced the proposed method in an actual workshop and confirmed its effectiveness in achieving the requirements elicitation method that gains sympathy from customers.

Keywords

Requirements engineering, requirements elicitation, design thinking, prototyping

References

- [1] Tim Brown, Change by Design, Revised and Updated: How Design Thinking Transforms Organizations and Inspires Innovation, Harper Business, 2019
- [2] Hasso Plattner Institute of Design at Stanford, an Introduction Design Thinking Process Guide, <https://dschool.stanford.edu/resources/getting-started-with-design-thinking>
- [3] Iso/IEC/IEEE 29148:2018, Systems and Software Engineering — Life Cycle Processes - Requirements Engineering.

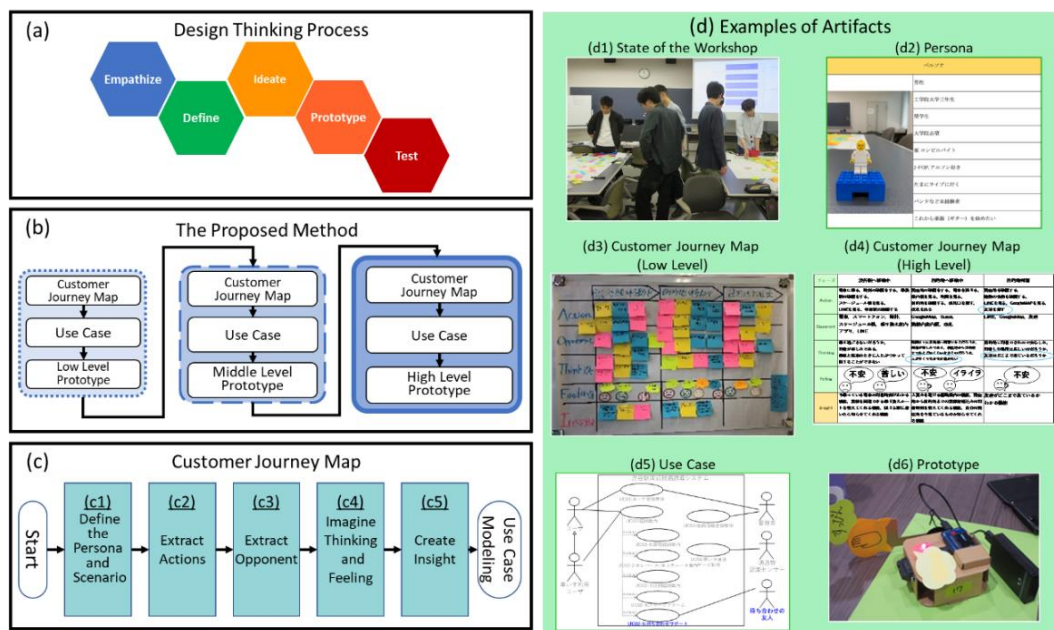


Fig. 1. Overview of the Proposed Method

Improvement of production resource planning process at DAIWA Vietnam Co., Ltd.*

Phuong-Thao Nguyen ^{1,a}, Hong Nguyen ^{1,b*}, Nhat-To Huynh ^{1,c}

¹ Faculty of Project Management, the University of Danang, University of Science and Technology

^a nguyen.nguyen6797@gmail.com, ^b nhnguyen@dut.udn.vn, ^c hnto@dut.udn.vn

Abstract

Process automation has been a focus of the industry for a long time. However, in some small and medium enterprises, production is still largely dependent on human factors. This not only reduces production speed but also leads to a high failure rate, which in turn affects the overall performance of the system. This study aims to propose an improvement in resource planning for DAIWA Vietnam Co., Ltd. whose main product is a fishing rod. A new input processing application is built to replace the repetitive reading of drawings, parameter checking and calculations from workers. The application is written in C# language on Visual Studio integrated development environment. The data entry process is simplified in three steps: selecting fishing rod type, entering parameters from the drawing, outputting results. Through the actual inspection at the factory, the measured results show that the calculation time is reduced by more than 50 percent compared to the previous method with equivalent outputs. If the application is applied to three remaining phases (painting, finishing, packaging), the efficiency of the entire manufacturing process will be greatly improved.



Fig. 1. Fishing rod product

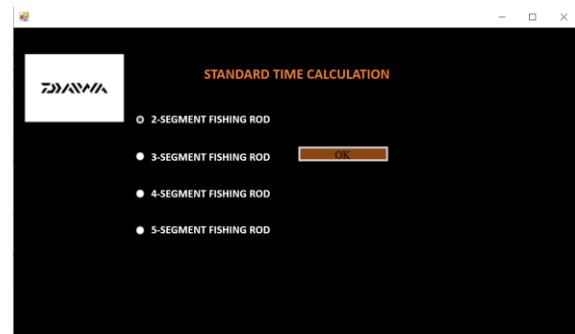


Fig. 2. First interface

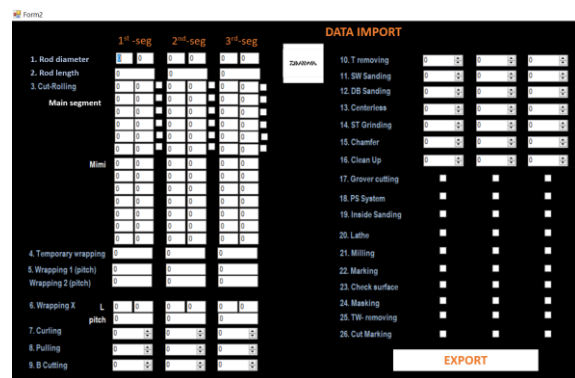


Fig. 3. Data import interface

The fishing rod product as shown in Fig. 1 is produced through 5 steps process includes: Fabric rolling, finishing, painting, assembling and packaging. Production department gets the orders from sales and plans for material purchasing and labor. From the design drawing, the required materials are calculated for shipping to the purchasing department. The number of employees is achieved from standard timing and production volumes. The data which used in this procedure is extracted from the design drawing. Then, engineers need to look up the parameter sheet and formula to calculate the results. Because of the dependence on human

* Poster paper presentation

factors, the process becomes slower, more complex and error prone.

This study proposes a new data processing which is integrated the application to support the calculation on Visual Studio environment. The engineers just need to import data from drawings, the application will automatically identify and select the appropriate calculation method. The first user interface is shown as Fig. 2. Here, the engineer need to choose the type of fishing rod. Then, data which is from drawings is import in the next window (rod diameter, rod length, fabric roll size, ...) as shown in Fig. 3. Results is exported in MS Excel file include: time of manufacturing every fishing rod segments, total manufacturing time, time of fabric rolling, finishing time and total time of fabric rolling-finishing process.

After implement at the factory, the data processing time is shortened up to 60 percent

(reduces from 15 mins to 6 mins) for each drawing. Therefore, the saved time per year is about 266.7 hours. The results will be further improved if the process is applied across the rest of the process.

Keywords

Resource Planning, Fishing Rod Producing, Data Input System, Standard Time, Visual Studio

References

- [1] Choubey NS, Agrawal M. 2016. Automation in Textile Industry. *International Journal on Textile Engineering and Processes*. 2: 30-33.
- [2] Ngan HYT, Pang GKH, Yung NHC. 2011. Automated fabric defect detection. *Image and Vision Computing*. 29: 442-458.
- [3] Fishing Rod Manufacturing Process. DAIWA Ltd., Co.

Development of cassava (*Manihot esculenta* Crantz) mechanical planter*

Ruel R. Guardarama ^{1,2 a*}, Rossana Marie C. Amongo ^{2,b}, Delfin C. Suministrado ^{2,c}, Engelbert K. Peralta ^{3d}

¹ Agricultural & Biosystems Engineering Department, College of Engineering, Central Mindanao University, Bukidnon, Philippines

²Agribiosystems Machinery & Power Engineering Division, Institute of Agricultural & Biosystems Engineering (IABE), University of the Philippines Los Baños (UPLB), Philippines

³Agricultural, Food & Bioprocess Engineering Division, IABE, UPLB, Philippines

^aguardarama.rr92@gmail.com, ^brcamongo@up.edu.ph, ^cdcsuministrado@up.edu.ph,

^dekperalta@up.edu.ph

Abstract

INTRODUCTION: Cassava is one of the important root crops in the Philippines, which is being utilized as food, feed ingredient and in the manufacture of industrial products. After sweet potato, cassava covers the second highest hectareage planted among root crops produced in the country ^[1]. The production of cassava requires high manpower to perform the different farm operations such as land preparation, planting, fertilization, weeding and harvesting operations. The labor requirement for cassava production is about 77.48 man-days per hectare with planting alone of around 8 man-days per hectare and weeding and harvesting as the highest labor requirement of 17.85 and 17.04 man-days per hectare, respectively ^[2].

Manual planting operation is a very tedious, time-consuming, drudgery imposing, and arduous work. Nevertheless, most of the conventional cassava production in the Philippines operates this way. Thus, a study to develop a cassava mechanical planter was conducted.

METHODOLOGY: The cassava mechanical planter is a four-wheel tractor-trailed equipment. It is designed to plant cassava stakes horizontally. Its parts include the hopper, cylindrical metering device, trans-mission system, delivery tube, furrow opener, furrow closer, chassis, and the three-point hitch linkage (Figure 1). The laboratory and field performance of the planter were evaluated in terms of uniformity of planting (UOP), field efficiency (%Eff) and percentage stake germination (%SG).

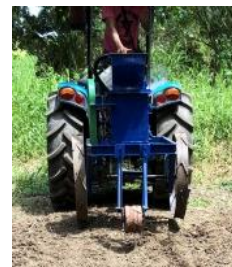


Fig 1. The developed cassava mechanical planter.

A 2 x 3 complete factorial experimental design was carried out and data obtained were analyzed using Analysis of Variance (ANOVA) for the test of significance of the hopper load and planter speed to the field efficiency and uniformity of planting.

RESULTS AND DISCUSSION: Figure 2 shows the three-dimensional graph showing that the UOP is proportional to the speed of the planter. The higher UOP occurs at faster speed and lowers at slower speed. Lower value is better because it shows a more or less uniform planting distance between stakes. The average UOP obtained were 18.12 cm, 28.52 cm and 41.58 cm for the speed of 3.0 kph, 3.4 kph and 3.8 kph, respectively.

The derived predictor equation describing the relationship of the UOP with the hopper load and planter speed based on the regression coefficients is described in Equation (1), where Y_1 = uniformity of planting, X_1 = hopper load, and X_2 = speed.

$$Y_1 = -69.90806 - 0.609613X_1 + 29.32949X_2 \quad (1)$$

* Oral paper presentation

The three-dimensional graph for the %Eff is shown in Figure 3. The average %Eff were 60.13%, 57.52% and 54.84% for 3.0 kph, 3.4 kph and 3.8 kph, respectively. The hopper load and the speed of the planter had significantly affected the %Eff of the machine.

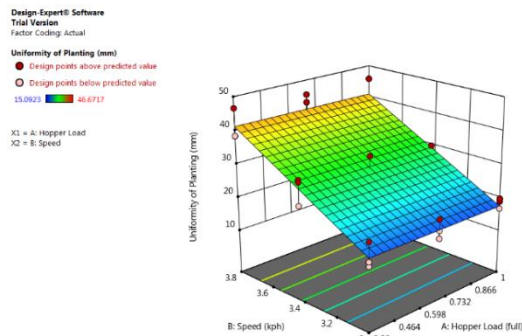


Fig. 2. Three-dimensional graph for uniformity of planting

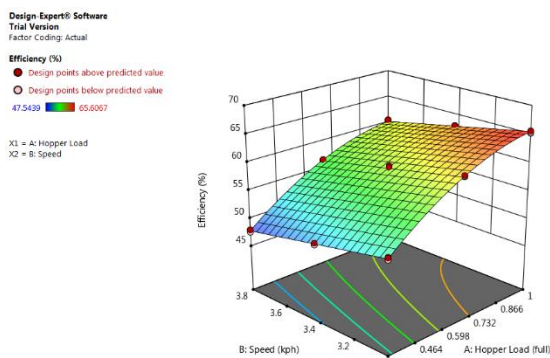


Fig. 3. Three-dimensional graph for field efficiency

The derived predictor equation describing the relationship of the field efficiency with the hopper load and planter speed based on the regression coefficients is described in equation (2), where Y_2 = field efficiency, X_1 = hopper load, and X_2 = speed.

$$Y_2 = 58.22926 + 45.73582X_1 - 5.44880X_2 + 0.546701X_1X_2 - 21.78823X_1^2 - 0.224614X_2^2 \quad (2)$$

The planted stakes achieved a 100% germination. The cost of the cassava mechanical planter was computed based on the total materials and labor costs for the final fabrication of the design amounting to Php 63,238.24.

The hopper load and planter speed were considered as the factors affecting the UOP and the %Eff of the developed cassava mechanical planter. The speed of the planter had greatly affected the UOP and % Eff of the machine. It had a proportional effect on both the UOP and % Eff. It had a negative effect on the UOP since as the speed becomes faster, the UOP becomes larger. The lesser the value of the UOP means that the spacing of stakes is more or less the same.

The hopper load had a significant effect on the %Eff of the machine. However, it had no significant effect on the UOP. Lower hopper capacity affects the field capacity in the sense that the loading of stakes contributed more unproductive time affecting the overall %Eff.

CONCLUSION AND RECOMMENDATIONS: The developed cassava mechanical planter can contribute to labor reduction, uniformity of planting, and increased field capacity thereby increasing field efficiency which would ease the burden of cassava farmers/growers.

Based on the testing and evaluation of the prototype cassava mechanical planter, the following are recommended for future studies:

- Redesigning of the hopper to include more stakes and to increase efficiency.
- Testing of the equipment using different available cassava varieties to further increase the viability of the developed cassava mechanical planter.

Keywords

Cassava mechanical planter, hopper load, uniformity of planting, field efficiency, field capacity

References

- [1] Philippine Council for Agriculture and Resources Research and Development (PCCARD) (1983). The Philippine Recommends for Cassava. 2nd Edition.
- [2] Philippine Statistics Authority, 2014. Costs and Returns of Cassava Production.

Structure of jet deflected by secondary flow^{*}

Yu Tamanoi ^{1,a,*}, Kotaro Sato ^{1,b}

¹ Mechanical Engineering Program, Graduate School of Engineering, Kogakuin University, Tokyo, Japan

^a am20042@ns.kogakuin.ac.jp, ^b at12164@ns.kogakuin.ac.jp

Abstract

Fluidic thrust vectoring is an active area of research because of its potential to improve the kinematic performance of next-generation aircraft^[1]. This technology can also be used as a substitute for moving nozzles, rudders, and louvers, and is expected to have broad applications in turbomachinery and air conditioning equipment. Previously, jet directions have been controlled using secondary flows of the Coanda surface and continuous jets, and it is reported that there is a dead zone, a deflection-controllable region, and a hypothetical saturation region^[2]. The expansion of the deflectable region is yet to be investigated in detail. Fluidic thrust vectoring requires several parameters for jet control, and there are numerous unknowns in the method using synthetic jets for secondary flow. In this study, a geometrical configuration with a secondary-flow slot exit near a semi-cylindrical Coanda wall was used as a control condition. Fig.1 shows the calculation conditions of the numerical simulation. The velocity distribution and structure of the primary jet downstream of the flow field were studied numerically for the case of the secondary flow as a synthetic jet. When the primary flow condition was fixed, the dimensionless frequency of the secondary flow changed to focus on the effects of the oscillatory characteristics of the synthetic jet on the flow field. The secondary flow is generated by the speaker. The typical velocity of the synthetic jet is determined by adjusting the amplitude UA and can be expressed by the following equation (1).

$$U_2 = \sqrt{\frac{1}{T} \int_0^T U_A^2 \sin^2 \frac{2\pi}{T} t dt} \quad (1)$$

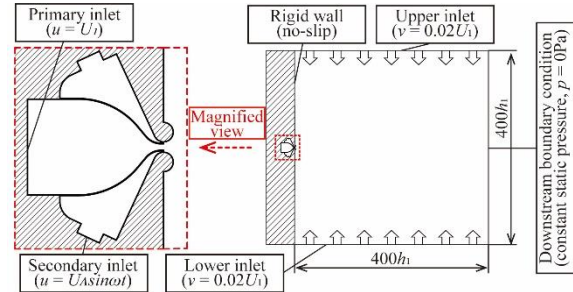


Fig. 1. Calculation conditions for numerical simulations

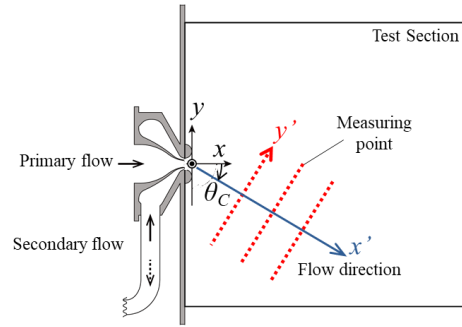


Fig. 2. Coordinate definitions and data measurement locations

Fig. 2 shows the data acquisition position of CFD. The data was acquired at intervals of 2° over a range of 98° with a radius of 100 mm from the origin, 0° for straight ahead, and -30° for the positive y-axis direction. The angle between the center of gravity obtained from the velocity distribution and the origin was defined as the deflection angle θ_c [deg]. We drew a line from the origin to the direction of the deflection angle and defined this as x' . The line perpendicular to this line was defined as y' . The linear velocity distribution was obtained on the x' at intervals of 50 mm from the origin at distances of 50 to 150 mm. y' direction was obtained at intervals of 2 mm from -50 to 50 mm. The main result of this study is that the flow direction control is achieved when staggered vortices array corresponding to the inverse Karman vortices street is formed downstream of the jet. Because

^{*} Oral paper presentation

the arrangement of the vortex arrays depends on the dimensionless frequencies, the jet structure can be determined by these dimensionless frequencies.

Nomenclature

| | | |
|-----------|---|---|
| h | : | Slot width [m] |
| R | : | Radius of Coanda surface ($= 15.0 \times 10^{-3}$ m) |
| U | : | Velocity of primary or secondary flow [m/s] |
| U_A | : | Velocity oscillation amplitude for secondary synthetic jet [m/s] |
| M | : | Momentum ratio ($= \rho U^2 h$) |
| ξ | : | Momentum ratio between the primary and secondary jets ($= M_2/M_1$) |
| ρ | : | Fluid density [kg/m ³] |
| f | : | Synthetic jet frequency [Hz] |
| f^* | : | Synthetic jet dimensionless frequency ($= fh_1/U_1$) |
| T | : | Velocity oscillation period at the slot exit ($= 1/f$) |
| Re | : | Reynolds number ($= U_1 h_1/\nu$) |
| ν | : | Kinematic viscosity [m ² /s] |
| x, y, z | : | Coordinate axes |

Subscripts

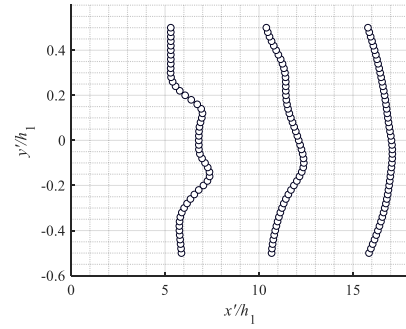
| | | |
|---|---|-----------|
| 1 | : | Primary |
| 2 | : | Secondary |

Keywords

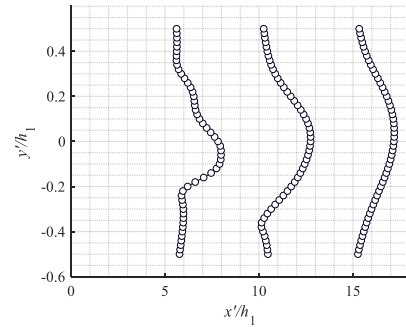
Fluidic thrust vectoring, synthetic jets, Coanda effect, thrust vectoring angle, secondary flow

References

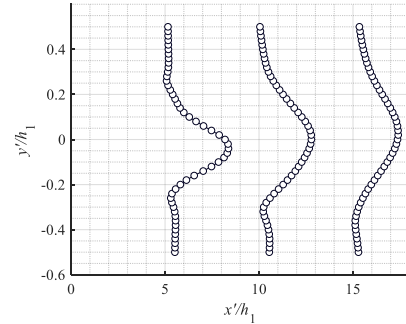
- [1] Alexander M. G., Harris F. K., Spoor M. A., Boyland S. R., Farrell T. E., and Raines D. M. 2016. Active Flow Control (AFC) and Insect Accretion and Mitigation (IAM) System Design and Integration on the Boeing 757 ecoDemonstrator. American Institute of Aeronautics and Astronautics.
- [2] Mark S. M, William J. C. June 10–12, 2002. FLUIDIC THRUST VECTORING OF LOW OBSERVABLE AIRCRAFT. CEAS Aerospace Aerodynamic Research Conference.



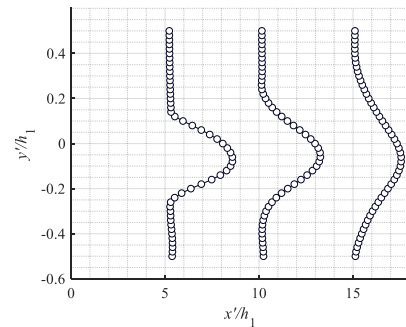
(a) $f^* = 6.7 \times 10^{-3}$ ($f = 10$ Hz)



(b) $f^* = 2.7 \times 10^{-2}$ ($f = 40$ Hz)



(c) $f^* = 4.7 \times 10^{-2}$ ($f = 70$ Hz)



(d) $f^* = 6.7 \times 10^{-2}$ ($f = 100$ Hz)

Fig. 3. Velocity distribution at different dimensionless frequencies ($h_1 = 1.0 \times 10^{-2}$ m, $h_2 = 2.0 \times 10^{-3}$ m, $U_1 = 15$ m/s, $U_A = 10$ m/s, $\xi = 4.4 \times 10^{-2}$)

Selection of polyhydroxyalkanoates (PHA) extraction and recovery protocol using AHP-GRA*

Princess J. Requiso ^{1,2,a}, Fidel Rey P. Nayve, Jr. ^{2,b}, Jey-R S. Ventura ^{1,c*}

¹ Biomaterials & Environmental Engineering Laboratory, Department of Engineering Science, College of Engineering & Agro-Industrial Technology, University of the Philippines Los Baños, Philippines

² National Institute of Molecular Biology & Biotechnology, University of the Philippines Los Baños, Philippines

^a pjrequiso@up.edu.ph, ^b fpnayve@up.edu.ph, ^c jsventura@up.edu.ph

Abstract

Polyhydroxyalkanoates (PHA) have gained immense attention for their potential as alternatives to conventional non-biodegradable plastics. These intracellular polyesters are biodegradable, biocompatible, and can be sustainably produced through microbial fermentation^[1]. However, since PHA is stored within microorganisms, its recovery is more challenging compared with the separation of other fermentation products. Previous works demonstrated energy intensive processes involving chlorinated and other harmful solvents, which relates to disadvantages in terms of production cost and environmental impact^[1]. One of the new strategies to improve PHA's market feasibility and reduce its ecological effects is a low-cost, efficient, and safe extraction and recovery process. Recent studies have already searched for PHA extraction protocols that are operationally fast and simple, improve polymer recovery, and minimize the use of toxic reagents^[1]. Nevertheless, choosing an appropriate protocol is quite complicated due to conflicting technical, economic, and environmental attributes that must be considered for evaluation.

To systematically select the best protocol for PHA extraction and recovery, this study employed two multi-criteria decision analysis (MCDA) tools, the analytic hierarchy process (AHP) and grey relational analysis (GRA). The proposed hybrid MCDA approach provides a better decision-making tool since it integrates both intangible (AHP) criteria and empirical (GRA) data in

prioritizing the proposed protocols for PHA extraction and recovery^[2].

With MCDA, the complex decision-making process was simplified by establishing a hierarchy involving goals, criteria, constraints and alternatives^[2]. AHP was first used to evaluate the proposed criteria in selecting the best PHA extraction and recovery protocol. A survey using pairwise comparisons was collected from different experts to clearly assess and rank both the aspects and criteria. At a given hierarchy level, elements were assessed and given relative importance values from a scale of 1-9. Values 1, 3, 5, 7, and 9 indicates equal, moderately more, strongly more, very strongly, and extremely more importance, respectively, while the remaining intermediate judgment values 2, 4, 6, and 8 were intended to compromise value of importance^[3]. Afterwards, a normalized quantitative analysis was carried out to calculate the overall weights for the proposed aspects and criteria (Table 1).

Environmental (0.377) and economic (0.342) aspects were both given higher priorities in the selection of the best PHA extraction protocol, while technical (0.281) aspect came in at third priority. Among the aspects, hazards and risks (0.194) received the highest overall importance. This stresses the importance of using non-toxic and ecologically benign extraction reagents. Extraction cost (0.179), which pertains to the total of material and processing cost, and purity (0.114), which quantifies the amount of PHA in the polymer extract, were also highly prioritized. Meanwhile, ease of operation (0.063) and disposal management (0.090) were given the lowest scores.

* Poster paper presentation

Table 1. Weights of the aspects and criteria for PHA extraction protocol selection

| Aspect | Weight | Criteria | Overall Weight |
|---------------|--------|---------------------|----------------|
| Technical | 0.281 | Recovery | 0.096 |
| | | Purity | 0.114 |
| | | Product degradation | 0.071 |
| Economic | 0.342 | Extraction cost | 0.179 |
| | | Recyclability | 0.100 |
| | | Ease of operation | 0.063 |
| Environmental | 0.377 | Disposal management | 0.090 |
| | | Hazards and risks | 0.194 |
| | | Carbon footprint | 0.093 |

Using GRA, twelve alternatives categorized into solvent extraction and precipitation, non-PHA cell mass (NPCM) dissolution, and assisted extraction methods were graded and ranked. A GRA scoring system was used to evaluate the proposed alternatives. A decision matrix was formulated by incorporating the scoring system with the set of criteria from AHP^[4]. The alternatives and their overall grades are presented in Table 2.

Table 2. Priority weights of the proposed PHA extraction protocol alternatives

| Category | Alternative (Rank) | Overall Weight |
|--------------------------------------|--|----------------|
| Solvent extraction and precipitation | 1,2-propylene carbonate (10) | 0.575 |
| | 1,3-dioxolane (6) | 0.637 |
| | Dimethyl carbonate (4) | 0.759 |
| | Butyl acetate (5) | 0.720 |
| | Cyclohexanone (11) | 0.559 |
| | Acetone / ethanol / 1,2-propylene carbonate (12) | 0.457 |
| Non-PHA cell mass (NPCM) dissolution | Sodium hypochlorite (9) | 0.580 |
| | Sodium hydroxide (1) | 0.797 |
| | Sodium hydroxide + sodium dodecyl sulfate (2) | 0.783 |
| Assisted extraction | Ammonia water (3) | 0.765 |
| | Ultrasound-assisted sodium hypochlorite (8) | 0.620 |
| | Microwave-assisted EDTA (7) | 0.634 |

The overall highest priority weights were given to NPCM dissolution protocols including sodium hydroxide (0.797), sodium hydroxide + sodium dodecyl sulfate (0.783), and ammonia water (0.765). The reagents involved in these protocols

are relatively safer and cheaper compared to the solvents used in other protocol alternatives, hence, the higher grades in both environmental and economic aspects. A sensitivity analysis showed that these protocols are excellent, particularly if extraction cost is given a higher priority. However, if hazards and risks as well as purity were given more importance, dimethyl carbonate and butyl acetate protocols are preferable than sodium hydroxide.

In conclusion, sodium hydroxide, sodium hydroxide + sodium dodecyl sulfate, and ammonia water were identified as the best PHA extraction and recovery protocols using AHP-GRA. Environmental and economic attributes of the protocol alternatives were highly prioritized, focusing on the hazards, risks and cost of the process. Further studies such as the validation and optimization of protocols, together with economic and life cycle analyses may be integrated with the results of this study to comprehensively determine a suitable PHA extraction and recovery protocol.

Keywords

analytic hierarchy process, extraction and recovery, grey relational analysis, multi-criteria decision analysis, polyhydroxyalkanoates

References

- [1] Pérez-Rivero C, López-Gómez J, Roy I. 2019. A sustainable approach for the downstream processing of bacterial polyhydroxyalkanoates: State-of-the-art and latest developments. *Biochemical Engineering Journal*. 150: 107283.
- [2] Requiso PJ, Nayve FRP Jr., Alfafara CG, Ventura RLG, Escobar EC, Ventura JS. 2018. Agricultural residue feedstock selection for polyhydroxyalkanoates production using AHP-GRA. *Philippine Journal of Science*. 147(4): 693-709.
- [3] Saaty TL. 1988. What is the analytic hierarchy process. *Mathematical Models for Decision Support*. 48: 109-121.
- [4] Kuo Y, Yang T, Huang GW. 2008. The use of grey relational analysis in solving multiple attribute decision-making problems. *Computers and Industrial Engineering*. 55: 80-93.

Fluorine concentration dependence on electrical and optical properties of In_2O_3 transparent film*

Kaito Oe ^{1,a}, Shinya Aikawa ^{1,b*}

¹ Kogakuin University, Tokyo, Japan

^acm20010@ns.kogakuin.ac.jp, ^baikawa@cc.kogakuin.ac.jp

Abstract

Transparent conductive films with high transmittance and low resistivity are demanded for enhancing the quality of liquid crystal displays, touch panel sensors, solar cells, and so on. For these applications, high transparency and conductivity are required for transparent conductive film, thus, it is necessary to improve both properties simultaneously. Sn-doped In_2O_3 (ITO) has a low electrical resistivity ($\sim 1 \times 10^{-4} \Omega\text{cm}$) because of its high carrier density (10^{21}cm^{-3}) and is widely used for commercial applications. It has a typical bandgap energy of $\sim 3 \text{ eV}$, which corresponds to the violet region near a wavelength of approximately 410 nm. This wide bandgap allows the transmission of most visible light spectra. In_2O_3 with a bandgap of 2.9 eV is often used as a mother material for transparent conductive film, increasing its carrier density by introducing oxygen vacancies or cation dopants such as Sn^{4+} of ITO. However, as the previous studies revealed that cation doping has limitation to further increase electrical conductivity, thus anion F^- doping is an alternative way to enhancing the electrical and optical properties of In_2O_3 -based transparent electrodes^[1]. Here, we focus on CaF_2 as an F dopant into In_2O_3 because CaF_2 has high transparency, and is inexpensive and safe material.

First of all, a glass substrate was ultrasonically cleaned with acetone and IPA, and then the substrate surface was cleaned by UV irradiation. After the cleaning, In_2O_3 co-doped with CaF_2 ($\text{In}_2\text{O}_3\text{:CaF}_2$) were prepared by RF magnetron sputtering using an In_2O_3 ceramic target and CaF_2 pellets. The discharge voltage was set at 100 W. The Ar and O_2 flow rate were fixed at 44 and 0.15 sccm, respectively. The deposition time was

adjusted as the film thickness to be 100 nm. $\text{In}_2\text{O}_3\text{:CaF}_2$ thin films with different F content were prepared by change in the number of the pellets placed on the target. In order to compare the effect of CaF_2 doping, In_2O_3 thin films without any dopants were also fabricated. The thin films were characterized using following equipment: room temperature Hall effect measurement system for the carrier density and mobility, X-ray diffractometer for the crystallinity, energy dispersive X-ray analysis (EDX) for the composition, four-point probe method for the sheet resistance, surface profiler for the thickness, and UV-vis-NIR spectrophotometer for optical transmittance.

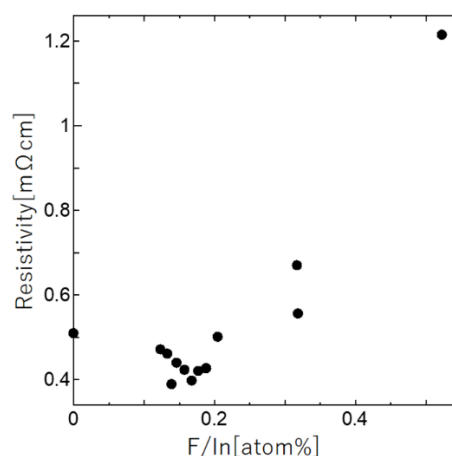


Fig. 1. Relationship between resistivity and F/In atomic ratio in the fabricated films

Fig. 1 shows the change in resistivity as a function of F/In atomic ratio in the films, which is estimated by EDX results. The resistivity becomes low when F/In is around 0.15, and then the resistivity increases as the F content increases. This might be related to the activation of F ions. More F ions in the film play a role in expansion of the lattice constant because of larger ionic radius of F^- , then

* Poster paper presentation

carrier mobility becomes decrease as the lattice constant widened, thus resistivity decreases. On the other hands, Ca was detected by EDX, but the effect of Ca has not yet been clarified at this moment.

Fig. 2 shows the comparison of the In_2O_3 , $\text{In}_2\text{O}_3:\text{CaF}_2$ (F/In = 1.44), and $\text{In}_2\text{O}_3:\text{CaF}_2$ (F/In = 0.174). By incorporation of CaF_2 in to In_2O_3 , transmittance spectrum becomes more transparent than pure In_2O_3 film, while the transmittance in the NIR region is degraded caused by the increase of carrier density, suggesting the free electron absorption. This is consistent to the result of the electrical properties.

In summary, we fabricated transparent In_2O_3 -based conductive films doped with CaF_2 . The F/In atomic ratio of around 0.15 showed minimum resistivity. Furthermore, the $\text{In}_2\text{O}_3:\text{CaF}_2$ film with 0.144 at.% of F content was more transparent than pure In_2O_3 . We successfully obtained lower resistivity and higher transparent In_2O_3 -based thin films by incorporation of CaF_2 .

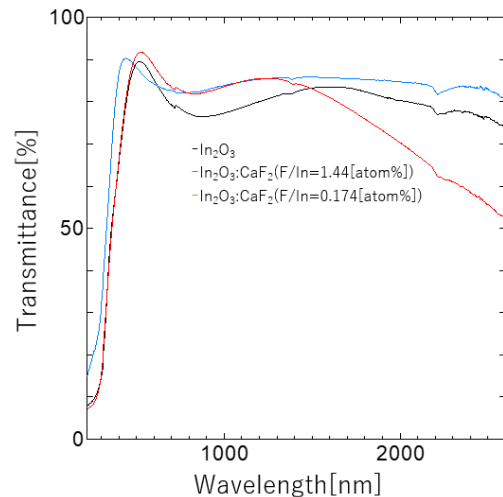


Fig. 2. Transmission spectra of typical In_2O_3 and $\text{In}_2\text{O}_3:\text{CaF}_2$ films.

Keywords

Transparent conductive film, In_2O_3 -based materials, Anion doping, CaF_2

References

- [1] Yuzo SHIGESATO, Naoko SHIN, Masayuki KAMEI, P. K. SONG and Itatu YASUI. Study on Fluorine-Doped Indium Oxide Films. Jpn. J. Appl. Phys. Vol. 39 (2000) pp. 6422–6426.

Performance evaluation of a locally designed water pump*

Aga-Angelica S. Pascual^{1, a*}, Arthur L. Fajardo^{1, b}, Omar F. Zubia^{1, c} and Roger A. Luyun Jr.^{2, d}

¹ Agribiosystems Machinery & Power Engineering Division, Institute of Agricultural & Biosystems Engineering (IABE), College of Engineering & Agro-Industrial Technology (CEAT), University of the Philippines Los Baños, Philippines

² Land & Water Resources Engineering Division, IABE, CEAT, UPLB, Philippines

^a aspascual2@up.edu.ph, ^b alfajardo@up.edu.ph, ^c ofzubia@up.edu.ph, ^d raluyun1@up.edu.ph

Abstract

The most common type of pump being utilized by farmers in Southeast Asia is the centrifugal pump. But due to the increasing cost of fuel, they use pumps that are energy-efficient alternatives to centrifugal pumps.

In Vietnam and Thailand, farmers use a pump called Axial Flow Pumps or AFPs. According to the Cereal Systems Initiative for South Asia (CSISA) Factsheet (2014) [1], AFPs can save more than 50% of the diesel/energy compared to the conventional centrifugal pumps when the lift is not more than 3 meters (9 feet).

Meanwhile, in the Philippines, local farmers in Region III - Central Luzon use a pump called *Voltron* pump (Figure 1). According to local farmers, this local pump design is as energy-efficient as AFPs but can lift more than 3 meters.



Fig. 1. Field installation of the Voltron pump.

Since there is no written study about *Voltron*, the study aimed to evaluate its performance. *Voltron* as shown in Figure 2, was tested at different pump shaft speed settings of 450, 600, and 700 rpm under different blade (impeller vanes) numbers of 6, 8, 9, and 10 using V-belts and B-section pulleys transmission. The shaft speed settings used were

based on the conducted farmers' survey while the number of impeller vanes was based on the angle with which the vanes can be easily fabricated.

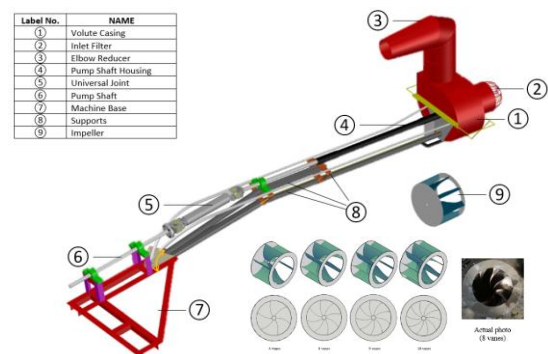


Fig. 2. Detailed drawing of the Voltron pump.

Testing and evaluation were conducted at the Mechanical Testing Facility of the Agricultural Machinery Testing and Evaluation Center - University of the Philippines Los Baños (AMTEC-UPLB), Laguna, Philippines using PAES 115:2000 - Centrifugal, Mixed Flow and Axial Flow Water Pumps – Methods of Test [2]. The schematic diagram of the test set up is shown in Figure 3.

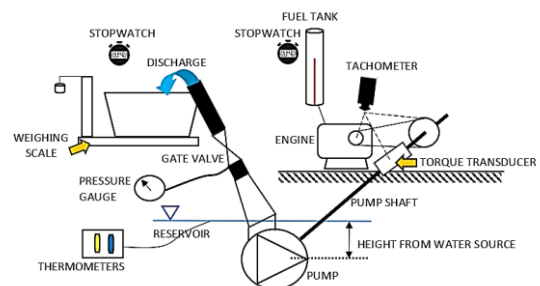


Fig. 3. Schematic diagram of the Test Set-up.

Statistical analysis was analyzed using Statistical Tool for Agricultural Research (STAR) 2.0.1 and R version 3.6.1. The experiment employed a Split

* Oral paper presentation.

Plot Design using a Completely Randomized Design.

The general trend observed from the pump characteristic curves were the indirect proportionality of the total head and discharge. The total head decreased as the discharge increased. Compared with most centrifugal pumps, the Voltron pump efficiency peak at a certain point then decreases after. Also, waterpower and fuel consumption increased as head, discharge and pumps shaft speed increased. Figure 4 shows the pump characteristic curve of Voltron with 8 vanes at different pump shaft speed.

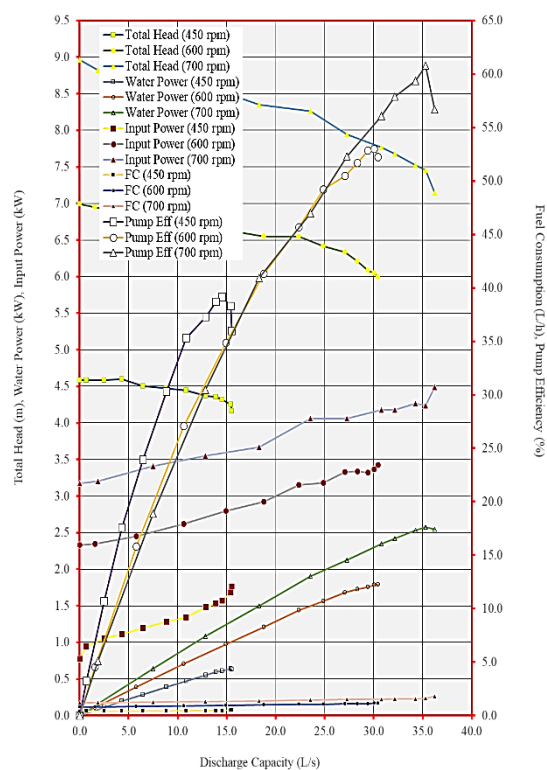


Figure 4. Performance characteristic curve of Voltron water pump with 8 vanes at different pump shaft speed.

The highest pump efficiency of 62.5% was observed using an 8-vane impeller under a 700-rpm setting. The existing pump parameters currently utilized by farmers are 8 vanes operating at 600 rpm. Statistical analysis showed that there is no significant difference between the pump efficiencies on the set speeds but there is a significant difference in the set number of vanes. On the other hand, the effects of speed, the head,

discharge, and fuel consumption increased as rotational speed was increased.

Overall, the behavior of the performance characteristics of this locally designed pump is similar as in the study of Chakraborty et al. (2012) [3] except for the effect of increasing the number of vanes on the head. Congruent to the study of Liu et al. (2010) [4], the study of Chakraborty et al. (2012) also concluded that increasing the number of vanes entailed increasing the head of the pump. On the contrary, this effect was not present on the behavior of the locally designed water pump as the total head has no significant difference between the number of vanes. This may be because of the way it is operated locally – submerged underwater – unlike centrifugal pumps that are operated above the water level and have a suction head.

Computing the fuel cost between the 8-vane impeller with a 700-rpm and a 600-rpm setting, the difference is around Php 17.61 per ha per day of operation favoring the usual setting. However, the 700-rpm setting will be more economical in the long run as it is determined to be more efficient than the normal setting being used in the field

Keywords

Voltron, water pump, pump performance

References

- [1] CSISA Factsheet. 2014. The Axial-Flow and Mixed Flow Pumps for Surface Water Irrigation, Drainage and Fisheries, 6–7.
- [2] PAES 115-2000. Agricultural Machinery – Centrifugal, Mixed Flow and Axial Flow Water Pumps – Methods of Test in *Philippine Agricultural Engineering Standards*
- [3] Chakraborty S, et al. 2012. Numerical Analysis of Effects of Blade Number Variations on Performance of Centrifugal Pumps with Various Rotational Speeds. *International Journal of energy and Power Engineering*, (2002),10.
- [4] Liu H, et al. 2010. Effects of Blade Number on Characteristics of Centrifugal Pumps. *Chinese Journal of Mechanical Engineering*. 23(06), 742. <https://doi.org/10.3901/CJME.2010.06.74>

Motion of gas bubbles induced by cavitation bubbles*

Kotaro Ono ^{1, a*}, Donghyuk Kang ², Yukio Tomita ³, Kotaro Sato ¹

¹ Graduate School of Engineering, Kogakuin University, Japan

² Department of Mechanical Engineering, Saitama University, Japan

³ Faculty of Education, Hokkaido University of Education, Japan

^a am19011@ns.kogakuin.ac.jp

Abstract

Cavitation phenomena are observed in the propeller of ships and various fluid machineries. Several researchers have been examining methods for avoiding cavitation erosion and vibration for a long period of time [1]. However, in recent years, technological research has been conducted using shock waves and microjets, such as sonoporation and drug-delivery systems, that are generated in the growth and collapse phase of cavitation bubbles [2]. Additionally, the microjets formed by the interaction of cavitation bubbles can generate a non-contact flow, and they are expected to be applied to flow field control. Given that the growth and collapse motion of bubbles is a complex phenomenon, the directional mechanism of the microjets produced by multiple interactions remains unclear.

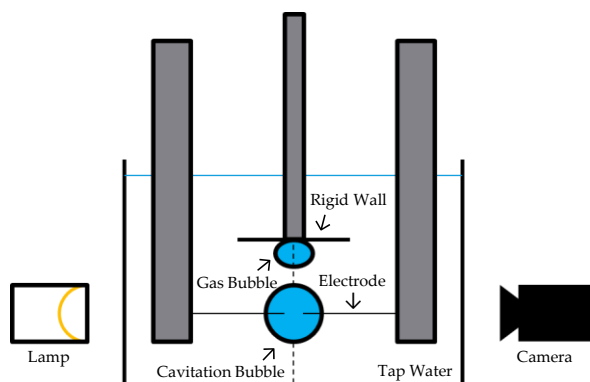


Fig. 1. Schematic of experimental equipment

In this study, we attempted to experimentally examine the interaction between a gas bubble attached to a rigid wall and cavitation bubble, which is one of the simplest cases among the interactions of multiple bubbles. We used the experimental equipment like shown in Fig. 1. A sufficiently large glass water tank ($W = 600 \text{ mm} \times$

$D = 300 \text{ mm} \times H = 360 \text{ mm}$) was filled with tap water, tungsten electrodes were placed on the top to generate cavitation bubbles, and an acrylic disc was placed on the top as a rigid wall. Gas bubbles were attached to the rigid wall using a syringe in an axisymmetric position with the cavitation bubbles, and their mutual interaction was captured using a high-speed camera with a metal halide lamp as the light source. The capture speed was 30000 fps and the shutter speed was 1/frame [s].

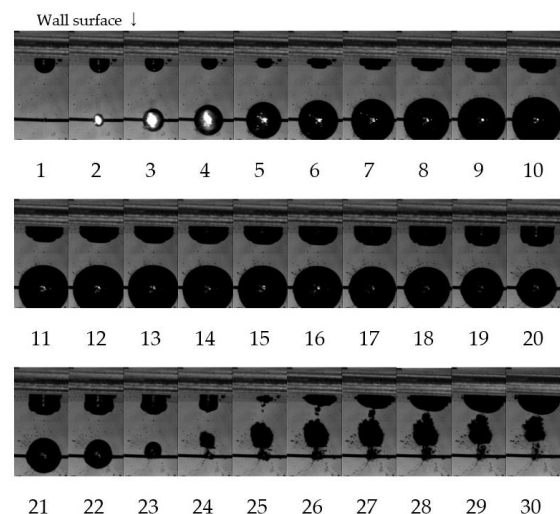


Fig. 2. Motion of the gas bubble attached a rigid wall ($R_{c,max} = 2.99 \text{ mm}$, $R_{g,0} = 1.23 \text{ mm}$, $L_0 = 7.25 \text{ mm}$, $R^* = 0.41$, $L_0^* = 2.43$)

The photograph frame interval is $33.3 \mu\text{s}$, and the distance ratio L_0^* is generally 2.5~3.0. Fig. 2 shows a small gas bubble, and the effect of the gas bubble is small. Fig. 3 shows the situation when the gas bubble is large, and the cavitation bubble behaves like a near free surface [3].

Fig. 4. shows the cavitation bubble doesn't behave any motion similar to near the rigid wall or the free surface [4]. By comparing and inspecting

* Oral paper presentation

these results, we attempted to clarify the motion of gas bubbles induced by the motion of cavitation bubbles and the change in the direction of jets generation with respect to the size ratio and distance ratio.

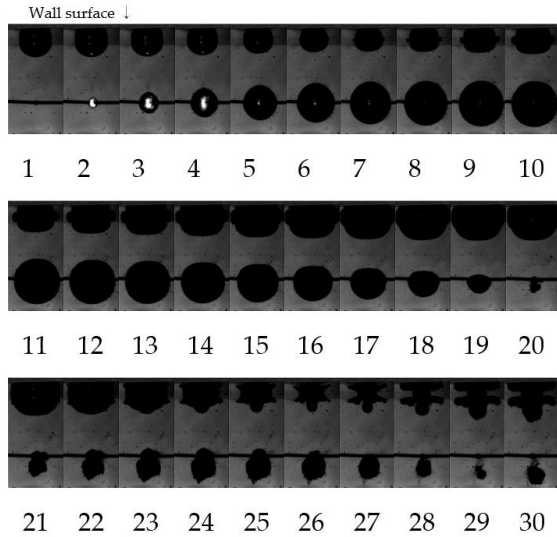


Fig. 3. Motion of the gas bubble attached a rigid wall ($R_{c,max} = 2.65$ mm, $R_{g,0} = 1.90$ mm, $L_0 = 7.10$ mm, $R^* = 0.71$, $L_0^* = 2.42$)

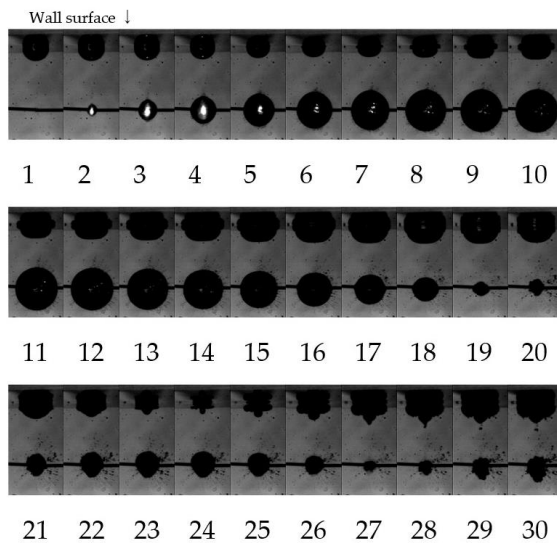


Fig. 4. Motion of the gas bubble attached a rigid wall ($R_{c,max} = 2.45$ mm, $R_{g,0} = 1.55$ mm, $L_0 = 7.15$ mm, $R^* = 0.63$, $L_0^* = 2.92$)

Keywords

Fluid dynamics, bubble dynamics, cavitation bubble, bubble interaction, microjet

References

- [1] Phillip, A. and Lauterborn, W. (1998), "Cavitation erosion by single laser-produced bubbles", *Journal of Fluid Mechanics*, vol. 361, pp. 75 - 116.
- [2] Bao, S., Thrall, B. D. and Miller, D. L. (1997): "Transfection of a reporter plasmid into cultured cells by sonoporation in vitro". *Ultrasound Med. Biol.*, Vol. 23, pp. 953-959.
- [3] Blake, J. R. and Gibson, D. C. (1981): "Growth and collapse of a vapour cavity near a free surface". *Journal of Fluid Mechanics*, Vol. 111, pp. 123-140
- [4] Zhang S., Duncan J.H., Chahine G.L. (1994): "The behavior of a cavitation bubble near a rigid wall". J. R. Blake et al. (eds.), *Bubble Dynamics and Interface Phenomena* pp. 429-436.

Development of a portable carrot harvester*

Zion Jemillinium S. Tam-awen ^{1,a}, Rossana Marie C. Amongo ^{1,b},
Fernando O. Paras Jr. ^{1,c}, Engelbert K. Peralta ^{2,d}

¹ Agricultural Machinery Division, Institute of Agricultural & Biosystems Engineering,
University of the Philippines Los Baños, Philippines

² Agricultural Food & Bio-process Engineering Division, Institute of Agricultural Engineering,
University of the Philippines Los Baños, Philippines

^a ztamawen@up.edu.ph, ^b rcamongo.edu.ph, ^c foparas1up.edu.ph, ^d ekperalta@up.edu.ph

Abstract

The Cordillera Administrative Region (CAR) particularly the province of Benguet is regarded as the top carrot producer in the Philippines because of its moderate temperature. Manual carrot harvesting is still the predominant practice in the country. Carrot harvesters available in the market which are usually imported from other countries are not appropriate for the mountainous topography of the carrot farms. Hence, this study was conducted to develop a portable carrot harvester that will adapt to the carrot farming conditions in Benguet province. The developed machine is capable of digging, sieving and exposing the roots from the farm plots. It is light in weight (81 kg) enough to be carried by two healthy farmers from one farm to another. The machine is made of locally available materials and fabricated adopting local manufacturing technology.



Figure 1. A farmer operating the portable carrot harvester

The machine has six major components namely: prime mover engine, power transmission system, body frame, digger blade, ground wheel and sieving web. Two types of blade (nose shape and comb shape) and three different lengths of sieving web (450 mm, 525 mm, and 600 mm) were tested and compared to get the best combination.



Figure 2. (a) Nose shape blade, (b) comb shape blade



Figure 3. Different sieving web lengths: (a) 450 mm, (b) 525 mm, (c) 600 mm

Results showed that except for fuel consumption, there is no significant difference on the length of sieving web in terms of effective field capacity, field efficiency, percent damaged root, lifting efficiency, and wheel slip. On the other hand, the blade type showed a significant difference in all the parameters measured. The best combination was obtained from the nose shape blade and 450

* Oral and poster paper presentation; title of poster: "Use of Portable Carrot Harvester in the Mountainous Carrot Farms of Benguet Province, Philippines"

mm sieving web length which resulted to an effective field capacity, field efficiency, percent damage root, lifting efficiency, wheel slip, and fuel consumption of 0.107 ha/h, 56.59%, 1.74%, 98.02%, 71.60%, and 0.802 L/h, respectively. Manual harvesting has effective field capacity of 0.0042 ha/h, percent damaged root of 0.53%, and lifting efficiency of 97.89%. There is a 1.06 kJ/min difference between the two methods which is equivalent to 0.024 hp decrease in drudgery when a farmer uses the machine instead of manual harvesting.

Keywords

Carrot harvester, digger blade, sieving web

References

- [1] Amin, E. A., Ismail, Z. E., El-Shabrawy, T. H., & Faleih, H. (2014). Influence Of Some Factors Affecting Carrot Harvesting. *Journal of Soil Sciences and Agricultural Engineering*, 5(6), 911–922. doi: 10.21608/jssae.2014.49417
- [2] Anitha, R., Kumar Singh, B., & Jahan, A. (2019). An Evaluation of Drudgery Reducing Agricultural Technologies Developed for Farm Women. *International Journal of Agricultural Science and Research*, 9(2), 35–42. doi: 10.24247/ijasrapr20195
- [3] Philippine Statistics Authority, C. A. R. (2017, October 25). <http://rssocar.psa.gov.ph/agriculture-releases/2016-crop-production-cabbage-carrot-and-potato>.
- [4] ShirwaL, S., Mani, I., Sirohi, N. P. S., & Kumar, A. (2015, December). Development and Evaluation of Carrot Harvester. Retrieved Sept 24, 2019, https://www.researchgate.net/profile/Sunil_Shirwal/publication/279334985_Development_and_Evaluation_of_Carrot_Harvester/links/56d565ed08ae2cd682bb68af.pdf?origin=publication_list

Flow control using interaction between synthetic and continuous jet*

Y. Suzuki ^{1a*}, K. Sato ^{2b}, K. Nishibe ^{3c}, K. Yokota ^{4d}

¹ Graduate School of Engineering, Kogakuin University, Tokyo, Japan

² Department of Mechanical System Engineering, Kogakuin University, Tokyo, Japan

³ Department of Mechanical Engineering, Tokyo City University, Tokyo, Japan

⁴ Department of Mechanical Engineering, Aoyamagakuin University, Tokyo, Japan

^a am19029@ns.kogakuin.ac.jp, ^b at12164@ns.kogakuin.ac.jp, ^c knishibe@tcu.ac.jp, ^d yokota@me.aoyama.ac.jp

Abstract

Synthetic jets can be used to control the direction of fluid flow. Research has been conducted previously to study the directional control of a single synthetic jet and its flow characteristics, and to determine the effect of frequency on fluid flow. However, few studies have focused on directional control using interference between continuous jets and synthetic jets, such as in the research reports by Smith and Glaetzer et al. Although it has been shown that the momentum ratio between the continuous jet and the synthetic jet is an important parameter, detailed flow characteristics such as the deflection mechanism have not been studied extensively.

The purpose of this study is to elucidate the basic flow characteristics under the interference condition between the continuous jet and the synthetic jet. The flow field was visualized using the smoke-wire method. The synthetic jet and continuous jet interfere under the condition of Reynolds number, $Re = U_0 b_0 / \nu = 600$ (slot width of synthetic jet $b_s = 3$ mm, flow velocity $U_{s0} = 3$ m/s). The velocity was measured with a hot-wire anemometer.

We investigated the momentum ratio in greater detail, which has a significant effect on jet deflection, and the effect of the slot width ratio. Fig. 1 shows the visualization results under typical conditions. As shown in the figure, the jet is affected by the interference and it is deflected. The oral presentation explains them in detail. The conclusion is shown below.

The direction of travel of a jet with a dimensionless frequency $l_0 = 10$ depends on the momentum ratio $\xi = U_{c0}^2 b_c / U_{s0}^2 b_s$. When the

slot width ratio is 1, the direction of travel remains straight at a low momentum ratio $\xi = 0.22 \sim 0.88$, deflects about 40 degrees toward the synthetic jet at an intermediate momentum ratio $\xi = 1.39 \sim 2.72$, and remains straight at a high momentum ratio $\xi = 3.56 \sim 4.5$.

It was found that the momentum ratio condition of jet deflection differs depending on the slot width ratio.

Within the range of this experimental condition, the dimensionless frequency $l_0 = 100$, which is a low frequency, is almost unaffected by the momentum ratio and the direction of jet is straight.

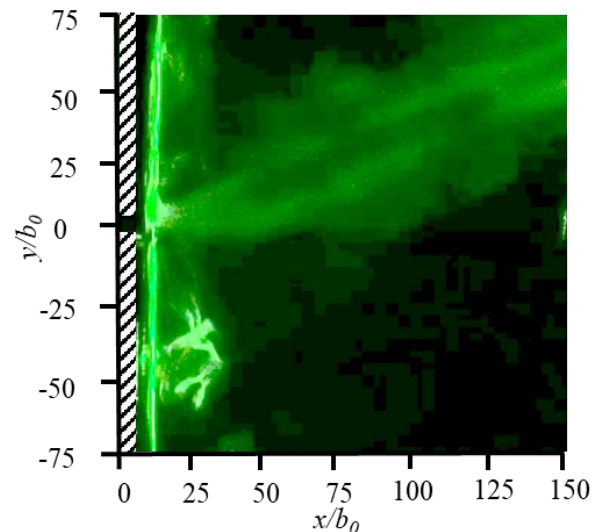


Fig. 1. Flow pattern of the continuous jet and synthetic jet from the smoke-wire method ($U_c = 6$ m/s, $b_c = 3$ mm, $U_s = 3$ m/s, $b_s = 3$ mm, $\xi = 2$)

* Oral paper presentation

Keywords

Synthetic jet, momentum ratio, flow control

References

- [1] Holman, R., Utturkar, Y., Mittal, R., Smith, B.L. and Cattafesta, L., "Formation criterion for synthetic jets". AIAA Journal, Vol. 43, No. 10, (2005), pp. 2110-2116.
- [2] Nishibe, K., Fujita, Y., Sato, K., Yokota, K. and Koso, T., "Experimental and numerical study on the flow characteristics of synthetic jets". Journal of Fluid Science and Technology, Vol. 6, No. 4, (2011), pp. 425-436.
- [3] Koso, T. and Morita, M., "Effects of stroke and Reynolds number on characteristics of circular synthetic jets". Journal of Fluid Science and Technology, Vol. 9, No. 2, (2014), pp. 1-15.
- [4] Watabe, Y., Sato, K., Nishibe, K. and Yokota, K., "The influence of an asymmetric slot on the flow characteristics of synthetic jets". Springer Proceedings in Physics, Vol. 185, (2016), pp. 101-107.
- [5] Kobayashi, R., Nishibe, K., Watabe, Y., Sato, K. and Yokota, K., "Vector control of synthetic jets using an asymmetric slot". Journal of Fluids Engineering, Vol. 140, No. 5, (2018), p. 051102.
- [6] Smith, B.L. and Glezer, A., "Jet Vectoring Using Synthetic Jets". Journal of Fluid Mechanics, Vol. 458 (2002), pp. 1-3.

Compositional analysis of black carbon aerosols by means of TOF-SIMS and SNMS*

Kentaro Sakai ¹, Ryota Koiwai ¹, Masato Morita ², Tetsuo Sakamoto ^{1,2,a*}

¹Graduate School of Electric Engineering & Electronics, Kogakuin University, Japan

²Department of Applied Physics, Kogakuin University, Japan

^a ct13087@ns.kogakuin.ac.jp

Abstract

There are many particles of small invisible size in atmosphere where we live. These fine solid or liquid particles suspended in the air are called "aerosol". Aerosols come from generation source of natural origin, such as yellow sand, and from urban areas, such as from railways and automobiles. In recent years, by the economic development of East Asia, aerosols emitted from industrial areas have become a large factor for air pollution. The components are analyzed by a filter and then subjected to a bulk analysis, for aerosols having various generation source as described above. In the bulk analysis, quantitative data can be obtained with a high accuracy, and can be performed relatively quickly. However, since only the average composition of the collected particles is known, it is impossible to identify the source focusing on individual particles or analyze the transfer history in principle [1].

Among aerosols, there is a kind of chain-like linked carbon, called BC (black carbon). There are made from incomplete combustion at factories, vehicles, forest fires, and so on. BC has a structure consisting of elemental carbon part and organic part. The organic part has many type of PAHs (polycyclic aromatic hydrocarbons), which is known one of the cancer risk. However, PAHs has analyzed only bulk analysis not mapping, and this does not show how PAHs affect in the human health.

In our research group, we developed an FIB-TOF-SIMS (focused ion beam time-of-flight secondary ion mass spectrometer) apparatus that can analyze individual particles of aerosol, the component distribution of the surface structure and internal structure [2]. On the other hand, we developed also SNMS (secondary

neutral mass spectrometry) function in the FIB-TOF-SIMS. This can analyze intact organic molecules from the organic part.

In this work, we analyzed BC by FIB-TOF-SIMS and SNMS to mapping of BC structure include organic and inorganic. BC has observed under frozen condition, because PAHs have characteristic of volatilize in high vacuum at room temperature. Therefore, we considered the detailed structure of BC. Finally we analyzed structure of BC, inorganic by FIB-TOF-SIMS and PAHs by SNMS. Fig.1 shows inorganic part of BC analyzed by FIB-TOF-SIMS. Fig. 2 shows mass count of BC analyzed by some apparatus with freezing mode. Therefore, we confirmed that our SNMS can analyze PAHs with freezing mode.

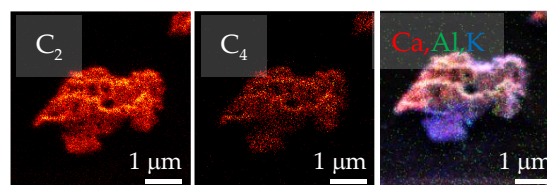


Fig. 1 Component Maps of BC analyzed by FIB-TOF-SIMS

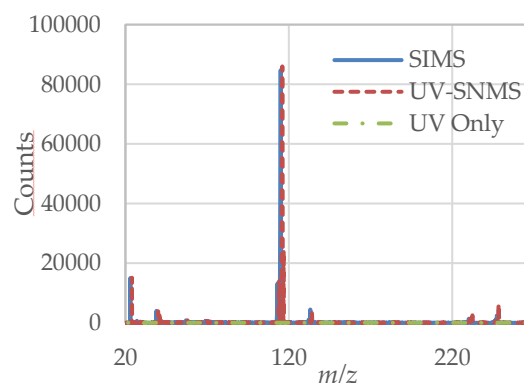


Fig. 2 Mass count of some apparatus with freezing mode

* Oral paper presentation

Keywords

Environment, aerosol, black carbon, FIB-TOF-SIMS, surface analysis

References

- [1] N. Takegawa, A. Takami. 2017. 4. Analysis of Aerosol Chemical Composition: An Overview. *Eurozoru Kenkyu*. 32: 118-124.
- [2] T. Sakamoto, M. Koizumi, J. Kawasaki, J. Yamaguchi. 2008. Development of a high lateral resolution TOF-SIMS apparatus for single particle analysis. *Applied Surface Science*. 255: 1617-1620.

Structure of jet with velocity oscillation at slot*

Chisato Ichihara ^{1,a}*and Kotaro Sato ^{1,b}

¹ Mechanical Engineering Program, Graduate School of Engineering, Kogakuin University, Tokyo, Japan

^a am20009@ns.kogakuin.ac.jp, ^b at12164@ns.kogakuin.ac.jp

Abstract

In the attitude control of aircraft and thermal management via refrigeration and air conditioning, flow control is widely employed using jet technology. As an alternative to continuous jets, the use of excited jets such as synthetic jets that can be easily generated using lightweight devices, is increasing. In synthetic jets, a jet structure with a substantial flow rate is formed downstream of the slot, despite zero net flow rate, due to repeated injection and suction. An attempt is made to control the jet traveling direction, without any geometrical change, by adjusting only the frequency of the jet. However, it is not suitable for large-scale fluid control because the momentum of the jets is small. In contrast, a pulsating jet, resulting from the addition of a velocity component to a steady jet, is one of the typical excited jets and is able to realize a large momentum. Pulsating jets have different properties from those of steady continuous jets owing to the behavior of vortices formed by the periodic velocity changes; unique control, including the diffusion characteristics of the flow, is expected. However, the influence of the velocity at the slot on the jet structure is not yet clear. In this study, we realize an unsteady outlet velocity with spatial velocity distribution and attempt to control the jet structure by superimposing the unsteady velocity component on the steady velocity at the slot. The flow characteristics of the pulsating jet with velocity distribution are mainly investigated by numerical simulations. In particular, the relationship between the oscillation characteristics and jet structure is discussed by investigating the effects of the frequency and phase of the slot outlet velocity distribution on the time-averaged maximum jet velocity and width using numerical calculations. When the

phase difference of the slot outlet velocity distribution is π , the vortex street is arranged in a staggered pattern; when the phase difference of the slot exit velocity distribution is 0, the symmetry of the flow field, including the vortex arrangement, is maintained. Therefore, the jet structure can be controlled based on the frequency under certain conditions.

The main symbols are shown below.

| | |
|-----------|--|
| b_0 | : Slot width ($= 5.0 \times 10^{-3}$ m) |
| f | : Frequency [Hz] |
| f^* | : Dimensionless frequency ($= fb_0/U_{p0} = \frac{fb_0}{U_{c0}}$ [-]) |
| Re | : Reynolds number ($= U_{p0} b_0/\nu$ [-]) |
| t | : Time [s] |
| T | : Period [s] |
| u | : Velocity in the x -direction [m/s] |
| u_0 | : Velocity in the x -direction at slot exit [m/s] |
| U_{c0} | : Steady velocity on slot exit [m/s] |
| U_{pa} | : Velocity amplitude on slot exit [m/s] |
| v | : Velocity in the y -direction [m/s] |
| v_c | : Inlet velocity at upper/lower boundary [m/s] |
| ω | : Vorticity [1/s] |
| φ | : Oscillating velocity phase difference between the upper and lower part of the nozzle |

In the numerical analysis, SC/Tetra (Software Cradle Co., Ltd.) for thermo-hydrodynamic analysis based on unstructured grid was used. A two - dimensional incompressible viscous flow is assumed and the k - ϵ model is used as a turbulence model. The mesh number is about 200,000. The computational domain is $400 b_0$ in the x -direction and $200 b_0$ in the y -direction. In this study, a velocity boundary condition at the nozzle entrance is given such that the slot exit velocity is $u_0 = U_{c0} + U_{pa} \sin(2\pi ft)$.

* Oral paper presentation

Fig. 1 shows typical flow patterns of pulsating jet for the slot width $b_0 = 5$ mm under the conditions of the jet steady velocity $U_{c0} = 6.0$ m/s, the velocity fluctuation amplitude $U_{pa} = 5.5$ m/s, the ratio $U_{pa}/U_{c0} = 0.92$, the Reynolds number $Re = 2050$, the frequency $f = 50$ Hz, and the dimensionless frequency $f^* = 4.17 \times 10^{-2}$. We can see the formation of vortex pairs due to winding at the slot outlet. At the slot exit velocity phase $\varphi = 0$, vortices are generated by the flow in the opposite region, and it can be confirmed that vortices are the object as well as the flow and form a vortex pair. At the slot outlet velocity phase $\varphi = \pi$, the time variation of the flow rate in the slot is 0. Since the phase of the velocity fluctuation changes π , it can be confirmed that the vortex row is staggered vortex street is generated.

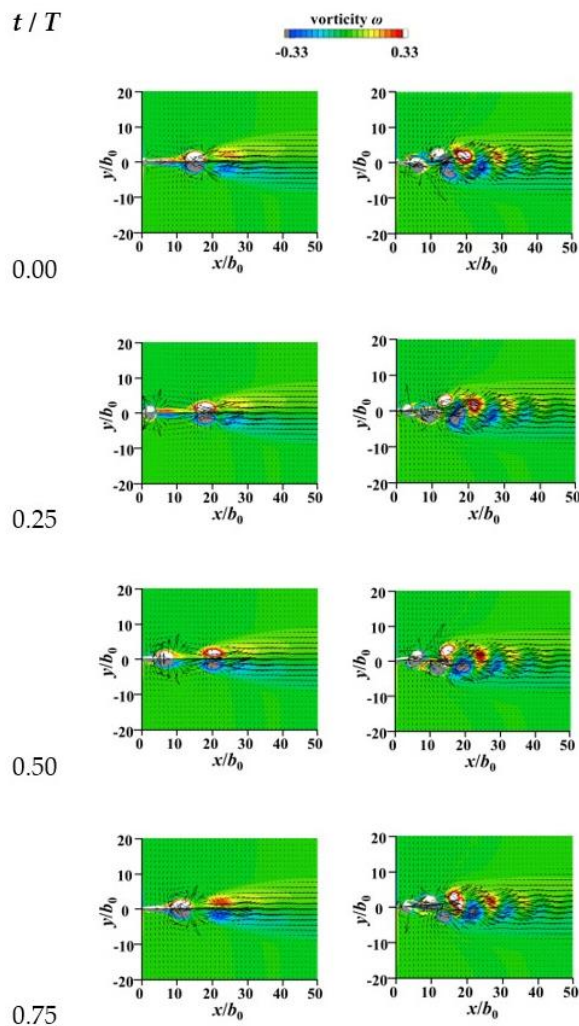


Fig. 1. Typical Flow Patterns of Pulsating Jet ($U_{c0} = 6$ m/s, $U_{pa} = 5.5$ m/s, $U_{pa}/U_{c0} = 0.92$, $f^* = 4.17 \times 10^{-2}$, $f = 50$, $Re = 2050$)

Fig. 2 shows effect of time variation on jet width. As for the jet width, the flow velocity near the slot outlet is the smallest, and the jet width becomes wider as the flow proceeds downstream. As for the time-averaged velocity distribution on the jet centerline, the velocity near the slot exit shows the maximum value, and the velocity decreases as the jet advances downstream. It is considered that these are caused by diffusion of the jet. In spite of the difference of dimensionless frequency, it seems to take the similar behavior of which the scale differs, because it tends to be similar, when it becomes dimensionless.

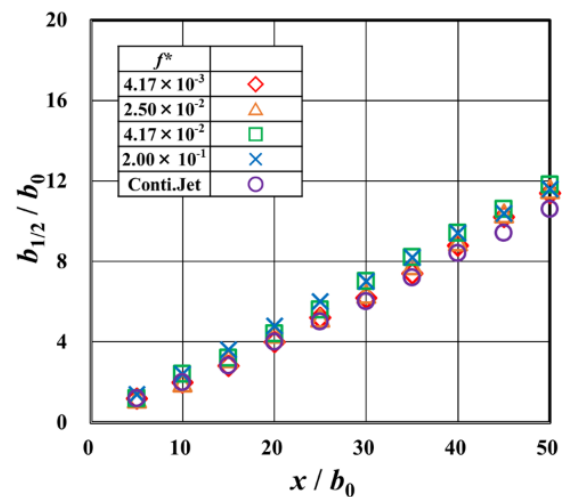


Fig. 2. Effect of time variation on jet width ($U_{c0} = 6$ m/s, $U_{pa} = 5.5$ m/s, $U_{pa}/U_{c0} = 0.92$, $Re = 2050$)

It is concluded that the jet structure can be controlled by the velocity distribution difference under specific conditions.

Keywords

Jet structure; Frequency-controlled; Velocity distribution; Oscillation characteristics; Synthetic jets

References

- [1] Nishibe, K., Fujita, Y., Sato, K., and Yokota, K. 2011. Study on the Fundamental Flow Characteristics of Synthetic Jets. *Journal of the Japan Society of Mechanical Engineers*. 77: 45-56.
- [2] Smith, B. L., and Glezer, A. 2002. *Jet Vectoring Using Synthetic Jets*. Cambridge University Press *J. Fluid Mech.* 458: 1-34.

Electrochemical evaluation of physical / chemical coated positive electrode for lithium-ion batteries*

Takumi Seki ^{1, a}, Kasane Takai ¹, Keitaro Takahashi ¹, Hibiki Miyauchi ¹, Shiro Seki ^{1*}

¹ Department of Environmental Chemistry & Chemical Engineering, School of Engineering, Kogakuin University, Tokyo, Japan

^a s316406@ns.kogakuin.ac.jp

Abstract

Lithium-ion batteries (LIBs) are widely used as electronic devices such as mobile phones and laptop computers. LIBs are expected to have high energy density and cycle performance. LIBs use lithium cobalt oxide (LCO) as the positive electrode active material, carbon material as the negative electrode active material, and organic solvent as the electrolyte. On the other hand, when a graphite negative electrode is used, the electrolyte decomposes as the initial stage of operating, and solid electrolyte interphase (SEI) is formed on the positive and negative electrode surfaces. For improvement of LIB system, multi-functionalization of SEI have been required and is expected to improve the input-output and cycle performances for the LIB. SEI forming configurations are categorized into physical and chemical methods. In this study, we evaluated the effect of physically and chemically formed SEI of the positive electrode on the battery properties.

Basic cell (bare LiCoO₂) was fabricated of LiCoO₂ as the positive electrode, Lithium metal as the negative electrode, and 1M-LiPF₆ (EC/DEC=3/7) as the electrolyte. The cell was prepared in the Argon filled glovebox. As a physical SEI forming method, barium titanate (BiTiO₃) film was coated on to the LiCoO₂ by sputtering or sol-gel process. As a chemical SEI forming method, two type additives vinylene carbonate (VC) and fluoroethylene carbonate (FEC) were added into electrolyte respectively, and SEI film was formed on to the LiCoO₂ during initial charge/discharge process by oxidative decomposition of additives. Prepared five type cells were measured by constant-current charge/discharge tests, and were evaluated the battery characteristics.

Physically, BiTiO₃ coated LiCoO₂ cells exhibited high capacity retention and low internal resistance.

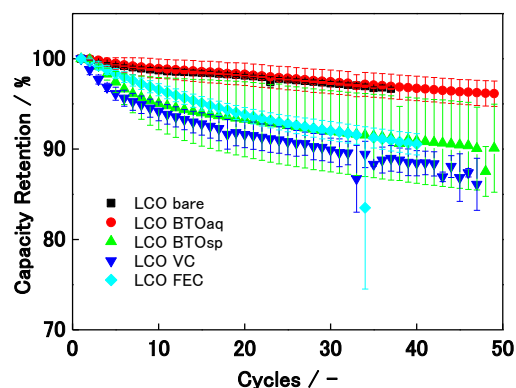


Fig. 1 Cycles number dependence of calculated retention capacities from discharge capacity of the [Li|1M-LiPF₆ EC/DEC|LCO] coin cell.

Physically SEI coating might have contributed to improvement of battery cycle characteristics, due to the suppression of the decomposition of the electrolyte solution.

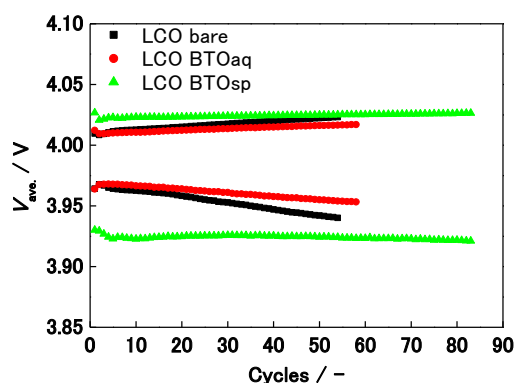


Fig. 2 Cycle number dependence of calculated average internal resistance from charge and discharge property of the [Li|1M-LiPF₆ EC/DEC| physically coated LCO] coin cell.

* Poster paper presentations

On the other hand, chemical SEI forming cells exhibited gradual increase of internal resistance with charge/discharge cycles and showed large capacity deterioration. Therefore, chemically formed LiCoO_2 might not be improved for battery cycle characteristics and large voltage drop.

Keywords

Electrochemical, lithium ion battery, solid electrolyte interphase

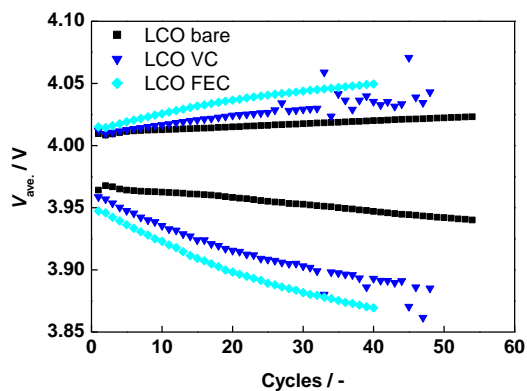


Fig. 3 Cycle number dependence of calculated average internal resistance from charge/discharge property of the $[\text{Li}|\text{1M-LiPF}_6 \text{ EC/DEC}| \text{chemically coated LCO}]$ coin cell.

Fabrication of core-shell structures using TiO₂ and PANI for methyl orange removal*

Marco Miguel P. Parel^{1,a,*}, Ivy R. Colambo^{1,b}, Marvin U. Herrera^{1,c}

¹ Institute of Mathematical Sciences and Physics, University of the Philippines Los Banos, Philippines

^a mpparel@up.edu.ph, ^b ircolambo@up.edu.ph, ^c muherrera@up.edu.ph

Abstract

This study aims to fabricate core-shell structures with n-type TiO₂ as core and p-type conducting PANI as the outer shell to remove methyl orange using photocatalysis and adsorption. TiO₂ [1-3] is a highly utilized n-type semiconductor due to its photocatalytic and electrical properties. In addition, PANI [4-6], which is a p-type conducting polymer is used to combine with TiO₂ to enhance the properties of TiO₂ that can be used in visible light photocatalysis. Methyl orange [7,8] is a known chemical pollutant that is used in studies to test dye removal or degradation. Fabrication of a core-shell structure using n-type TiO₂ and p-type PANI maximizes the amount of interface as a result of a pn-heterojunction, where depletion region occurs to execute visible light photocatalysis for methyl orange removal.

Core-shell structures were fabricated using simple soaking method, wherein TiO₂ powders were functionalized by immersing in silane aniline-ethanol solution (1g : 5mL ratio). The silane aniline-ethanol solution was prepared by mixing absolute ethanol and N-[3-(Trimethoxysilyl)propyl] aniline coupling agent (0.8% v/v). Moreover, the grafted aniline molecules were polymerized by oxidative method by soaking consecutively in 0.8 M HCl-aniline monomer mixture (10% v/v) and 0.2 M APS solution.

The sample was characterized using SEM and EDX Analyses and FTIR Spectroscopy for methyl orange removal using photocatalysis and adsorption for varying sample mass and varying dye concentration. Fig. 1 illustrates the possible configuration of the chemical structure of PANI molecules attached on functionalized TiO₂ based on the peaks found in the FTIR spectra and the elements found in the SEM and EDX Analyses, which are Ti, O, Si, S and P. The

structure shows Si-O bond which indicates linkage between TiO₂ and the aromatic rings. Moreover, the structure shows the presence of quinoid rings, benzenoid rings and polarons.

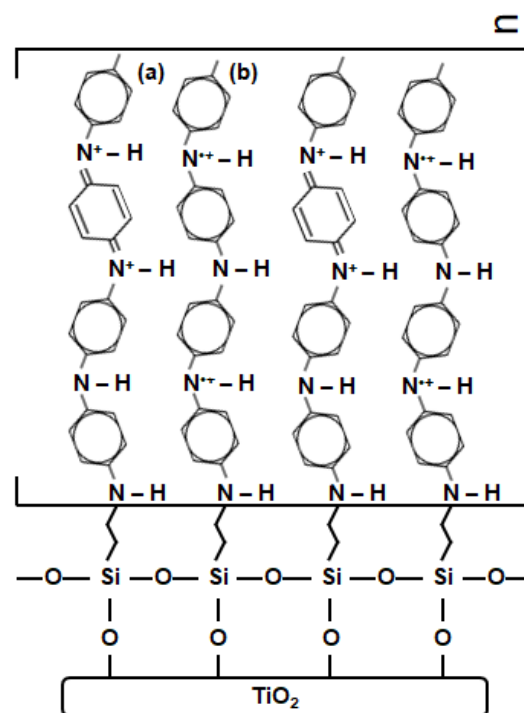


Fig. 1. Possible configuration of growth of PANI on silane-aniline grafted TiO₂ with different structures (a,b).

Using photocatalysis and adsorption methods, the ratio (*R*), which is given by

$$R = \frac{|C_L - C_{NL}|}{C_{NL}} \quad (1)$$

is obtained where *C_L* is the removed methyl orange concentration using light and *C_{NL}* is the removed methyl orange concentration without light. Fig. 2 shows that using photocatalysis and adsorption methods for a constant dye concentration of 20 ppm, *R* is highest when the sample mass is 0.02 g. Furthermore, Fig. 3 shows that using photocatalysis and adsorption

* Oral paper presentation

methods for a constant sample mass of 0.02 g, R is highest when the dye concentration is 20 ppm.

With this observation, we can conclude that the ratio of methyl orange removal between using light and without is when using 0.02 g of TiO_2 -PANI sample at a dye concentration of 20 ppm. In conclusion, core-shell structures were successfully fabricated using TiO_2 and PANI for removal of methyl orange.

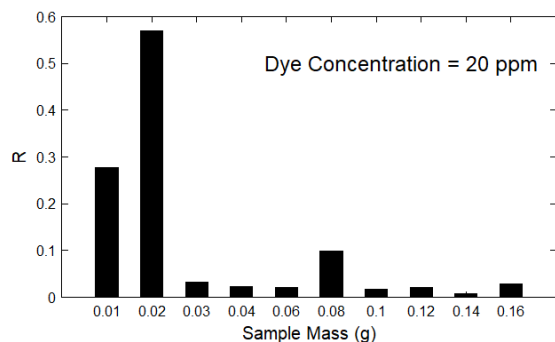


Fig. 2. Plot of the ratio (R) with respect to the varying mass of TiO_2 -PANI for a constant dye concentration of 20 ppm.

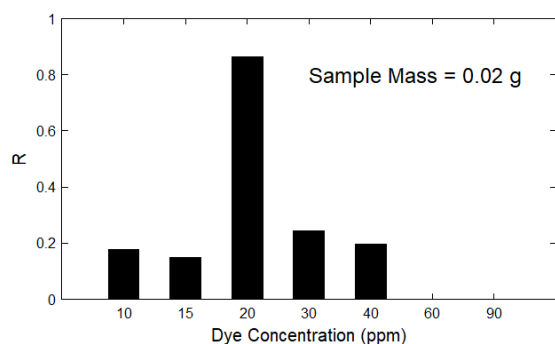


Fig. 3. Plot of the ratio (R) with respect to the varying dye concentration for a constant mass of TiO_2 -PANI of 0.02 g. $R = 0$ for 60 ppm and 90 ppm.

Keywords

Core-shell, polyaniline, TiO_2 , p-n heterojunction, photocatalysis

References

- [1] Fujishima A, Rao TN, Tryk DA. 2000. Titanium dioxide photocatalysis, *J. Photochem. Photobiol. C* 1: 1-21.
- [2] Hoffman MR, Martin ST, Choi W, Bahnemann DW. 1995. Environmental applications of

semiconductor photocatalysis, *Chem. Rev.* 95: 69-96.

- [3] Zhang MY, Shao CL, Guo ZC, Zhang ZY, Mu JB, Cao TP, Liu YC. 2011. Hierarchical

nanostructures of Copper (II) phthalocyanine on electrospun TiO_2 nanofibers: controllable

solvothermal-fabrication and enhanced visible photocatalytic properties, *Appl. Mater. Interfaces* 3: 369-377.

- [4] Yang S, Ishikawa Y, Itoh H, Feng Q. 2011. Fabrication and characterization of core/shell structured TiO_2 /polyaniline nanocomposite. *Journal of Colloid and Interface Science* 356: 734-740.

- [5] Mousli F, Chaouchi A, Hocine S, Lamouri A, Vilar MR, Kadri A, Chehimi MM. 2019. Diazonium-modified TiO_2 /polyaniline core/shell nanoparticles. Structural characterization,

interfacial aspects and photocatalytic performances. *Applied Surface Science* 465: 1078-1095.

- [6] Yang C, Dong W, Cui G, Zhao Y, Shi X, Xia X, Tang B, Wang W. 2017. Enhanced

photocatalytic activity of PANI/ TiO_2 due to their photosensitization-synergetic effect.

Electrochimica Acta 247: 486-495.

- [7] Jamshidi E, Manteghi F. 2020. Methyl Orange Adsorption by Fe_2O_3 @Co-Al-Layered Double Hydroxide. *Proceedings* 2019, 41(1), 64.

- [8] Trabelsi H, Khadhraoui M, Hentati O, Ksibi M. 2013. Titanium dioxide mediated photo-degradation of methyl orange by ultraviolet light. *Toxicological & Environmental Chemistry* 95: 1-16.

Ferroelectric characteristics of $\text{SrBi}_2\text{Ta}_2\text{O}_9$ thin film and application

Wen-Cheng Tzou ^{1,a,*} and Cong-Cheng Li ^{1,b}

¹Department of Electro-Optical Engineering, Southern Taiwan University of Science & Technology, Taiwan

^awjtzou@stust.edu.tw, ^bm9410203@stust.edu.tw

Abstract

Ferroelectric thin films have been extensively investigated for nonvolatile memory application, because ferroelectric random access memories (FeRAMs) have the characteristics of lower writing voltage, faster writing speed and better endurance. Among ferroelectric materials, $\text{Pb}(\text{Zr,Ti})\text{O}_3$ (PZT) is an important material for ferroelectric memory devices because of high remanent polarization and low-temperature crystallization, whereas it has few serious problems such as fatigue and Pb pollution^[1]. For above mentioned reasons, $\text{SrBi}_2\text{Ta}_2\text{O}_9$ -base thin films of Bi-layered ferroelectric have drawn much attention for nonvolatile random access memory (NVRAM) applications due to their fatigue endurance of up to 10^{12} switching cycles, good retention and lower leakage current^[2-3]. However, the high processing temperature and low remanent polarization of SBT thin films are considerable problems for practical applications. For a metal/ferroelectric/semiconductor (MFS) structure, the unwanted silicon oxide layer and the interfacial layer can be formed between the ferroelectric thin film and substrate as the ferroelectric thin film is deposited on the semiconductor substrate. The ferroelectric properties of MFS structures, degraded by the low dielectric silicon oxide layer and interfacial layer, can be improved by inserting a high dielectric buffer layer^[4]. In this study, the SBT and BZT thin films deposited on Si substrates using RF magnetron sputtering will be presented. In this study, ferroelectric thin films of $\text{SrBi}_2\text{Ta}_2\text{O}_9$ (SBT) or bilayered $\text{SrBi}_2\text{Ta}_2\text{O}_9/\text{Ba}(\text{Zr}_{0.1}\text{Ti}_{0.9})\text{O}_3$ (SBT/BZT) are successfully deposited on Si substrate under the optimal RF magnetron sputtering conditions, and their electrical and ferroelectric characteristics are discussed.

The C-V measurement, applied voltage is swept at a speed of 0.4 V/s from -20 to +20 V and then from

+20 to -20 V, is used to measure the ferroelectric memory behavior of deposited SBT thin films under the various oxygen concentrations. The memory windows and capacitances of Al/SBT/Si structures increase with the increase of oxygen concentrations, and those have the maximum value at the 40% oxygen atmosphere as shown in Fig. 1.

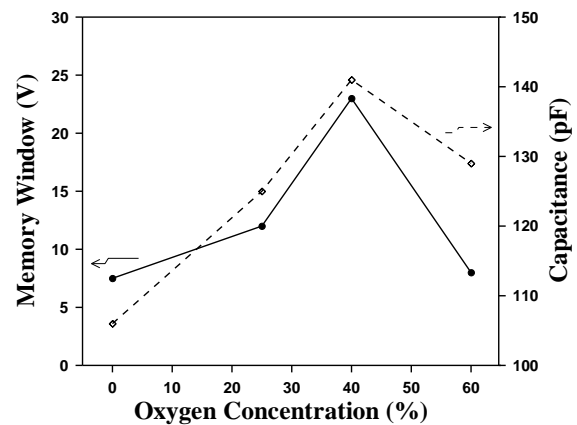


Fig. 1. Memory windows and capacitance of the MFS structure using SBT thin films deposited at various oxygen concentrations.

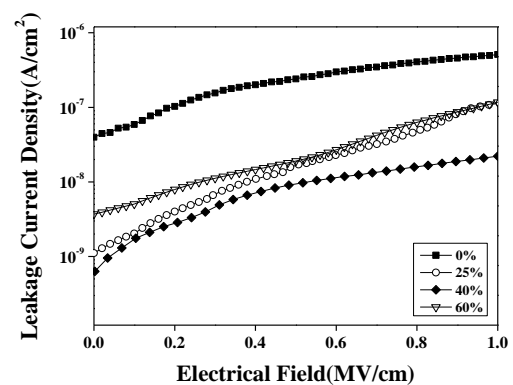


Fig. 2. The leakage current density versus electrical field of SBT thin films deposited at various oxygen concentrations.

Fig. 2 shows the leakage current density versus electrical field (J-E) curves of SBT thin films deposited on Si substrates under various oxygen

concentrations. The leakage current density decreases with the increase of oxygen concentrations.

The C-V characteristics of single-layer and bilayer MFS structure are shown in Fig. 3. The MFS with single SBT film and one with bilayered SBT/BZT film obtain the memory window of 23 V and 30 V, respectively. The memory window of bilayered SBT/BZT structure shows larger than one of single layer SBT structure. The leakage current density versus applied voltage (J-V) curves of MFS structures are shown in Fig. 4. The leakage current density is 9.7×10^{-9} A/cm² for the Al/SBT/Si MFS structure and 1.4×10^{-7} A/cm² for the Al/SBT/BZT/Si one at a field strength of 0.5 MV/cm, respectively.

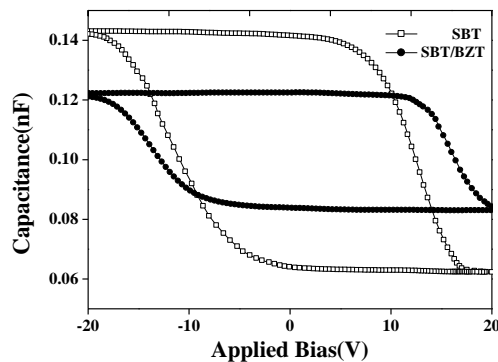


Fig. 3. C-V characteristics of Al/SBT/Si and Al/SBT/BZT/Si structures.

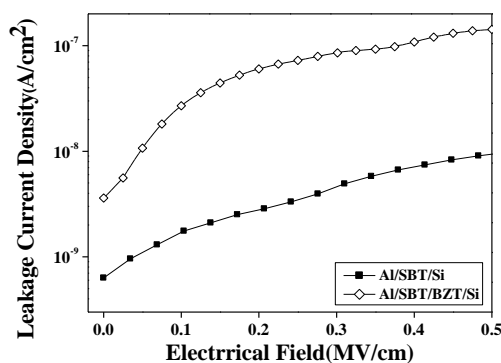


Fig. 4. Leakage current density versus electrical field of MFS structures.

Keywords

Ferroelectric thin film, memory window, leakage current density

References

- [1] Park Hye. H., Park Hyu. H., Hill R. H. 2004. Stacking effect on the ferroelectric properties of PZT/PLZT multilayer thin films formed by photochemical metal-organic deposition. *Applied Surface Science*. 237: 427-432.
- [2] Das R. R., Bhattacharya P., Katiyar R. S. 2002. Leakage current behavior of SrBi₂Ta₂O₉ ferroelectric thin films on different bottom electrodes. *J. Appl. Phys.* 92: 6160-6164.
- [3] Coondoo I., Jha A. K. 2007. Investigations of structural, dielectric and ferroelectric behavior of europium substituted SrBi₂Ta₂O₉ ferroelectric ceramics. *Solid State Commun.* 142: 561-565.
- [4] Hirai T., Nagashima K., Koike H., Matsuno S., Tarui Y. 1996. Crystal and Electrical Characterizations of Epitaxial CexZr1-xO2 Buffer Layer for the Metal/ Ferroelectric/ Insulator/ Semiconductor Field Effect Transistor. *Jpn. J. Appl. Phys.* 35: 5150-5154.

To enhance mechanical property of PBI thin-film by E-beam irradiation

Hsiao-Wu Lai ^{1,a*}

¹ Dept of Chemical & Materials Eng, Southern Taiwan University of Science & Technology, Taiwan

^a swlai@stust.edu.tw

Abstract

Recent years, acid-doped polybenzimidazole (PBI) polymer as a proton conducting membrane is used for fuel cell membrane, which have attracted great attention due to its relatively high proton conductivity at temperature higher than 100°C. However, it has some drawbacks for proton conducting membrane of PBI-based high temperature PEMFCs such as high cost and large membrane resistance. In addition, PBI membrane can be protonated by doping in phosphoric acid to be used as an ionic conductive membrane. The acid doping level can achieving 5-8 mol phosphoric acid per repeat unit of the PBI polymer and the membrane thickness ranges were around 200 to 50 μm .

In this study, we report the improvement of cross-linking degree of PBI polymers by electron beam irradiation method, leads to an enhancement of mechanical property in PBI membrane. The

commercial pristine PBI membrane with ultra-thin thickness of 20 μm were used. To the best of our knowledge, there are few report exists on the application of such thinner membrane for PEM fuel cells. The cross-linking of ultra-thin PBI membrane was prepared via electron beam radiation with different electron fluences and characterized by TGA, UV-Vis, and mechanical analysis. Preliminary experiments indicated that some advantages can be gained, in terms of mechanical property, by using ultra-thin PBI membrane exposed to electron beam irradiation. To investigate the electrochemical properties, the PA doping level, impedance, and fuel cell performance were measured at operating temperature.

Keywords

Polybenzimidazole, e-beam irradiation, polymer cross-linking

Aerodynamic characteristics of soccer balls focusing on drag crisis*

Yuki Sakamoto ^{1, a*}, Shinichiro Ito ^{2, b} and Masaki Hiratsuka ^{2, c}

¹ Graduate School of Kogakuin University, Tokyo, Japan

² Kogakuin University, Tokyo, Japan

^a am19022@ns.kogakuin.ac.jp, ^b ito@cc.kogakuin.ac.jp, ^c hiratsuka@cc.kogakuin.ac.jp

Abstract


In soccer, the aerodynamic characteristics of the ball have a significant effect on the development of the game. A new type of soccer ball is introduced at each World Cup and other major international tournaments, and the shape of the panels that make up the ball has a significant influence on its behavior. The influence of the panel shape on the ball's flight path has become an essential aspect of the ball design. Various aerodynamic studies have been conducted to elucidate the mechanism of this effect. Goff et al. ^[1] reported the aerodynamic difference of non-spinning several soccer balls by the different panel shapes. Hong et al. ^[2] showed that the separation point changed depending on the number of seams by a 2D-particle image velocimetry method. Previous visualization measurements have mainly focused on the laminar and turbulent regions. The critical region, which is considered important in twin vortices and irregular orbital changes, is still unexplored.

In this study, we visualized and measured the effects of panel type and ball orientation on the flow and the ball's flight path in the critical region. First, drag measurements were performed on 11 kinds of different soccer balls with a wind tunnel and a three-components load cell whose maximum load was 50.0 N on each component. The wind tunnel we used is an open type with a sirocco fan. The outlet's size is 0.38 m × 0.38 m, and the length of the measurement section is 0.78 m. The samplings were conducted at 1000 Hz for 9.0 seconds from a wind speed of 3 to 29 m/s in every 1 m/s under computer control, and the experimental values were averaged. This speed range covers most of the speed of a soccer ball that is kicked in a real game. All of the balls were

employed in past international competitions as shown in Table 1.

Next, we measured the separation points of the flow in the critical region by oil film experiments and 2D-PIV measurements for selected balls. Three velocity ranges were measured: subcritical region (laminar flow), critical region, and supercritical region (turbulent flow). The PIV images were taken with a NAC MEMRECAM HX-3 at 2000 FPS with a resolution of 5 megapixels. A Lee Laser MODEL LDP-100MQG was used as the laser light source, with a peak pulse power of 2.0 kW. We used Koncerto II, an analysis software from Seika Digital Image. The laser light sheet was placed on a meridian line of the soccer ball and photographed from the side with a high-speed camera. The high-speed camera's shooting interval was set to 15 μs and the average frame rate was 2000 fps, and the thickness of the laser light sheet was set to 3 mm. The smoke of Dioctyl sebacate was used as tracer particles.

Table 1. Soccer balls used in this experiments

| | | | |
|--|---|---|---|
| Telstar18 | Krasava | Finale | Vantaggio |
|  |  |  |  |
| Ordem | Evopower | Delta | Tango12 |
|  |  |  |  |
| Teamgeist | Jabulani | Merlin | |
|  |  |  | |

* Oral paper presentation

Figure 1 shows the C_D diagram for each ball. Drag crisis is a phenomenon in which the drag coefficient drops off suddenly as the Reynolds number increases. The drag coefficients of balls changed rapidly from about 0.5 to 0.2 at a Reynolds number in the range of 1.0×10^5 and 2.4×10^5 , as shown here. This corresponds to the flow aspect change around the ball from the laminar separation to the turbulent separation. In order to explain these phenomena, the drag crisis was defined as the Starting and the Ending Reynolds number. The Starting Reynolds number and the Ending one was lowest at 1.0×10^5 and 1.2×10^5 , respectively, on the Evopower, and they were highest at 1.8×10^5 and 2.4×10^5 , respectively, on the Jabulani. It was found that the flow around the Evopower turned into a turbulent flow on about 5 m/s. however, the flow around the Jabulani turned into a turbulent flow on about 12 m/s. We considered that the cause of these phenomena was the difference in the panel shape of the ball.

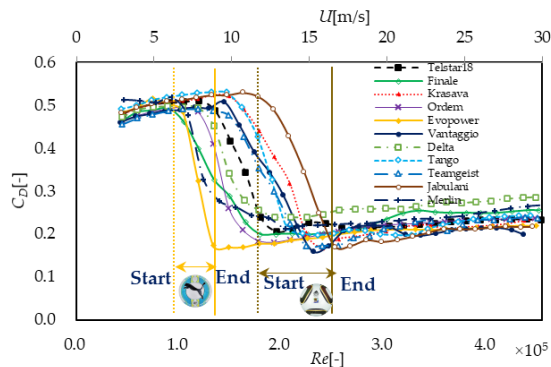


Fig.1. The C_D diagram of each ball

Tables 2 show the 2D-PIV results of the Evopower. In all cases of the subcritical and supercritical regions of drag crisis, it could be seen that the separation point and the flow direction of the wake flow were the same despite the change in the panel orientation. In the subcritical state of drag crisis, where Re was less than 1.8×10^5 (as shown in Figure 1), the flow separation occurred around 90° when the center of the left front of the ball was defined as 0° . The C_D in this state was about 0.5 in the Reynolds number, less than 1.0×10^5 in Figure 1. This was because the width of the turbulent ball wake became large on account of the separation occurred at around 90° . However, the separation point occurred in more than 90° in the supercritical state and the C_D became smaller to

about 0.2 in the Reynolds number, more than 2.5×10^5 in Figure 1. This was because as the Reynolds number increased the ball grooves stimulated the boundary layer, and the turbulent boundary layer, which was strong against flow separation, was created. Therefore, the flow separation was delayed, resulting in a narrow wake turbulence width. In the drag crisis state, the position of the separation point and the flow expansion direction of the wake varied depending on the orientation of the panel in any ball. Accordingly, it was found that the laminar separation and the turbulent separation were mixed depending on the panel in the drag crisis state, and the flow around the ball was partially different.

Table 2. The 2D-PIV Results of the Evopower

| Subcritical (6m/s) $Re = 9.3 \times 10^4$ | Critical (8m/s) $Re = 1.2 \times 10^5$ | Supercritical (15m/s) $Re = 2.2 \times 10^5$ |
|--|---|---|
| | | |
| | | |
| | | |

KEYWORDS

drag crisis, soccer ball, flow separation, oil film, particle image velocimetry (PIV)

REFERENCES

- [1] Goff, J., Asai, T., Hong, S., J. Sports Eng. Technol, 228, 188–194 (2014).
- [2] Hong, S., Asai, T., Seo, K., Procedia Eng., 112, 391–394 (2015).

Technical Presentations

Water Resources Engineering

| | | |
|---------------------|---|---|
| Moderator | : | Dr. Rubenito M. Lampayan |
| Panelists | : | Dr. Marion Lux Y. Castro, Dr. Omar F. Zubia, Dr. Joan Cecilia C. Casila |
| Technical Assistant | : | Ms. Mary Ann M. Porlay |
| 01:30PM – 01:35PM | Welcome Remarks and Introduction of Panel Members | |
| 01:35PM – 01:50PM | Assessing the impacts of climate change on irrigation diversion water requirement in the Philippines | <u>Lanie A. Alejo*</u> , Victor B. Ella, Rubenito M. Lampayan, Aurelio A. Delos Reyes Jr. (UPLB) |
| 01:50PM – 02:05PM | Suitability Analysis for SSIP through GIS-based Water Resources Assessment | <u>Alfred F. Fortu Jr.*</u> , RP Javellonar, AM Pascua, MAA Saet, MP Lambonao (UPLB) |
| 02:05PM – 02:20PM | GIS-based Suitability Analysis of Small Water Impounding Projects (SWIPs) In CALABARZON Region | Rossana Marie C. Amongo, Ronaldo B. Saludes, Roger A. Luyun, Jr., Patrick Lemuel P. Relativo, Maria Victoria L. Larona, <u>Ronnie C. Valencia*</u> , Ria Salustia dG. Duminding, Michel G. Acosta, Kobe Conrad R. Abellera, John Carlo L. Navasero, Romel A. Arrobang (UPLB) |
| 02:20PM – 02:35PM | Simulating the impacts of Deficit Irrigation on Corn Yield and Water Productivity using Coupled DSSAT Ceres-Maize and Aquacrop Models | <u>Marilyn S. Painagan*</u> , Victor B. Ella (UPLB) |

Suitability analysis for SSIP through GIS-based water resources assessment*

Alfredo F. Fortu Jr. ^{1,a*}, Mary Rose P. Lambonao ^{1,b}, Alex M. Pascua ^{2,c}

¹ Romblon State University, Liwanag, Odiongan, Romblon, Philippines

² Marinduque State College, Boac, Marinduque, Philippines

^a alfred_fortujr@yahoo.com, ^b lambonaomrose@gmail.com, ^c aleyanpascua@gmail.com

Abstract

This study focused mainly on the identification of suitable sites for small scale irrigation projects in the provinces of Romblon and Marinduque through Geographic Information System-based water resources assessment. Collection of primary and secondary data and validation of existing small scale irrigation projects in the provinces of Romblon and Marinduque were conducted. All data collected were consolidated, analysed and used in the processing of needed thematic maps using Geographic Information System and Remote Sensing techniques. Validation shows that Diversion Dams, Small Water Impounding Project, Shallow Tube Well, Pump Irrigation System Open Source are the main irrigation systems both in Romblon and Marinduque. Using the obtained coordinates, the location maps of validated existing Small Scale Irrigaion Projects and suitability maps were generated.

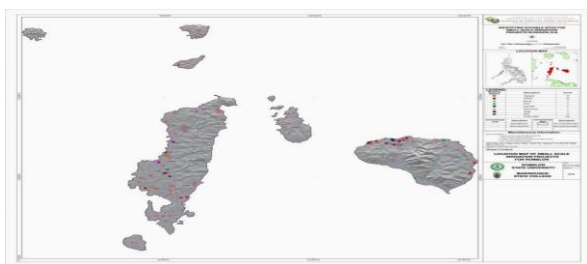


Fig. 1 Location Map of Validated Existing Small Scale Irrigation Projects in the Province of Romblon

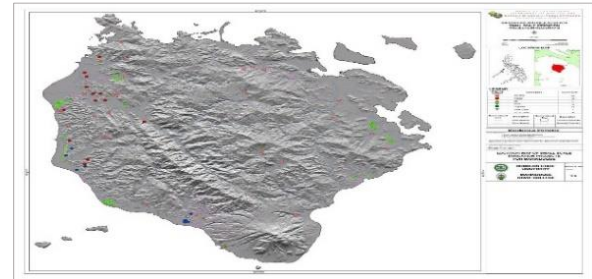


Fig. 2 Location Map of Validated Existing Small Scale Irrigation Projects in Marinduque Province

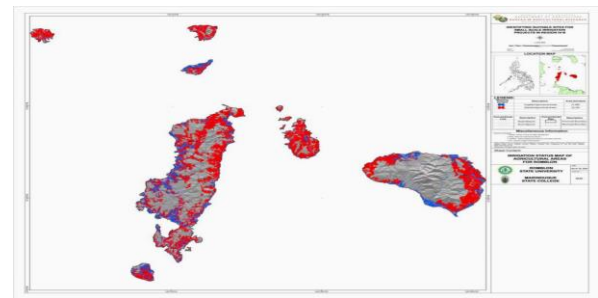


Fig. 3 Irrigation Status Map of Romblon

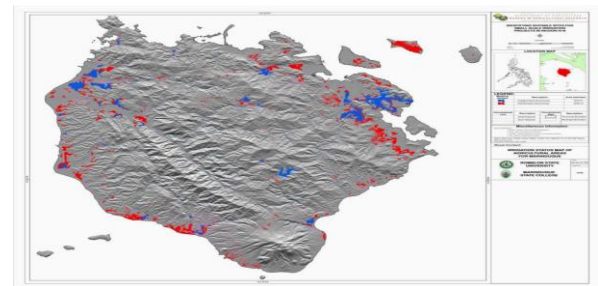


Fig. 4 Irrigation Status Map of Marinduque

Analysis shows that Romblon and Marinduque have high suitability for SFR, STW, and PISOS development.

* Oral paper presentation

SMALL FARM RESERVOIR SUITABILITY MAP

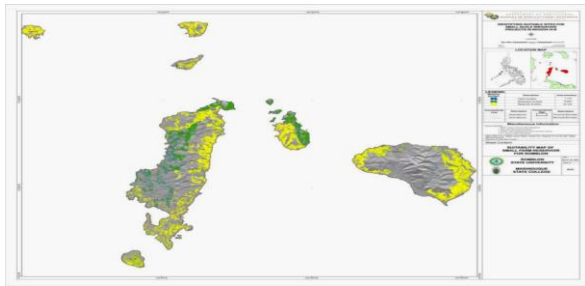


Fig. 5 SFR Suitability Map of Romblon

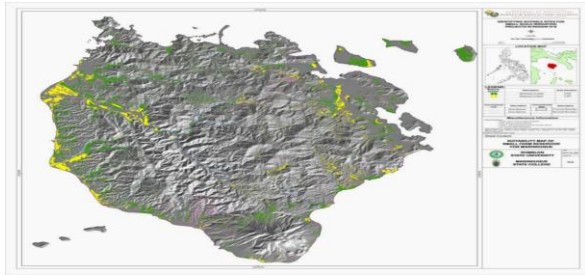


Fig. 6 SFR Suitability Map of Marinduque

PUMP IRRIGATION SYSTEMS FOR OPEN SOURCE SUITABILITY

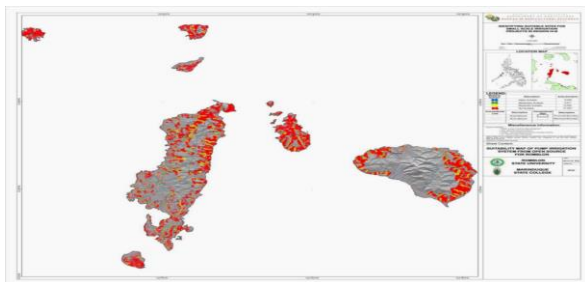


Fig. 7 PISOS Suitability Map of Romblon

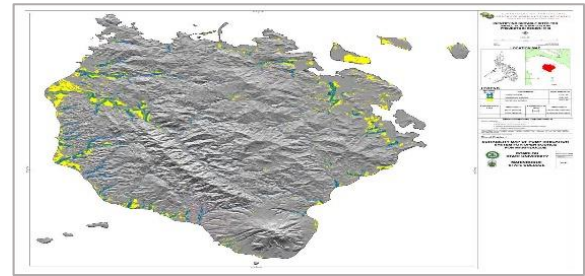


Fig. 8 PISOS Suitability Map of Marinduque

SHALLOW TUBE WELL SUITABILITY MAP

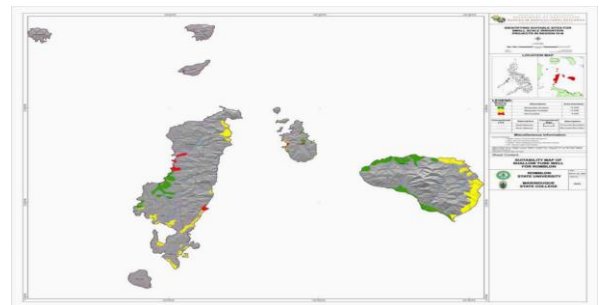


Fig. 9 STW Suitability Map of Romblon

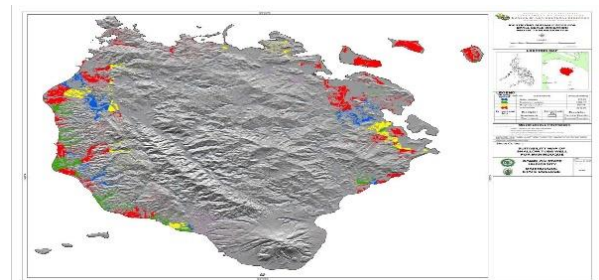


Fig. 10 STW Suitability Map of Marinduque

Keywords

Geographic Information System, remote sensing, small scale irrigation project, suitability map, thematic map.

Simulating the impacts of deficit irrigation on corn yield and water productivity using coupled DSSAT CERES-Maize and Aquacrop models*

Marilyn S. Painagan ^{1 a*} and Victor B. Ella ^{2,b}

¹ Department of Agricultural & Biosystems Engineering, College of Engineering & Information Technology, University of Southern Mindanao, Kabacan, Cotabato, Philippines

² Land & Water Resources Division, Institute of Agricultural & Biosystems Engineering, College of Engineering & Agro-Industrial Technology, University of the Philippines Los Baños, Laguna, Philippines.

^a mspainagan@usm.edu.ph, ^b vbella@up.edu.ph

Abstract

This study aimed to simulate the effects of deficit irrigation or intentional under-irrigation on corn yield and water productivity using DSSAT CERES-Maize and AquaCrop Models. The crop simulation models were calibrated and validated using observed crop production data. Both models performed satisfactorily during calibration and validation based on standard statistical indices such as RMSE, NRMSE, R², d-stat and NSE. The calibrated and validated models were then coupled and used to simulate the effect of various levels of deficit irrigation on corn yield. Model simulation results showed that a 15 % level of deficit irrigation results to maximum yield while a 60% level of deficit irrigation leads to maximum water productivity. Results suggest that maintenance of soil moisture very close to field capacity does not necessarily lead to increased crop yield and water productivity. A net application depth of 77 mm proved to be optimum when a 60% deficit irrigation is imposed. Model simulation results also showed that tasseling stage and silking stage until grain filling stage are the most susceptible to water stress. This study demonstrated that deficit irrigation is a practical water saving management strategy. The use of coupled crop simulation model (DSSAT CERES-Maize and AquaCrop) proved to be a viable tool to support decision making in corn production systems in the Philippines, especially when imposing deficit irrigation.

Keywords

AquaCrop, crop simulation, deficit irrigation, DSSAT CERES-Maize, water productivity

References

- [1] BONDAD, R. M., ELLA, V. B., SALUDES, R. B., REYES, M. R., & MERCADO, A. R. 2015. Simulating the impact of conservation agriculture on corn yield in the Philippines using the DSSAT CERES-Maize model. *The Philippine Agricultural Scientist*, 98(2): 190-201.
- [2] COSTA, J.M., ORTUÑO, M.F., CHAVES, M.M. 2007. Deficit irrigation as a strategy to save water: physiology and potential application to horticulture. *J. Integr. Plant Biol.* 49: 1421–1434.
- [3] DENMEAD O.T. AND R.H. SHAW. 1960. The effects of Soil Moisture Stress at Different Stages of Growth on the Development and Yield of Corn. *Agronomy Journal*. J-3064: 272-274.
- [4] ELLA, V.B. 2019. Annual report for the CHED-PCARI project entitled "Development of Wireless Sensor Network-Based Water Information System for Efficient Irrigation Water Management in the Philippines".
- [5] ERTEK A., B. KARA. 2013. Yield and quality of sweet corn under deficit irrigation. *Agricultural Water Management* 129: 138– 144. <http://dx.doi.org/10.1016/j.agwat.2013.07.012>.
- [6] FAO Reference Manual, Chapter 2. June 2012 – AquaCrop, Version 4.0
- [7] FERERES, E., SORIANO, M.A. 2007. Deficit irrigation for reducing agricultural water use. Special issue on 'Integrated approaches to sustain and improve plant production under drought stress' *J. Exp. Bot.* 58: 147–159.
- [8] GEERTS, S., RAES, D., GARCIA, M., MIRANDA, R., CUSICANQUI, J.A., TABOADA,

* Oral paper presentation

- C., MENDOZA, J., HUANCA, R., MAMANI, A., CONDORI, O. 2009. Simulating yield response of quinoa to water availability with AquaCrop. *Agron. J.* 101: 499–508.
- [9] GEERTS, S., DIRK RAES. 2009. Deficit Irrigation as an on-farm strategy to maximize crop water productivity in dry areas. *Agrl. Water management.* 96: 1275-1284.
- [10] HOOGENBOOM, G., JONES, J.W., PORTER, G.H., WILKENS, P.W., BOOTE, K.J., BATCHELOR, W.D., HUNT, L.A., TSUJI, G.Y. 2004. DSSAT v.4.0, vol. 1, Overview. ICASA, Univ. of Hawaii, Honolulu, USA.
- [11] HOOGENBOOM, G. 2000. Contribution of agrometeorology to the simulation of crop production and its applications. *Agric. For. Meteorol.* 103: 137–157.
- [12] LAMM, F. R., MANGES, H. L., STONE, L. R., KHAN, A. H., & ROGERS, D. H. 1995. Water requirement of subsurface drip-irrigated corn in Northwest Kansas. *Transactions of the ASAE.* 38: 441–448.
- [13] PAINAGAN, M. S., GUTIERREZ, H. M. 2014. Simulation of Corn Yield in Carmen, North Cotabato Philippines, using AquaCrop Model. *USM R&D journal.* 22(1): 1-8.
- [14] SINGH, J., KNAPP, H. V., & DEMISSIE, M. 2004. Hydrologic modeling of the Iroquois river watershed using HSPF and SWAT. *Journal of the American Water Resources Association, Illinois State Water Survey.*
- [15] TOUMI, J.; ER-RAKI, S.; EZZAHAR, J.; KHABBA, S.; JARLAN, L.; CHEHBOUNI, A. 2016. Performance assessment of AquaCrop model for estimating evapotranspiration, soil water content and grain yield of winter wheat in Tensift Al Haouz (Morocco): Application to irrigation management. *Agric. Water Manag.* 163: 219–235.
- [16] WANG, Y.-M., NAMAONA, W., TRAORE, S., ZHANG, Z. 2009b. Seasonal temperature-based models for evapotranspiration estimation under semi-arid conditions of Malawi. *Afr. J. Agric. Res.* 4: 878–886.
- [17] WILLMOTT, C. J. 1981. On the validation of models. *Physical Geography* 2: 184–194.

Assessing the impacts of climate change on irrigation diversion water requirement in the Philippines*

Lanie A. Alejo ^{1,a}, Victor B. Ella ^{2,b}, Rubenito M. Lampayan ^{2,c}, Aurelio A. Delos Reyes Jr. ^{2,d}

¹ Dept of Agric & Biosystems Engineering, College of Engineering, Isabela State University, Philippines

² Land & Water Resources Engineering Division, Institute of Agricultural & Biosystems Engineering, College of Engineering & Agro-Industrial Tech, University of the Philippines, Philippines

^a lhan_1023@yahoo.com / laalejo@up.edu.ph, ^b vbella@up.edu.ph, ^c rmlampayan@up.edu.ph,

^d aadelosreyes2@up.edu.ph

Abstracts

If temperatures continue to rise in agricultural areas as a result of climate change, the requirements for crop water and irrigation water at different levels are expected to increase as evapotranspiration rises. Consequently, to produce food, more water would be needed. This is exacerbated by the fact that, by the end of the century, rainfall is expected to decrease, thereby reducing water supplies for food production [1,2]. Based on the World Risk Survey, the Philippines ranks 3rd in terms of disaster risk [3]. The Department of Agriculture has accounted for massive economic losses due to climate change and disasters to hit PHP163.6 billion in agriculture from 2011 to 2015. A single incident of prolonged drought caused by El Niño in 2010 resulted in an economic loss of 12 billion pesos (US\$235 million, 1Php = US\$54) in agriculture that adversely affected the livelihoods of many farmers. It has been shown that climate change increases the frequency and magnitude of the El Niño Southern Oscillation phenomena [4–6].

This research evaluated the impacts of climate change on the water diversion criteria for the planning and development of irrigation systems in the Philippines. From each of the four climatic types in the region, representative sites with a high potential for irrigation development were selected. Based on evapotranspiration and effective rainfall, cropping calendars were generated. The CROPWAT software was used to evaluate the net irrigation requirement from which, based on estimated irrigation efficiencies, the irrigation diversion requirements were obtained. Climate projections recently published

using representative concentration pathways have been used as scenarios for climate change.

The results of this study showed that climate change could lead to a substantial increase in the demand for water for diversion. The increase in diversion water requirement was projected to reach +43% during dry years, +32% during normal years and +42% during wet years.

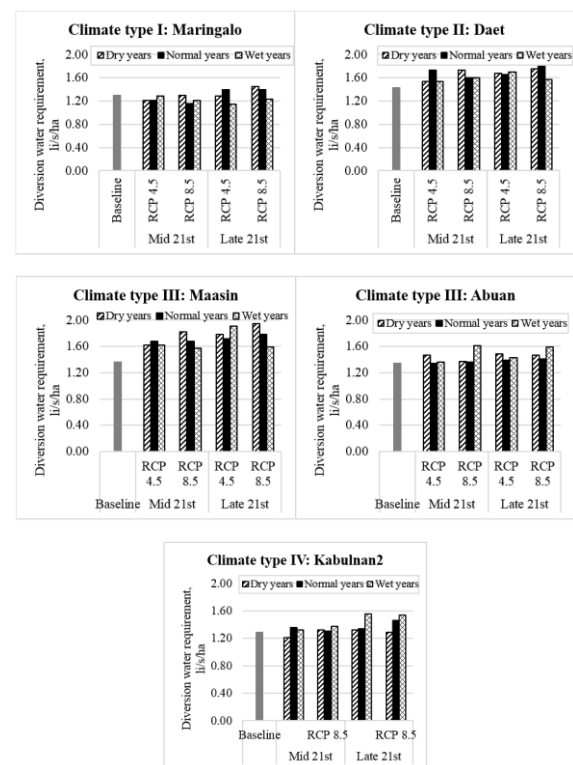


Fig. 1. The diversion water requirement across climate change scenarios

A favorable reduction in diversion water requirement due to timely occurrence of rainfall was however observed at the site with distinct wet and dry season during dry years (up to -7%),

* Oral paper presentation

normal years (up to -11%) and wet years (up to -12%). Within and across climate types, the cropping patterns differed (Figure 2).

For the planning and development of the irrigation system, the projected estimates of the diversion water requirements produced in this study could be used in particular to assess water storage requirements and design irrigable areas. Results could also be used as part of planning and design criteria for dams and reservoirs, and thereby contribute to climate proofing of irrigation systems. The use of the methods developed in this study to estimate diversion water requirements with climate change integration can be applied to other parts of the country and other parts of the world for more climate-resilient planning of water resources

Keywords

climate change, CROPWAT, diversion water requirement

References

[1] Philippine Atmospheric Geophysical and Astronomical Services Administration, Observed Climate Trends and Projected Climate Change in the Philippines, Quezon City, Philippines, 2018.

[2] Jose, A.M., Cruz, N.A., Climate change impacts and responses in the Philippines: Water resources, *Clim. Res.*, 1999, vol. 12, 77–84. <https://doi.org/10.3354/cr012077>.

[3] Heintze, H., Kirch, L., Küppers, B., Mann, H., Mischo, F., Mucke, P., Pazdzierny, T., Prütz, R., Katrin Radtke, K., Strube, F., Weller, D., World Risk Report 2018 Focus: Child Protection and Children's Rights, 2018.

[4] Lou, S., Yang, Y., Wang, H., Lu, J., Smith, S.J., Liu, F., Rasch, P.J., Black carbon increases frequency of extreme ENSO events, *J. Clim.*, 2019, vol. 32, 8323–8333. <https://doi.org/10.1175/JCLI-D-19-0549.1>.

[5] Cai, W., Borlace, S., Lengaigne, M., Van Rensch, P., Collins, M., Vecchi, G., Timmermann, A., Santoso, A., Mcphaden, M.J., Wu, L., England, M.H., Wang, G., Guilyardi, E., Jin, F.F., Increasing frequency of extreme El Niño events due to greenhouse warming, *Nat. Clim. Chang.*, 2014, vol. 4, 111–116. <https://doi.org/10.1038/nclimate2100>.

[6] Villafuerte, M.Q., Matsumoto, J., Kubota, H., Changes in extreme rainfall in the Philippines (1911–2010) linked to global mean temperature and ENSO, *Int. J. Climatol.*, 2015, vol. 35, 2033–2044. <https://doi.org/10.1002/joc.4105>.

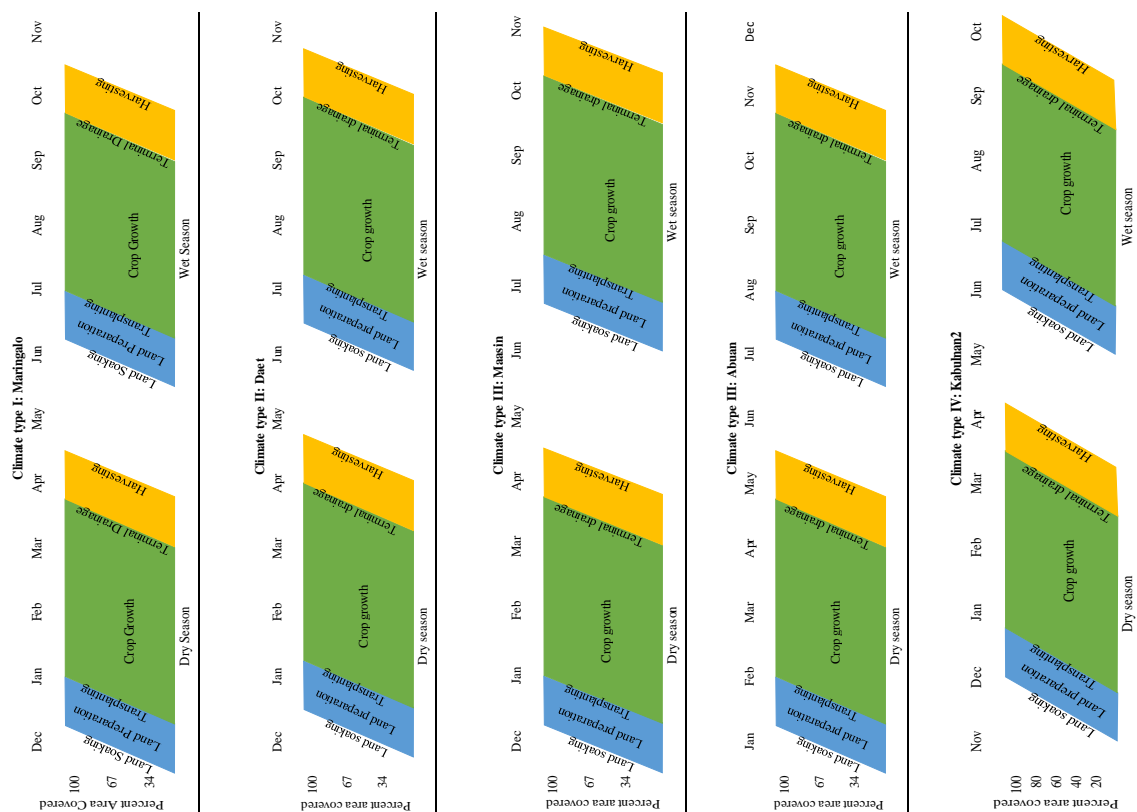


Fig. 2. Cropping calendar for each of the sites based on corresponding rainfall-potential evapotranspiration curve

GIS-based suitability analysis of small water impounding projects (SWIPs) in CALABARZON region

Rossana Marie C. Amongo ^{1,a}, Ronaldo B. Saludes ^{1,b}, Roger A. Luyun, Jr. ^{1,c}, Patrick Lemuel P. Relativo ^{1,d}, Maria Victoria L. Larona ^{2,e}, Ronnie C. Valencia ^{1,f}, Ria Salustia dG. Duminding ^{1,g}, Michel G. Acosta ^{1,h}, Kobe Conrad R. Abellera ^{1,i}, John Carlo L. Navasero ^{3,j}, Romel A. Arrobang ^{1,k}

¹Institute of Agricultural & Biosystems Engineering, College of Engineering & Agro-Industrial Technology, University of the Philippines Los Baños, Laguna, Philippines

²Center for Agri-Fisheries and Biosystems Mechanization, College of Engineering & Agro-Industrial Technology, University of the Philippines Los Baños, Laguna, Philippines

³UP Rural High School, College of Arts and Sciences, University of the Philippines Los Baños, Laguna, Philippines

^arcamongo@up.edu.ph, ^brbsaludes@up.edu.ph, ^craluyun1@up.edu.ph, ^dpprelativo@up.edu.ph,

^emllarona@up.edu.ph, ^frcvalencia1@up.edu.ph, ^grdduminding@up.edu.ph,

^hmgacosta3@up.edu.ph, ⁱkrabellera1@up.edu.ph, ^jjlnavasero@up.edu.ph, ^kraarrobang@up.edu.ph

Abstract

INTRODUCTION: Small water impounding project or SWIP is a type of small-scale irrigation system (SSIP) that collects water from rainfall and runoff to irrigate 25 to 150 ha of farmlands. It has an earth dam structure between 5 to 15 m high that are built across narrow depressions or valleys ^[1]. The rapid increase of population growth causes more demand for food production thus puts stress on the country's water resources. The agriculture sector alone utilizes about 80% of the total water withdrawal of the country, where irrigation is the largest water user ^[2]. Another factor that causes stress to water resources is the effect of climate change on temperature and rainfall occurrences. The posed threats to the limited water resources require the need to proper management and allocation of available water and proper planning for the development of new irrigation systems. The need to develop a Geographic Information System (GIS)-based maps as a decision support framework to optimize and identify locations for disaster and climate-resilient . SWIPs are one of the important irrigation sources for the country's sustainable food production. A study on site suitability analysis of SWIPs in CALABARZON was conducted using a GIS-based water resources assessment procedure for optimum water resource allocation and utilization.

METHODOLOGY: The study involved primary data collection through needs and design assessment survey of farmer-respondents

utilizing SWIPs, and geo-tagging of existing SWIPs in the CALABARZON region. Secondary data inputs were also gathered from various institutions to generate the thematic maps and the potential suitability maps for SWIPs. Location maps of existing and potential sites for the development of SWIPs in CALABARZON were generated through GIS-based mapping. The generated SWIP potential suitability map was classified as highly suitable, moderately suitable, or marginally suitable based on the range of weighted scale average ^[2].

There were eight factors considered in site suitability mapping of SWIP namely: average annual total rainfall, soil texture, slope, road accessibility, potential irrigable area (PIA), geology, watershed area, and reservoir area ^[2]. The generated thematic maps for the region were reclassified based on the suitability scales formulated during the review and planning workshop attended by researchers and experts from different Higher Education Institutions (HEIs) and government agencies^[3]. The suitability scores were computed through the GDAL raster calculator. Final reclassification of maps was performed based on the suitability ratings. The symbols used in the generated suitability map highlight the stream segments and geographical location markers of potential SWIP sites.

RESULTS & DISCUSSION: Based on the site suitability analysis presented in Fig. 1, 350 sites were found suitable for SWIP development in CALABARZON region ^[2]. Table 1 also shows the

distribution of SWIP suitable sites per province in the region.

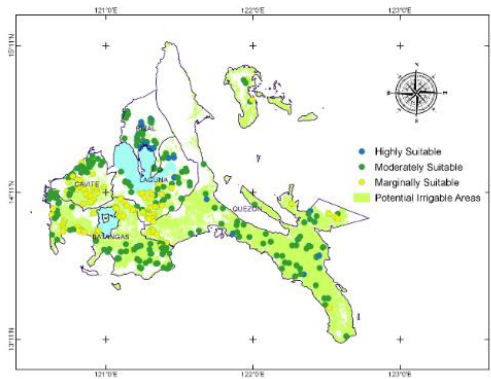


Fig. 1. Suitability map for SWIP development in CALABARZON, 2020 ^[2].

Table 1. Distribution of SWIP suitable sites per province in CALABARZON, 2020 ^[2].

| Province | Marginally suitable | Moderately suitable | Highly suitable |
|--------------|---------------------|---------------------|-----------------|
| Cavite | 25 | 30 | 0 |
| Laguna | 37 | 33 | 4 |
| Batangas | 37 | 66 | 0 |
| Rizal | 0 | 30 | 14 |
| Quezon | 14 | 54 | 6 |
| TOTAL | 113 | 213 | 24 |

The generated SSIP suitability maps were validated by superimposing the geo-tagged existing SSIPs with the spatial distribution of suitable areas in the region. There were 31 documented SWIP sites in the region and all were located within the identified suitable sites. Of these, 28 SWIPs were identified as moderately suitable sites, while the remaining 3 SWIPs were within marginally suitable sites. These results suggest that the conditions in the crop production areas of the region promote reservoirs as an on-farm water storage strategy ^[2].

CONCLUSION & RECOMMENDATIONS: The SWIP suitability analysis in the region showed 350 sites identified as suitable for SWIP development. About 7% of the potential sites identified are

highly suitable for SWIP development, around 61% are moderately suitable, and roughly 32% are marginally suitable. Validation of the generated suitability maps also showed that all the identified existing SWIPs were located within the region's suitable areas for SWIP development. The results can serve as a tool for SWIP planning and development to augment irrigation requirements for sustainable food production in the region. For future studies, the changes on the effect of rainfall variability, land use, and land cover can be considered. Generating irrigated areas for wet and dry seasons is also recommended. In addition, seasonal rainfall maps can be used instead of the annual rainfall.

Keywords

GIS-based mapping, water resources assessment, small water impounding project (SWIP), small scale irrigation projects (SSIPs)

References

- [1] Philippine National Standard. 2017. Rainwater and Runoff Management – Small Water Impounding System (PNS/BAFS/PAES 225:2017). Bureau of Agriculture and Fisheries Standards. Retrieved November 17, 2020, from <http://bafs.da.gov.ph/>
- [2] Amongo R, Saludes R, Luyun R, Jr., Relativo P, Larona M, Valencia R, Duminding R, Acosta M, Abellera K, Navasero J, Arrobang R. 2020. Site Suitability Analysis of Small Water Impounding Projects (SWIPs) in CALABARZON Region Using GIS-Based Water Resources Assessment. *Philippine Journal of Agricultural and Biosystems Engineering*, 16(2), 13-28.
- [3] Amongo R, Saludes R, Luyun R, Jr., Relativo P, Larona M, Valencia R, Acosta M, Abellera K, Navasero J, Duminding R. 2019. Utilization of Established Protocol in Identifying Potential Sites for Small Farm Reservoirs in Quezon Province, Philippines. *Philippine Journal of Agricultural and Biosystems Engineering*, 15(2), 43-54.

Poster Presentations

| Architecture & Civil Engineering | |
|--|--|
| Research on Housing Thermal Environment and Improvement of Insulation Performance in Australia | Ayaka Masuda, Yusuke Nakajima |
| Artificial Intelligence & Smart Systems | |
| Pulse Signal-Based Emotion Classification Study by Support Vector Machine | Boyao Zhang, Hisaya Tanaka |
| Development of Individual Cell Components Analysis Method for Tissue Sample with TOFS-SIMS | Kenta Shirasu, Kazuya Tamura, Masato Morita, Kumiko Nagase, Wakako Hamanaka, Masatoshi Kakihana, Tatsuo Ohira, Norihiko Ikeda, Tetsuo Sakamoto |
| 3-Dimensional Analysis of Cochlear Structure using CT Data | Hsu Sungchun, Fukuoka Yutaka |
| Using Genetic Algorithm and Gini Coefficient Neural Network Parameter Optimization | Okusu Yoshiyumi, Naoya Takahashi, Hidetoshi Saito |
| Development of a Low-cost UAV Pesticide Sprayer for Rice Production System | Eldon P. De Padua, Rossana Marie C. Amongo, Erwin P. Quillooy, Delfin C. Suministrado, Jessie C. Elauria |
| Neural-Network-based Classifier for Breast Cancer using FITR Signals obtained from Tissues | Rock Christian V. Tomas, Anthony Jay Sayat, Andrea Nicole Atienza, Jannah Lianne Danganan, Ma. Rollene Ramos, Allan Fellizar, Lara Mae Angeles, Ruth Bangaoil, Abegail Santillan, Pia Marie Albano |
| Effects of Variations in the Parameters of EBMA in Motion Estimation Accuracy | Melvin C. Ilang-Ilang (UPLB) |
| An Intelligent Control for Robot by Using Internet | Nguyen Hoang Mai, Nguyen Van Thuan, Phan Thi Mai and Le Van Hung and Nguyen Dac Quy |
| The Development of Phalaenopsis Cultivation Environmental Monitoring and Control System Based on IoT Devices | Ding-Horng Chen, Tasi-Rong Chang, Chien-Chuan Ko and Tzu-Ying Wang |
| Extracting Keywords from Videos to Build a Content-based Search and Recommended System | Shu-Chen Cheng, Jin-Fong Tseng |

POSTER PRESENTATIONS

| Energy & Transportation | |
|---|--|
| Research on Refrigeration Machine and Transportation Power of District Heating and Cooling | Satoshi Katase, Yusuke Nakajima |
| A Pilot Study on Using Rice Straw as Fuel for Paddy Drying | Maria Victoria P. Migo- Sumagang, Monet Concepcion Maguyon- Detras, Martin Gummert, Catalino G. Alfafara, Myra G. Borines, Jewel A. Capunitan and Nguyen Van Hung |
| Isolation, Characterization and Screening of Purple Non-Sulfur Bacteria for Biohydrogen Production | Floriebelle D. Querubin, Saul M. Rojas, Nacita B. Lantican, Ruby Lynn G. Ventura, Fidel Rey P. Nayve Jr., Jey-R S. Ventura |
| Comparison of Temperature and Relative Humidity as Exogenous Variables for Weekday-Load Forecasting | Michael Angelo A. Racelis, Kim Jay R. Rosano, Elvin D. Dulce, Gabriela Monica M. Gonzales, Raymond S. Mabilangan |
| Evaluation of the Capacity Value of a Solar Power Plant in the Visayas Grid, Philippines | Kyrstynne D. Ureta, Elvin D. Dulce |
| A Proposed Self-powered Data Acquisition System for an Agricultural Pump Testing Rig | John Paolo A. Ramoso, Dexter Jed S. Matibag, Thea Claire M. Chua, Lorwin Felimar B. Torrizo, Christian Paul R. Esteban, Erwin P. Quilloy, Arthur L. Fajardo, Romulo E. Eusebio |
| Food & Health Session | |
| Disease Indexing for Mango (<i>Mangifera indica</i> L. cv. 'Carabao') Fruits Using Machine Vision | Marijoree A. Sapigao, Kevin F. Yaptenco, Jessie C. Elauria, Delfin C. Suministrado, Erwin P. Quilloy |
| Effects of Thin-Layer Drying Temperature and Tempering on hybrid rice seed | Rina A. Bawar, Joanne P. Foliente, Kevin F. Yaptenco |
| Utilization of Waste Onion Leaves for Food Applications | Rona Joyce B. Landoy, Myra G. Borines, Rex B. Demafelis, Wilson T. Tan, Jewel A. Capunitan, Lisa Stephanie H. Dizon, Raymund C. Rodriguez |
| Visible and Near-Infrared spectroscopy for rapid prediction of sugarcane quality | Jeric H. Rosales, Mary Jane L. Quindoy, Kevin F. Yaptenco |
| Human Engineering | |
| Reducing Bias and Improving Contrast of Parametric Images in Positron Emission Tomography | Paulus Kapundja Shigwedha, Takahiro Yamada, Kohei Hanaoka, Kazunari Ishii, Yuichi Kimura, Yutaka Fukuoka |
| A Study of the Folding Umbrella Stick with Solar-powered LED Lighting | Zhi-Fang Xu, Hsinn-Jyh Tzeng |

| Information & Communications Technology | |
|---|--|
| Tx Power Optimization of Pico-eNB for Multiband Heterogeneous Mobile Networks | Ayumi Yoneyama, Fumiya Kemmochib, Hiroyuki Otsukac |
| GPS Positioning Accuracy Improvement by Using Drone in Relay Type GPS | Kouhei Yoshida*, Takatoshi Sugiyama |
| Electrical Characterization of Zr-based ReRAM with a Sandwiched Resistive Switching Layer | Keito Toyama, Daiki Naniwa, Shinya Aikawa |
| Fabrication of monolithic blue u-LED pixels and color conversion by phosphors | H. Chikui, S. Takeda, T. Abe, T. Onuma, T. Yamaguchi, T. Honda |
| Comparative Study on Radiation Patterns of MgO and AlN by Angle-resolved Cathodoluminescence Measurements | Y. Igari, K. Kudo, W. Kosaka, K. Kaneko, T. Yamaguchi, T. Honda, S. Fujita, T. Onuma |
| Parametric Study of Fabrication Processes of Micro-LEDs Array and Characterization of Emission Properties | Shoma Takeda, Hiroyoshi Chikui, Tomohiro Yamaguchi, Takeyoshi Onuma, Tohru Honda |
| Improving Belief Propagation Decoding Performances of Polar Codes using Permuted Factor Graphs | Naoya Takahashi, Hidetoshi Saito |
| Fundamental Research for Full Duplex Communications | Rion Okazaki, Hiroyuki Otsuka |
| Printed 8-port MIMO Antennas for 5G C-band Access Point Applications | Pin-Feng Chen, Wen-Shan Chen |
| Four-port MIMO Antennas on USB Device for 5G C-band Applications | Guan-Hua Huang, Wen-Shan Chen |
| MIMO Antennas of Coupled-fed PIFAs for Laptop Computers | Ching-Hsiang Yang, Yue-ying Lin, Wen-Shan Chen |

| Materials, Mechanical & Manufacturing Engineering | |
|--|--|
| Design Thinking Driven Requirements Elicitation Method Based on Role-Based Prototyping | Senju Nakajima, Takayuki Kitagawa, Tadaihisa Kondo, Mari Inoki |
| Fluorine Concentration Dependence on Electrical and Optical Properties of In2O3 Transparent Film | Kaito Oe, Shinya Aikawa |
| Electrochemical Evaluation of Physical/ Chemical coated Positive Electrode for Lithium-ion Batteries | Takumi Seki, Kasane Takai, Keitaro Takahishi, Hibiki Miyauchi, Shiro Seki |
| Synthesis of Polyhydroxybutyrate / Cellulose / Calcium Carbonate Bioplastic Composites Using Heat-assisted Solution Casting Method | Joemer A Adorna Jr, Ruby Lynn G Ventura, Van Dien Dang, Ruey-An Doong, Jey-R S. Ventura |
| Selection of Polyhydroxyalkanoates (PHA) Extraction and Recovery Protocol Using AHP-GRA | Princess J. Requiso, Fidel Rey P. Nayve Jr., Jey-R S. Ventura |
| Use of Portable Carrot Harvester in the Mountainous Carrot Farms of Benguet Province, Philippines | Zion Jemillinium S. Tam- awen, Rossana Marie C. Amongo, Fernando O. Paras Jr., Engelbert K. Peralta |
| Improvement of Production Resource Planning Process at DAIWA Vietnam Co., Ltd. | Phuong – Thao – Nguyen, Hong – Nguyen, Nhat – To, Huynh |
| Water Resources Engineering | |
| GIS-based Suitability Analysis of Small Water Impounding Projects (SWIPs) In CALABARZON Region | Rossana Marie C. Amongo, Ronaldo B. Saludes, Roger A. Luyun, Jr., Patrick Lemuel P. Relativo, Maria Victoria L. Larona, Ronnie C. Valencia, Ria Salustia dG. Duminding, Michel G. Acosta, Kobe Conrad R. Abellera, John Carlo L. Navasero, Romel A. Arrobang |

Pictures of the ISAT-19 Conference



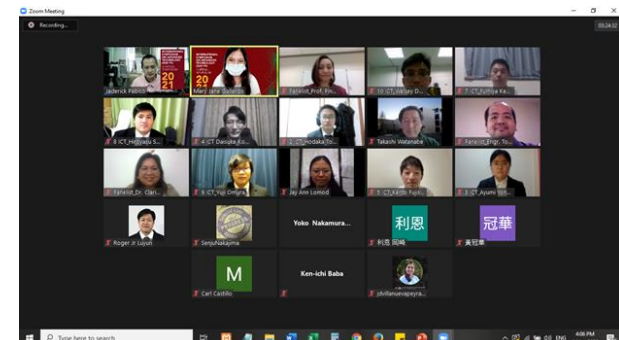
Architecture & Civil Engineering Parallel Session



Human Engineering and Artificial Intelligence & Smart Systems Parallel Session



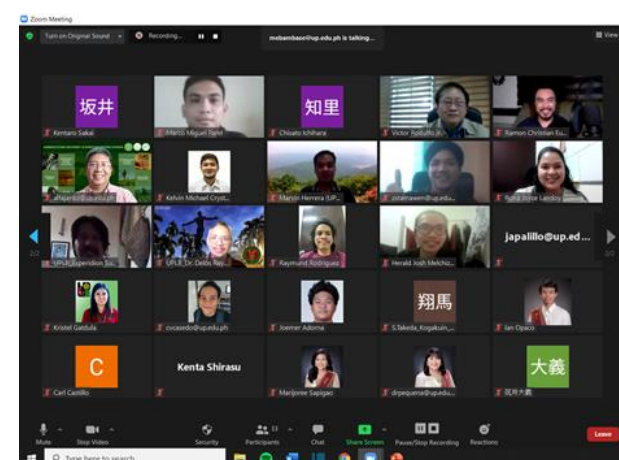
Food & Health Parallel Session



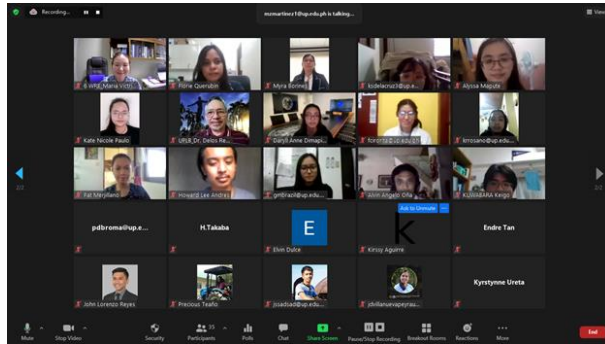
Information & Communications Tech Parallel Session



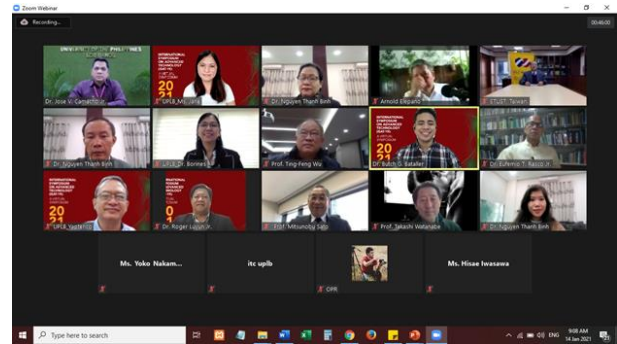
Materials, Mechanical & Manufacturing Engineering Parallel Session



PICTURES OF THE ISAT-19 CONFERENCE



Water Resources and Energy & Transportation



Plenary Presentations

YouTube Links to Video Presentations and Recorded Presentations

Audio-Visual Presentations of the ISAT Consortium Universities

<https://youtube.com/playlist?list=PLS68jiQ1Z2aTGAr3k8tO4rD77hFnnqRNo>

Plenary Session

<https://youtu.be/slc9kZUCvgA>

Parallel Sessions

Architecture & Civil Engineering

<https://youtu.be/zvMeeMshRVM>

Food & Health

<https://youtu.be/BmVPkFzakXw>

Human Engineering / Artificial Intelligence & Smart Systems

<https://youtu.be/z2ZWF3AqcjM>

Information & Communications Technology

https://youtu.be/Kao6ZiYqN_k

Materials, Mechanical & Manufacturing Engineering

<https://youtu.be/lRimyoMILQ>

Water Resources Engineering / Energy & Transportation

<https://youtu.be/ARJawxHQ4Cg>

Poster Session

<https://isat.uplb.edu.ph/events/about-isat-19/poster-presentation/>

Best Paper Awardees

| Session Topic | Title of Presentation | Authors | Ranking* |
|---|--|--|----------|
| Water Resources Engineering / Energy & Transportation | GIS-based suitability analysis of small water impounding projects (SWIPs) in CALABARZON Region | Rossana Marie C. Amongo, Ronaldo B. Saludes, Roger A. Luyun, Jr., Patrick Lemuel P. Relativo, Maria Victoria L. Larona, Ronnie C. Valencia , Ria Salustia dG. Duminding, Michel G. Acosta, Kobe Conrad R. Abellera, John Carlo L. Navasero, Romel A. Arrobang | 1 |
| Food & Health | Recirculating system with gravel and fluidized sand filter for catfish production | John Paul A. Palillo , Aurelio A. Delos Reyes Jr. | 1 |
| | Evaluation of simulation model for constant temperature deep-bed drying of hybrid rice seeds | Luther John R. Manuel , Joanne P. Foliente, Mengke Lu and Kevin F. Yaptenco | 2 |
| Architecture & Civil Engineering | Study on strong motion characteristics near active faults | Takumi Kiryu , Yoshiaki Hisada, Shinya Tanaka | 1 |
| | Development of concrete compressive strength predictive models based on non- destructive evaluation | Bien Dave Papasin , Richelle G. Zafra, Jedidiah Joel C. Aguirre, and Mark Joel B. Uaje | 2 |
| | Development of the diagnosis and repair technologies for deteriorated wood materials | Yusuke Harada , Masaki Tamura | 3 |
| Human Engineering / Artificial Intelligence & Smart Systems | Automatic cell segmentation and defect detection in electroluminescence images of solar photovoltaic modules | Keh-Moh Lin, Harshad K. Dandage , Horng-Horng Lin, You-Teh Lin and Yeou-Jiunn Chen | 1 |
| | A study on motion measurement for early screening for neurological disease | Tatsuro Sato , Shigeo Yamashita, Shinichiro Morichi, Hisashi Kawashima, Gaku Yamanaka, Satoru Kizawa, Ayuko Saito | 2 |
| | Motion analysis of infants using musculoskeletal model | Tomoaki Ichikawa , Shigeo Yamashita, Shinichiro Morichi, Hisashi Kawashima, Gaku Yamanaka, Yoshikazu Kobayashi, Ayuko Saito | 3 |

* Only student-presenters were considered for the Best Paper Awards, hence, there were limited winners in some Parallel Sessions

BEST PAPER AWARDEES

| Session Topic | Title of Presentation | Authors | Ranking |
|--|--|---|---------|
| Materials, Mechanical & Manufacturing Engineering | Development of a portable carrot harvester | Zion Jemillinium S. Tam-awen , Rossana Marie C. Amongo, Fernando O. Paras Jr., and Engelbert K. Peralta | 1 |
| | Flow control using interaction between synthetic and continuous Jets | Y. Suzuki , K. Sato, K. Nishibe, K. Yokota | 2 |
| | Compositional analysis of black carbon aerosols by means of TOF-SIMS and SNMS | Kentaro Sakai , Ryota Koiwai, Masato Morita, Tetsuo Sakamoto | 3 |
| Information & Communications Technology | A study on dynamic path establishment method using superposition coding in EON | Hiroyasu Sato , Ken-ichi Baba | 1 |
| | Performance of adaptive control CRE in multi-band heterogeneous mobile networks | Kento Fujisawa , Hiroyuki Otsuka | 2 |
| | User throughput improvement by three- dimensional beamforming in mobile systems | Yuji Omura , Hiroyuki Otsuka | 3 |

Best Poster Awardees

| Session Topic | Title of Presentation | Authors | Ranking* |
|---|---|--|----------|
| Human Engineering / Artificial Intelligence & Smart Systems | Pulse signal-based emotion classification study by support vector machine | Boyao Zhang, Hisaya Tanaka | 1 |
| | 3-dimensional analysis of cochlear structure using CT data | Hsu Sungchun, Fukuoka Yutaka | 2 |
| | Reducing bias and improving contrast of parametric images in positron emission tomography | Paulus Kapundja Shigwedha, Takahiro Yamada, Kohei Hanaoka, Kazunari Ishii, Yuichi Kimura, Yutaka Fukuoka | 3 |
| Water Resources Engineering / Energy & Transportation | Isolation, characterization, and screening of purple non-sulfur bacteria for biohydrogen production | Floriebelle D. Querubin, Saul M. Rojas, Nacita B. Lantican, Ruby Lynn G. Ventura, Fidel Rey P. Nayve Jr., Jey-R S. Ventura | 1 |
| | Potential Areas for Small Water Impounding Project (SWIP) Development in CALABARZON Region | Rossana Marie C. Amongo, Ronaldo B. Saludes, Roger A. Luyun, Jr., Patrick Lemuel P. Relativo, Maria Victoria L. Larona, Ronnie C. Valencia, Ria Salustia dG. Duminding, Michel G. Acosta, Kobe Conrad R. Abellera, John Carlo L. Navasero, Romel A. Arrobang | 2 |
| | A proposed self-powered data acquisition system for an agricultural pump testing rig | John Paolo A. Ramoso, Dexter Jed S. Matibag, Thea Claire M. Chua, Lorwin Felimar B. Torrizo, Christian Paul R. Esteban, Erwin P. Quillooy, Arthur L. Fajardo, Romulo E. Eusebio | 3 |

* All poster entries were considered for the Best Poster Awards; sessions with only one poster were still evaluated if the poster score was 75% or higher.

BEST POSTER AWARDEES

| Session Topic | Title of Presentation | Authors | Ranking |
|---|---|---|---------|
| Materials, Mechanical & Manufacturing Engineering | Synthesis of polyhydroxy-butyrate / cellulose / calcium carbonate bioplastic composites using heat-assisted solution casting method | Joemer A Adorna Jr, Ruby Lynn G Ventura, Van Dien Dang, Ruey-An Doong, Jey-R S Ventura | 1 |
| | Selection of polyhydroxy-alkanoates (PHA) extraction and recovery protocol using AHPGRA | Princess J. Requiso, Fidel Rey P. Nayve Jr., Jey-R S. Ventura | 2 |
| | Use of portable carrot harvester in the mountainous carrot farms of Benguet Province, Philippines | Zion Jemillinium S. Tam-awen, Rossana Marie C. Amongo, Fernando O. Paras Jr., and Engelbert K. Peralta | 3 |
| Food & Health | Synthesis of modified chitosan containing multi-hydroxyl group for adsorption boron | Quyen Hong Ho, Masashi Kurashina, and Mikito Yasuzawa | 1 |
| | Utilization of waste onion leaves for food applications | Rona Joyce B. Landoy, Myra G. Borines, Rex B. Demafelis, Wilson T. Tan, Jewel A. Capunitan, Lisa Stephanie H. Dizon, Raymund C. Rodriguez | 2 |
| | Effects of thin-layer drying temperature and tempering on hybrid rice seed | Rina A. Bawar, Joanne P. Foliente, Kevin F. Yaptenco | 3 |
| Architecture & Civil Engineering | Research on housing thermal environment and improvement of insulation performance in Australia | Ayaka Masuda, Yusuke Nakajima | 1 |
| Information & Communication Technology | Fabrication of monolithic blue μ -LED pixels and their color conversion by phosphors | H. Chikui, S. Takeda, T. Abe, T. Onuma, T. Yamaguchi, T. Honda | 1 |
| | Comparative study on radiation patterns of MgO and AlN by angle-resolved cathodoluminescence measurements | Y. Igari, K. Kudo, W. Kosaka, K. Kaneko, T. Yamaguchi, T. Honda, S. Fujita, T. Onuma | 2 |
| | Parametric study of fabrication of micro-LED array and characterization of emission properties | Shoma Takeda, Hiroyoshi Chikui, Tomohiro Yamaguchi, Takeyoshi Onuma, Tohru Honda | 3 |

Steering Committee

- Chair: Dr. Jose V. Camacho, Jr., Chancellor, UP Los Baños, Philippines
- Co-Chairs: Prof. Mitsunobo Sato, President, Kogakuin University of Technology & Engineering (KUTE), Japan
- Prof. Deng-Maw Lu, President, Southern Taiwan University of Science & Technology (STUST), Taiwan
- Prof. Dean Quang Vinh, Rector, Danang University of Science & Technology (DUT), Vietnam
- Members: Dr. Arnold R. Elepano, Dean, College of Engineering & Agro-Industrial Technology (CEAT), UPLB
- Prof. Takashi Watanabe, Vice President, KUTE
- Prof. Min-Tsai Lai, Vice President, STUST
- Dr. Le Thi Kim Oanh, Vice Rector, DUT

Program & Registration Committee

- Chair: Dr. Myra G. Borines, Associate Dean, CEAT-UPLB
- Co-Chairs: Dr. Kanta Tachibana, Faculty of Informatics, Department of Information System and Applied Mathematics, KUTE
- Dr. Kenjiro Sugiyama, School of Advanced Engineering Department of Applied Chemistry, KUTE
- Dr. Koji Hasegawa, Faculty of Engineering Department of Mechanical Engineering, KUTE
- Prof. Cheng-Chien Wang, Dean, College of Engineering, STUST
- Dr. Tao Quang Bang, Deputy Director, Science Research & International Cooperation Office, DUT

Technical Committee

- Chair: Dr. Kevin F. Yaptenco, Chair, Agricultural Food & Bio-Process Engineering Division, CEAT-UPLB
- Co-Chairs: Prof. Masaki Tamura, School of Architecture, Department of Architecture, KUTE
- Dr. Kazuhiro Suga, Faculty of Engineering Department of Mechanical Engineering, KUTE
- Dr. Osamu Ohno, School of Advanced Engineering, Department of Chemistry & Life Sciences, KUTE
- Prof. Ming-Tsung Tsai, Chair, Department of Electrical Engineering, STUST
- Dr. Huynh Nhai To, Chair, Department of Industrial Engineering & Management, DUT

Evaluators: Dr. Monet Concepcion Maguyon-Detras, Dr. Victoria Migo, Dr. Rossana Marie C. Amongo, Engr. Erwin Quilloy, Engr. JP Ramoso, Dr. Diana de Silva, Engr. JD Revilla, Engr. JR Ventura, Dr. Maria Victoria Larona, Engr. Jose D. de Ramos, Dr. Victor A. Rodulfo, Dr. Art Fajardo, Engr. K. Gatdula, Engr. K. Rosano, Dr. Marloe Sundo, Dr. Bernadette Lim, Engr. JC. Aguirre, Dr. Richelle Zafra: College of Engineering & Agro-Industrial Technology, UP Los Baños

Dr. Angelina Felix, Ms. Marjorie Ann Layosa: Institute of Human Nutrition & Food, College of Human Ecology, UP Los Baños

Dr. Allan Padama: Institute of Mathematical Sciences & Physics, College of Arts & Sciences, UP Los Baños

Awards Committee

Chair: Dr. Roger A. Luyun, Jr., OIC-Director, Institute of Agricultural & Biosystems Engineering, CEAT, UPLB

Co-Chairs: Prof. Ichiro Takano, Vice President, Faculty of Engineering, Department of Electrical & Electronics Engineering, KUTE

Prof. Kazuyoshi Endo, Vice President, School of Architecture, Department of Architecture, KUTE

Prof. Yasutada Imamura, Vice President, School of Advanced Engineering Department of Chemistry & Life Sciences, KUTE

Prof. Jia-Shing Shih, Asst Prof., Department of Electrical Engineering, STUST

Dr. Nguyen Hoang Mai, Department of Electrical Engineering, DUT

Technical & Administrative Support

Abril Moldez, John Eric Dao, Diana DR. Magbanua, (Information Technology Center, UP Los Baños)

John Glen S. Sarol (Office of Public Relations, UP Los Baños)

Dr. Butch G. Bataller, Mary Jane Gallardo, Joanne Foliente, Marcelina T. Miranda (College of Engineering & Agro-Industrial Technology, UP Los Baños)

Yoko Nakamura (Kogakuin University, Japan)